Ocean Waves Breaking and Marine Aerosol Fluxes

Atmospheric and Oceanographic Sciences Library

38

Stanislaw R. Massel

Springer

Ocean Waves Breaking and Marine Aerosol Fluxes

ATMOSPHERIC AND OCEANOGRAPHIC SCIENCES LIBRARY

VOLUME 38

Ocean Waves Breaking and Marine Aerosol Fluxes

Stanisław R. Massel

Institute of Oceanology of the Polish Academy of Sciences, Sopot, Poland

Springer

Stanisław R. Massel
Institute of Oceanology of the Polish
Academy of Sciences, Sopot, Poland
Powstańców Warszawy 55
Sopot 81–712
smas@iopan.gda.pl

Library of Congress Control Number: 2006940907

ISBN-13: 978-0-387-36638-8 e-ISBN-13: 978-0-387-69092-6
ISBN-10: 0-387-36638-5 e-ISBN-10: 0-387-69092-1

Printed on acid-free paper.

9 8 7 6 5 4 3 2 1

springer.com

To my wife Barbara

Preface

The atmosphere and the ocean form a coupled system which exchanges heat, momentum and water at the air–sea interface. The interface is dynamic and masses and energy are continually transferred across the air–sea interface. The energy flow from the atmosphere to the ocean generates an aerodynamically rough sea surface. If the energy flow is sufficiently intense, at some points the surface waves will lose their stability and eventually break. Breaking is a very localized and non-stationary phenomenon that is a source of vorticity and turbulence. Dissipated energy becomes available for mixing the water layers and for whitecapping of various scales. Whitecapping is a strongly nonlinear process, which involves instability of the surface waves with space and time scales several orders of magnitude smaller than those associated with gravity wave motion. Whitecaps are usually formed at or near the crests of the larger waves and occur in groups with successive crests breaking downwind of one another.

Wave breaking is the dominant generator of the 'primary' marine aerosol (sea salt) and it is a major factor in the air–sea exchange of gases (including carbon dioxide). Most of the aerosol generated from natural waters is in the form of jet and film drops from the bursting of air bubbles (Monahan and Van Patten, 1989). The enriched aerosols associated with the ejected droplets are very important in maintaining a source of salt-laden cloud condensation nuclei as well as interfacial fluxes of trace constituents, including bacteria, viruses, heavy metals, radioactivity and organic material (Kerman, 1986). The aerosol droplets, which can be very easily transported by wind over large distances, may transfer water vapour, heat, pollutants and bacteria through the air–water interface. Moreover, foam and bubbles at the surface alter the reflectivity properties of the ocean surface. Therefore, accurate optical remote sensing of ocean productivity, measured for example by chlorophyll a, must account for the statistics of breaking. The heat and mass transfer associated with aerosols are of vital importance for aquatic life and water quality, and on a global scale they are important factors for the Earth's weather and climate changes.

Much of the uncertainty in sea aerosol production and gas transfer exchange arises from weaknesses in the parameterization of wave breaking and related processes. Due to the high complexity and highly nonlinear nature of the phenomena, wave breaking remains a hydrodynamic process that is still not fully known. Therefore, in this book, the mechanisms of wave breaking are discussed,

taking advantage of modern theoretical and experimental achievements published in the professional literature, and the author's results. Special attention is dedicated to selection of wave breaking criteria, and to development of the wave breaking probability and estimation of the energy dissipation due to breaking.

Another objective of this book is to examine the relationship between wave breaking and marine aerosol fluxes and gas transfer from the sea surface. The philosophy of a close link between wave breaking and marine aerosol fluxes is adopted in this book, which provides a very comprehensive and up-to-date discussion of the fundamental scientific concepts of wave mechanics and their applications. The amount of marine aerosol rising from the sea surface depends on the coverage of the sea by breaking waves or whitecaps, and on the rate of intensity of breaking. Wind speed, commonly used in the prediction of whitecap coverage, is only one of the factors determining wave energy and the probability of breaking occurrence. It is more appropriate to seek the linkage between the percentage of sea surface covered by whitecaps and sea state characteristics, such as the significant wave height H_s and peak frequency ω_p, as well as the relation of the energy dissipated during wave breaking and the amount of aerosol fluxes. The combination of these relationships – namely, the percentage of sea surface covered by whitecaps versus the probability of breaking and the amount of aerosol fluxes versus energy dissipated during breaking – provides an opportunity to quantify the aerosol fluxes rising from a given sea basin and its possible seasonal variation.

In order to achieve both of these objectives, the evolution of scientific efforts, theoretical and experimental, in breaking wave dynamics during the past is reviewed. Moreover, the experimental results on marine aerosol fluxes in the field and in the laboratory are discussed in detail.

The book is intended for professionals and researchers in the area of ocean physics and meteorology, and as a useful book for graduate students, PhD students, postdoctoral students and engineers working on ocean environmental problems. The reader is assumed to have a working knowledge of calculus, and a knowledge of hydrodynamic and aerodynamic concepts would be helpful.

The book structure can be summarized as follows: Chapter 1 deals with the air–sea interaction in the global perspective, and the roles of surface wave breaking and aerosol fluxes for air–sea processes are elucidated.

Chapters 2–7 are dedicated to wave breaking phenomena. In particular, in Chapter 2 the mechanics of steep and breaking waves in deep water are examined, including instabilities of wave train, numerical modelling and onset of breaking. Chapter 3 deals with statistics of ocean waves and the methodology of the Gaussian and non-Gaussian sea surface description. The experimental data on mechanisms of wave breaking collected in the field and the laboratory are summarized in Chapter 4. In Chapter 5 the various breaking criteria are discussed in detail. Chapter 6 is dedicated to the important problems of energy dissipation due to wave breaking in deep waters. The experimental and theoretical methods of estimation of energy loss are given in detail. Another attempt is

made to provide some rationale behind existing methods, and to extend some methods and provide some practical outcomes from these approaches. Finally, experimental and theoretical methods of whitecap coverage prediction of the sea surface are examined in Chapter 7.

Chapters 8–11 are focused on the fundamentals of marine aerosols, a review of the existing experimental data on aerosol production, the estimation of aerosol fluxes by various methods, the links of aerosol fluxes with sea state parameters and the seasonal variation of aerosol fluxes in deep water seas.

In Appendix A, the mathematical formulae of the nonlinear surface representation and the relationships between spectral amplitudes are listed. In Appendices B and C, useful information on modern methods of experimental data analysis, namely the wavelet and the Hilbert transforms, are given. Finally in Appendix D, practical expressions for sea state characteristics and spectral moments are listed.

Some figures in the book have been adopted from previously published figures, and this is indicated in the legends. Many thanks are due to all those who gave permission to reproduce their original figures.

I apologize for the inevitable errors which may occur in this book, despite my efforts to eliminate them. Please bring these errors to my attention.

I would like to express my thanks to the Institute of Oceanology for support during the preparation of this book. I am grateful to Associate Professor Jacek Piskozub and Doctor Tomasz Petelski for commentary and very valuable discussion on the marine aerosol fluxes phenomena. I also wish to acknowledge the stimulating discussions provided by many colleagues and members of the staff of the Institute. I am grateful to Danuta Pruszczak for her expertise in preparation of the copy. Special thanks go to my wife Barbara for her support and encouragement during the writing.

Contents

Chapter 1

Basic processes near the air–sea interface

1.1 Introduction

The ocean–atmosphere system is intrinsically coupled, although feedbacks across the air–sea interface are often masked by temporal and spatial differences. Interactions between the ocean and atmosphere occur at the air–sea interface. The ocean surface forms a barrier to the exchange of heat, moisture, momentum and trace constituents (Rogers, 1995). The fundamental processes that connect the atmosphere and ocean are the energy input to the ocean by the wind, the net freshwater flux, expressed as precipitation and evaporation, and the net surface heat flux. The oceans play a substantial role in the changing radiative balance of the Earth and the climate. In particular, they affect gas and aerosol concentrations in the atmosphere as well as contemporary fluxes from the atmosphere to the ocean and from the ocean to the atmosphere. The energy from the atmosphere to the ocean surface enhances mixed layer during the circulation of the upper ocean. On the other hand, energy from the ocean affects atmospheric circulation, weather and climate. Among the influences of the oceans is their effect on gas and aerosol concentrations in the atmosphere. The global ocean is known to be a net sink of anthropogenic CO_2 and hence the oceans have effectively slowed the build-up of this greenhouse gas in the atmosphere.

Recently, the importance of connecting small-scale process studies, investigating the exchange of heat, moisture momentum and trace constituents across the air–sea interface, with the large-scale processes of global climate change and ocean circulation has been highlighted. The small-scale exchange processes are related to the global-scale problems via flux parameterizations measured at the sea surface or from satellites. It is convenient to divide air–sea interaction studies into two categories: small- and large-scale ocean–atmosphere interactions. From the large-scale perspective, quantifying and understanding the sources and sinks in the coupled ocean–atmosphere system and corresponding fluxes is

a key to determining the role played by the ocean in the global climate system. Through the late 1950s, large-scale field programmes and open ocean measurements of the fluxes were carried out, such as the Barbados Oceanographic and Meteorology Experiment (BOMEX), Atlantic Trade Winds Experiment (ATEX), Global Atmospheric Research Program Atmospheric Tropical Experiment (GATE), Joint Air-Sea Interaction Experiment (JASIN), Marine Remote Sensing Experiment (MARSEN), Storm Transfer and Response Experiment (STREX), Humidity Exchange Over the Sea (HEXOS), Marginal Ice Zone Experiment (MIZEX), Frontal Air-Sea Interaction Experiment (FASINEX), TOGA COARE experiment, and the Surface of the Ocean, Fluxes and Interactions and Atlantic Stratocumulus Transition SOFIA/ASTEX experiment (Rogers, 1995). The reader is referred to Geernaert (1990) for a more detailed overview of these studies and their results.

For the purpose of this book, the connecting small-scale processes such as the exchange of mass, heat, moisture, momentum and trace constituents across the air–sea interface are the most important. An understanding of the processes at the air–sea interface requires knowledge of how energy is transferred across the stable layers connecting the interiors of the ocean and atmosphere with their respective boundary layers.

1.2 Sea water

1.2.1 Water on Earth

The most important liquid on Earth is water. Water is a ubiquitous, life-sustaining substance covering 71% of the Earth surface. Of the Earth's total water content, some 97.2% is contained in the oceans, 2.15% is stored in ice sheets and glaciers, 0.62% is ground water, and only 0.03% flows through rivers, streams and fresh-water lakes (Strahler and Strahler, 1992). For major portions of the Atlantic, Pacific and Indian oceans, the average depth is nearly 4 km, but it is the surface water, together with the very small amount of ground water, that supports all life on land and in the oceans.

Evaporation from the oceans, which are the basic reservoirs of free water, is approximately 419,000 km^3/year, while evaporation from soil, plants and water on the continents is only about 69,000 km^3/year. The total quantity of the evaporated water, 488,000 km^3/year, must be returned annually to a liquid or solid state through precipitation over the oceans and continents. Precipitation over continents is about 37,000 km^3/year greater than evaporation. This excess of quantity flows over or under the ground to reach the sea. The hydrologic cycle is pronounced evidence of the strong link between the atmosphere and ocean. The input of energy from the atmosphere drives water motion in the form of waves and currents. Moreover, through the ocean surface, oxygen and carbon dioxide – gases vital for the growth of marine organisms – enter the ocean from the atmosphere. In contrast to the upper ocean layer, at great ocean depths

water motion is extremely slow and water temperature remains uniform and low.

1.2.2 Sea water density

Water has many unique chemical and physical properties. Unlike most substances, which contract when frozen, water expands, allowing ice to float on the surface of water basins. It is well known that water forms a necessary constituent of the cells of all animals and plant tissues. Most of the water present in living organisms acts as an irrigant, distributing nutrients and removing waste products. The principal sea water state parameter is *density*, or mass per unit volume. The density of water controls many fundamental processes in the ocean, e.g. the hydrostatic equilibrium or motion of water particles and propagation of internal waves, turbulence and mixing in water column, heat transfer, concentration of plankton and sediment transport, locomotion of marine species, and many others. Even small alterations in the density of sea water result in great changes in water flow and its thermal and chemical status. Density is normally symbolized by ρ and in the SI system it is expressed in kilograms per cubic metre (kg/m^3). For example, the density of pure water is approximately 1000 kg/m^3, being 770 to 890 times that of air at sea level (Massel, 1999).

The density of sea water is usually determined through its dependence on pressure, p, temperature, T, and salinity, S. Pressure, p, has an insignificant effect on the density of water for most applications, unless one is dealing with water at great depths within the ocean. The density is much more dependent on temperature, generally decreasing as the temperature increases. However, the density of freshwater is not a monotonic function of temperature; water density reaches a maximum at temperature of 3.98°C under normal atmospheric pressure. Normal atmospheric pressure at sea level is defined to be 1.01325×10^5 Pa at 15°C, in which 1 Pa is equal to 1 N/m^2. This anomalous dependence of the density of freshwater on temperature is a result of the specific molecular structure of water (Dera, 1992).

Salinity is another factor which influences water density. Away from coasts, the salinity of ocean water varies from 32 to 37 ppm (parts per million). The variations in salinity result from differences in the relative rates of precipitation and evaporation from the surface of the ocean. When the temperature, T, and pressure, p, are constant, density of sea water increases with salinity and the relative change in the density of sea water is roughly proportional to the change in salinity. At constant pressure and at salinity greater than ∼24.7 ppm, the density of sea water increases monotonically with decreasing temperature right down to the freezing point. At 0°C, freshwater turns into ice, and its density abruptly decreases from 999 to about 917 kg/m^3. When sea water freezes, its salt is extruded and sea ice floats like freshwater ice at the surface. A difference of 1 ppm in salinity has an effect on the density of sea water which is about five times greater than the change caused by a difference of 1°C in

temperature.

The general dependence of sea water density $\rho_w(S,T,p)$ on salinity, S, temperature, T, and pressure, p, is called the equation of state for sea water. There have been many attempts to establish the relationship $\rho_w(S,T,p)$ in the past (for more details see Dera, 1992) and the modern algorithm of determination of density for given salinity, S, temperature, T, and pressure, p, was developed by the international group of experts on standards (UNESCO, 1987). Here, only some values of $\rho_w(S,T,p)$, frequently used in the book, are given (Massel, 1999):

$$\begin{aligned}
\rho_w(0, 10^\circ, p_{norm}) &= 999.702 \text{ kg/m}^3 \\
\rho_w(35, 10^\circ, p_{norm}) &= 1026.952 \text{ kg/m}^3 \\
\rho_w(0, 20^\circ, p_{norm}) &= 998.206 \text{ kg/m}^3 \\
\rho_w(35, 20^\circ, p_{norm}) &= 1024.763 \text{ kg/m}^3
\end{aligned}$$

in which p_{norm} denotes normal atmosphere.

1.2.3 Sea water viscosity

Viscosity is a property which is a measure of a fluid's resistance to 'deformation' during motion. Within a fluid, momentum of rapidly moving particles is exchanged with the momentum of relatively slower particles. Those exchanges produce a shearing stress. In general we can write for shear stress τ

$$\tau = \mu \frac{du}{dz}, \tag{1.1}$$

in which τ is shear stress acting on the horizontal (x,y) plane. The proportionality coefficient, μ, between the shear stress, τ, and vertical shear of velocity, du/dz, is the coefficient of dynamic molecular viscosity. It has units of newtons $\times$ seconds per square metre (N s/m^2). The dynamic molecular viscosity of sea water depends on temperature, T, and salinity, S. Colder water is more 'resistant' to motion than warmer water. The dependence of μ on salinity is weaker than its dependence on temperature. A fluid which shows this direct proportionality between the applied shear stress and the resulting rate of deformation is called a 'Newtonian' fluid. Many biological materials, such as blood, synovial fluid and mucus of various consistencies, cannot be treated as Newtonian fluids. Some of them have a memory of previous shape and elasticity.

As force on an element of fluid varies with μ but the mass of that element varies with ρ, the acceleration and hence the velocity field is determined by the ratio μ/ρ, known as the coefficient of kinematic viscosity, ν

$$\nu = \frac{\mu}{\rho}, \tag{1.2}$$

where ν has units of m^2/s. For example, the kinematic viscosity for sea water of salinity $S = 35$ ppm and of temperature $T = 20$°C is 1.064×10^{-6} m^2/s. It is interesting to note that there is almost no liquid with viscosity lower than that of water, and that $\nu_{air} \approx 15 \times \nu_{water}$. Both coefficients, μ and ν, are physical

properties of fluid, independent of fluid motion. In the oceans and atmosphere, eddies and turbulent motions in the flow can be so effective in moving particles among themselves that the effects of molecular diffusion are overwhelmed. For such situations, the coefficient of kinematic viscosity, ν, is replaced by the coefficient of turbulent viscosity, A, which is several hundred to many thousand times larger. By analogy to molecular exchange, the turbulent viscosity coefficients result from the hypothesis that the turbulent momentum flux is proportional to the averaged turbulent flow velocity. Here we only note that the estimates of the turbulent viscosity coefficient in the ocean vary enormously, from 10 to 10^4 m^2/s in the horizontal plane, and from 10^{-4} to 10^{-1} m^2/s in the vertical plane. The larger values can be found for the horizontal motion on an oceanic scale such as the diffusion of mass or momentum associated with the meandering flow of the Gulf Stream (Massel, 1999).

1.3 The state of matter near the interface

1.3.1 Surface tension

At the sea surface, the most important molecular forces are those related to surface tension. Surface tension tends to reduce the area of free surfaces or interfaces, and therefore it affects the shape of spray droplets and suspended air bubbles. Surface tension γ is a force that is needed to bring molecules from the interior to the surface, and it is expressed in newtons per metre. At the air–water boundary, the surface tension is greater than that at the boundary of air with most other fluids occurring in the natural environment. The surface tension of sea water is slightly greater than that of fresh water at the same temperature, and can be expressed as follows (Kraus and Businger, 1994)

$$\gamma = (75.63 - 0.144\,T + 0.221\,S) \times 10^{-3} \quad [\mathrm{N/m}], \tag{1.3}$$

where temperature T is specified in °C and salinity S in ppt.

If the interface can be represented by a surface $z = \zeta(x, y)$ which does not deviate much from the plane $z = 0$, the relationship between increased pressure Δp and the interface curvature takes the form

$$\Delta p = -\gamma \nabla^2 \zeta. \tag{1.4}$$

The influence of the surface tension becomes dominant if the volume of bubbles and spray is relatively small. Then, the surface tension forces the bubbles and droplets to form a sphere and relationship (1.4) becomes

$$\Delta p = \frac{2\gamma}{r}. \tag{1.5}$$

1.3.2 Characteristics of moist air

In stormy weather, spray, rain or fog droplets, salt particles, and other suspended particulate matter affect to some extent the density of the moist air mixture. The equation of state for the mixture of gases with partial pressure p_n and specific concentrations C_n is (Kraus and Businger, 1994)

$$p = \sum_n p_n = R_1 T \sum_n \frac{C_n}{m_n}, \tag{1.6}$$

in which T is the absolute temperature, m_n are the molecular masses and R_1 is the universal gas constant $R_1 = 8.31436\,\mathrm{m^2/(s\,K)}$. Let us specify the vapour content of air by the humidity mixing ratio r as follows

$$r = \frac{\rho_\mathrm{v}}{\rho_\mathrm{a}}, \tag{1.7}$$

where ρ_v is the vapour density and ρ_a is the density of dry air. Therefore, the equation of state for moist air becomes

$$p \approx \rho \left(\frac{R_1}{m_\mathrm{a}}\right) T \left(1 + \frac{3}{5}\,\frac{r}{1+r}\right), \tag{1.8}$$

when ρ is the density of moist air and m_a is the mean molecular mass of the dry air mixture $m_\mathrm{a} = 28.97$. Then

$$\frac{R_1}{m_\mathrm{a}} = 287.04\ \mathrm{J/(kg\,K)}. \tag{1.9}$$

From (1.8) it follows that moist air is less dense than dry air of the same pressure and temperature. The density of ideal gases with water vapour plays a role for the definition of droplet radius r, as discussed in Chapter 8. It should be noted that evaporation causes the interface to act as a source of water vapour in the atmosphere and of salinity in the ocean. As the vapour diffuses easily through air, the molecular sublayers, close to the interface, become anomalously saline and dense, and spray droplets can be emitted from the surface with a higher salinity than bulk sea water.

Another important quantity characterizing marine aerosol particles is the potential temperature Θ, which is defined as the temperature that would be acquired by the air when brought adiabatically to a standard pressure p_0 of $10^5\,\mathrm{Pa}$. The first law of thermodynamics yields the following expression for temperature Θ

$$\Theta = T \left(\frac{1000}{p}\right)^{2/7}, \tag{1.10}$$

when pressure is expressed in millibars.

1.3.3 Sea surface temperature and the energy budget

The sea surface temperature (SST) cannot be measured directly. However, it is known that SST is often a few tenths of a degree colder than the bulk temperature of the ocean, which represents the ocean temperature some distance below the surface, where the water is well mixed. To estimate the temperature difference $\Delta T = T_\mathrm{b} - T_0$, where T_b refers to bulk temperature and T_0 is the SST, we consider first the energy budget at the surface as follows

$$Q_\mathrm{w} = F_\mathrm{n} + Q_\mathrm{a} + \mathrm{LE}, \tag{1.11}$$

in which Q_w is the heat flux in the ocean, Q_a is the sensible heat flux in the atmosphere, LE is the latent heat flux, and F_n is the net irradiance. To define the net irradiance, we denote the radiance as the radiation energy per unit time coming from a specific direction and passing through a unit area perpendicular to that direction. Hence the irradiance or radiant flux density, F_i, becomes the radiant energy that passes through a unit horizontal area per unit time coming from all directions above it (Dera, 1992; Kraus and Businger, 1994), and the net irradiance can be presented as follows

$$F_\mathrm{n} = F_\mathrm{e} + F_\mathrm{i}, \tag{1.12}$$

where F_e is the irradiance from below per unit area. To evaluate flux Q_w and temperature difference ΔT, all terms in (1.11) need to be considered. In particular, Kraus and Businger (1994) suggest the following expression for ΔT

$$\Delta T = -\frac{13 Q_\mathrm{w}}{c_\mathrm{p}\, \rho_\mathrm{w}\, u_*}, \tag{1.13}$$

where c_p is the specific heat at constant pressure and u_* is the friction velocity. For example, under the assumption of light wind conditions when $u_* \approx 0.1\,\mathrm{m/s}$, we obtain $\Delta T \approx 0.2^\circ\mathrm{C}$. It should be noted that formula (1.13) is valid at night when the short-wave radiation is zero, and $Q_\mathrm{w} = 200\,\mathrm{W/m^2}$ is approximately the daily solar radiation absorbed in the ocean at middle latitudes. However, when short-wave absorption near the surface is no longer negligibly small, the above expression cannot be applied.

The heat resulting from short-wave absorption is distributed over the ocean mixed layer by the turbulent mixing. Mixing induces some heat transport downward, which increases the temperature of the mixed layer, while the part of heat transported upward contributes to $Q_\mathrm{w}(0)$ and consequently increases the SST.

Another factor influencing the SST is evaporation and precipitation. When precipitation is greater than evaporation, water salinity decreases. The opposite is true for areas with dominant evaporation. It should be noted that the lower salinity and resulting lower density may suppress turbulence; however, the resulting stable layer will be sooner or later eroded by the wind-generated turbulence.

1.3.4 The liquid–gas interface and role of wave breaking

The air–sea boundary is not a simple continuous surface. In fact, bubbles in the water and droplets in the air extend the area of interaction between the two fluids. For bubbles and spray droplets, the Reynolds number is usually equal to unity or less. Therefore, the inertial acceleration is negligibly small and the motion through a fluid at rest is governed only by the buoyancy and viscosity. According to Batchelor (1967), the terminal fall velocity of small droplets is

$$w_{\mathrm{d}} \approx -\frac{2}{9}\frac{\rho_{\mathrm{w}}}{\rho_{\mathrm{a}}}\frac{gr^2}{\nu_{\mathrm{a}}}. \tag{1.14}$$

On the other hand, the terminal velocity of rising of a clean small bubble becomes

$$w_{\mathrm{b}} \approx \frac{1}{3}\frac{gr^2}{\nu_{\mathrm{w}}}. \tag{1.15}$$

Symbols ν_{a} and ν_{w} in the above expressions denote the kinematic viscosity of air and water, respectively. Air bubbles that rise through the sea collect surface-active material such as algae and bacteria on their surface. The resulting rise velocity of such 'dirty' bubbles becomes smaller than that of 'clean' bubbles with the same radius. Thorpe (1992) and Wu (1992) reported some empirical formulae for the rise velocity of dirty bubbles as a function of their diameter.

Water waves are generated by wind when wave heights grow with wind speed, its fetch and time of action. However, the heights of wind-induced waves do not increase infinitely, but are limited by the breaking phenomenon or energy dissipation due to bottom friction. Wave breaking occurs whenever a momentarily high crest reaches an unstable condition. The free surface breaks up as fluid appears to erupt from a point just forward of the crest and air is entrained, forming bubbles. The most obvious expression of breaking at the sea surface in deep ocean is whitecaps caused by entrained air. Wave breaking and resulting whitecaps are observed when the wind speed is greater than approximately 3 m/s. There is a lack of a universal feature identifying breaking with a large variety of scales of observed whitecaps, extending from $\mathcal{O}(1\ \mathrm{m})$ up to $\mathcal{O}(100\ \mathrm{m})$. Wave breaking is an intermittent process in space and time and its frequency depends on the severity of the sea. Nevertheless this process, occurring only over a small fraction of the ocean surface, is very significant as wave breaking over the ocean plays an important role in controlling many physical processes at the air–sea interface. In particular, the importance of wave breaking in air–sea interactions includes the following phenomena (Melville, 1996):

- reducing the height of surface waves,
- being a source of vorticity and turbulence,
- dissipating wave energy and transferring it to turbulent mixing,
- generating ocean currents using a part of wave momentum flux,

- enhancing gas and heat transfer via surface turbulence and bubble entrainment,
- generating sound at the ocean surface that can be used as a diagnostic tool for air–sea interaction studies and
- providing passive and active microwave signatures that may prove useful in remote sensing of the ocean.

The air entrainment associated with a breaker produces bubbles that are carried below the surface for possible dissolution or gaseous accretion depending on the size distribution of the bubble cloud and the saturation level of gas in the water. This mechanism provides an exchange process for the transfer of gases between the atmosphere and ocean (Csanady, 1990). When they return to the surface, the bubbles either remain stabilized in a foam patch or rupture, carrying a thin skin enriched with particles collected by impact scavenging during their rise (Blanchard, 1983).

1.3.5 Transport of gases across the interface

Turbulent mixing is the main factor for diffusion in the water body and adjacent atmospheric layer. Close to the interface turbulent motion is suppressed and the exchange of mass is mostly dependent on molecular diffusivity. The transition from one layer to another is continuous, but the resistance to the transfer of gases in particular sublayers is different, and the thin diffusive sub-layers provide the largest resistance to the transfer. The second factor, affecting the transition between the layers, is the 800-fold difference in the density of water and air. In fact the air–water boundary can be considered as the boundary flow of fluids over a solid porous wall, which helps to formulate the well justified scheme of heat and mass transfer at such interfaces. Donelan and Wanninkhof (2002) summarized the physical and chemical background to processes of gas transfer through the air–sea interface. This paper is an introductory paper in the recently published monograph *Gas Transfer at Water Surface* (Donelan et al., 2002) presenting progress in the theoretical and experimental efforts to understand and describe the fundamentals of gas transition between the atmosphere and oceans. The monograph is an excellent source of modern knowledge on this subject.

Chapter 2

Mechanics of steep and breaking waves

2.1 Introduction

Gravity surface waves, due to the nonlinear character of their motion, undergo various types of modulation on the way of propagation. Depending on the basic wave parameters, the shape of wave profile can vary, from very gentle to very steep. However, the steepening of the wave profile is not unlimited and for some wave parameters waves lose their stability and break. As in this book we are focusing on the wave breaking, it is quite appropriate to discuss first the mechanics of steep waves in some detail as steep waves represent an initial phase to breaking waves, both regular waves and irregular wind-induced waves.

In this chapter, historical and more recent attempts to describe the evolution of steep waves are discussed. In the past, a lot of attention has been given to the limiting forms of steep gravity waves. Though the theory of water waves of low or moderate steepness is well developed, the situation is still very different for surface waves whose steepness is such that the waves are close to breaking, despite great efforts made in the last 30 years, starting with the theoretical and numerical studies of Longuet–Higgins and Fox (1977, 1978), Cokelet (1977), Williams (1981) and others (see Section 2.2 for a more detail).

The experimental and numerical study of Lake et al. (1977) showed that evolution of a nonlinear wave train, in the absence of dissipative effects, exhibited the Fermi-Pasta-Ulam recurrence phenomenon, when the modulation periodically increases and decreases, and the wave form returns periodically to its previous form. Modulation was caused by the growth of the two dominant sidebands of the Benjamin–Feir instability at the expense of the carrier. The measurements showed a marked asymmetry between the upper and lower sidebands, which leads to the lower sideband increasing to an amplitude greater than that of the primary wave. The onset of the asymmetry corresponds to the onset of wave breaking.

In Section 2.3, a more recent summary of theoretical results on nonlinear wave evolution is presented. In particular, Tulin and Waseda (1999) pointed out the usefulness of the nonlinear Schrödinger equation (NSE) proposed by Zakharov (1968) to study the stability of wave motion.

In Section 2.4, the numerical methodology to represent the time history of space-periodic irrotational, nonlinear and unsteady free surface waves is addressed. More specifically, the mechanism of onset of wave breaking for modulating waves and a universal threshold of some wave parameters determining onset of breaking are proposed.

2.2 Theory of the almost-highest waves

All theoretical studies of wave hydrodynamics which are relevant to non-breaking waves are formulated for irrotational flow. However, for surface waves whose steepness is such that the waves are close to breaking the theory needs some modification. A possible limiting form for the crest of a gravity wave in which the free surface forms a sharp corner with a 120° internal angle was suggested by Stokes (1880). In a frame of reference travelling with the phase speed the fluid at the crest is at rest. This satisfies the kinematic breaking criterion that the fluid velocity matches or exceeds the phase velocity. To define the limiting flow we take polar coordinates (r, θ) with the origin at a distance a above the wave crest (see Fig. 2.1). Let us further assume that the crest is formed by two intersecting straight lines which are tangents to the real water surface curvature.

The velocity potential in the region of the crest in the polar coordinate system (r, θ) becomes (Massel, 1989)

$$\phi(r, \theta) = Br^n \sin(n\theta), \tag{2.1}$$

where B and n are the coefficients to be evaluated. As the surface is a streamline, the tangential velocity component becomes

$$u_\theta = -\frac{1}{r}\frac{\partial \phi}{\partial \theta} = 0. \tag{2.2}$$

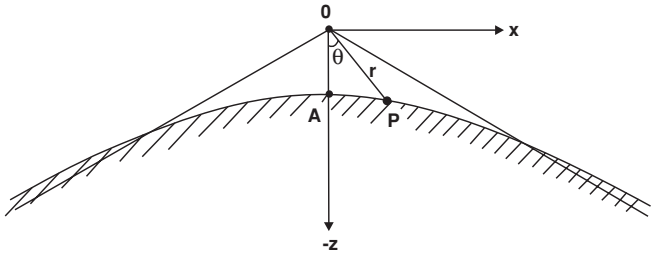

Figure 2.1: Travelling coordinate system in the physical plane.

Therefore, from (2.1) we have

$$\frac{\partial \phi}{\partial \theta} = \cos(n\theta) = 0 \quad \text{at} \quad \theta = \theta_0, \tag{2.3}$$

or

$$n\theta_0 = \frac{\pi}{2}. \tag{2.4}$$

At the free surface, pressure must be a constant. Taking this constant to equal zero, the Bernoulli equation simplifies as follows

$$\frac{1}{2}\left(u_r^2 + u_\theta^2\right) + gz = 0, \tag{2.5}$$

where u_r and u_θ are the normal and tangential velocity components, respectively, and $z = -r\cos\theta$ is the surface ordinate. Substituting velocities $u_r = -\frac{\partial \phi}{\partial r}$ and $u_\theta = -\frac{1}{r}\frac{\partial \phi}{\partial \theta}$ into (2.5) yields

$$\frac{1}{2} n^2 B^2 r^{2n-3} = g\cos\theta_0 = \text{const}. \tag{2.6}$$

Since the right-hand side of (2.6) is a constant, the power of r must be zero, namely

$$2n - 3 = 0 \quad \text{or} \quad n = \frac{3}{2}. \tag{2.7}$$

Thus from (2.4) we have

$$\theta_0 = 60^\circ \quad \text{and} \quad 2\theta_0 = 120^\circ. \tag{2.8}$$

Using now (2.6) we obtain the value of the coefficient B equal to $\frac{2}{3}\, g^{\frac{1}{2}}$.

The final form of the velocity potential now becomes

$$\phi(r,\theta) = \frac{2}{3}\, g^{\frac{1}{2}}\, r^{\frac{3}{2}} \sin\left(\frac{3}{2}\theta\right). \tag{2.9}$$

Solution (2.9) suggests that the profile approaches 120° corner flow with the velocity and acceleration components as follows (Massel, 1989)

$$\left.\begin{aligned} u_r &= -\frac{\partial \phi}{\partial r} = -g^{\frac{1}{2}}\, r^{\frac{1}{2}} \sin\left(\frac{3}{2}\theta\right) \\ u_\theta &= -\frac{1}{r}\frac{\partial \phi}{\partial \theta} = -g^{\frac{1}{2}}\, r^{\frac{1}{2}} \cos\left(\frac{3}{2}\theta\right) \end{aligned}\right\} \tag{2.10}$$

and

$$\left.\begin{aligned} a_r &= u_r \frac{\partial u_r}{\partial r} + \frac{u_\theta}{r}\frac{\partial u_r}{\partial \theta} - \frac{u_\theta^2}{r} \\ a_\theta &= u_r \frac{\partial u_\theta}{\partial r} + \frac{u_\theta}{r}\frac{\partial u_\theta}{\partial \theta} + \frac{u_r u_\theta}{r} \end{aligned}\right\}. \tag{2.11}$$

Table 2.1: Wave steepness for kinematically limited deep water waves (adapted from Massel, 1989)

Author	$\frac{H}{L}$	ka	$\frac{C}{C_0}$
Miche (1944)	0.142	0.461	1.10
Chappelear (1961)	0.1428	0.4486	1.10
Schwartz (1974)	0.1412	0.4436	1.0922
Longuet–Higgins (1976)	0.1411	0.4433	1.0923
Cokelet (1977)	0.1411	0.4433	1.0921
Longuet–Higgins and Fox (1977)	0.14107	0.4432	1.0923
Williams (1981)	0.141063	0.4432	1.09228

Substituting (2.10) into (2.11) we obtain

$$a_\theta = 0 \tag{2.12}$$

and

$$a_r = \frac{1}{2}\,g\sin^2\left(\frac{3}{2}\theta\right) + \frac{3}{2}\,g\cos^2\left(\frac{3}{2}\theta\right) - g\cos^2\left(\frac{3}{2}\theta\right), \tag{2.13}$$

or

$$a_r = \frac{1}{2}\,g. \tag{2.14}$$

The particle acceleration near the crest is directed radially downward from the crest with a magnitude of $\frac{1}{2}\,g$ in the coordinate system given in Fig. 2.1.

The solution (2.9) refers only to the steepest possible waves. When $r > 0$, the crests are still rounded. Longuet–Higgins and Fox (1977) showed that near the summit of a steep progressive gravity wave, a smooth local flow exists which satisfies the free-surface conditions and which tends to Stokes' corner flow when the radial distance r becomes large compared with the quantity $a = \frac{v^2}{2g}$, where v is the particle velocity at the crest in a reference frame moving with the wave speed.

Numerical calculations indicate that the free surface crosses its asymptote at about $\frac{r}{a} = 3.32$ and $\frac{r}{a} = 68.5$, then approaches it in very slowly damped oscillations. Between the two crossings of the asymptote, the maximum angle of slope slightly exceeds 30° and the computed value is 30.37°. This small deviation from Stokes' 30° asymptote angle provides the vertical acceleration of a particle at the crest equal to $0.388\,g$. In the far field, as $\frac{r}{a} \to \infty$, the acceleration tends to the value of $0.5\,g$, appropriate to Stokes' corner flow.

For deep water waves, a commonly quoted property of the 'highest' wave is wave steepness, i.e. the ratio of $\frac{H}{L}$, in which H is the wave height and L is the wavelength. The values obtained theoretically by various authors have been collected in Table 2.1. The steepness ka was calculated from $\frac{H}{L}$ as follows

$$\frac{H}{L} = \frac{2ak}{2\pi} = \frac{ka}{\pi}, \tag{2.15}$$

where a is the wave amplitude and k is the wave number. For completeness in Table 2.1, the ratio of nonlinear phase velocity C to the velocity C_0, calculated by the small amplitude wave theory was added. It should be noted that in the limiting steepness $\left(\frac{H}{L}\right) \approx 0.141$, the wavelength should be considered as the Stokes limiting wavelength, which is about 20% greater than that of ordinary sinusoidal waves of the same frequency. Thus, for the limiting wave height we have

$$H \approx 0.141\, L = 0.141(1.2\,\frac{g}{2\pi}\,T^2) = 0.027\, g\, T^2, \tag{2.16}$$

where

$$L = 1.2\,\frac{g}{2\pi}\,T^2. \tag{2.17}$$

Equation (2.16) is a very well known breaking criterion for regular waves. Comparison of this criterion with experimental data will be discussed in the following chapters.

Let us assume for a moment that a wave is described by the linear expression

$$\zeta = a\cos(kx - \omega t). \tag{2.18}$$

Therefore, the limiting vertical acceleration according to (2.14) becomes

$$a\omega^2 = \frac{1}{2}\,g, \tag{2.19}$$

and the corresponding slope of the limiting Stokes wave is

$$\varepsilon_{\max} = \tan\left(\frac{\pi}{6}\right) = \frac{1}{\sqrt{3}} = 0.577. \tag{2.20}$$

It should be noted that the exact maximum slope of the limiting Stokes wave, corresponding to angle 30.37°, found by Longuet–Higgins and Fox (1977), is slightly bigger

$$\varepsilon_{\max} = \tan(30.37^\circ) = 0.586. \tag{2.21}$$

Using the linearized theory of small-amplitude for obviously nonlinear steep waves can be considered as an approximation only. For example, applying the linear dispersion relation and using (2.19) we find the maximum wave steepness in deep water to be

$$\varepsilon_{\max} = (ak)_{\max} = \frac{a\omega^2}{g} = 0.500, \tag{2.22}$$

which compares with the actual value (2.20) or (2.21), and with the prediction of the nonlinear theory of Longuet–Higgins and Fox which provides the maximum steepness $\varepsilon_{\max} = 0.4432$ (see Table 2.1). So we are now in error by 12%.

Moreover, the ratio of wave height to wavelength would be

$$\frac{H}{L} = \frac{2a}{L} = \frac{ak}{\pi} = \frac{a\omega^2}{\pi g} = \frac{1}{2\pi} = 0.159, \tag{2.23}$$

corresponding to the value of 0.141, given above. Hence by adopting Stokes' criterion of (2.19) we may be in error by about 10%.

2.3 Instabilities of uniform wave trains

Theoretical and experimental studies provide convincing evidence that regular two-dimensional wave trains in deep water are liable to a number of instabilities which lead to wave breaking without external forcing, for an initial wave train which is steep enough. From Longuet–Higgins' (1978a,b) analytical studies on normal-mode perturbations of steep gravity waves it follows that there are two distinct types of instability. At low wave steepness, 'subharmonic' instabilities of the horizontal scales greater than the basic wavelength and with fairly low rates of growth appear. At higher wave steepness there are apparently local 'superharmonic' instabilities, having the horizontal scale less than the fundamental wavelength, leading directly to wave breaking. Between these two types of instabilities is an intermediate range of wave steepness where the unperturbed wave train is neutrally stable.

If we introduce a small disturbance in the form of two modes with 'sideband' frequencies, adjacent to the fundamental frequency, the sideband modes will be forced to increase exponentially due to nonlinear interaction mechanisms, and primary wave motion becomes unstable due to this form of disturbance. Such instability of periodic wave trains is known as Benjamin-Feir instability. Benjamin and Feir (1967) examined a primary, deep-water wave of finite amplitude a and frequency ω superimposed by two 'sidebands' of infinitesimal amplitude ϵa and of frequencies $\omega(1 \pm \delta)$, respectively, where ϵ and δ are small quantities. They found that motion becomes unstable and the sidebands tend to grow in amplitude at the expense of the primary wave, provided that

$$2(ak)^2 > \delta^2. \tag{2.24}$$

The rate of growth of the sidebands is given by (Longuet–Higgins, 1978b)

$$\frac{d(\ln \epsilon)}{dt} = 2\omega\delta^2 \left(\frac{a^2}{a_0^2} - 1 \right)^{\frac{1}{2}}, \tag{2.25}$$

where a_0 denotes critical amplitude resulting from (2.24). The growth of sidebands causes a slow modulation of the wave envelope with a spatial wave number Δk related to δ by the group velocity

$$\frac{\delta\omega}{\Delta k} = \frac{\omega}{2k} = C_g. \tag{2.26}$$

However, the asymptotic theory of Benjamin and Feir (1967) is valid only asymptotically for sufficiently small values of wave steepness ak and the modulation frequency δ. In particular, Longuet–Higgins (1978b) found that subharmonic instabilities of the Benjamin-Feir type are confined to waves whose 'steepness' ak lay within a certain finite range with the upper limit at $ak \approx 0.37$. The growth rate is about 14% per period, which value occurs at $ak \approx 0.32$. As ak increases beyond ≈ 0.346, wave modes become stable again. A comparison of the calculated growth rates showed good agreement with the observations reported by Benjamin (1967) in the wave steepness range $0.07 < ak < 0.17$.

Local or superharmonic instabilities having the same horizontal scale as the fundamental wave, or less, appear first when $ak \approx 0.41$. Their rates of growth are much higher than for the 'subharmonic' case and these instabilities lead directly to the overturning of the free surface and to wave breaking. Unlike Benjamin–Feir instability, superharmonic instability is not symmetric in the sidebands, but arises as a function of the upper sideband and the primary wave, being strongly localized near breaking.

The experimental and numerical study of Lake et al. (1977) showed that evolution of a nonlinear wave train, in the absence of dissipative effects, exhibited the Fermi-Pasta-Ulam recurrence phenomenon, where the modulation periodically increases and decreases, and the wave form returns periodically to its previous form. Modulation was caused by the growth of the two dominant sidebands of the Benjamin-Feir instability at the expense of the carrier. For small steepness, the original three-wave system was almost recovered. When the initial steepness is large enough, wave trains experience strong modulations followed by demodulations; however, the spectral peak is downshifted to a lower sideband. This is the frequency downshift phenomenon.

As we are mostly interested in breaking waves, the data on wave trains leading directly to wave breaking are very valuable. In particular, Melville (1982) undertook a laboratory experiment with waves generated by a hydraulically actuated servo-controlled paddle driven by a sinusoidal signal generator. For ak in the range 0.16–0.29, a uniform deep-water wave train undergoes a Benjamin-Feir instability with the modulation frequency predicted by Longuet–Higgins (1978b). The measurements showed a marked asymmetry between the upper and lower sidebands, which leads to the lower sideband increasing to an amplitude greater than that of the primary wave. The onset of the asymmetry corresponds to the onset of wave breaking. This asymmetry extends to the higher harmonics of the primary wave, and there is a marked reduction of the energy in these upper sidebands in the breaking region. For $ak \geq 0.31$, a full three-dimensional instability dominates the Benjamin-Feir instability and leads rapidly to breaking.

A more recent summary of theoretical results on nonlinear wave evolution was presented by Tulin and Waseda (1999), who pointed out the usefulness of the NSE. The NSE well describes the recurrence process, while the frequency downshift phenomenon is not predicted by solutions of this equation. Dysthe (1979) and Trulsen and Dysthe (1996) extended the NSL equation to broader bandwidths, and a further useful modification of the Zakharov equation was proposed by Krasitskii (1994) through his reduced four-wave interaction model. Fully nonlinear computations by Tulin and Waseda (1999) showed that Krasitskii's Hamiltonian type equation predicts correctly the major features of the increase of energy in the lower sideband relative to the upper sideband. They found that the spectral peak downshifting to a lower sideband appears despite the absence of breaking. This fact demonstrates the role of the balance between momentum losses and energy dissipation in the shifting of energy between sidebands.

Tulin and Waseda (1999) found that most of the experiments on wave instability were conducted for a range of steepnesses, but with a single fixed or naturally determined modulational frequency. This means that the monochromatic wave-generator motion was not modulated, and this modulation naturally evolved from background noise. To examine the evolution of wave groups with much wider parameter range, Tulin and Waseda performed an experiment for waves with wavelengths of 1–4 m, initial steepnesses $\varepsilon = ka = 0.1-0.28$ and normalized sideband frequency differences $\frac{\delta\omega}{\varepsilon\omega} = (0.1-1.5)$. Two types of experiments have been considered, i.e. the 'unseeded' experiment where modulation evolves naturally from background noise and the modulational frequencies are naturally determined, and the 'seeded' experiment where modulation is imposed at the wave generator, which provides the opportunity to change not only the sideband frequencies but also the initial sideband amplitudes and the strength of modulation.

In the 'seeded' experiment, the wave train in its initial stage is represented as follows (Tulin and Waseda, 1999)

$$\zeta = a_c \sin(\omega_0 t) + b_+ \sin(\omega_+ t + \varphi_+) + b_- \sin(\omega_- t + \varphi_-), \tag{2.27}$$

in which ω_0 is the carrier frequency, ω_+ and ω_- are the upper and lower sideband wave frequencies, respectively, φ_+ and φ_- are the corresponding phases and b_+ and b_- denote the amplitudes of the upper and lower sideband perturbations, which satisfy the following relation

$$a_0^2 = a_c^2 + b_+^2 + b_-^2, \tag{2.28}$$

in which a_0 is the amplitude of the equivalent wave train with initial steepness $\varepsilon = a_0 k$.

The modulational instability is a result of interaction among the above three monochromatic wave trains of the following frequencies: carrier (ω_0), upper (ω_+) and lower (ω_-) sidebands satisfying the following conditions

$$\left.\begin{aligned} 2\omega_0 &= \omega_+ + \omega_- \\ \omega_\pm &= \omega_0 \pm \delta\omega \\ 2k_0 &= k_+ + k_- + \Delta k \end{aligned}\right\}, \tag{2.29}$$

where Δk is a slight mismatch of the wave number from Phillips' four wave resonance conditions (Phillips, 1977).

The corresponding initial growth rate

$$\beta_x = \frac{d(\ln a_0)}{d\,(kx)} \tag{2.30}$$

is predicted by Benjamin and Feir (1967) in the form

$$\beta_x = \beta_{BF} = \varepsilon^2\,\hat{\delta}(2 - \hat{\delta}^2)^{1/2}, \tag{2.31}$$

where $\hat{\delta} = \frac{\delta\omega}{\varepsilon\omega_0}$. The instability requires that $0 < \hat{\delta} \leq \sqrt{2}$, and the maximum growth appears when $\hat{\delta} = 1.0$ and $\varphi_+ = \varphi_- = -\frac{\pi}{2}$.

Krasitskii's (1994) four-wave reduced equation yields the growth rate in the form

$$\beta_K = \varepsilon^2 \left(C_+ C_-\right)^{1/2} \sin\varphi, \tag{2.32}$$

in which

$$C_+ = \left(\frac{\omega_0}{2k_0}\right)\left(\frac{\omega_-}{2k_-}\right)^{1/2}\left(\frac{\omega_+}{2k_+}\right)^{-3/2} T_{1123}, \tag{2.33}$$

$$C_- = \left(\frac{\omega_0}{2k_0}\right)\left(\frac{\omega_+}{2k_+}\right)^{1/2}\left(\frac{\omega_-}{2k_-}\right)^{-3/2} T_{1123}, \tag{2.34}$$

$$\begin{aligned}\cos\varphi \;=\; & 0.5\left\{\frac{\Delta k}{\epsilon^2 k} - \left[\frac{\omega_0}{2k_0}\left(\frac{k_+}{\omega_+}\right) T_{1212}\right.\right. \\ & \left.\left. +\; \frac{\omega_0}{2k_0}\left(\frac{k_-}{\omega_-}\right) T_{1313} - 2T_{1111}\right]\right\}\left(C_+ C_-\right)^{-1/2},\end{aligned} \tag{2.35}$$

where T_{1111}, T_{1212} and T_{1123} are the normalized interaction coefficients given in Krasitskii (1994).

In Fig. 2.2, the most unstable modulational frequency, resulting from various theoretical solutions, is presented as a function of initial steepness ε. The

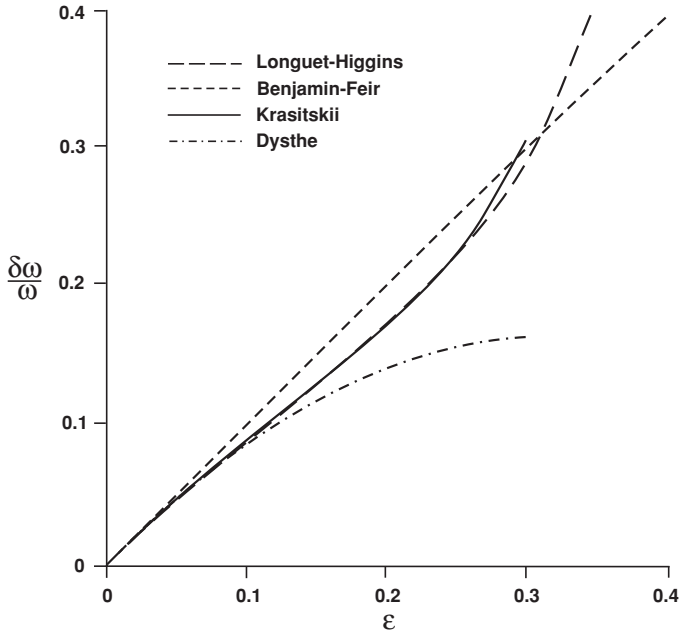

Figure 2.2: The most unstable modulational frequency as a function of wave steepness ε (adapted from Waseda and Tulin, 1999).

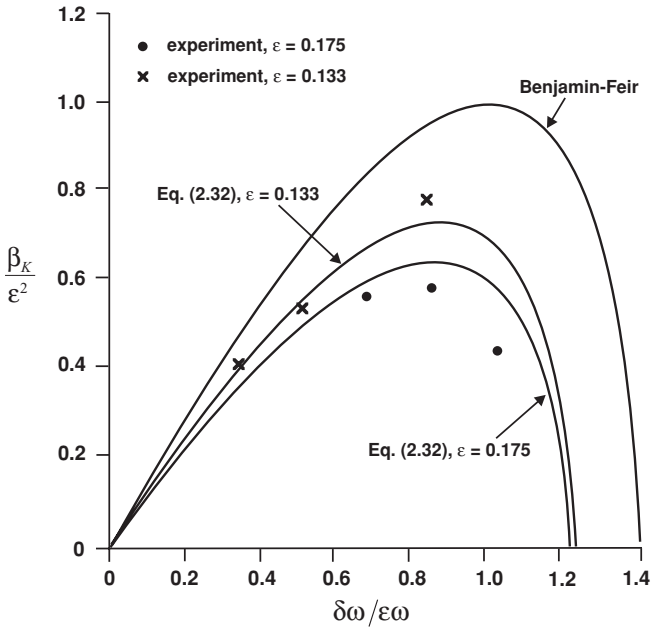

Figure 2.3: Growth rate of the sidebands for two-wave steepnesses (adapted from Waseda and Tulin, 1999).

comparison indicates that Krasitskii's solution agrees very well with the exact theory of Longuet–Higgins (1980), in which the frequency of the fastest growing instabilities have been determined precisely. In Fig. 2.3 the growth rate of the sidebands is shown for waves of frequency $\omega_0 = 1$ Hz and initial steepness $\varepsilon = 0.133$ and 0.175. The experimental data of Waseda and Tulin (1999) have been compared with the theoretical predictions of Benjamin and Feir (1967) and Krasitskii (1994). Clearly Benjamin and Feir's theory overestimates the growth rate but Krasitskii's solution agrees very well with measurements.

Waseda and Tulin (1999) also reported some results on the influence of wind on the growth rate. They found that in the 'unseeded' case (modulation naturally evolves from background noise), the growth rates increase for all wind speeds. However, above 8.5 m/s, the growth rate started to decrease, while still being larger than without wind. The estimated growth rates agree very well with prediction by Krasitskii's theory. In the case of seeded experiments, the wind induces the change of the inviscid growth for a given modulational frequency and change of this frequency is a function of the wave's age. A combination of both effects determines the enhancement or suppression of the modulational instability. For moderate and old wind sea waves, say when $u_*/C < 0.2$, in which u_* is the friction velocity and C is the phase speed the net effect of wind on modulational instability is small.

Tulin and Waseda conducted two separate series of experiments on the evolution of wave groups with breaking effects. In the first one, waves of 1.2 m length,

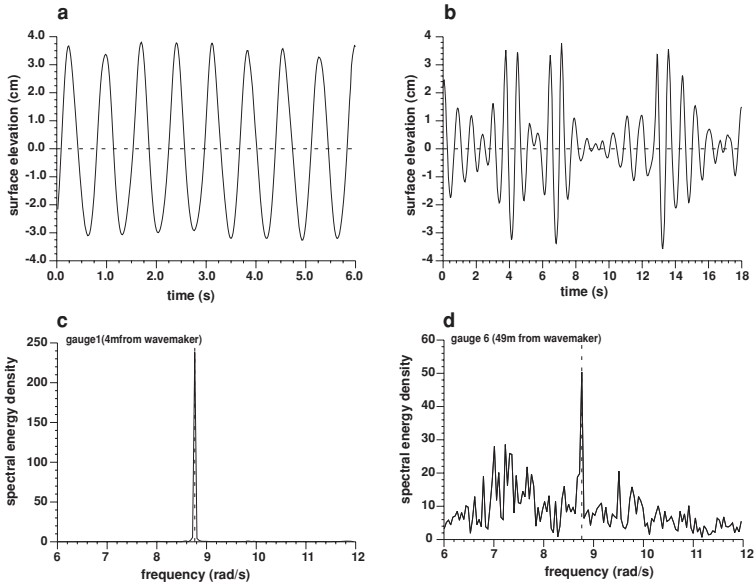

Figure 2.4: Disintegration of the regular wave train in the laboratory channel (adapted from Massel, 2001b).

steepness $\varepsilon = 0.133$ and normalized sideband frequency differences $\hat{\delta} = 0.785$ were used. In the second series, wavelength was equal to 2.3 m with steepness $\varepsilon = 0.12 - 0.28$ and $\hat{\delta} = 0.1 - 1.5$. They found that waves did not break in a strictly two-dimensional pattern across the tank, and spatially periodic patterns were observed when alternate breaking occurred at the sides and then at the tank centre. The wave steepness of $\varepsilon = 0.133$ corresponds closely to the values typically appearing in the ocean. The effect of breaking increases the asymmetry $(b_- - b_+)$. The energy residing largely in the carrier wave is divided roughly between the original carrier and the lower sideband. The evolution of longer waves indicates that near peak modulation the lower sideband amplitude exceeds the upper sideband amplitude. The amplitudes of both sidebands start to deviate earlier than the onset of breaking. In particular, asymmetric development of sidebands was seen earlier for the case of recurrence without breaking. This means that the asymmetric growth of the sidebands does not require the appearance of breaking. The energy difference between the lower sideband and the upper sideband remains large when breaking is present but returns to zero when no breaking occurs. The dependence of maximum wave steepness at breaking $\varepsilon_{\max} = \frac{kH}{2}$ on the initial steepness ε is almost linear in the ε ranges from 0.1 to 0.3 when the steepness $\frac{kH}{2}$ changes from 0.25 to 0.35 with some scatter.

Figure 2.4 shows the simple case of the 'unseeded' laboratory experiment on mechanically generated waves (Massel, 2001b). Two stations in the wave flume, 1 and 6, were located at 4 m and 49 m from the wavemaker, respectively.

Incident waves of height $H = 0.06$ m and frequency $\omega_0 = 8.76318$ rad/s were generated in water depth of 0.4 m, thus steepness $ka = 0.235$. The comparison of both records clearly indicates that an initially sinusoidal wave train (see Fig. 2.4a) undergoes substantial modifications with a strong grouping at station 6 (see Fig. 2.4b). This signal disintegration is also seen in the spectral structure of both records (see Fig. 2.4c and d for stations 1 and 6, respectively) when wave energy, initially concentrated at the wavemaker frequency ω_0, after propagating a distance of 45 m, redistributes over a broad spectrum.

It should be noted that Huang et al. (1999) argued that the commonly used Fourier spectrum is a very poor method to analyse the downshift phenomenon and shift of peak of the frequency spectrum as the Fourier spectrum is not sensitive to local change of frequency. On the other hand, the frequency downshift during wave evolution is not a slowly varying process, but rather a sudden jump. This fact creates the main difficulty for theoretical analysis by NSE type models and their modifications which are based on a slowly varying phase, frequency and amplitude. Therefore, Huang et al. (1999) suggested using analysis based on the Hilbert Transform in which a variation of frequency can be defined much more precisely and locally. More information on the Hilbert Transform is given in Chapter 4 and Appendix C.

Another form of instability, leading to wave breaking, was observed by Duncan et al. (1994a,b) and considered theoretically by Longuet–Higgins (1990, 1994). In this case, spilling breakers with wavelengths of 2 m or more were generated. Parasitic capillary waves tend to form on the forward face of the wave, at a point some way ahead of the crest. The flow beneath the capillaries separates and the crest quickly becomes turbulent. The fluid in the crest advances down the forward face of the wave without any overturning of the free surface. Longuet–Higgins argued that the parasitic capillaries produce a rectified vorticity which is swept back into the crest of the wave. The resulting shear flow is unstable and breaks into shear waves and then into turbulence. In the final stage, as was observed by Koga (1982), flow appeared to separate from the free surface along a line making angles of 10° to 50° with the horizontal line. This line forms a boundary between the relatively smooth flow ahead of the separation line, and a rough, apparently turbulent region behind the line. Koga's observations are compared with a theoretical model of local flow separation in the immediate neighbourhood of the point of separation, and several features of the flow separation near the crests of steep waves are in agreement with Longuet–Higgins' (1994) model.

It should be noted that in the natural conditions, better known instabilities such as whitecaps develop on the forward face of progressive gravity waves having a wavelength greater than a few metres superimposed very short wavelengths, less than about 10 cm, with pockets of air in the waves troughs. All these instabilities contributing to the variable amplitude and short crests of deep-water waves make the attempts to develop simple breaking criteria, such as are known for waves on beaches, very difficult (see Chapter 5 for more details).

2.4 Numerical modelling of steep waves and their evolution to breaking

2.4.1 Note on second-order mechanically generated waves

Many computational studies have been motivated by experiments in wave flumes. However, laboratory studies of surface waves are complicated due to contaminations contributed to the wave motion by wavemakers, as simple harmonic motion produces a wave train not only with the wavemaker's frequency but also with its higher harmonics. Massel (1996b) examined a possible maximum wave height in a regular mechanically generated wave train propagating over constant water depth. When restricting ourselves to the second order of approximation, surface elevation can be written in the form

$$\zeta(x,t) = a\cos(kx-\omega t) + a^{(2)S}\cos 2(kx-\omega t) + a^{(2)F}\cos(lx-2\omega t+\pi), \quad (2.36)$$

in which a is the amplitude of the first harmonic, $a^{(2)S}$ is the second bound harmonic and $a^{(2)F}$ is the second free harmonic. The corresponding wave numbers k and l satisfy the following dispersion relations:

$$\omega^2 = gk\tanh(kh) \quad \text{and} \quad 4\omega^2 = gl\tanh(lh). \quad (2.37)$$

It is most likely that waves start to break at points in which $\zeta(x,t) = \zeta_{\max}$. To find the distance $x = x_{\max}$ and time $t = t_{\max}$, corresponding to the wave breaking, we adopt a coordinate system moving with phase speed $C = \frac{\omega}{k}$. In this system (2.36) takes the form

$$\zeta(x,t) = a + a^{(2)S} + a^{(2)F}\cos[(l-2k)x+\pi]. \quad (2.38)$$

Thus

$$x_{\max} = \frac{(2n-1)\pi}{l-2k} \quad \text{and} \quad t_{\max} = \frac{(2n-1)\pi k}{(l-2k)\omega}. \quad (2.39)$$

From the above relationships it follows that the repetition distance L_{r} between two succeeding maxima of the wave profile is

$$L_{\mathrm{r}} = \frac{2\pi}{l-2k}. \quad (2.40)$$

It should be noted that the distance L_{r} also depends slightly on wave amplitude (Longuet–Higgins, 1977), but for simplicity this dependence was here omitted.

Due to higher harmonics generation, the kinematic breaking criterion at $x = x_{\max}$ and $t = t_{\max}$ takes the form (Massel, 1996b)

$$u(x_{\max}, t_{\max}) = C, \quad (2.41)$$

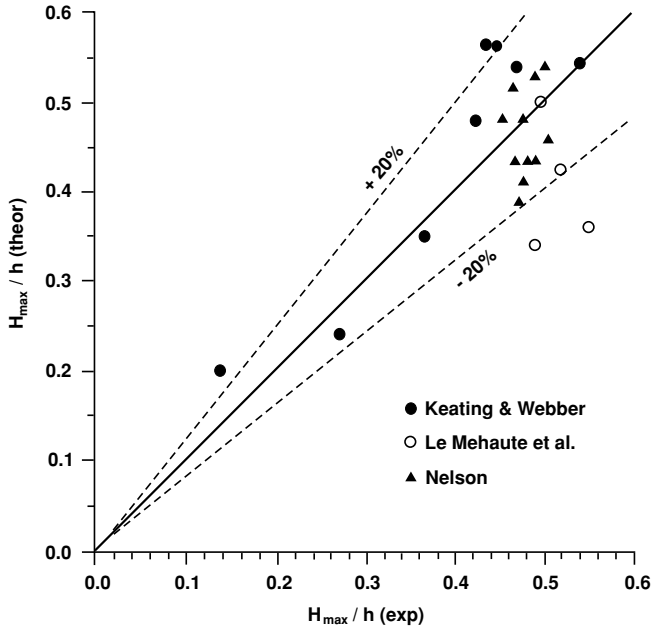

Figure 2.5: Comparison of theoretical and experimental maximum wave heights (adapted from Massel, 1996b).

or

$$\frac{gka}{\omega}\,\frac{\cosh k(\zeta_{\max}+h)}{\cos kh}+\frac{3}{4}\,\omega ka^2\,\frac{\cosh 2k(\zeta_{\max}+h)}{\sinh 4(kh)}$$
$$+\,\frac{gla^{(2)F}}{2\omega}\,\frac{\cosh l(\zeta_{\max}+h)}{\cosh(lh)}=C, \tag{2.42}$$

in which u is the horizontal component of the orbital velocity at the wave crest. Comparison of the maximum wave height resulting from the above condition with the experimental one is shown in Fig. 2.5. Discrepancies between experiments and theory are less than 20%.

2.4.2 Numerical modelling of steep wave evolution

In computational studies, steep waves are usually formed by applying a point pressure disturbance at the wave surface or are obtained from sufficiently energetic initial conditions. Longuet–Higgins and Cokelet (1976) in their pioneer study developed a new method for following the time-history of space-periodic irrotational, nonlinear and unsteady free surface waves. Basically the method involves solving an integral equation along the fluid surface to determine the spatial dependence of the motion and the new normal component

of velocity at each time step. The potential theory is used by adopting a Eulerian form and the marked particle of the Lagrangian description by following the quality of the particles and their Eulerian velocity potential through time. When the application of surface pressure is raised to an energy level exceeding the maximum for a steady progressive wave, the wave develops in time, ultimately turning over and plunging towards the forward face of the wave.

Other unsteady numerical computations, available in the literature, all follow Longuet–Higgins and Cokelet (1976) in using the boundary integral method. However, in these solutions, more robust, more accurate, and more efficient integration schemes have been developed and analytical solutions for free-surface flows approaching plunging breakers have been proposed. For example, Longuet–Higgins (1983a) gave a semi-Lagrangian representation of the jet in the form of a Dirichlet hyperbola which is ejected from the crest of a breaking wave. Peregrine et al. (1980) discovered from numerical computations that the water rising up the front of the wave into the jet is subject to large acceleration with maxima around $5\,g$, where g is the gravitational acceleration. Moreover, New (1983) found that a certain region of the surface profile beneath the overturning crest of a plunging breaker can be well approximated by an ellipse with axes in the ratio $\sqrt{3}$. Another solution for the same region was proposed by Longuet–Higgins (1982). It should be noted that all these models accounted for only a limited part of the wave profile. To overcome this limitation, Greenhow (1983) developed a solution combining both the ellipse model of New and the jet model of Longuet–Higgins. This model describes the forward face, loop under overturning wave, front jet and rear of the wave in a fairly realistic way. Comparison of Greenhow's model with the numerical breaking-wave profiles of Vinje and Brevig (1980) shows a good agreement.

In the previous section we found that the subharmonic instabilities of the Benjamin-Feir type were found to be confined to waves with steepness ak within a finite range with the upper limit $ak \approx 0.37$, and local or superharmonic instabilities appear when $ak \approx 0.41$ and they lead directly to breaking. Longuet–Higgins and Cokelet (1978) carefully examined the growth rates of each type of instability, employing their time-stepping method (Longuet–Higgins and Cokelet, 1976) where waves are treated as theoretically free waves under the simplest possible conditions of constant and uniform pressure at the free surface. Calculations confirmed that 'local' superharmonic instabilities lead directly to wave breaking with final overturning (see figures 15 and 18 in their paper). In two computational examples they found also that waves of even lower amplitude than $ak = 0.25$ will develop subharmonic instabilities to the point of breaking with a shortening of the individual wavelength. The crest profiles for the overturning wave when $ak = 0.41$ and $ak = 0.25$ are very similar, suggesting that the dynamics of the final stage of overturning are determined mainly by local conditions near the wave crest.

Dommermuth et al. (1988) reported the results of high-resolution experiments and computations to study steep and overturning gravity waves produced by a piston wavemaker in a wave flume. In the numerical simulation, a refined mixed Eulerian–Lagrangian scheme under the assumptions of potential flow was used. Similarly to the approach of Longuet–Higgins and Cokelet (1976), a dynamically controlled time-stepping procedure was applied to capture the large accelerations in the breaking waves. The numerical simulation compared extremely well with the experimental measurements for free-surface elevations, and for horizontal and vertical velocities below and above the still-water level. This good agreement confirms the validity and usefulness of nonlinear potential-flow computations for predicting steepening and overturning waves in the ocean.

The steepening and breaking of deep water waves was also a subject of numerical studies by Schultz et al. (1994). The solution of the initial boundary value problem was described by a complex potential $w(z) = \phi + i\psi$, in which ϕ is the velocity potential and ψ is the stream function in the complex plane z. At every time step, unknown boundary values of velocity potential ϕ are found using the Cauchy integral theorem. To study breaking onset, three different experimental configurations have been considered, i.e. converging sidewalls, a submerged disturbance and wave focusing. When the complex potential became known along the domain boundary, the solution was stepped forward in time using the Bernoulli equation and the kinematic boundary conditions, in a way similar to Vinje and Brevig (1980). This solution enabled the development of breaking onset criteria based on the square root of the potential energy calculation rather than on peak-to-peak wave height (or steepness) determination. Schultz et al. (1994) concluded that the rms potential energy computed over a local wavelength provides significantly less scatter for the various breaking scenarios they investigated. They also suggested an absolute breaking criterion as the ratio of potential energy/total wave energy exceeding 0.52. However, this kind of criterion does not appear to be valid in rotational flows, where the ratio potential energy/total wave energy has been shown to vary significantly as a function of the strength of background vorticity (Teles da Silva and Peregrine, 1988). Moreover Millinazzo and Saffman (1990) reported significant changes to the wave shape and hence the potential energy in the presence of a surface shear layer. Therefore, it is unlikely that a criterion involving a potential energy threshold can be valid universally. It can be seen that this kind of criterion also fails to explain the nature of instability.

The observed strong connection between sideband instability and wave breaking was supported by numerical calculations of Cointe and Boudet (1991). They studied the correlations between wave breaking and wave grouping, since there is growing evidence that wave groups at sea are a consequence of sideband instability when the dispersive properties of surface waves leads to modulation of the wave envelope (Tulin and Li, 1992). The observed connections are summarized in Fig. 2.6. More information on the influence of wave groups on wave breaking will be given in the next section.

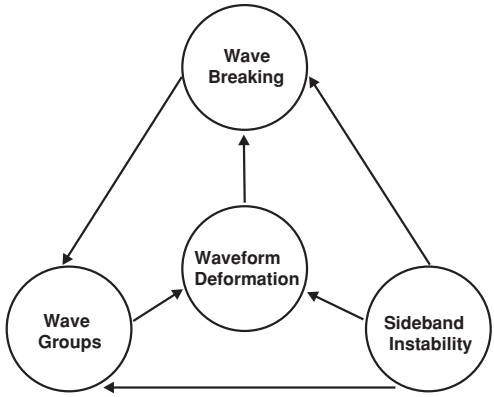

Figure 2.6: Schematic connections of wave breaking to sideband instability, wave grouping and waveform deformation (adapted from Tulin and Li, 1992).

2.4.3 Onset of breaking for modulating surface waves

The above sections showed the mathematical progress made in studying the nonlinear modulational processes in model equations. In some of these studies, the onset of wave breaking was also included (see for example Longuet–Higgins and Cokelet (1976), Peregrine et al. (1980), Greenhow (1983) and Tulin and Li (1992)). The results of these studies have served to draw more attention to the problem of deformation of steep waves. Underlying issues involved an understanding what determines the onset of wave breaking and whether it is controlled by a universal threshold of some wave parameter or parameters. Banner and Tian (1998) approached this problem through a detailed numerical study of the fully nonlinear two-dimensional problem on a periodic spatial domain. They used the free-surface code developed by Dold and Peregrine (1986) to study the evolution of wave groups composed of a fundamental carrier wave with small upper and lower sideband components, using as parameters the initial carrier wave steepness $(ak)_0$ and N, the number of waves in one modulational length. Their initial wave group had the structure of a uniform, finite-amplitude, steady deep-water wave train whose linear approximation is $\zeta = a\cos(kx)$.

Dold and Peregrine showed that for a given N an initial carrier wave steepness threshold $(ak)_0$ differentiates wave groups of two modes of behaviour, i.e. recurrence of the initial state without breaking or the rapid onset of breaking. According to Banner and Tian (1998), the recurrence occurs when the relative growth rates of the mean momentum and energy densities at their envelope maxima reach the threshold of 0.2 and then begin to decrease immediately. On the other hand, breaking occurs when these relative growth rates are sustained at around this threshold level during the final interval of order of the half wave period, just prior to breaking. The common feature of the observed evolution is

the fact that either for breaking or recurrence towards the original wave group, the evolution induced by the nonlinear group dynamics is accompanied by a systematic mean convergence of the energy density towards the local maximum of the evolving wave group. However, in contrast to the strong dependence of the evolution on the parameter space $\{N, (ak)_0\}$, the actual steepness at breaking $(ak)_{break}$ has no clear trend with N.

Song and Banner (2002) provided a detailed analysis of the wave group composed of a fundamental carrier wave with small upper and lower sideband components with the primary goal of identifying the difference between evolution to recurrence and to breaking onset. They found that the local energy and its growth rate within the wave group evolves in a complex fashion, with a fast oscillation superimposed on a longer mean trend. This trend reflects a systematic mean energy convergence toward (or away from) the maximum energy region within the wave group, which results finally in breaking or recurrence behaviour.

To distinguish breaking from recurrence, Song and Banner (2002) proposed the non-dimensional growth rate as in the form

$$\delta = \frac{1}{\omega_c} \frac{D < \chi_l^2 >}{Dt}, \tag{2.43}$$

in which ω_c is the initial mean carrier wave frequency and $< \chi_l^2 >$ is the local average of the square value of the steepness of carrier waves

$$\chi_l^2 = \frac{E}{\rho g} k^2 \tag{2.44}$$

and E is the depth-integrated local wave energy density given as the sum of the kinetic and potential energy of the fluid particles along the vertical profile at x and a given time t (Song and Banner, 2002)

$$E(x,t) = \int_{-h}^{\zeta} \frac{1}{2}\rho(u^2 + w^2)dz + \frac{1}{2}\rho g \overline{\zeta}^2, \tag{2.45}$$

where u and w are the x and z velocity components, h is the still water depth and $\zeta = \zeta(x,t)$ is the free surface elevation and

$$\frac{D}{DT} \equiv \frac{\partial}{\partial t} + \vec{u} \times \text{grad}. \tag{2.46}$$

The detailed methodology for computing δ is described by Song and Banner (2002). In particular, their calculations indicate that the threshold value $\delta_{\text{th}} = (1.30 - 1.50) \times 10^{-3}$ can be used as the basis for distinguishing recurrence cases from breaking cases, independently of the group structure or number of waves N in the group. Breaking occurs whenever $\delta(t)$ exceeds δ_{th}, while the minimum value of $\delta(t)$ for recurrence cases remains below δ_{th}. Thus we have:

$\delta_{\text{th}} < (1.30 - 1.50) \times 10^{-3}$ – recurrence case,
$\delta_{\text{th}} > (1.30 - 1.50) \times 10^{-3}$ – breaking case.

In the second part of the paper, Banner and Song (2002) investigated the influence of wind forcing and surface shear on the threshold value of the non-dimensional growth rate δ_{th}. The wind forcing was introduced into the free surface dynamic boundary condition in the Dold and Peregrine (1986) model as an additional surface distribution of pressure, being in phase with the wave slope as follows:

$$p_{\mathrm{w}}(x,t) = \alpha_{\mathrm{w}} \rho_{\mathrm{a}} u_*^2 \frac{\partial \zeta(x,t)}{\partial x}, \tag{2.47}$$

in which u_* is the friction velocity, ρ_{a} is the air density and α_{w} is an empirical constant. This constant was specified using its relationship with the non-dimensional spectral wind wave growth rate γ, normalized by the wave frequency f

$$\frac{\gamma}{f} = 2\pi\alpha_{\mathrm{w}} \left(\frac{\rho_{\mathrm{a}}}{\rho_{\mathrm{w}}}\right) \left(\frac{u_*}{C}\right)^2, \tag{2.48}$$

where C is the wave phase speed.

The experimental data reported by Komen et al. (1994) showed that for $\frac{u_*}{C} \sim 0.2$, the constant α_{w} becomes $\alpha_{\mathrm{w}} \sim 32.5$. It should be noted that inverse wave age in range $0.05 < \frac{u_*}{C} < 0.2$ corresponds to wind sea situations, from very young to very old sea, while the range $\frac{u_*}{C} > 0.2$ is relevant to short fetch wave tank conditions. Computations for wave age $\frac{u_*}{C}$ in the range (0.05, 0.2) showed that wind forcing only marginally modifies the geometry of the wave surface, and the critical threshold range of $(1.30 - 1.50) \times 10^{-3}$ for δ_{th}, found for zero surface forcing, is also applicable for the wind forcing case.

Banner and Song applied the surface layer current of order $0.03 \times V_{10}$ (V_{10} is the mean wind speed at the reference height of 10 m above the mean sea level), decreasing linearly over a depth of one significant wave height H_{s}, to simulate the influence of a uniform surface shear. The presence of the shearing current destabilizes the wave group from recurrence to breaking and accelerates its onset. However, the onset of breaking is still determined by the threshold δ_{th} value given above. Including the wind forcing and surface layer shear results in only small changes from the irrotational motion and the corresponding breaking threshold δ_{th} is still applicable for wind forcing and shear current, typical for open ocean conditions. This confirms the previous conclusion that the nonlinear hydrodynamic energy fluxes within wave groups dominate the evolution to recurrence or breaking even in the presence of other mechanisms. However, to clarify the importance of surface drift for the process of wave group evolution, in the next sections we examine the influence of surface drift on incipient wave breaking from a different perspective.

Chapter 3

Spectral and statistical properties of ocean waves

3.1 Introduction

The fundamental property of surface waves induced by wind is their irregularity. The prediction of wave parameters can be achieved through stochastic analysis only. This analysis can be developed in two basic domains, i.e. frequency and probability domains. Frequency analysis mainly deals with an evaluation of the distribution of wave energy among various frequencies and directions. In this chapter we start with the basic properties of frequency analysis of the time series to interpret the frequency spectra of ocean surface waves. In general, the resulting shape of the frequency spectrum depends on the external wave generation conditions (wind speed, wind fetch and duration, water depth, swell presence, and storm stage) as well as on internal mechanisms in the wave field (nonlinear interaction between wave components, energy dissipation due to wave breaking or bottom friction). However, the spectrum shape is not arbitrary and some fundamental properties of energy distribution apply for all spectra. The wave spectral energy reaches its maximum at frequency $\omega = \omega_{\mathrm{p}}$ and decreases for both lower and higher frequencies. Usually the reduction in the low-frequency range is faster than that for the high-frequency band. The lowest frequency for wind-induced gravity waves is estimated at approximately 0.03 Hz (0.2 rad/s). Energy at frequencies lower than this value is for surf beat, seiches or tides (Massel, 1996a).

The highest frequency of wind-induced gravity waves corresponds to the minimum phase velocity of 23 cm/s at a minimum wavelength of 1.7 cm (in clean water at 20°C). Thus, the highest frequency is 13.6 Hz (85 rad/s). For higher frequencies, the restoring force is predominantly the result of surface tension, which is typical for capillary waves. The limiting frequencies given above are theoretical approximations only. In practice we consider a much smaller frequency band of gravity, wind-induced waves.

Furthermore, spectra often show regularity, such as power-law regions, where $S(\omega) \sim \omega^{-n}$ for some power n. A good example of such regularities is provided by the saturation range (or equilibrium range) in the wave spectrum, when a spectrum shows ω^{-5} (or ω^{-4}) dependence. The saturation range expresses some equilibrium between energy loss, mainly due to breaking, and the same rate of energy acquired by waves from the wind. To include the most energetic part of the spectrum, a variety of power functions multiplied by some exponential functions have been proposed. This variety of the spectra is mostly a result of various experimental time series which are the base for spectrum formulation and which reflect various wave generation conditions.

Due to the complicated energy transfer from the atmosphere to the sea, the resulting surface waves are multidirectional. Only part of the wave energy is aligned with the wind direction. Because of the limitation of observational methods, knowledge of directional spreading is relatively poor compared to the frequency spectrum.

In the probability domain, wave parameters are considered as elementary random events. The digitized data of a particular parameter usually form a set of random realizations of a random variable, when the time sequence of the parameter is not taken into account. The final results in this approach are expressed in terms of probability density functions for such parameters as wave surface elevation, wave height, wave period and wave slope. In the next sections we follow mainly the approach of Massel (1996a).

3.2 Spectral properties of ocean waves

3.2.1 Frequency spectra of ocean waves

3.2.1.1 Spectral moments and spectral width parameters

The frequency function $S(\omega)$ represents a distribution of wave energy in the frequency domain. Thus,

$$\int_0^\infty S(\omega)\, d\omega = \sigma_\zeta^2 = m_0. \tag{3.1}$$

The variance σ_ζ^2 is also called the zero moment of the spectrum. In general, the spectral moments m_n are defined as

$$m_n = \int_0^\infty \omega^n S(\omega)\, d\omega. \tag{3.2}$$

The first few moments are of special importance for the spectral description of ocean waves. For example, the first moment m_1 determines the mean wave frequency and mean wave period, i.e.

$$\bar{\omega} = \frac{m_1}{m_0} \qquad \text{and} \qquad \bar{T} = \frac{2\pi}{\bar{\omega}} = 2\pi \frac{m_0}{m_1}. \tag{3.3}$$

An alternative estimate of the mean frequency (period) also exists. It is called the average frequency of up-crossing of the mean level $\bar{\omega}_0$ (and average period $\bar{T}_0$)

$$\bar{\omega}_0 = \sqrt{\frac{m_2}{m_0}} \qquad \text{and} \qquad \bar{T}_0 = \frac{2\pi}{\bar{\omega}_0} = 2\pi\sqrt{\frac{m_0}{m_2}}. \tag{3.4}$$

As well as moments m_n, the central spectral moments $\tilde{m}_n$ are also used. They are defined as

$$\tilde{m}_n = \int_0^\infty (\omega - \bar{\omega})^n S(\omega) d\omega. \tag{3.5}$$

Thus,

$$\tilde{m}_0 = m_0, \qquad \tilde{m}_1 = m_1 - \bar{\omega} m_0 = 0, \qquad \tilde{m}_2 = m_2 - \frac{m_1^2}{m_0}. \tag{3.6}$$

The central moment $\tilde{m}_2$ is a measure of concentration of the spectral wave energy around frequency $\bar{\omega}$. When we normalize $\tilde{m}_2$ in (3.6) by product $(\bar{\omega}^2 \tilde{m}_0)$, we obtain non-dimensional parameter ν^2 as follows

$$\nu^2 = \frac{\tilde{m}_2}{\bar{\omega}^2\, \tilde{m}_0} = \frac{m_0\, m_2}{m_1^2} - 1. \tag{3.7}$$

Parameter ν^2 is a convenient, lower-order quantity which is a measure of the spectral width. Equation (3.7) clearly indicates that when all wave energy is concentrated in the single frequency $\omega = \bar{\omega}$, then $\nu^2 \to 0$. When wave energy is broadly distributed among frequencies, then ν^2 increases. In typical storm conditions, the spectral width parameter ν is approximately equal to 0.3. The relationships between the spectral moments and sea state parameters, such as the significant wave height, peak frequency, wind speed and wind fetch are discussed in Appendix D.

Another measure of spectral width appears when developing the statistics of wave amplitude (see Section 3.3). The corresponding spectral width parameter was first defined by Cartwright and Longuet–Higgins (1956) as

$$\epsilon^2 = \frac{1}{2\, m_0\, m_4} \int_0^\infty \int_0^\infty S(\omega_1) S(\omega_2) \left(\omega_1^2 - \omega_2^2\right)^2 d\omega_1 d\omega_2, \tag{3.8}$$

or

$$\epsilon^2 = \frac{m_0 m_4 - m_2^2}{m_0 m_4}. \tag{3.9}$$

It follows that

$$0 < \epsilon^2 \leq 1.$$

When the wave spectrum $S(\omega)$ is extremely narrow, say $S(\omega) = \sigma_\zeta^2\, \delta(\omega - \omega_\mathrm{p})$ where $\delta(\,)$ is the Dirac's delta, then $\epsilon^2 \to 0$.

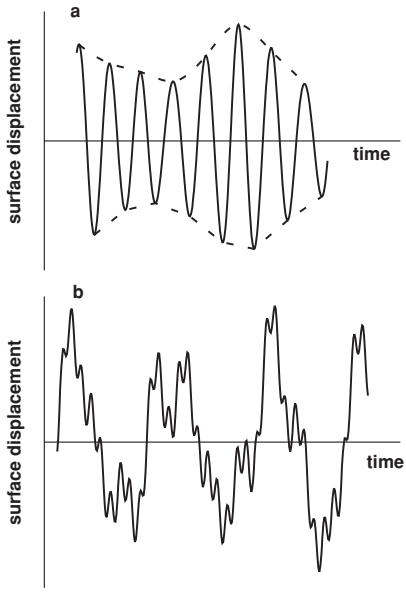

Figure 3.1: Wave profiles corresponding to narrow (a) and wide spectra (b).

Typical wave profiles, corresponding to narrow and wide spectra, are shown in Fig. 3.1. It is seen that waves of a narrow spectrum have almost the same frequency but gradually varying amplitudes. The upper and lower envelopes coincide exactly with crests and troughs, and form a pair of symmetrical curves with respect to the mean value. In such a case, the positive and negative maximum excursions of the wave surface are equal to each other, and equal to wave amplitude. In the case of a wide spectrum, waves of many frequencies are present and these ride on each other to produce local maxima below mean sea level as well as above it.

3.2.1.2 Typical spectral forms

(1) *Saturation spectrum:* The growth of waves under the influence of wind is not infinite. The energy supplied by the wind is balanced by wave interactions which transfer energy from a given frequency band to other frequencies, and by energy dissipation. In deep water, the dissipation frequently takes the form of 'whitecaps' of a scale smaller than the wavelength. More details on whitecaps are given in Chapter 7.

Another form of the limitation of wave growth is related to the formation of capillary waves just in front of sharp primary wave crests. These capillary waves extract energy from primary waves of high curvature (Phillips, 1977). We also note that the surface drift layer produced by wind stress enhances wave breaking at a greatly reduced wave amplitude. More information on wave breaking in deep water is given in subsequent chapters.

The occurrence of any such mechanism is an indication of a stage of saturation of wave components in which a balance between energy supplied by wind and that lost by dissipation is achieved. Therefore, the saturation range should be exclusively described by local physical parameters that govern the extreme configuration of waves, i.e. gravitational acceleration (g), friction velocity of the wind over the wave surface (u_*) and local frequency (ω). Phillips (1958), using dimensional arguments, found that

$$S(\omega) = f\left(\frac{\omega u_*}{g}\right) g^2 \omega^{-5}. \tag{3.10}$$

When the surface drift is unimportant, i.e. when $\frac{\omega u_*}{g} \ll 2$ in which $u_* = \left(\frac{\tau}{\rho_a}\right)^{1/2}$ and τ is mean tangential stress, (3.10) yields

$$S(\omega) = \beta g^2 \omega^{-5} \qquad \left(\omega_{\mathrm{p}} \ll \omega \ll \frac{2g}{u_*}\right), \tag{3.11}$$

in which β is a constant ($\beta = 1.23 \times 10^{-2}$).

Although (3.11) may have been found useful as a first approximation to the high-frequency part of the spectrum, the accurate representation of more careful measurements by Toba (1973) showed that his wind-tunnel data were better expressed by a spectrum of the form

$$S(\omega) \sim u_* g \omega^{-4}. \tag{3.12}$$

This form has been confirmed in field observations by Kawai et al. (1977) and Donelan et al. (1985). Taking these facts into account Phillips (1985) suggested that the 'ideas underlying (3.11) are found to be no longer viable' and should be replaced by a more accurate form (3.12).

(2) *Deep water ocean: the Pierson–Moskowitz spectrum*: Spectral forms discussed so far are restricted to the saturation range only, when $\omega > \omega_{\mathrm{p}}$. To include the most energetic part of the spectrum, a variety of power functions multiplied by exponential functions have been proposed. A general form of the spectral density function was suggested as

$$S(\omega) = A\omega^{-p} \exp\left[-B\,\omega^{-q}\right], \tag{3.13}$$

in which A, B, p and q are free parameters. The spectral moments defined by (3.2) are given now as follows

$$m_r = AB^{(r-p+1)/q} \left(\frac{1}{q}\right) \Gamma\left(\frac{p-r-1}{q}\right), \tag{3.14}$$

in which $\Gamma(x)$ is a gamma function (Abramowitz and Stegun, 1975).

Probably the most popular spectrum among all proposed forms is that proposed by Pierson and Moskowitz (1964), who, using the field data and theoretical discoveries of Phillips (1958) and Kitaigorodskii (1962), showed that

$$S(\omega) = \beta g^2\, \omega^{-5} \exp\left[-B\Big(\frac{g}{\omega V_{19.5}}\Big)^4\right], \tag{3.15}$$

where $\beta = 8.1 \times 10^{-3}$, $B = 0.74$ and $V_{19.5}$ is a wind speed at an elevation of 19.5 m above the sea surface.

Thus, the shape of the wave spectrum is controlled by a single parameter–wind speed $V_{19.5}$. The spectrum of (3.15) was proposed for fully developed sea, when phase speed is approximately equal to wind speed. The experimental data given by Pierson and Moskowitz yield

$$\frac{V_{19.5}\omega_{\mathrm{p}}}{g} = \text{const} = 0.879 \quad \text{and} \quad \frac{V_{19.5}\omega_{\mathrm{p}}}{2\pi g} = 0.13, \tag{3.16}$$

where ω_{p} is the peak frequency. After substitution into (3.15) we obtain

$$S(\omega) = \beta g^2 \omega^{-5} \exp\left[-\frac{5}{4}\left(\frac{\omega}{\omega_{\mathrm{p}}}\right)^{-4}\right]. \tag{3.17}$$

Some mathematical problems arise when calculating the spectral fourth moment using (3.17). This moment, which physically denotes the mean-squared acceleration measured at a Eulerian point, is unbounded. To remedy this shortcoming, a cutoff frequency is usually imposed, i.e.

$$m_4 = \int_0^{\omega_{\mathrm{c}}} \omega^4 S(\omega)\, d\omega, \tag{3.18}$$

in which $\omega_{\mathrm{c}} = n\omega_{\mathrm{p}}$ and n is usually taken as $n > 3$.

(3) *Fetch-limited sea: the JONSWAP spectrum*: The JONSWAP spectrum is based on an extensive wave measurement programme (Joint North Sea Wave Project) carried out in 1968 and 1969 in the North Sea (Hasselmann et al., 1973). The JONSWAP spectrum as a function of non-dimensional frequency $\hat{\omega} = \frac{\omega}{\omega_{\mathrm{p}}}$ takes the form

$$S(\hat{\omega}) = \frac{\beta g^2}{\omega_{\mathrm{p}}^4}\hat{\omega}^{-5} \exp\left(-\frac{5}{4}\hat{\omega}^{-4}\right)\gamma^r, \tag{3.19}$$

in which γ is the peak enhancement factor of the standard value of 3.3, and function r takes the form

$$r = \exp\left[-\frac{1}{2}\frac{(\hat{\omega}-1)^2}{\sigma_0^2}\right], \tag{3.20}$$

in which

$$\sigma_0 = \begin{cases} 0.07 & \text{when} \quad \omega < \omega_{\mathrm{p}} \\ 0.09 & \text{when} \quad \omega \geq \omega_{\mathrm{p}}. \end{cases} \tag{3.21}$$

The Phillips constant β and peak frequency ω_{p} are given by Hasselmann et al. (1973) as follows

$$\beta = 0.076\left(\frac{gX}{V_{10}^2}\right)^{-0.22} \tag{3.22}$$

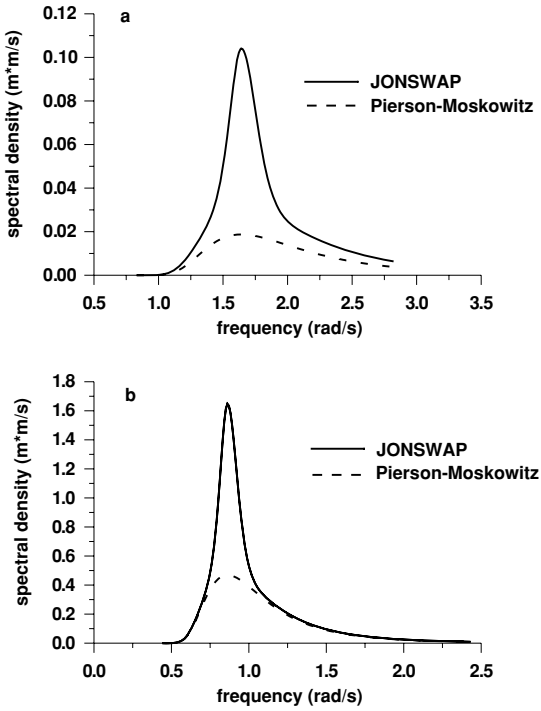

Figure 3.2: Comparison of the Pierson–Moskowitz and the JONSWAP spectra: (a) fetch limited conditions and (b) fully developed sea.

and

$$\omega_{\mathrm{p}} = 7\pi \left(\frac{g}{V_{10}}\right) \left(\frac{gX}{V_{10}^2}\right)^{-0.33} . \tag{3.23}$$

The Pierson–Moskowitz spectrum can be obtained as a special case of the JONSWAP spectrum when the peak enhancement factor γ is equal to 1. In Fig 3.2 the Pierson–Moskowitz spectrum and the JONSWAP spectrum are compared for two different regimes. The first figure illustrates fetch limited conditions when fetch $X = 25$ km and wind velocity $V_{10} = 10$ m/s. The resulting peak frequency and wave development parameters are $\omega_{\mathrm{p}} = 1.64$ rad/s, and $\omega_{\mathrm{p}} V_{10}/g = V_{10}/C_{\mathrm{p}} = 1.673$ (C_{p} is a phase velocity corresponding to the peak frequency). The second figure presents the spectra for a fully developed sea ($X = 200$ km, $V_{10} = 10$ m/s, $\omega_{\mathrm{p}} = 0.862$ rad/s and $\frac{\omega_{\mathrm{p}} V_{10}}{g} = 0.879$). The Pierson–Moskowitz spectrum applies only for the fully developed case. On the other hand, the JONSWAP spectrum, extrapolated to the fully developed limit, retains its enhanced peak, which is in contrast to a much broader fully developed spectrum.

(4) *Donelan et al. spectrum fitted to ω^{-4} power at high frequencies*: Donelan et al. (1985) fitted a set of spectra obtained from Lake Ontario to ω^{-4} power at

high frequencies and proposed the frequency spectrum $S(\omega)$ in the form

$$S(\omega) = \alpha_{\mathrm{d}}\, g^2 \omega^{-4} \omega_{\mathrm{p}}^{-1} \exp\left[-\left(\frac{\omega_{\mathrm{p}}}{\omega}\right)^4\right] \gamma_{\mathrm{d}}^{r_1}, \tag{3.24}$$

where

$$\gamma_{\mathrm{d}} = \begin{cases} 1.7 & \text{for} \quad 0.83 < \dfrac{V_{10}}{C} < 1 \\ 1.7 + 6 \log\left(\dfrac{V_{10}}{C}\right) & \text{for} \quad 1 \le \dfrac{V_{10}}{C} < 5 \end{cases}, \tag{3.25}$$

$$\alpha_d = 0.006 \left(\frac{V_{10}}{C}\right)^{0.55} \quad \text{for} \quad 0.83 < \frac{V_{10}}{C} < 5, \tag{3.26}$$

$$r_1 = \exp\left[-\frac{(\omega - \omega_{\mathrm{p}})^2}{2\sigma_{\mathrm{d}}^2\, \omega_{\mathrm{p}}^2}\right], \tag{3.27}$$

$$\sigma_{\mathrm{d}} = 0.08 \left[1 + 4\left(\frac{V_{10}}{C}\right)^3\right] \quad \text{for} \quad 0.83 < \frac{V_{10}}{C} < 5, \tag{3.28}$$

$$\frac{V_{10}}{C} = \frac{V_{10}\, \omega_{\mathrm{p}}}{g}. \tag{3.29}$$

and

$$\omega_{\mathrm{p}} = 11.6 \left(\frac{g}{V_{10}}\right) \left(\frac{gX}{V_{10}^2}\right)^{-0.23}. \tag{3.30}$$

Representation (3.24) gives a better fit to the experimental data in the equilibrium range $(1.5 - 3)\, \omega_{\mathrm{p}}$. However, it should be noted that the popular prediction model WAM imposes an ω^{-5} tail for $\omega \ge 3\, \omega_{\mathrm{p}}$ (WAMDI, 1988). The wind speed V_{10} is assumed to be a wind component of the 10 m height in the mean direction of propagation of the waves at the spectral peak. Another forms of the frequency spectra for deep water as well as for coastal zones were discussed by Massel (1996a), Druet (2000) and others.

3.2.2 Directional spectral functions

Due to energy transfer from the atmosphere to the sea and due to wave-wave interactions the resulting surface waves are multidirectional. Only part of the wave energy is aligned with the wind direction. More specifically, wave energy associated with the frequencies $\omega \approx \omega_{\mathrm{p}}$ is primarily propagated in the direction of the wind, whereas wave energy associated with lower or higher frequencies is distributed over a range of directions. Wave multidirectionality is also a result of the superposition at a given point of various wave trains, which may be generated by different remote atmospheric forcing systems.

Directional spreading is a fundamental property of a random wave field and is a key element for understanding ocean wave mechanics, as well as generation, propagation and breaking. Information about the directional distribution of wave energy is required for the proper prediction of various oceanographic and geomorphological phenomena in shallow and in deep waters (Massel and Brinkman, 1998).

Due to the limitation of observational methods, knowledge of the directional spectrum is relatively poor compared to the frequency spectrum. The basic approach to the two-dimensional spectrum $\hat{S}(\omega, \Theta)$ is to multiply the frequency spectrum $S(\omega)$ by an empirically determined directional spreading function $D(\Theta)$. A more general expression for $\hat{S}$, which includes a variety of commonly used directional spreading representations, can be written as (Niedzwecki and Whatley, 1991)

$$\hat{S}(\omega, \Theta) = S(\omega)\, D\left(\Theta; \omega, p_1, p_2, \ldots\right), \tag{3.31}$$

in which $p_1, p_2, \ldots$ represent the various parameters associated with the various directional spreading functions.

Historically, the first attempt to model directional energy spreading was suggested by Pierson et al. (1955) in the form of the cosine type function (Fig. 3.3)

$$D(\Theta) = \frac{2}{\pi}\cos^2\Theta, \quad -\frac{\pi}{2} \le \Theta \le \frac{\pi}{2}. \tag{3.32}$$

From (3.32) it follows that in the wind direction about 64% of wave energy is propagated. In a direction normal to wind direction, waves do not propagate.

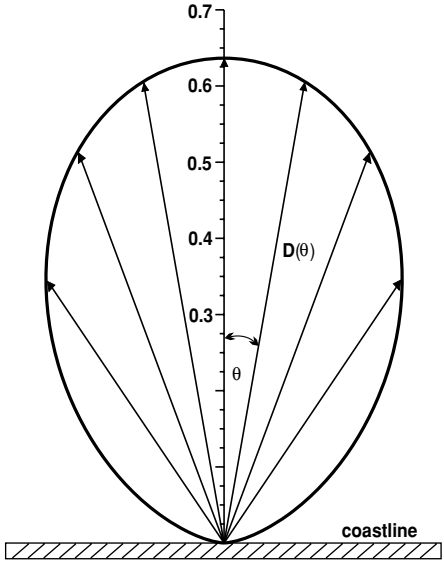

Figure 3.3: Directional spreading function (3.32).

This directional spreading function gives the same directional divergence of all frequency components.

On the basis of a field study with a pitch-and-roll buoy, Longuet–Higgins et al. (1961) proposed a more elaborate form of the cosine type spreading function as (Massel, 1996a)

$$D(\Theta; s) = \frac{2^{2s-1}}{\pi} \frac{\Gamma^2(s+1)}{\Gamma(2s+1)} \cos^{2s}\left(\frac{\Theta - \Theta_0}{2}\right), \quad -\pi \le \Theta \le \pi, \tag{3.33}$$

or

$$D(\Theta; s_1) = \frac{1}{\sqrt{\pi}} \frac{\Gamma\left(1 + \frac{s_1}{2}\right)}{\Gamma\left[\frac{(1+s_1)}{2}\right]} \cos^{2s_1}(\Theta - \Theta_0), \quad -\frac{\pi}{2} \le \Theta \le \frac{\pi}{2}, \tag{3.34}$$

in which Θ_0 is the main peak frequency direction, s and s_1 are the empirical functions of $\left(\frac{V_{10}}{C}\right)$ and $\Gamma(x)$ is a gamma function (Abramowitz and Stegun, 1975).

Various representations have been proposed in the past for s or (s_1). All of them show the wave frequency dependent nature of the directional spreading function D. For example, Krylov et al. (1966) found that

$$D(\Theta; \omega) = 2^{1.8/\omega_*} \frac{\Gamma\left[2\left(\frac{1.8}{\omega_*} + 1\right)\right]}{\Gamma^2\left(\frac{1.8}{\omega_*} + 1\right)} \left[\cos(\Theta - \Theta_0)\right]^{1.8/\omega_*}. \tag{3.35}$$

So $s_1 = \frac{1.8}{\omega_*}$ and $\omega_* = \frac{\omega}{\bar{\omega}}$. Hence, the low-frequency components ($\omega \ll \bar{\omega}$) possess very narrow directional spreading, concentrated around main direction, Θ_0, while the high-frequency components ($\omega > \bar{\omega}$) are spread in a wider directional band. In the vicinity of the spectral maximum ($\omega_* \approx 0.9$), the directional spreading function $D \sim \cos^2\Theta$.

In most of the experiments, the characteristic asymmetry in frequency dependence of parameter s was observed. The parameter s reaches its maximum value for peak frequency and decreases both for lower and higher frequencies. The decreasing trends are different, and more rapid decrease is observed in the low-frequency range. Using the cloverleaf buoy data, Mitsuyasu et al. (1975) suggest the following dependence for s in (3.33)

$$\frac{s}{s_{\mathrm{p}}} = \begin{cases} \left(\frac{\tilde{\omega}}{\tilde{\omega}_{\mathrm{p}}}\right)^{5} & \text{for} \quad \tilde{\omega} \le \tilde{\omega}_{\mathrm{p}} \\ \left(\frac{\tilde{\omega}}{\tilde{\omega}_{\mathrm{p}}}\right)^{-2.5} & \text{for} \quad \tilde{\omega} \ge \tilde{\omega}_{\mathrm{p}}, \end{cases} \tag{3.36}$$

where $\tilde{\omega} = \frac{\omega V_{10}}{g}$, $\tilde{\omega}_{\mathrm{p}} = \frac{\omega_{\mathrm{p}} V_{10}}{g}$, and $s_{\mathrm{p}} = 11.5\,\tilde{\omega}_{\mathrm{p}}^{-2.5}$.

It should be noted that parameter s increases when ω_{p} decreases. Hence, the directional distribution becomes narrower with the development of waves.

Similar dependence of parameter s on wave frequency was found during the JONSWAP experiment (Hasselmann D. et al., 1980). They defined parameter s as follows

$$s = s_{\mathrm{p}} \left(\frac{\omega}{\omega_{\mathrm{p}}} \right)^{\mu}, \tag{3.37}$$

in which

$$\left.\begin{array}{rcl} s_{\mathrm{p}} & = & 6.97 \pm 0.83 \\ \mu & = & 4.06 \pm 0.22 \end{array}\right\} \text{ for } \omega < \omega_{\mathrm{p}}, \tag{3.38}$$

and

$$\left.\begin{array}{rcl} s_{\mathrm{p}} & = & 9.77 \pm 0.43 \\ \mu & = & -(2.33 \pm 0.06) - (1.45 \pm 0.45) \left(\dfrac{V}{C} - 1.17 \right) \end{array}\right\} \text{ for } \omega \geq \omega_{\mathrm{p}}. \tag{3.39}$$

The parameterization (3.37), proposed by Hasselmann D. et al. (1980), is based on the assumption that the spectral shape for $\omega \leq \omega_{\mathrm{p}}$ is governed by nonlinear interactions when we should expect dependence of s on the ratio $\left(\frac{\omega}{\omega_{\mathrm{p}}}\right)$.

Field observations show that the crosswind component constitutes a significant portion of the ocean surface mean square slope of the order of 88% (Hwang and Wang, 2002). However, such a high level of the crosswind component is not satisfactorily explained by the above-mentioned models of wave directional distributions. In fact, the directional spectral analysis of the three-dimensional surface topography obtained from an airborne scanning lidar system indicates that the present unimodal directional distribution exists only in a narrow wave number range near the spectral peak. For wave components shorter than the peak wavelength, the directional distribution becomes bimodal (Zakharov and Shrira, 1990). Such distribution results from nonlinear wave–wave interactions (Hwang and Wang, 2002). It was shown by Young et al. (1995) that using the bimodal directional distribution function provides the calculated average ratio between crosswind and upwind slope components being in good agreement with field measurements.

3.2.3 Wave energy balance in spectral form

In order to develop an energy balance equation we assume for a moment that the dispersion relation does not depend on time, but is rather a slowly changing function of space coordinates. It can also depend on local properties such as water depth, current velocity or ambient density current, i.e.

$$\omega = \Omega \left[\vec{k}, f \left(\vec{x}, h, \vec{U}, \rho, \ldots \right) \right]. \tag{3.40}$$

If the medium itself is moving with velocity $\vec{U}$, the frequency of waves passing a field point is

$$\omega = \Omega \left(\vec{k}, \vec{x} \right) = \sigma + \vec{k} \times \vec{U} = \left[gk \tanh(kh) \right]^{1/2} + \vec{k} \times \vec{U}. \tag{3.41}$$

Usually the quantity ω is called the observed or apparent frequency, while σ is the intrinsic frequency, whose functional dependence on $\vec{k}$ is known as a classical dispersion relation

$$\sigma^2 = gk \tanh(kh). \tag{3.42}$$

It is well known that the number of wave crests passing a given point per unit time is determined by the kinematical conservation equation (Massel, 1989)

$$\frac{\partial \vec{k}}{\partial t} + \nabla_h \omega = 0, \quad \frac{\partial k_i}{\partial x_j} - \frac{\partial k_j}{\partial x_i} = 0, \quad i,j = 1,2. \tag{3.43}$$

Substituting (3.40) into (3.43) gives

$$\frac{\partial k_i}{\partial t} + C_{g_j}\left(\vec{x},\vec{k},t\right)\frac{\partial k_j}{\partial x_i} = -\frac{\partial \Omega}{\partial x_i}, \tag{3.44}$$

in which $C_{g_j} = \frac{\partial \Omega}{\partial k_j}$ is group velocity.

Equation (3.44) can be rewritten as

$$\frac{dk_i}{dt} = -\frac{\partial \Omega}{\partial x_i} \quad \text{and} \quad \frac{dx_i}{dt} = \frac{\partial \Omega}{\partial k_i}. \tag{3.45}$$

Equations (3.45) are identical to the Hamilton equations in mechanics. The vectors $\vec{x}$ should be interpreted as coordinates and vectors $\vec{k}$ represent the momenta, and the frequency $\Omega\left(\vec{k},\vec{x},t\right)$ is taken to be the Hamiltonian (Whitham, 1974; Massel, 1989).

For free surface waves, the mean densities of potential and kinetic energy are equal. Therefore, $2\hat{\Psi}\left(\vec{k},\vec{x},t\right)$ is the mean spectral density of total wave energy in the unit volume $d\vec{k} \times d\vec{x}$ in phase space $\left(\vec{k},\vec{x}\right)$ at a given time t in which $\hat{\Psi}\left(\vec{k},\vec{x},t\right)$ is the wave number spectrum. According to Liouville's theorem, this energy should be conservative during volume evolution

$$\frac{\partial \hat{\Psi}}{dt} + \frac{\partial \Omega}{\partial k_i}\frac{\partial \hat{\Psi}}{\partial x_i} - \frac{\partial \Omega}{\partial x_i}\frac{\partial \hat{\Psi}}{\partial k_i} = 0, \tag{3.46}$$

when (3.45) is used.

If the wave field is subjected to processes of generation, dissipation, nonlinear interaction between spectral components and other possible interactions with atmospheric boundary layer and various ocean movements (currents, internal waves, etc.), (3.46) should be supplemented by a source–sink term at the right-hand side, i.e.

$$\frac{\partial \hat{\Psi}}{dt} + \frac{\partial \Omega}{\partial k_i}\frac{\partial \hat{\Psi}}{\partial x_i} - \frac{\partial \Omega}{\partial x_i}\frac{\partial \hat{\Psi}}{\partial k_i} = Q\left(\vec{k},\vec{x},t\right), \tag{3.47}$$

in which $Q = \sum_i Q_i$.

The first term at the left-hand side of (3.47) expresses the local evolution of the spectrum in time, while the second term represents the evolution of the spectrum for the horizontally non-homogeneous wave field. This term shows that energy is transported at the group velocity. The third term reflects the effects of refraction and shoaling due to a non-horizontal bottom or due to current. The spectral energy balance equation is also known as the radiative transfer equation or the transport equation.

In oceanographic practice the two-dimensional spectrum $\hat{S}\left(\omega,\Theta;\vec{x},t\right)$ is frequently used, rather than the wave number spectrum $\hat{\Psi}\left(\vec{k};\vec{x},t\right)$. To evaluate spectrum $\hat{S}\left(\omega,\Theta;\vec{x},t\right)$, we adopt the following variables transformation

$$k_x=\chi\left(\omega,\vec{x}\right)\cos\Theta,\quad k_y=\chi\left(\omega,\vec{x}\right)\sin\Theta, \tag{3.48}$$

where function $\chi\left(\omega,\vec{x}\right)=k$ is a solution of the dispersion relation

$$\omega^2=gk\,\tanh(kh). \tag{3.49}$$

Variables transformation yields the following relationship between $\hat{S}\left(\omega,\Theta;\vec{x},t\right)$ and $\hat{\Psi}\left(\vec{k};\vec{x},t\right)$ spectra

$$\hat{\Psi}\left(\vec{k};\vec{x},t\right)=J\hat{S}\left(\omega,\Theta;\vec{x},t\right)=f\left(\omega,\Theta;\vec{x},t\right), \tag{3.50}$$

in which J is a Jacobian of the transformation, i.e. (Massel, 1996a)

$$J=\frac{\partial(\omega,\Theta)}{\partial(k_x,k_y)}=\left[\frac{\partial(k_x,k_y)}{\partial(\omega,\Theta)}\right]^{-1}. \tag{3.51}$$

Thus,

$$J=\left\{\begin{vmatrix}\dfrac{\partial\chi}{\partial\omega}\cos\Theta, & -\chi\sin\Theta\\ \dfrac{\partial\chi}{\partial\omega}\sin\Theta, & -\chi\cos\Theta\end{vmatrix}\right\}^{-1}=\frac{C_{\mathrm{g}}}{\chi}, \tag{3.52}$$

where C_{g} is the group velocity corresponding to a particular wave frequency. After substituting (3.50) into (3.47) we obtain (Krasitskii, 1974)

$$\frac{\partial}{\partial t}(CC_{\mathrm{g}}\hat{S})+C_{\mathrm{g}}\cos\Theta\,\frac{\partial}{\partial x}(CC_{\mathrm{g}}\hat{S})+C_{\mathrm{g}}\sin\Theta\,\frac{\partial}{\partial y}(CC_{\mathrm{g}}\hat{S})+$$

$$+\frac{C_{\mathrm{g}}}{C}\left[\sin\Theta\,\frac{\partial C}{\partial x}-\cos\Theta\,\frac{\partial C}{\partial y}\right]\frac{\partial}{\partial\Theta}(CC_{\mathrm{g}}\hat{S})=CC_{\mathrm{g}}\,\hat{Q}\left(\omega,\Theta,\vec{x},t\right), \tag{3.53}$$

in which $\hat{Q}=\sum_i\hat{Q}_i$.

Equation (3.53) can apply for a dispersion relation not depending on time, when an ambient current is uniform in space. If waves propagate on a non-stationary and non-uniform current $\vec{U}\left(\vec{x},t\right)$, the intrinsic frequency σ may vary in space and time. In such a case, the spectral energy density will not be

conserved. Bretherton and Garrett (1969) showed that the quantity called wave action density $N = \frac{\hat{\Psi}(\vec{k};\vec{x},t)}{\sigma}$ is conserved in a moving medium. Therefore, instead of (3.47), we apply a more general principle of conservation of wave action density N in the form

$$\frac{\partial N}{\partial t} + \frac{\partial \Omega}{\partial k_i}\frac{\partial N}{\partial x_i} - \frac{\partial \Omega}{\partial x_i}\frac{\partial N}{\partial k_i} = \frac{Q}{\sigma}. \tag{3.54}$$

In order to illustrate the relationship between wave action density N and energy density $\hat{\Psi}$ let us consider the example of a steady unidirectional wave train in deep water on a variable current $U(x)$ (source term $Q \equiv 0$). Then, (3.54) reduces to

$$\frac{\partial}{\partial x}\left[\hat{\Psi}\left(\frac{U + C_{\mathrm{g}}}{\sigma}\right)\right] = 0. \tag{3.55}$$

For gravity waves in deep water $\sigma = g/C$ and $C_{\mathrm{g}} = \frac{1}{2}C$. Thus,

$$\hat{\Psi}\left(U + \frac{1}{2}C\right)C = \mathrm{const} = \frac{1}{2}\hat{\Psi}_0 C_0^2. \tag{3.56}$$

Although the flux of wave action is constant, the flux of wave energy is not. For example, as C decreases in an adverse current, the energy flux of the wave motion increases because of the work done by 'radiation stress' (Longuet–Higgins and Stewart, 1964; Massel, 1989).

The basic difficulty in solving (3.47) or (3.54) is evaluation of the function Q. In general, Q is a function of wave number $\vec{k}$ and a functional of $\hat{\Psi}$, i.e. $Q = Q\left(\vec{k}, \hat{\Psi}\right)$. Function Q can also be dependent on other parameters which are functions of $\vec{x}$ and t (for example, wind velocity). The reader should consult Massel (1996a) for an in-depth discussion.

3.3 Statistical properties of ocean waves

3.3.1 Probability density functions of surface ordinates

In this section, an overview of the statistical properties of ocean waves with a special emphasis on extreme events is presented. We start with the central limit theorem (Ochi, 1990), stating that observed sea surface displacement $\zeta(t)$ is normally distributed with mean $\overline{\zeta}$ and variance σ_ζ^2. Thus, the probability density function $f(\zeta)$ takes the form (Massel, 1996a)

$$f(\zeta) = \frac{1}{\sqrt{2\pi}\sigma_\zeta}\exp\left[-\frac{(\zeta - \overline{\zeta})^2}{2\sigma_\zeta^2}\right]. \tag{3.57}$$

The mean and variance are the first and second central moments of the probability density μ_1 and μ_2, respectively

$$\mu_1 = \overline{\zeta} = E[\zeta] = \int_{-\infty}^{\infty} \zeta f(\zeta) d\zeta, \tag{3.58}$$

and

$$\mu_2 = \sigma_\zeta^2 = E[(\zeta - \overline{\zeta})^2] = \int_{-\infty}^{\infty} (\zeta - \overline{\zeta})^2 f(\zeta) d\zeta. \tag{3.59}$$

In practical applications, the standardized Gaussian probability density function is also used

$$f(\xi) = \frac{1}{\sqrt{2\pi}} \exp\left(-\frac{1}{2}\xi^2\right), \tag{3.60}$$

which is obtained from (3.57) by transformation of variables

$$\xi = \frac{\zeta - \bar{\zeta}}{\sigma_\zeta} \tag{3.61}$$

and

$$f(\xi) = f\left[g(\xi)\right] \left|\frac{dg(\xi)}{d\xi}\right| \qquad \text{and} \qquad g(\xi) = \sigma_\zeta\, \xi + \bar{\zeta}. \tag{3.62}$$

It can be shown that all odd numbered central moments of the Gaussian random variable are equal to zero, while even numbered moments are

$$\mu_{2n} = 1 \cdot 3 \cdot 5 \cdots (2n-1)\sigma_\zeta^{2n}, \tag{3.63}$$

where

$$\mu_n = \int_{-\infty}^{\infty} (\zeta - \bar{\zeta})^n f(\zeta)\, d\zeta. \tag{3.64}$$

The distribution (3.60) is usually abbreviated as $N(0,1)$, as the first two moments of the standardized probability density function are 0 and 1, respectively. In general, the moments of the standardized Gaussian probability density function (3.60) may be written as

$$\hat{m}_n = \int_{-\infty}^{\infty} \xi^n f(\xi) d\xi. \tag{3.65}$$

Thus,

$$\hat{m}_n = \begin{cases} 1 \cdot 3 \cdot 5 \cdots (n-1) & \text{for} \quad \text{even numbered moments} \\ 0 & \text{for} \quad \text{odd numbered moments} \end{cases} \tag{3.66}$$

and

$$\hat{m}_n = \frac{\mu_n}{\sigma_\zeta^n}. \tag{3.67}$$

To describe deviation of the observed distribution from the Gaussian distribution, the third and fourth central moments are used to determine so-called skewness and kurtosis, i.e.

skewness

$$\gamma_1 = \frac{\mu_3}{\sigma_\zeta^3}, \tag{3.68}$$

and kurtosis

$$\gamma_2 = \frac{\mu_4}{\sigma_\zeta^4}, \tag{3.69}$$

where

$$\mu_n = \int_{-\infty}^{\infty} (\zeta - \overline{\zeta})^n f(\zeta) d\zeta. \tag{3.70}$$

Skewness and kurtosis are quantities of a higher order and are related to nonlinearities in the wave field. In particular, skewness is a statistical measure of the vertical asymmetry of the sea surface, characterized by the sharp crests and rounded troughs of waves. Kurtosis is a measure of the peakedness of the distribution. It should be mentioned that for a purely Gaussian distribution $\gamma_1 = 0$ and $\gamma_2 = 3$. Sometimes so-called excess of kurtosis ($\gamma_2 - 3$) is used to characterize the deviation from normal distribution. A positive value of the excess of kurtosis corresponds to a distribution with a peak sharper than the Gaussian one.

Equation (3.70) is the theoretical expression valid for infinite time series. If number of data N is finite, the estimates for the third and fourth moments are (Massel, 1996a)

$$\mu_3 = E[(x - \overline{x})^3] = \frac{N^2}{(N-1)(N-2)}\, \tilde{m}_3 \tag{3.71}$$

and

$$\mu_4 = E[(x - \overline{x})^4] = \frac{N(N^2 - 2N + 3)\tilde{m}_4 - 3N(2N-3)\tilde{m}_2}{(N-1)(N-2)(N-3)}, \tag{3.72}$$

where

$$\tilde{m}_n = \frac{1}{N} \sum_{i=1}^{N} (x_i - \overline{x})^n. \tag{3.73}$$

Equations (3.71) and (3.72) represent unbiased and consistent estimates of the true central moments.

Instinctively a relationship between surface slope, spectrum shape and surface skewness should be expected. In particular, for an extremely narrow spectrum, Srokosz and Longuet–Higgins (1986) showed that

$$\gamma_1 = 6\pi \frac{\sigma_\zeta}{L_\mathrm{p}}, \tag{3.74}$$

where L_p is the wavelength corresponding to the peak frequency.

When the frequency spectrum $S(\omega)$ has the form

$$S(\omega) = \begin{cases} \alpha\omega^{-n}, & \omega > \omega_{\mathrm{p}}, \quad n > 3 \\ 0, & \omega < \omega_{\mathrm{p}}, \end{cases} \tag{3.75}$$

the same authors found

$$\gamma_1 = \frac{6(n-1)}{n-2}\,\pi\left(\frac{\sigma_\zeta}{L_{\mathrm{p}}}\right). \tag{3.76}$$

In particular, for the so-called Phillips spectrum, $S(\omega) \sim \omega^{-5}$, we obtain $\gamma_1 = 8\pi\left(\frac{\sigma_\zeta}{L_{\mathrm{p}}}\right)$.

3.3.2 Numerical simulation of Gaussian and non-Gaussian sea surface

There are basically three approaches to obtain the data for an estimation of the statistical characteristics of wind-induced waves. In the first approach the wave staffs or wave buoys are installed and wave records are collected. The second approach is based on remote sensing techniques and use of various satellites sensors. However, both these approaches are expensive. To overcome this, in current oceanographic and laboratory practice numerical simulation techniques are becoming more and more popular. In particular, in the laboratory simulated time series are served as an input to the wave generators.

Usually the irregular records of sea surface ordinates of a given duration are represented in the form of many independent harmonics travelling in various directions, i.e.

$$\zeta(\mathbf{x}, t) = \sum_{m=1}^{N}\sum_{n=1}^{N} A_{mn}, \cos\psi_{mn}, \tag{3.77}$$

in which

$$\psi_{mn} = k_m(x\cos\theta_n + y\sin\theta_n) - \omega_m t + \epsilon_{mn}, \tag{3.78}$$

when the wave number k_m satisfies the dispersion relation

$$\omega_m^2 = gk_m\tanh(k_m h); \quad k_m = |\mathbf{k_m}|. \tag{3.79}$$

The deterministic spectral amplitudes A_{mn} are related to the one-dimensional energy spectrum $S_\zeta(\omega_m, \theta_n)$ by the following formula (Massel and Brinkman, 1998)

$$S_\zeta(\omega_m, \theta_n) = \frac{1}{2}\,\frac{A_{mn}^2}{\Delta\omega\Delta\theta}, \tag{3.80}$$

in which $\Delta\omega$ and $\Delta\theta$ are the discrete frequency and angle intervals, respectively. The random phase ϵ_{mn} is assumed to be uniformly distributed in the range

$(-\pi, \pi)$, and M and N are the number of frequencies and directions taken for simulation. If the numbers of frequencies M and directions N are high enough, simulated linear process ζ will become Gaussian distributed, with zero skewness and excess of kurtosis (Massel, 1996a; Massel and Brinkman, 1998).

There are essentially two procedures for carrying out the numerical simulation of time series of sea surface, pressure or orbital velocities. In both methods the amplitudes of the component waves have to be derived from the spectrum to be simulated. The first method is based on the assumption that the harmonic amplitudes are deterministic quantities given by the formula (3.80). However, the amplitudes of elementary waves are in fact random variables also and this is assumed in the second method of random sea simulation. In the following, both methods will be discussed shortly.

3.3.2.1 Simulation of linear random sea with random phases only

The simplest representation of a confused sea is the summation of many independent harmonics travelling in various directions as given by (3.77). The angles θ are usually specified at a constant interval. The preferred number of directional components should be greater than 30. Frequencies ω_m should be selected as non-correlating and non-harmonic forming (e.g. specified at non-constant intervals) to prevent wave profiles from repeating themselves with the period of $2M$ data points. Although no definite figure can be specified, the number of frequency components should be very large, typically some thousands when steep, extreme waves are considered. For example, Stansberg (1998) in his numerical synthesis procedure of time history of 4.5-h duration of storm used over 16,000 frequencies.

3.3.2.2 Simulation of linear random sea with random phases and amplitudes

In the second simulation method, the amplitudes of elementary wave components are also treated as random variables. Following Massel and Brinkman (1998) let us rewrite (3.77) as follows

$$\zeta(\mathbf{x}, t) = \sum_{m=1}^{M} \sum_{n=1}^{N} [b_{mn} \cos \psi_{mn} - c_{mn} \sin \psi_{mn}], \tag{3.81}$$

in which amplitudes b_{mn} and c_{mn} are

$$b_{mn} = A_{mn} \cos(\epsilon_{mn}), \quad c_{mn} = A_{mn} \sin(\epsilon_{mn}). \tag{3.82}$$

Due to random phases ϵ_{mn}, amplitudes b_{mn} and c_{mn} are independent random variables which should be generated from a Gaussian distribution with common variance $\sigma^2_{mn} = S(\omega_m) D(\theta_n) \Delta\omega_m \, \Delta\theta_n$. Therefore, the sum of (3.81) is used to produce the final simulated record. Massel and Brinkman (1998) used $M = 155$ frequencies, non-uniformly distributed in the frequency band $0.5\omega_\mathrm{p} < \omega < 3\omega_\mathrm{p}$, and $N = 180$ directions ($\Delta\theta = 2^\circ$) to simulate the target JONSWAP spectrum

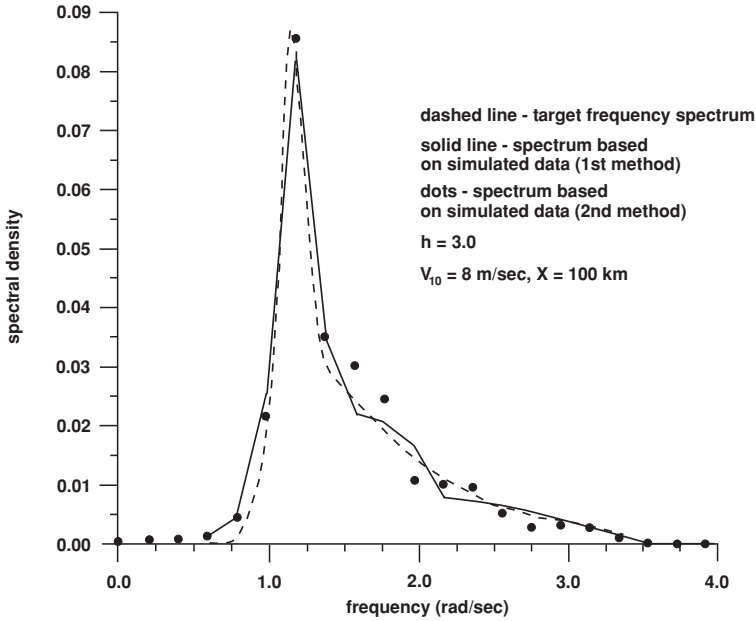

Figure 3.4: Comparison of target JONSWAP spectrum and frequency spectrum resulting from random simulation (adapted from Massel and Brinkman, 1998).

(wind speed $V = 8$ m/s, wind fetch $X = 100$ km and water depth $h = 3$ m). The frequency spectrum calculated by both methods conformed closely to the target one (see Fig. 3.4). Moreover, the product $M \times N = 27,900$ of independent elementary waves produced a surface elevation which is very close to a Gaussian process. They showed that the scattering of simulated probability density for wave height, resulting from both methods, with reference to the theoretical Rayleigh distribution, is approximately the same (see Fig. 3.5). In addition, both methods produce very similar period distributions, but both distributions are very different from the theoretical one developed, for example by Longuet–Higgins (1983b) – see Section 3.3.9. It should be noted that Tucker et al. (1983) pointed out that the first method with deterministic amplitude A_{mn} may incorrectly reproduce the distribution of wave group lengths.

3.3.2.3 Simulation of non-Gaussian random sea

Steep surface waves which are close to breaking typically display a vertical skewness in terms of higher crests and shallower, more rounded troughs. Field and laboratory experiments have shown that the largest crest heights deviate systematically from the Rayleigh model, while extreme peak-to-peak wave heights are usually reasonably well predicted by the Rayleigh theory (Massel,

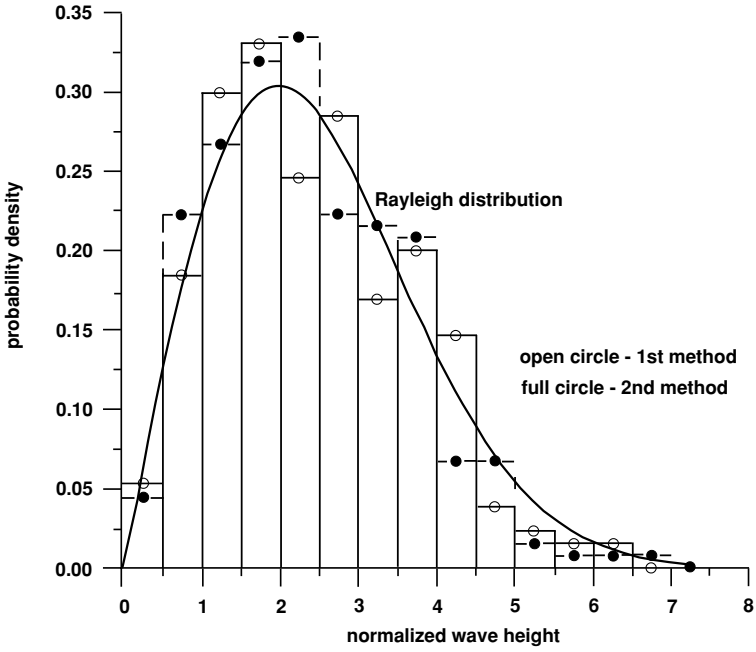

Figure 3.5: Comparison of probability density function of wave height resulting from simulation with Rayleigh distribution (adapted from Massel and Brinkman, 1998).

1996a). The observations of recent years provide evidence that for large waves in storm conditions, nonlinear effects should be taken into account. In order to simulate the non-Gaussian sea, a better description of large steep waves is needed. In the professional literature, a few second-order random wave models exist (Longuet–Higgins, 1962; Massel, 1973; Krylov et al. 1976; Hudspeth and Chen, 1979; Sharma and Dean, 1981; Biesel, 1982; Stansberg, 1998). In all of them, to the second approximation, the surface elevation $\zeta(t)$ takes the form

$$\zeta(t) = \zeta^{(1)}(t) + \zeta^{(2)}(t), \tag{3.83}$$

in which $\zeta^{(1)}(t)$ is given by (3.77) and a second-order contribution becomes (Massel, 1973)

$$\begin{aligned} \zeta^{(2)}(\mathbf{x},t) &= \sum_{n=1}^{N}\sum_{m=1}^{N} \frac{g k_n k_m}{2\omega_n \omega_m} A_n A_m \\ &\quad \times \left[M^{(+)} \cos(\psi_m + \psi_n) + M^{(-)} \cos(\psi_m - \psi_n) \right], \end{aligned} \tag{3.84}$$

in which

$$|\mathbf{k}_m \pm \mathbf{k}_n| = \left[k_m^2 + k_n^2 \pm 2 k_m k_n \cos(\theta_m - \theta_n) \right]^{1/2}; \; |\mathbf{k_n}| = k_n, \; |\mathbf{k_m}| = k_m \tag{3.85}$$

and

$$\psi_m \pm \psi_n = (\omega_m \pm \omega_n)t - [x(k_n \cos\theta_n + k_m \cos\theta_m) + y(k_n \sin\theta_n + k_m \cos\theta_m)]. \quad (3.86)$$

Amplitudes $M^{(+)}$ and $M^{(-)}$ are given in Appendix A.

Stansberg (1998) reported some results of nonlinear second-order numerical simulation of a random two-dimensional sea when $\theta = 0$. He used $N = 4096$ frequencies. The 4.5-h records of various sea states have been simulated, all of which are of the JONSWAP type with peak period $T_\mathrm{p} = 14\,\mathrm{s}$ and significant wave height $H_\mathrm{s} = 5$, 10, 15 or 20 m, while the spectral shape factor $\gamma = 1.0$, 2.0, 3.0 and 4.0. The statistically expected skewness and kurtosis resulting from simulations were compared with theoretical values of γ_1 and γ_2, suggested by Longuet–Higgins (1963), and Marthinsen and Winterstein (1992), showing a good agreement, except for 10% lower values for the simulations in the steepest sea states. Broad-banded spectra show higher skewness than narrow-banded ones.

3.3.3 Probability density function of extreme wave displacements

For a rough sea the most important statistical characteristics are the expected number of maxima and their probability distribution (Rice, 1944; Cartwright and Longuet–Higgins, 1956; Middleton, 1960; Tikhonow, 1966; Ochi, 1990; Massel, 1996a). In particular, Cartwright and Longuet–Higgins (1956) showed that the probability distribution of positive maxima of the surface elevation becomes

$$f_{\max}^{(+)}(\xi) = \frac{2}{1+\sqrt{1-\epsilon^2}}\left\{\frac{\epsilon}{\sqrt{2\pi}}e^{-\xi^2/2\epsilon^2} + \sqrt{1-\epsilon^2}\xi e^{-\xi^2/2}\Phi\left(\frac{\sqrt{1-\epsilon^2}}{\epsilon}\xi\right)\right\}, \quad (3.87)$$

in which ϵ^2 is given by (3.9). $\Phi(z)$ is a cumulative distribution function of the standardized normal probability density, also known as the probability integral (Abramowitz and Stegun, 1975)

$$\Phi(z) = \frac{1}{\sqrt{2\pi}}\int_{-\infty}^{z} e^{-t^2/2}dt = \frac{1}{2}\left[1 + erf(\frac{z}{\sqrt{2}})\right], \quad (3.88)$$

where the error function $erf(z)$ has the form

$$erf(z) = \frac{2}{\sqrt{\pi}}\int_0^z \exp(-t^2)\,dt. \quad (3.89)$$

Let us define the non-dimensional ξ value as

$$\xi = \frac{\zeta_{\max}}{\sqrt{m_0}}. \quad (3.90)$$

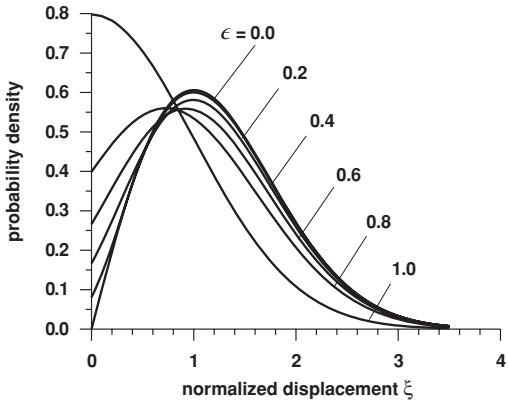

Figure 3.6: Probability density function of positive maxima as a function of parameter ϵ (adapted from Massel, 1996a).

The probability density function $f_{\max}^{(+)}(\xi)$ for various values of ϵ is shown in Fig. 3.6. In two special cases, the probability density function $f_{\max}^{(+)}(\xi)$ simplifies considerably. In particular for $\epsilon = 0$, which corresponds to a narrow-band random process (Massel, 1996a), (3.87) yields

$$f_{\max}^{(+)}(\xi) = \xi\, e^{-\xi^2/2}, \tag{3.91}$$

which is the Rayleigh probability density function for normalized positive maxima of the sea surface elevation. On the other hand if $\epsilon = 1$, the sea surface displacement represents the wide-band process and (3.87) becomes

$$f_{\max}^{(+)}(\xi) = \sqrt{\frac{2}{\pi}}\, e^{\xi^2/2}, \tag{3.92}$$

which is a truncated normal distribution.

The probability density functions of all extreme crests (positive and negative) are (Cartwright and Longuet–Higgins, 1956)

$$f_{\max}(\xi) = \frac{\epsilon}{\sqrt{2\pi}} e^{-\xi^2/2\epsilon^2} + \sqrt{1-\epsilon^2}\,\xi e^{-\xi^2/2}\,\Phi\left(\frac{\sqrt{1-\epsilon^2}}{\epsilon}\xi\right),\ -\infty < \xi < \infty. \tag{3.93}$$

The function (3.93) is illustrated in Fig. 3.7 for various values of ϵ. Again for a narrow-band process, (3.93) simplifies to the Rayleigh probability density function (3.91), and for a wide-band process we obtain a normal probability density function

$$f_{\max}(\xi) = \frac{1}{\sqrt{2\pi}}\, e^{-\xi^2/2}. \tag{3.94}$$

Stansberg (1998) compared the average simulated extreme crest heights with the theoretical estimations suggested by Winterstein (1988). He used the Hermite transformation to modify the Gaussian/Rayleigh estimates. The theoretical predictions compare quite well with simulated values. Moreover, the comparisons confirm about 15% increase in the extreme crest of a typical 100-year storm with reference to the Rayleigh estimate.

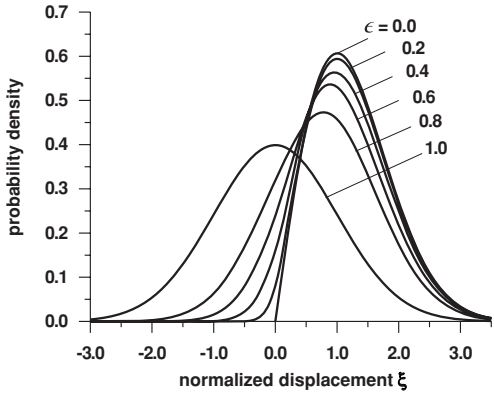

Figure 3.7: Probability density function of positive and negative maxima as a function of parameter ϵ (adapted from Massel, 1996a).

3.3.4 Structure of extreme waves

The formulae (3.87) and (3.93) determine the probability of occurrence of extreme wave crests of a given height and at a given location. This probability depends on the sea severity described by variance m_0 and on the bandwidth parameter ϵ. Although we cannot predict where or when in a random sea extreme crests or troughs will appear, Boccotti (1981, 1989) and Phillips et al. (1993a,b) discovered the expected configuration of the sea surface in the vicinity of sea surface maxima, say when $\zeta(\mathbf{x},t) > \gamma\sigma_\zeta$, in which γ is large. In particular, they obtained the expected profile of the surface displacement surrounding an extreme crest as follows

$$\frac{\overline{\zeta}(\mathbf{x}+\mathbf{r},t+\tau)}{\overline{\zeta}(\mathbf{x},t)|\zeta > \gamma\sigma_\zeta} = \rho(\mathbf{r},\tau), \tag{3.95}$$

in which $\rho = \rho(\mathbf{r},\tau)$ is the correlation function between two sea surface ordinates, i.e. $\zeta_1 = \zeta(\mathbf{x},t)$ and $\zeta_2 = \zeta(\mathbf{x}+\mathbf{r},t+\tau)$. Thus, the expected spatial configuration of extreme waves is approximately proportional to the two-dimensional spatial autocorrelation function of the wave field as a whole. Near the crests of extreme waves, the variance about the expected profile is very small. With increasing distance $\mathbf{r}$ or time τ from the crest, the variance increases, but always remains less than or equal to σ_ζ^2. The comparison of (3.95) with buoy data obtained during the surface wave dynamics experiment (SWADE) showed the agreement to be remarkably good.

3.3.5 Probability density function of local surface slopes of short and long crested waves

Wind-induced waves are basically three-dimensional and they exhibit same directional spreading against the wind direction (Massel, 1996a). This directional

spreading plays an important role when we try to use the limiting wave steepness as the wave breaking criterion (see Chapter 5). Therefore, it will be useful to examine the influence of the energy directional distribution on the probability density function for the local surface slope $\frac{\partial\zeta(x,t)}{\partial x}$ for wind-induced wave having different directional spectral characteristics.

Let us define ε_1 as a local surface slope in the direction θ_1. Therefore, for two slope components along x and y axes we have

$$\frac{\partial\zeta}{\partial x} = \varepsilon_1 \cos\theta_1; \quad \frac{\partial\zeta}{\partial\zeta} = \varepsilon_1 \sin\theta_1, \tag{3.96}$$

in which angle θ_1 increases from x axis in an anticlockwise direction.

Longuet–Higgins (1957) found that the two-dimensional probability density function $f(\varepsilon_1, \theta_1)$ takes the form

$$f(\varepsilon_1,\theta_1) = \frac{\varepsilon_1}{2\pi\sqrt{\Delta}} \times \\ \times \exp\left\{-\frac{\varepsilon_1^2(m_{02}\cos^2\theta_1 - 2m_{11}\sin\theta_1\cos\theta_1 + m_{20}\sin^2\theta_1)}{2\Delta}\right\}, \tag{3.97}$$

in which

$$m_{20} = \overline{\left(\frac{\partial\zeta}{\partial x}\right)^2}; \quad m_{02} = \overline{\left(\frac{\partial\zeta}{\partial y}\right)^2}; \quad m_{11} = \overline{\frac{\partial\zeta}{\partial x}\frac{\partial\zeta}{\partial y}} \tag{3.98}$$

and

$$\Delta = \begin{vmatrix} m_{20} & m_{11} \\ m_{11} & m_{02} \end{vmatrix}. \tag{3.99}$$

The overbar is a symbol of the statistical averaging.

If the x axis is parallel to the main wave direction, the moment m_{11} is equal to zero and (3.97) becomes

$$f(\varepsilon_1,\theta_1) = \frac{\varepsilon_1}{2\pi\sqrt{\Delta}} \exp\left\{-\frac{\varepsilon_1^2(m_{02}\cos^2\theta_1 + m_{20}\sin^2\theta_1)}{2\Delta}\right\}, \tag{3.100}$$

with $\Delta = m_{20}m_{02}$.

To determine the variances m_{02} and m_{20} we assume sea surface ordinates in a form of the Fourier-Stjeltjes integral (Massel, 1996a)

$$\zeta(x,y,t) = \int_{-\infty}^{\infty}\int_{-\pi}^{\pi} \exp[ik(x\cos\Theta + y\sin\Theta) - i\omega t]\, dA(\omega,\Theta), \tag{3.101}$$

in which Θ is the direction of a particular wave spectral component. For the surface slope components along the x and y axes we can write

$$\zeta_x = \frac{\partial\zeta}{\partial x} = \int_{-\infty}^{\infty}\int_{-\pi}^{\pi} (ik\cos\Theta)\exp[ikx\cos\Theta + y\sin\Theta) - i\omega t]\, dA(\omega,\Theta) \tag{3.102}$$

and

$$\zeta_y = \frac{\partial \zeta}{\partial y} = \int_{-\infty}^{\infty} \int_{-\pi}^{\pi} (ik \sin\Theta) \exp[ikx \cos\Theta + y \sin\Theta) - i\omega t]\, dA(\omega, \Theta). \tag{3.103}$$

The spectral amplitude $A(\omega, \Theta)$ is related to the two-dimensional energy spectrum $\hat{S}(\omega, \Theta)$ as

$$\overline{dA(\omega, \Theta)\, dA^*(\omega', \Theta')} = \hat{S}(\omega, \Theta)\delta(\omega - \omega')\delta(\Theta - \Theta')\, d\omega\, d\omega'\, d\Theta\, d\Theta', \tag{3.104}$$

in which $\delta(\,)$ is Dirac's delta and $(*)$ denotes the complex conjugate value. Using (3.98) and the known relation (Lighthill, 1975)

$$\int_{-\infty}^{\infty} \delta(x - y)\, dy = f(x), \tag{3.105}$$

we obtain the variances of surface slopes in the form

$$\left.\begin{aligned} m_{20} &= \sigma_{\zeta_x}^2 = \int_{-\infty}^{\infty} \int_{-\pi}^{\pi} k^2 \cos^2\Theta\, \hat{S}(\omega, \Theta)\, d\omega\, d\Theta \\ m_{02} &= \sigma_{\zeta_y}^2 = \int_{-\infty}^{\infty} \int_{-\pi}^{\pi} k^2 \sin^2\Theta\, \hat{S}(\omega, \Theta)\, d\omega\, d\Theta \end{aligned}\right\}. \tag{3.106}$$

When the deep water dispersion relation $\omega^2 = gk$ is applied, moments become

$$\left.\begin{aligned} m_{20} &= \sigma_{\zeta_x}^2 = \int_{-\infty}^{\infty} \int_{-\pi}^{\pi} \tfrac{\omega^4}{g^2} \cos^2\Theta\, \hat{S}(\omega, \Theta)\, d\omega\, d\Theta \\ m_{02} &= \sigma_{\zeta_y}^2 = \int_{-\infty}^{\infty} \int_{-\pi}^{\pi} \tfrac{\omega^4}{g^2} \sin^2\Theta\, \hat{S}(\omega, \Theta)\, d\omega\, d\Theta \end{aligned}\right\}. \tag{3.107}$$

Let us present the two-dimensional spectrum $\hat{S}(\omega, \Theta)$ in the form of the product of the frequency spectrum $S(\omega)$ and an empirically determined directional spreading function $D(\Theta)$

$$\hat{S}(\omega, \Theta) = S(\omega) D(\Theta). \tag{3.108}$$

After substituting (3.108) into (3.107) we obtain

$$\left.\begin{aligned} m_{20} &= \sigma_{\zeta_x}^2 = \tfrac{1}{g^2} \int_{-\infty}^{\infty} \omega^4\, S(\omega) d\omega \int_{-\pi}^{\pi} \cos^2\Theta D(\Theta)\, d\Theta \\ m_{02} &= \sigma_{\zeta_y}^2 = \tfrac{1}{g^2} \int_{-\infty}^{\infty} \omega^4\, S(\omega)\, d\omega \int_{-\pi}^{\pi} \sin^2\Theta\, D(\Theta)\, d\Theta \end{aligned}\right\}. \tag{3.109}$$

Taking into account that the integral against frequency is simply the fourth spectral moment, we can rewrite (3.109) as follows

$$\left.\begin{aligned} m_{20} &= \sigma_{\zeta_x}^2 = \frac{m_4}{g^2} \int_{-\pi}^{\pi} \cos^2\Theta D(\Theta)\, d\Theta = \frac{m_4}{g^2} I_{\mathrm{c}} \\ m_{02} &= \sigma_{\zeta_y}^2 = \frac{m_4}{g^2} \int_{-\pi}^{\pi} \sin^2\Theta\, D(\Theta)\, d\Theta = \frac{m_4}{g^2} I_{\mathrm{s}} \end{aligned}\right\}, \tag{3.110}$$

where

$$m_4 = \int_{-\infty}^{\infty} \omega^4 \, S(\omega) \, d\omega \tag{3.111}$$

and

$$I_{\mathrm{c}} = \int_{-\pi}^{\pi} \cos^2 \Theta D(\Theta) \, d\Theta, \tag{3.112}$$

$$I_{\mathrm{s}} = \int_{-\pi}^{\pi} \sin^2 \Theta D(\Theta) \, d\Theta. \tag{3.113}$$

It should be noted that

$$m_{20} + m_{02} = \sigma_{\zeta_x}^2 + \sigma_{\zeta_y}^2 = \frac{m_4}{g^2} \int_{-\pi}^{\pi} D(\Theta) \, d\Theta = \frac{m_4}{g^2}. \tag{3.114}$$

After substituting m_{02} and m_{20} into (3.100) we obtain

$$f(\varepsilon_1, \theta_1) = \frac{\varepsilon_1}{2\pi \, \frac{m_4}{g^2} \sqrt{I_{\mathrm{c}} \, I_{\mathrm{s}}}} \exp \left\{ -\frac{\varepsilon_1^2}{\frac{m_4}{g^2}} \, \frac{I_{\mathrm{s}} \cos^2 \theta_1 + I_{\mathrm{c}} \sin^2 \theta_1}{2 \, I_{\mathrm{c}} \, I_{\mathrm{s}}} \right\}, \tag{3.115}$$

or

$$f(\varepsilon_1, \theta_1) = \frac{\varepsilon_1}{2\pi \tilde{m}_4 \sqrt{I_{\mathrm{c}} \, I_{\mathrm{s}}}} \exp \left\{ -\frac{\varepsilon_1^2}{\tilde{m}_4} \, \frac{I_{\mathrm{s}} \cos^2 \theta_1 + I_{\mathrm{c}} \sin^2 \theta_1}{2 I_{\mathrm{c}} \, I_{\mathrm{s}}} \right\}, \tag{3.116}$$

where

$$\tilde{m}_4 = \frac{m_4}{g^2}. \tag{3.117}$$

For a fixed value of θ_1, the root mean square slope can be estimated from (3.115) as follows (Longuet–Higgins, 1957)

$$\left\{ \frac{\int_0^{\infty} \varepsilon_1^2 f(\varepsilon_1, \theta_1) d\varepsilon_1}{\int_0^{\infty} f(\varepsilon_1, \theta_1) d\varepsilon_1} \right\}^{1/2} = \left\{ \frac{2 I_{\mathrm{c}} I_{\mathrm{s}}}{I_{\mathrm{s}} \cos^2 \theta_1 + I_{\mathrm{c}} \sin^2 \theta_1} \right\}^{1/2}. \tag{3.118}$$

Therefore, the maximum rms slope of $2I_{\mathrm{c}}$ appears in the direction $\theta_1 = 0$, i.e. in the principal direction. The minimum slope of $2I_{\mathrm{s}}$ is in the direction at right angles to the principal direction ($\theta_1 = \pi/2$).

For the limiting case of uniform direction spreading is

$$D(\Theta) = \frac{1}{2\pi} \tag{3.119}$$

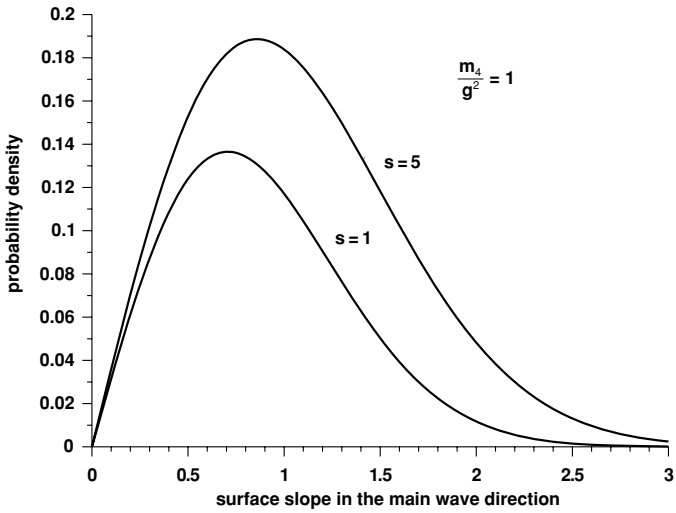

Figure 3.8: Probability density function of surface slopes in the direction of wave propagation for two directional spreadings of wave energy and for $\frac{m_4}{g^2} = 1$.

and

$$I_{\mathrm{c}} = I_{\mathrm{s}} = \frac{1}{2}. \tag{3.120}$$

Therefore, the probability density function (3.116) becomes

$$f(\varepsilon_{\mathrm{l}}, \theta_1) = \frac{\varepsilon_{\mathrm{l}}}{\pi\, \tilde{m}_4} \exp\left(-\frac{\varepsilon_{\mathrm{l}}^2}{\tilde{m}_4}\right). \tag{3.121}$$

After integration against angle θ_1 we have

$$f(\varepsilon_{\mathrm{l}}) = 2\frac{\varepsilon_{\mathrm{l}}}{\tilde{m}_4} \exp\left(-\frac{\varepsilon_{\mathrm{l}}^2}{\tilde{m}_4}\right). \tag{3.122}$$

Thus, for a short crested uniformly distributed wave field, the surface slope distribution is the Rayleigh distribution and it does not depend on the direction θ_1.

For further calculations we adopt the directional spreading function in a frequently used form (3.33), namely

$$D(\Theta; s) = \frac{2^{2s-1}}{\pi} \frac{\Gamma^2(s+1)}{\Gamma(2s+1)} \cos^{2s}\left(\frac{\Theta}{2}\right), \quad -\pi \le \Theta \le \pi. \tag{3.123}$$

For $s = 1$ in (3.123), when $D(\Theta) = \frac{1}{\pi}\cos^2\left(\frac{\Theta}{2}\right)$, the functions $I_{\mathrm{c}} = I_{\mathrm{s}} = \frac{1}{2}$. Therefore, the probability density function $f(\varepsilon_{\mathrm{l}}, \theta_1)$ becomes the same as

function (3.121)! This means that the probability density of local slopes for short crested waves with the directional spreading $D(\Theta) = \frac{1}{\pi}\cos^2\left(\frac{\Theta}{2}\right)$ also does not depend on the direction θ_1.

The probability density function (3.115) for $s = 1$ and $s = 5$, and for $\frac{m_4}{g^2} = \tilde{m}_4 = 1$ and $\theta_1 = 0$ is given in Fig. 3.8. The maximum of probability appears for slope 0.71 when $s = 1$, and for slope 0.87 when $s = 5$. Both probability densities exhibit the Rayleigh type function.

Integrating (3.115) against θ_1 we obtain the probability density function for surface slopes, regardless of direction θ_1, in the form

$$f(\varepsilon_1) = \frac{\varepsilon_1}{\frac{m_4}{g^2}\sqrt{I_c\, I_s}} \exp\left[-\frac{\varepsilon_1^2}{4\frac{m_4}{g^2} I_c\, I_s}\right]\, I_0\left[\frac{\varepsilon_1^2 (I_c - I_s)}{4\frac{m_4}{g^2} I_c\, I_s}\right], \tag{3.124}$$

in which $I_0(x)$ is the modified Bessel function of the zero order and imaginary argument (Abramowitz and Stegun, 1975).

Let us make the following variable transformation in (3.124)

$$\xi = \frac{\varepsilon_1}{\left(\frac{m_4}{g^2}\right)^{1/2}} = \frac{\varepsilon_1}{(\tilde{m}_4)^{1/2}}. \tag{3.125}$$

After substituting the above relation into (3.124) we obtain

$$f(\xi) = \frac{\xi}{\sqrt{I_c I_s}} \exp\left[-\frac{\xi^2}{4 I_c I_s}\right]\, I_0\left[\frac{\xi^2}{4}\,\frac{I_c - I_s}{I_c I_s}\right]. \tag{3.126}$$

Again, in two extreme cases, the above expression simplifies considerably. Namely for uniform direction spreading we have

$$f(\xi) = 2\xi \exp(-\xi^2). \tag{3.127}$$

For a wave field with short crests uniformly distributed in all directions θ_1, the surface slope distribution corresponds to the Rayleigh distribution. The same is true for the directional spreading $D(\Theta) = \frac{1}{\pi}\cos^2\left(\frac{\Theta}{2}\right)$.

On the other hand, when all spectral components propagate along the x axis, the directional spreading is simply

$$D(\Theta) = \delta(\Theta - \Theta_0), \tag{3.128}$$

where $\Theta_0 = 0$. From (3.112) and (3.113) we have

$$\left.\begin{aligned} I_c &= 1 \\ I_s &= 0 \end{aligned}\right\}. \tag{3.129}$$

Thus, $\frac{\xi^2}{4}\,\frac{I_c - I_s}{I_c\, I_s} \to \infty$ and the asymptotic approximation of the Bessel function $I_0()$ now becomes (Abramowitz and Stegun, 1975)

$$I_0\left[\frac{\xi^2}{4}\,\frac{I_c - I_s}{I_c I_s}\right] \approx \frac{1}{\sqrt{2\pi}}\,\frac{\exp\left[\frac{\xi^2}{4}\,\frac{I_c - I_s}{I_c\, I_s}\right]}{\frac{\xi}{2}\sqrt{\frac{I_c - I_s}{I_c\, I_s}}}. \tag{3.130}$$

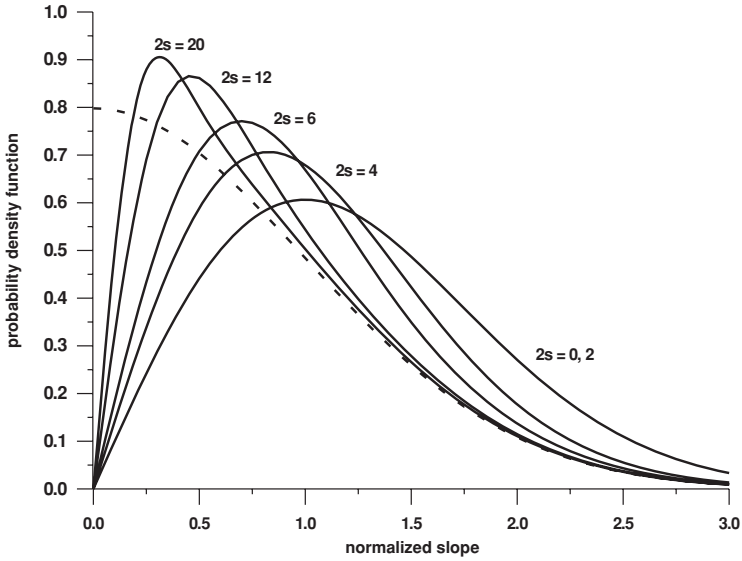

Figure 3.9: Probability density function for sea surface slope for different directional spreadings of wave field

Using above relation in (3.126) yields

$$f(\xi) = \sqrt{\frac{2}{\pi}} \exp\left(-\frac{1}{2}\xi^2\right). \tag{3.131}$$

The above equation indicates that in a two-dimensional random wave field, when crests are very long, surface slopes are normally distributed (truncated normal distribution).

In Fig. 3.9 the probability density function $f(\xi)$ is illustrated for various values of directional spreading parameter $2s$, namely for $2s = 0$, 2, 4, 6, 12 and 20, as well as for extreme narrow directional spreading (3.128). It should be noted that the probability density functions for the normalized slope ξ for spreading parameter $2s = 0$ and $2s = 2$ are the same as in both cases the parameters $I_c = I_s = \frac{1}{2}$. The dashed line in Fig. 3.9 denotes the probability density function for an extremely narrow wave field, when $\frac{I_c - I_s}{I_c\, I_s} \to \infty$.

3.3.6 Probability density function of wave heights

Wave amplitude can be detected in the simplest way under the assumption of a narrow-band spectrum in which the positive and negative maximum excursions of wave surface process are equal to each other, and equal to wave amplitude. However, this is not usually the case for real ocean surface waves. A typical record of ocean waves for a non-narrow-band spectrum is given in Fig. 3.10. It is clear that the envelopes of the process are not symmetrical curves. Therefore, the positive and negative amplitudes are different. In order

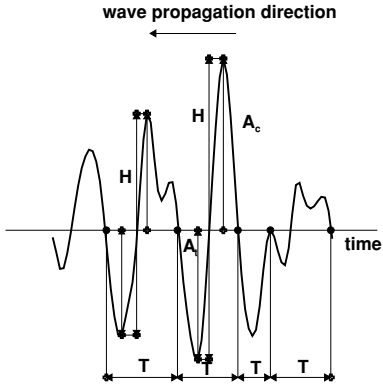

Figure 3.10: Definition of zero-down-crossing waves.

to overcome this uncertainty, in physical oceanography the crest-to-trough excursion is used and wave height is defined as the sum of the two values of the upper and lower amplitudes. Only for a narrow-band spectrum is the wave height equal to twice the upper (or lower) amplitude.

It should be noted that the definition of individual wave height depends entirely on the choice of the trough occurring before or after the crest. Here we will adopt the zero-down-crossing method when the wave trough occurs before the wave crest (Fig. 3.10).

Consider the unidirectional wave motion of a narrow-band frequency spectrum at a given point

$$\zeta(t) = \sum_{i=1}^{\infty} a_i \cos\left(\omega_i t - \epsilon_i\right). \tag{3.132}$$

Using frequency ω_p, which corresponds to the spectrum peak, we can rewrite (3.132) as

$$\zeta(t) = A_\mathrm{c}(t)\cos\left(\omega_\mathrm{p} t\right) - A_\mathrm{s}(t)\sin\left(\omega_\mathrm{p} t\right), \tag{3.133}$$

in which

$$\left.\begin{array}{rcl} A_\mathrm{c}(t) & = & \sum_{i=1}^{\infty} a_i \cos\left[\left(\omega_i - \omega_\mathrm{p}\right) t - \epsilon_i\right] \\ A_\mathrm{s}(t) & = & \sum_{i=1}^{\infty} a_i \sin\left[\left(\omega_i - \omega_\mathrm{p}\right) t - \epsilon_i\right] \end{array}\right\}. \tag{3.134}$$

Because of the narrowness of the process, the amplitudes $A_\mathrm{c}(t)$ and $A_\mathrm{s}(t)$ are very slowly varying functions of time. Hence

$$\zeta(t) = A(t)\cos\left[\omega_\mathrm{p} t + \varphi(t)\right], \tag{3.135}$$

where

$$A(t) = \sqrt{A_\mathrm{c}^2(t) + A_\mathrm{s}^2(t)}, \tag{3.136}$$

$$\varphi(t) = \tan^{-1}\left[A_\mathrm{s}(t)/A_\mathrm{c}(t)\right], \tag{3.137}$$

and

$$A_{\mathrm{c}}(t) = A(t)\cos\varphi(t), \quad A_{\mathrm{s}}(t) = A(t)\sin\varphi(t). \tag{3.138}$$

It should be noted that, in the case of a narrow-band spectrum, the amplitude A is equal to the amplitude of the wave envelope, which varies slowly in time. In virtue of the central limit theorem, A_{c} and A_{s} are Gaussian processes with mean value equal to zero and variance σ_ζ^2 as

$$E\left[A_{\mathrm{c}}^2\right] = E\left[A_s^2\right] = E\left[\zeta^2\right] = \sigma_\zeta^2. \tag{3.139}$$

It can be shown that $E\left[A_{\mathrm{c}}A_{\mathrm{s}}\right] = 0$. Thus, ζ_c and ζ_s are independent variables and the two-dimensional probability density function becomes

$$f_2\left(A_{\mathrm{c}}, A_{\mathrm{s}}\right) = f\left(A_{\mathrm{c}}\right) f\left(A_{\mathrm{s}}\right) = \frac{1}{2\pi\sigma_\zeta^2}\exp\left[-\frac{A_{\mathrm{c}}^2 + A_{\mathrm{s}}^2}{2\sigma_\zeta^2}\right], \tag{3.140}$$

or

$$f_2\left(A, \varphi\right) = \frac{A}{2\pi\sigma_\zeta^2}\exp\left(-\frac{A^2}{2\sigma_\zeta^2}\right). \tag{3.141}$$

Finally, the one-dimensional probability densities for amplitude A and phase φ are obtained through integration of (3.141), with respect to phase φ and amplitude A, respectively

$$f(A) = \int_{-\pi}^{\pi} f_2\left(A, \varphi\right) d\varphi = \frac{A}{\sigma_\zeta^2}\exp\left(-\frac{A^2}{2\sigma_\zeta^2}\right), \tag{3.142}$$

and

$$f(\varphi) = \frac{1}{2\pi}\int_0^{\infty}\frac{A}{\sigma_\zeta^2}\exp\left(-\frac{A^2}{2\sigma_\zeta^2}\right) dA = \frac{1}{2\pi}. \tag{3.143}$$

Equation (3.142) represents the well-known Rayleigh distribution for wave amplitude. Result (3.143) indicates that for a narrow-band process, the phase is uniformly distributed in the range (π, π).

As mentioned above, in physical oceanography and ocean engineering, the wave height H is preferred to wave amplitude A. The assumption of a narrow-band spectrum leads to the conclusion that $H \approx 2A$. The transformation of variable A to H in (3.142) gives the Rayleigh distribution in terms of wave height H

$$f(H) = \frac{H}{4\sigma_\zeta^2}\exp\left(-\frac{H^2}{8\sigma_\zeta^2}\right), \tag{3.144}$$

or

$$f(\xi) = \frac{1}{4}\xi\exp\left(-\frac{1}{8}\xi^2\right), \tag{3.145}$$

in which $\xi = \frac{H}{\sigma_\zeta}$.

The moments of wave height can be presented as follows

$$E\left[H^m\right] = \overline{H^m} = 2^{3m/2}\,\sigma_\zeta^m\,\Gamma\left(1+\frac{m}{2}\right). \tag{3.146}$$

In particular, the mean wave height $\bar{H}$ and the root-mean-square wave height $H_{\rm rms}$ are obtained from (3.146), if $m=1$ and $m=2$, respectively

$$\bar{H} = \sqrt{2\pi}\sigma_\zeta, \quad H_{\rm rms} = 2\sqrt{2}\sigma_\zeta = \frac{2}{\sqrt{\pi}}\bar{H}. \tag{3.147}$$

Using (3.147), the distribution (3.144) can be rewritten as

$$f(H) = \frac{2H}{H_{\rm rms}^2}\exp\left(-\frac{H^2}{H_{\rm rms}^2}\right), \tag{3.148}$$

or

$$f(\xi) = 2\xi\exp\left(-\xi^2\right), \tag{3.149}$$

in which $\xi = \frac{H}{H_{\rm rms}}$, and

$$f(H) = \frac{\pi}{2}\,\frac{H}{\bar{H}^2}\exp\left[-\frac{\pi}{4}\left(\frac{H}{\bar{H}}\right)^2\right]. \tag{3.150}$$

Although various wave height relations based on the Rayleigh distribution can be found elsewhere (for example Massel, 1989), here we only discuss one specific wave height frequently used in practice, namely the significant wave height $H_{\rm s}$. The wave height $H_{\rm s}$ is defined as the average of the highest one-third of wave heights. Assuming a narrow-band wave spectrum, we calculate the threshold wave height H^* which has the probability of exceedance of $\frac{1}{3}$ which corresponds to value $H^* = \frac{H}{\sigma_\zeta} \approx 3.0$ (see Fig. 3.11).

Using (3.148) we have

$$Pr\left\{H > H^*\right\} = \int_{H^*}^{\infty}\frac{2H}{H_{\rm rms}^2}\,\exp\left[-\left(\frac{H}{H_{\rm rms}}\right)^2\right]dH = \frac{1}{3}. \tag{3.151}$$

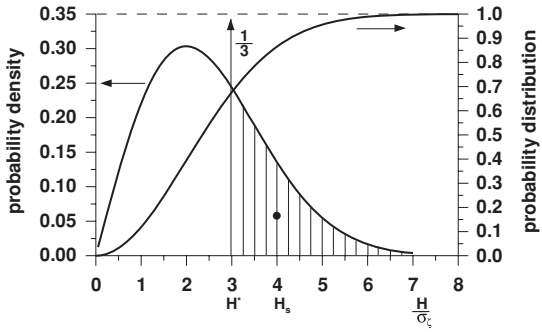

Figure 3.11: Determination of significant wave height $H_{\rm s}$.

Thus,

$$H^* = \sqrt{\ln 3}\, H_{\rm rms} = 1.048\, H_{\rm rms}. \tag{3.152}$$

According to the definition, the significant wave height corresponds to the centre of gravity of the shaded area in Fig. 3.11. The balance of moments with respect to the origin yields

$$\frac{1}{3} H_{\rm s} = \int_{H^*}^{\infty} H\, f(H)\, dH, \tag{3.153}$$

or

$$H_{\rm s} = \left\{ \frac{3\sqrt{\pi}}{2}\, erfc\left(\sqrt{\ln 3}\right) + \sqrt{\ln 3} \right\} H_{\rm rms} \approx 1.416 H_{\rm rms}, \tag{3.154}$$

where the complementary error function $erfc(z)$ is given by (Abramowitz and Stegun, 1975)

$$erfc(z) = \frac{2}{\sqrt{\pi}} \int_z^{\infty} \exp^{-t^2}\, dt. \tag{3.155}$$

Using the second relation of (3.147), the significant wave height can be expressed as

$$H_{\rm s} = 1.416\, H_{\rm rms} = 4.004 \sigma_\zeta = 1.6\, \bar{H}. \tag{3.156}$$

Except for $H_{\rm s}$, being the mean of the highest one-third of wave height, significant wave height is commonly estimated from wave records using relation (3.156) when standard deviation is calculated from the frequency spectrum $S(\omega)$. This significant wave height is usually noted as H_{m_0}, i.e.

$$H_{m_0} = 4.004 \sqrt{m_0}. \tag{3.157}$$

In other words, H_{m_0} is an energy-based significant wave height, determined as four times the square root of the area contained under the energy spectrum $S(\omega)$. Height H_{m_0} is approximately equal to $H_{\rm s}$ except when waves are very steep. In situations where H_{m_0} is equal to $H_{\rm s}$, either can be used. However, when H_{m_0} differs from $H_{\rm s}$, it cannot be used directly to estimate wave height statistics.

Above analysis (3.151) can be generalized to evaluate the average of the highest $1/N$ th wave heights $\bar{H}_{1/N}$, based on the Rayleigh distribution, i.e.

$$\bar{H}_{1/N} = \left\{ \frac{N\sqrt{\pi}}{2}\, erfc\left(\sqrt{\ln N}\right) + \sqrt{\ln N} \right\} H_{\rm rms}. \tag{3.158}$$

In Table 3.1 the values of $\bar{H}_{1/N}$ are listed for selected values of N.

Table 3.1: Characteristic wave heights based on the Rayleigh distribution

N	$\bar{H}_{1/N}/H_{\rm rms}$	$\bar{H}_{1/N}/\bar{H}$	$\bar{H}_{1/N}/\sigma_\zeta$	Remarks
500	2.680	3.023	7.580	
200	2.503	2.823	7.078	
100	2.359	2.662	6.671	Highest 1/100th wave
50	2.206	2.488	6.239	
25	2.042	2.303	5.775	
10	1.800	2.030	5.090	
5	1.591	1.795	4.499	
3	1.416	1.597	4.004	Significant wave
1	0.886	1.000	2.505	Mean wave

3.3.7 Probability density function of wave amplitudes of non-Gaussian sea

In Section 3.3.1, the Gaussian distribution was used to describe the probability density of the surface ordinates. However, surface waves that are close to breaking typically display a vertical skewness in terms of higher crests and shallower, more rounded troughs. The exact theoretical form of the distribution of nonlinear wave crests is not known under general conditions. There have been some attempts to approximate the distributions of nonlinear wave crests. For example, a deep water approximation based on Edgeworths form of the Gram-Charlier distribution was derived by Longuet–Higgins (1964). The approximations by Tayfun (1980), Huang et al. (1983) and Kriebel and Dawson (1993) predict the observed properties of laboratory generated waves as well as the field data quite well for the narrow-band sea model. Tayfun and Al-Humond (2002) predicted the least upper bound distribution for nonlinear wave amplitudes. They showed that the probability density function for non-dimensional amplitude takes the form

$$f(y) = \frac{2}{\Delta}\left(1 - \frac{1}{\sqrt{1+2\,\Delta y}}\right)\exp\left[-\left(\frac{\sqrt{1+2\,\Delta y}-1}{\Delta}\right)^2\right], \tag{3.159}$$

in which

$$y = \frac{A}{A_{\rm rms}} \tag{3.160}$$

and

$$\Delta = A_{\rm rms}\,\bar{k}. \tag{3.161}$$

The root-mean-square wave amplitude $A_{\rm rms}$ becomes

$$A_{\rm rms} = (2m_0)^{1/2} \tag{3.162}$$

and the spectral-mean wave number $\bar{k}$ is

$$\bar{k} = \frac{\overline{\omega^2}}{g} \quad \text{and} \quad \overline{\omega^2} = \frac{\mathrm{m}_2}{\mathrm{m}_0}. \tag{3.163}$$

Therefore,

$$\bar{k} = \frac{m_2}{g\, m_0}. \tag{3.164}$$

It should be noted that the frequency $\omega_0 = \sqrt{\overline{\omega^2}}$ is called the root-mean-square frequency.

After substituting (3.162) and (3.164) into (3.161) we obtain

$$\Delta = A_{\mathrm{rms}}\, \bar{k} = \sqrt{2}\, \frac{m_2}{g\, \sqrt{m_0}}. \tag{3.165}$$

The quantity Δ is a measure of the root-mean-square surface steepness. In the dimensional form, the probability density (3.159) becomes

$$f(A) = \frac{2}{B_1\, A_{\mathrm{rms}}}\, B_2 \exp\left(-B_2^2\right), \tag{3.166}$$

in which

$$B_1 = \sqrt{1 + 2\,\Delta\, \left(\frac{A}{A_{\mathrm{rms}}}\right)} \tag{3.167}$$

and

$$B_2 = \frac{\sqrt{1 + 2\,\Delta\, \left(\frac{A}{A_{\mathrm{rms}}}\right)} - 1}{\Delta}. \tag{3.168}$$

In Fig. 3.12, the probability density $f(A)$ is shown for a random wave field characterized by the JONSWAP spectrum. Waves are induced by wind of velocity $V_{10} = 8\,\mathrm{m/s}$ and fetch $X = 100\,\mathrm{km}$. Resulting parameters are: peak period $T_{\mathrm{p}} = 5.61\,\mathrm{s}$, significant wave height $H_{\mathrm{s}} = 1.64\,\mathrm{m}$, $A_{\mathrm{rms}} = 0.58\,\mathrm{m}$ and $\Delta = 0.11$. Due to small value of Δ used in the calculations, the difference between both probability densities is also small, with the largest discrepancy around the wave amplitude $A \approx 0.75\, A_{\mathrm{rms}}$.

For comparison, in the same figure, the probability density for linear waves is given. This function results from (3.166) as follows

$$\sqrt{1 + 2\Delta \left(\frac{A}{A_{\mathrm{rms}}}\right)} \approx 1 + \Delta \left(\frac{A}{A_{\mathrm{rms}}}\right) - \frac{1}{2}\Delta^2 \left(\frac{A}{A_{\mathrm{rms}}}\right)^2 + \cdots. \tag{3.169}$$

For $\Delta \to 0$, from (3.166) results the Rayleigh distribution, i.e.

$$f(A) = \frac{2A}{A_{\mathrm{rms}}^2} \exp\left[-\left(\frac{A}{A_{\mathrm{rms}}}\right)^2\right], \tag{3.170}$$

or

$$f(y) = 2y \exp(-y^2). \tag{3.171}$$

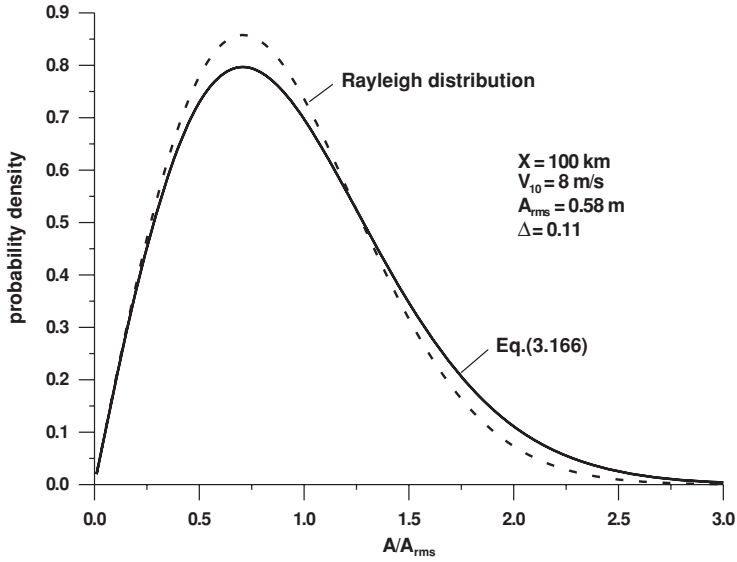

Figure 3.12: Comparison of wave amplitude probability density for non-Gaussian field and Rayleigh's distribution.

3.3.8 Joint probability density function of wave amplitudes and wave periods for narrow bandwidth waves

There are a lot formulae on the two-dimensional probability density of wave parameters. Extended comments on them can be found in the book by Massel (1996a). For our purpose, the Longuet–Higgins (1983b) probability density function for wave height and wave period is used

$$\tilde{f}(R,\tau) = \frac{2}{\sqrt{\pi}\nu}\left(\frac{R}{\tau}\right)^2 \exp\left\{-R^2\left[1+\left(1-\frac{1}{\tau}\right)^2/\nu^2\right]\right\} L(\nu), \tag{3.172}$$

where

$$R = \frac{A}{(2m_0)^{1/2}}; \quad \tau = \frac{T}{\overline{T}}, \tag{3.173}$$

$$L(\nu) = \frac{2\sqrt{1+\nu^2}}{1+\sqrt{1+\nu^2}}, \tag{3.174}$$

$$\overline{T} = \frac{2\pi}{\bar{\omega}} = 2\pi\frac{m_0}{m_1}. \tag{3.175}$$

A denotes the wave amplitude, T is the wave period and ν the parameter of spectrum width given by (3.7).

For further analysis we transform the two-dimensional probability density $\tilde{f}(R,\tau)$ into probability $f(\rho,\tau)$, where $\rho = \frac{2A}{H_s} = \frac{H}{H_s}$. Therefore, we have

$$f(\rho,\tau)d\rho = \tilde{f}(R,\tau)dR, \tag{3.176}$$

or

$$f(\rho,\tau) = \tilde{f}(R,\tau)\frac{dR}{d\rho}. \tag{3.177}$$

After some algebra we obtain

$$f(\rho,\tau) = \frac{8}{\sqrt{2\pi}\,\nu}\left(\frac{\rho}{\tau}\right)^2 \exp\left\{-2\rho^2\left[1+\left(1-\frac{1}{\tau}\right)^2/\nu^2\right]\right\} L(\nu), \tag{3.178}$$

where the relationship

$$H_s = 4\sqrt{m_0} \tag{3.179}$$

is used. In Fig. 3.13 the non-dimensional probability function $f(\rho,\tau)/f_{\max}$ is illustrated for $\nu = 0.4$.

The position of the maximum value of $f(\rho,\tau)$ is found from the condition that $\partial f/\partial\rho$ and $\partial f/\partial\tau$ both vanish. Hence we find

$$\rho = \frac{1}{\sqrt{2(1+\nu^2)}}; \quad \tau = \frac{1}{1+\nu^2}. \tag{3.180}$$

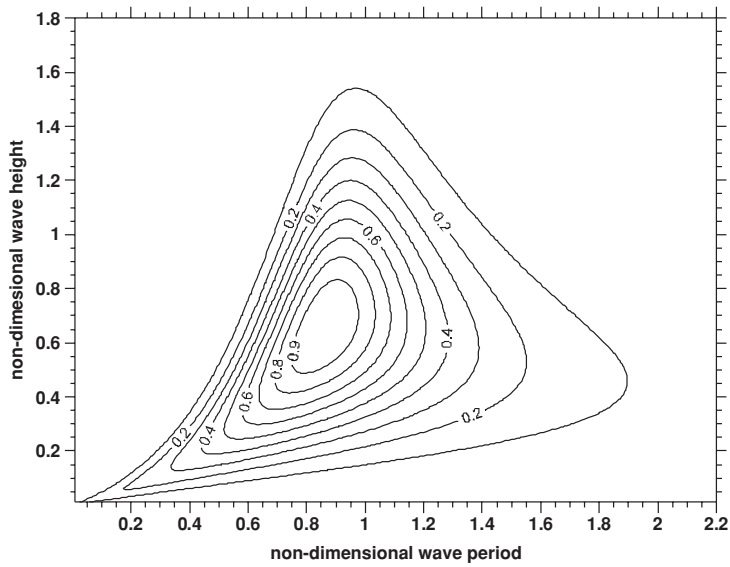

Figure 3.13: The non-dimensional probability function $f(\rho,\tau)/f_{\max}$ for $\nu = 0.4$.

The value of $f(\rho,\tau)$ at this point is

$$f_{max} = f(\rho,\tau) = 0.587(\nu + \nu^{-1})\, L(\nu). \tag{3.181}$$

It should be noted that the probability density functions (3.172) and (3.178) are valid for the sufficiently narrow spectrum when $\nu^2 \ll 1.0$. An advantage of using these functions is their dependence on the lowest spectral moments m_0, m_1 and m_2, which can be calculated for the most typical spectral density functions.

3.3.9 Probability density function of wave periods

The probability density function of period T, regardless of wave height H, is found by integrating probability density function $\tilde{f}(R,\tau)$ with respect to R over $0 < R < \infty$. Using the Longuet–Higgins distribution (3.172) we obtain

$$f(\tau) = \frac{4\sqrt{2\pi}C_{\mathrm{L}}}{\tau^2}\left[1 + \frac{1}{\nu^2}\left(1 - \frac{1}{\tau}\right)^2\right]^{-3/2}, \tag{3.182}$$

in which

$$C_{\mathrm{L}} = \frac{1}{4\sqrt{2\pi}\nu\left[1 + (1+\nu^2)^{-1/2}\right]}. \tag{3.183}$$

Function (3.182) is shown in Fig. 3.14 for some representative values of ν. The distribution is asymmetric in accordance with observations. It depends on the three lowest moments m_0, m_1, m_2 of the spectral density function (by using spectral width parameter ν). The mode of the distribution decreases with ν as

$$\tau_m = \frac{2}{\sqrt{9 + 8\nu^2} - 1}. \tag{3.184}$$

In particular, the mean of the distribution is theoretically infinite, since for large values of τ the density $f(\tau)$ behaves like τ^{-2}. However, using the exact value of the average frequency of up-crossings of the mean level, it can be found that mean zero-crossing wave period $\bar{T}_0$ is

$$\bar{T}_0 = \frac{\bar{T}}{\sqrt{1+\nu^2}} = 2\pi\sqrt{\frac{m_0}{m_2}}, \tag{3.185}$$

in which

$$\bar{T} = 2\pi\,\frac{m_0}{m_1} \tag{3.186}$$

is the mean wave period. For comparison, in Fig. 3.14 the empirical distribution proposed by Davidan et al. (1985) was shown

$$f(\tau) = 3A\,\tau^2 \exp\left(-A\tau^3\right), \tag{3.187}$$

in which $A = \Gamma^3\left(\frac{4}{3}\right) \approx 0.712$. This distribution, based on a large set of data, is included in the Russian oceanographic tables.

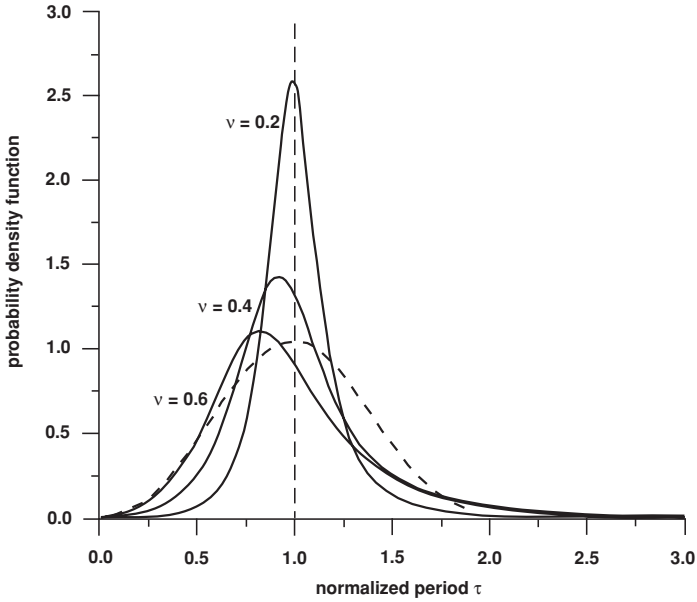

Figure 3.14: Probability density function for wave period for $\nu = 0.2$, 0.4 and 0.6 – solid lines; distribution according to Davidan et al. (1985) – dashed line (adapted from Massel (1996a)).

3.3.10 Joint probability density function of wave amplitudes and wave periods for finite bandwidth waves

Due to complex atmospheric systems and nonlinear wave generation processes, wave energy is usually distributed over a finite and not necessarily narrow frequency band. Therefore, the assumption that bandwidth parameter $\nu \ll 1$ used in Longuet–Higgins' model for the joint probability density function of wave amplitudes and wave periods, is not satisfied. To avoid this restriction, Papadimitrakis (2005) proposed a new joint probability density applicable for narrow as well as for finite bandwidth spectra. His model is based on the solution of Yuan et al. (1986) and it is expressed in terms of wave amplitude A and frequency ω

$$f(A,\omega) = E_1(\omega)A^2 \exp[-E_2(\omega)A^2], \tag{3.188}$$

$$E_1(\omega) = \frac{4}{\sqrt{2\pi}\,\alpha_2^2(\chi+1)\sqrt{\chi^2-1}m_0{}^{\frac{3}{2}}\,\omega_0} \tag{3.189}$$

and

$$E_2(\omega) = \frac{1}{2m_0}\left\{1 + \frac{\left[1-\frac{1}{\alpha_2}\left(\frac{\omega}{\omega_0}\right)^2\right]^2}{(\chi^2-1)}\right\}, \tag{3.190}$$

where

$$\omega_0 = \sqrt{\frac{m_2}{m_0}} \quad \text{and} \quad \chi = \sqrt{\frac{m_0\, m_4}{m_2^2}}. \tag{3.191}$$

Coefficient α_2 is a positive coefficient dependent also on χ, ω_0 and spectral peak frequency ω_{p}. In fact, it is a ratio of the expected number of wave extremes and number of zero-crossings per unit time. It can serve also as a measure of the spectrum bandwidth being related to the parameter ϵ, introduced by Cartwright and Longuet–Higgins (1956) and given by (3.9). It can be shown that

$$\chi^2 = \frac{1}{1-\epsilon^2}. \tag{3.192}$$

Thus, for a narrow band spectrum $\epsilon = 0$ and $\chi = 1$, while for an extremely broad spectrum we have $\epsilon = 1$ and χ becomes unbounded.

To avoid the difficulties with determination of the high spectral moments due to noise tail of the spectrum, the low-pass filtering technique was used. In particular, Papadimitrakis applied the Glazman (1986) approach where the filtered moments are defined as follows:

$$m_0 = \int_{-\pi}^{\pi}\int_{0}^{\infty} Z^2(\omega, T_c)\, \hat{S}(\omega,\theta) d\omega\, d\theta, \tag{3.193}$$

$$m_1 = \int_{-\pi}^{\pi}\int_{0}^{\infty} Z^2(\omega, T_c)\, \omega \hat{S}(\omega,\theta) d\omega\, d\theta, \tag{3.194}$$

$$m_2 = \int_{-\pi}^{\pi}\int_{0}^{\infty} Z^2(\omega, T_c)\, \omega^2 \hat{S}(\omega,\theta) d\omega\, d\theta, \tag{3.195}$$

$$m_4 = \int_{-\pi}^{\pi}\int_{0}^{\infty} Z^2(\omega, T_c)\, \omega^4 \hat{S}(\omega,\theta) d\omega\, d\theta, \tag{3.196}$$

in which

$$Z(\omega, T_c) = \frac{\sin\left(\omega \frac{T_c}{2}\right)}{\omega \frac{T_c}{2}} \tag{3.197}$$

and T_c is the cutoff period. The filter function (3.197) removes from the spectrum all components with periods shorter than T_c. According to Papadimitrakis, the cutoff period should be in the range $T_c < (0.1 - 0.2)T_{\mathrm{p}}$, where T_{p} is the spectral peak period.

The coefficient α_2 was introduced to satisfy the condition that the expected energy density of the finite bandwidth spectrum should theoretically be equal to half of the amplitude squared. Calculations show that

$$\alpha_2 = \left(\frac{\omega_{\mathrm{p}}}{\omega_0}\right) \frac{7}{2 + \sqrt{[25 + 21\sqrt{(\chi^2 - 1)}]}}. \tag{3.198}$$

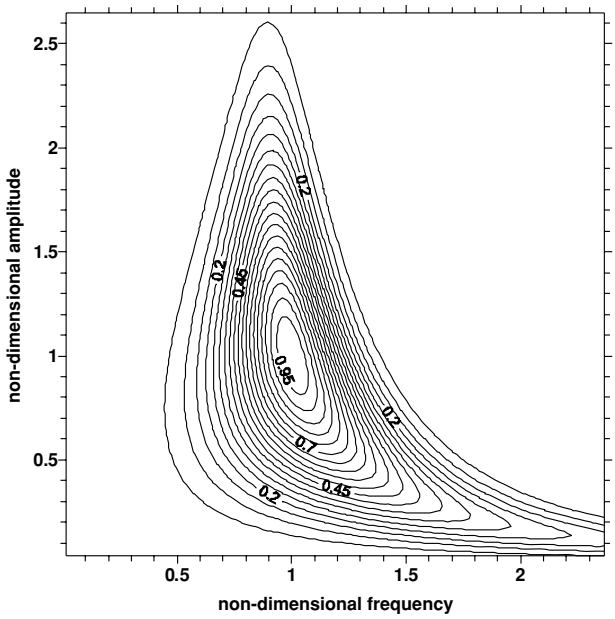

Figure 3.15: Probability density function for normalized amplitude and frequency of wind waves.

It should be noted that for $\chi = 1$, α_2 should also be equal to 1. However, from (3.198) it follows that $\alpha_2 = \left(\frac{\omega_\mathrm{p}}{\omega_0}\right)$. The field and laboratory data indicate that usually this ratio $\approx 1.15 - 1.20$.

The probability density $f(A, \omega)$ reaches a maximum at point $(A_{\max}, \omega_{\max})$, when

$$A_{\max} = \left\{ \frac{\chi^2 - 1}{\chi^2 + 1 - (3\chi^2 + 1)^{1/2}} \right\}^{1/2} \sqrt{\frac{m_0}{2}} \tag{3.199}$$

and

$$\omega_{\max} = \left\{ \alpha_2 \left[-1 + \left(3\chi^2 + 1 \right)^{1/2} \right] \right\}^{1/2} \omega_0. \tag{3.200}$$

In Fig. 3.15 the normalized probability density given by (3.188) is shown for wind waves generated by wind of speed $V_{10} = 10\,\mathrm{m/s}$ and fetch of 50 km. The amplitudes and frequencies are normalized against the $\omega_{\max}$ and $A_{\max}$ values, respectively. The JONSWAP spectrum with enhancement factor $\gamma = 7$ was adopted. As a result the following characteristic parameters were obtained: $H_\mathrm{s} = 1.65$ m, $\omega_\mathrm{p} = 1.30$ rad/s, $\epsilon = 0.564$, $\nu = 0.265$ and $\chi = 1.21$.

3.3.11 Probability density function of the highest wave in a record

The steady wave theory indicates that the maximum or limit wave height will depend at least on the local water depth and the local wave period. However in a real sea state, due to the variability of wave period and the irregularity of the profile of each individual wave, the highest wave height will not reach the theoretical limit wave height, H_{limit}. The highest wave height will be dependent on temporal evolution of the intensity of the sea state and on statistical variability within the sea state. Thus, in a real sea state, $H_{\max}$ is a random variable and its complete description is provided by the probability distribution. Assuming that the occurrence of wave height is an independent event and that the wave spectrum is narrow-banded, the probability density function and cumulative distribution function for the highest wave $H_{\max}$ in a stationary record of N waves become (Massel, 1996a)

$$f_{H_{\max}}(H_{\max}) = N f_H(H_{\max}) \left[F_H(H_{\max})\right]^{N-1} \tag{3.201}$$

and

$$F_{H_{\max}}(H_{\max}) = \left[F_H(H_{\max})\right]^N, \tag{3.202}$$

where $f_H(H_{\max})$ is the probability density function of individual wave height, and $F_H(H_{\max})$ is the corresponding cumulative distribution function.

Usually, the functions (3.201) and (3.202) are normalized with root-mean-square wave height of the stationary record H_{rms}. Therefore, we obtain

$$f_{\rho_{\max}}(\rho_{\max}) = N\, f_\rho(\rho_{\max})[F_\rho(\rho_{\max})]^{N-1} \tag{3.203}$$

and

$$F_{\rho_{\max}}(\rho_{\max}) = \left[F_\rho(\rho_{\max})\right]^N, \tag{3.204}$$

in which $\rho = H/H_{\text{rms}}$.

When the Rayleigh distribution is used for individual waves, i.e.

$$f_\rho(\rho_{\max}) = 2\rho_{\max}\, \exp(-\rho_{\max}^2) \tag{3.205}$$

and

$$F_\rho(\rho_{\max}) = 1 - \exp(-\rho_{\max}^2), \tag{3.206}$$

equations (3.203) and (3.204) yield

$$f_{\rho_{\max}}(\rho_{\max}) = 2N\rho_{\max}\, \exp(-\rho_{\max}^2)[1 - \exp(-\rho_{\max}^2)]^{N-1} \tag{3.207}$$

and

$$F_{\rho_{\max}}(\rho_{\max}) = [1 - \exp(-\rho_{\max}^2)]^N. \tag{3.208}$$

A normalized mean and the most probable maximum wave heights for large N take the forms (Massel and Sobey, 2000)

$$\overline{\rho}_{\max} = \frac{\overline{H}_{\max}}{H_{\rm rms}} \approx \sqrt{\ln N} + \frac{\gamma}{2}\frac{1}{\sqrt{\ln N}} \tag{3.209}$$

and

$$\rho_{\max}\Big|_{\text{max prob.}} = \frac{H_{\max}}{H_{\rm rms}}\Big|_{\text{max prob.}} \approx \sqrt{\ln N} \quad \text{for large } N \text{ and large } \rho_{\max}, \tag{3.210}$$

in which $\gamma = 0.57722\ldots$ is Euler's constant.

That the Rayleigh distribution overpredicts the probabilities of the higher waves in a record has long been recognized (Myrhaug and Kjeldsen, 1986; Sobey et al., 1990). Observations from a data set of 20-min record segments during a tropical cyclone *Victor* in March 1986 on Australia's North West Shelf showed that the ratio of Rayleigh's theory over measurement is 1.062 ± 0.101, being mean $\pm$ standard deviation.

There are numerous theoretical and empirical alternatives to the Rayleigh model, but none can be identified as the model of choice. Massel and Sobey (2000) found that the theoretical models share the same fundamental basis as the Rayleigh model, namely the theory of Gaussian random noise. With the exception of the 'Epstein/Naess' model (Massel and Sobey, 2000), all the alternatives in the literature retain the independent wave assumption and focus attention on the population distribution for individual wave heights. The Epstein/Naess model retains the 'lag 1' correlation between consecutive waves. These models predict trends in general agreement with the Rayleigh model and average values are consistently lower than that of the Rayleigh model. Though most are tightly grouped, there is no especially compelling argument to identify any one of these models for universal application.

In contrast to the above alternatives, Massel and Sobey (2000) introduced a simulation methodology to retain the essential features of the theoretical background in Gaussian random noise but to avoid further compromising assumptions in the interpretation of wave height in the amplitude domain. A probability distribution for the highest wave can be associated directly with an empirical or measured variance spectrum. Spectral shape has an influence on the location and width of the predicted distributions. Sharper spectral forms are associated with higher maximum waves.

Chapter 4

Experimental insights into mechanisms of wave breaking

4.1 Introduction

In spite of many years of theoretical efforts to gain insight into the mechanics of breaking waves, a more complete understanding of wave breaking and its onset as well as energy dissipated during breaking is still lacking (Banner and Grimshaw, 1992).

Most of the information on wave breaking which has been collected in the past is a result of experimental observations in the field and in laboratory tanks. The visual recording of wave breaking occurrence is probably the most reliable method. Also other methods have been reported in the literature based on measurements of surface elevation, velocities and accelerations. Some of these techniques are often laborious and not sufficiently efficient to be applied in practice. Banner and Peregrine (1993) provide an overview of deep water breaking wave detection technology. Although it is generally recognized that an individual wave-breaking event usually starts when water particle velocity at the wave crest reaches the velocity of wave propagation, surface fluid velocity is difficult to measure in the field. Therefore, indirect methods have been developed to detect and quantify wave breaking. They are related to various surface geometry signatures including a jump in the slope of the water surface at the breaker, an optical contrast of the sea surface associated with breaking, void fraction, whitecap coverage, subsurface turbulence, underwater sound, infrared properties of the surface, microwave backscatter, radar reflectivity and others. Some of these techniques will be described in this chapter, but other methods, particularly optical methods, related to whitecapping will be left for discussion in Chapter 7.

In recent years some modern indirect methods of wave breaking detection, based on processing of the recorded sea surface oscillations, have been proposed. Among the most promising methods, such approaches as application of the wavelet transform (Liu, 1994; Liu and Mori, 2001; Massel, 2001b) and

the phase-time method based on the Hilbert transform (Huang et al. 1999, Zimmermann and Seymour, 2002) are the most promising.

4.2 Definitions of parameters of steep and breaking waves

In general, the breaking process can be characterized by various measurable quantities such as (Hwang et al., 1989):

- onset of breaking
- time scale of breaking
- length scale of breaking
- intensity of breaking
- phase of breaking inception, and
- multiplicity of breaking.

Following Hwang et al. let us provide short definitions of the above quantities:

Onset of breaking – definition of the onset of breaking is twofold. In experimental studies it means that observed waves exceed some threshold behaviour, related to foam formation on the sea surface and high curvature of the wave crest. In numerical calculation, wave breaking onset is associated with a threshold linked for example to nonlinear wave group hydrodynamics.

Probability of breaking occurrence – defined as the ratio between the number of breaking waves and the total number of waves recorded (Longuet–Higgins and Smith, 1983; Ochi and Tsai, 1983; Hwang et al., 1989).

Time scale of breaking Δt_b – the breaking duration, defined as the time interval during which the threshold variable exceeds the critical value.

Vertical length scale of breaking $\Delta\zeta_\mathrm{b}$ – elevation jump defined as the difference in surface elevations during breaking.

Horizontal length scale of breaking Δl_b – length of breaking wave usually derived from the measured breaking duration (Δt_b) and the period of the corresponding breaking wave (T_b). Using the fact that $C_\mathrm{b} = \frac{g}{2\pi} T_\mathrm{b}$ is the phase speed of the breaking wave, the quality $l_\mathrm{b} = C_\mathrm{b}\,\Delta t_\mathrm{b} = \frac{g}{2\pi} T_\mathrm{b}\,\Delta t_\mathrm{b}$ is the horizontal length scale of a breaking patch (Phillips, 1985).

Intensity of breaking – quantity which determines the energy loss during breaking. It can be measured by two other measurable or calculable quantities, namely the elevation jump $\Delta\zeta_\mathrm{b}$, being proportional to the potential energy loss, and $\Delta Q_\mathrm{b} = u^2 + w^2$, representing the kinematic energy loss during breaking

(u and w are the horizontal and vertical components of the particle velocity at the sea surface, respectively).

Phase of breaking inception – a phase angle θ_b relative to the wave crest of the first point where the threshold variable exceeds the critical value.

Multiplicity of breaking – number of breaking events divided by the number of breaking waves. This index is related to the event when two or more breakings occur during one wave.

Forms of breaking waves in deep water are generally classified into two types (Massel, 1989):

plunging – the whole front face of the wave steepens until vertical; the crest curls over the front face and falls into the base of the wave, sometimes by the projection of a small jet.

spilling – white water appears at the wave crest and spills down the front of the wave. The upper 25% of the front may become vertical before breaking.

Experimental studies on two-dimensional wave breaking fall into four main categories in which the first three categories are related to mechanically generated waves, while the last one is related to waves generated by air flow above the water surface (Griffin et al., 1996):

(a) the focusing of essentially two-dimensional waves in the lateral direction,

(b) the towing of a submerged object, such as a hydrofoil, to produce steady breakers,

(c) the focusing of variable-length waves from a modulated wavemaker to produce unsteady breakers, and

(d) the overturning of an irregular wave train to produce unsteady breakers.

It should be noted that the common global wave steepness defined as $\varepsilon_{\mathrm{g}} = \frac{H}{gT^2}$, where H is the total wave height and T is the wave period, does not define steep asymmetric waves close to breaking in a random sea uniquely. Several asymmetric waves can be observed with the same global steepness ε_{g}, but with very different steepness of the wave crests. To evaluate the complex three-dimensional sea surface pattern, many wave parameters describing the geometry of individual waves are in use. Usually these parameters are based on a zero-downcross analysis, such as crest front steepness, vertical asymmetry parameter, horizontal asymmetry parameter, front inflection point steepness, maximum crest curvature and others. In particular, to account for the asymmetry of waves Myrhaug and Kjeldsen (1986) introduced three main parameters characterizing single asymmetric waves in a given time series – see Fig. 4.1

– crest front steepness ε_{f}:

$$\varepsilon_{\mathrm{f}} = \frac{\zeta_{\mathrm{c}}}{\left(\frac{g}{2\pi}\right) T \times T'}, \tag{4.1}$$

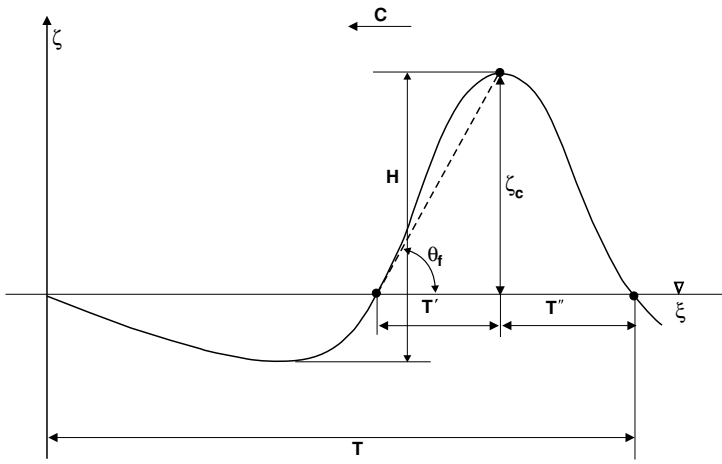

Figure 4.1: Basic definitions for irregular steep wave according to Myrhaug and Kjeldsen (1986).

– vertical asymmetry λ_{v}:

$$\lambda_{\mathrm{v}} = \frac{T''}{T'}, \tag{4.2}$$

– horizontal asymmetry parameter λ_{h}:

$$\lambda_{\mathrm{h}} = \frac{\zeta_{\mathrm{c}}}{H}, \tag{4.3}$$

where ζ_{c} is the crest elevation, T' and T'' are times defining the position of the wave crest relative to the zero-crossing points in the time domain, and T is the zero-downcross wave period. The parameter ε_{f} can be interpreted as the mean crest front inclination in the time domain. For a regular sinusoidal wave, (4.1)–(4.3) give $\varepsilon_{\mathrm{f}} = 8\pi\frac{\zeta_{\mathrm{c}}}{gT^2} = 4\pi\,\varepsilon_{\mathrm{g}} = 2\varepsilon_{\mathrm{H}}$, where $\varepsilon_{\mathrm{H}} = \frac{H}{L}$, $\lambda_{\mathrm{v}} = 1$ and $\lambda_{\mathrm{h}} = \frac{\zeta_{\mathrm{c}}}{H} = \frac{1}{2}$. It should be noted that the λ_{h} parameter describes asymmetry with respect to the current horizontal axis at the mean water level. Therefore, a trend in the mean values has to be removed.

Using times T' and T'', another vertical asymmetry parameter λ'_{v} can be obtained following Goda (1985)

$$\lambda'_{\mathrm{v}} = \frac{T'}{T' + T''} = \frac{1}{1 + \lambda_{\mathrm{v}}}. \tag{4.4}$$

The inspection shows that λ'_{v} is bounded between 0 and 1. For symmetric sinusoidal waves $\lambda'_{\mathrm{v}} = \frac{1}{2}$.

It is not practical to use local geometry parameters to characterize a long time series of steep irregular waves. The geometry of irregular surface elevation should be given by some statistical or spectral parameters. The most

appropriate is so-called significant wave steepness defined as follows

$$\varepsilon_{\mathrm{s}} = \frac{H_{\mathrm{s}}}{gT_{\mathrm{p}}^2}, \tag{4.5}$$

in which H_{s} is the significant wave height and T_{p} is the spectral peak period.

4.3 Field observations on wave breaking

4.3.1 Wave gauge method

Wave breaking in the field may be a result of direct wind forcing, wave–wave interaction, or wave instabilities. Longuet–Higgins and Smith (1983) reported probably the first direct, instrumental measurements of breaking waves through detecting the small jumps or discontinuities in surface elevation associated with spilling or plunging breakers. Observations of surface elevation were made with a capacitance wire wave recorder attached to a free floating spar buoy. It was assumed that any progressive wave in which inclination of the surface exceeds the critical value $\tan\theta_{\mathrm{cr}} = 0.586$ ($\theta_{\mathrm{cr}} = 30.37^\circ$) must be breaking. This threshold angle θ_{cr} follows from the extension of Stokes' theory given by Longuet–Higgins and Fox (1977) – see Section 2.2.

In Longuet–Higgins and Smith's experiment the experimental slope was estimated as follows

$$\theta = \arctan\left(\frac{R}{C}\right), \tag{4.6}$$

in which $R = \frac{\Delta\zeta}{\Delta t}$ and C is the phase velocity.

Records were obtained in wind speeds ranging from 1 to 14 m/s. The observed values of $\left(\frac{R}{C}\right)$ lie somewhat above the critical value $\tan\theta_{\mathrm{cr}}$. At wind speed of 14 m/s the number of 'jumps', indicating either steep or breaking waves, was of the order of 1 every 100 wave periods. This number is consistent with previous theoretical estimates (Longuet–Higgins, 1969) and with visual observations of whitecap coverage.

However, it should be mentioned that the 'jump meter' technique was designed for detecting larger waves and many small breaking waves were ignored. It is reasonable to suggest that small breaking waves occur more often than large breaking waves. Hence Longuet–Higgins and Smith's count would be much lower than all of the other methods described below in this section.

Weissman et al. (1984) developed a detection scheme that uses the energy in a very high frequency band (18–32 Hz) to test for turbulence at the surface with some suitable threshold for breaking events. Application of the method to data collected on Lake Washington showed that the temporal intermittency of wave breaking (fraction of time spent in breaking regions) for wind speed 5.9 m/s and fetch 7 km was found to be only 1.2%. However, the fraction of high-frequency energy in those regions was 12%. Elevations of the breaking

crests were much less than expected and the mean crest height was a quarter of the values predicted by nonlinear theories of steady waves.

Thorpe (1993) distinguished two scales of wave breaking. The first, small-scale breaking, is related to the formation of small-scale ripples of capillary-gravity waves formed on the crest or leading face of steep gravity waves and producing flow separation (see Section 2.3 for a discussion in more detail). However, the more familiar breaking occurs on a larger scale when plunging or spilling waves manifest themselves as whitecaps. Sometimes the results of observations of wave breaking are presented as a frequency of wave breaking N_{br} defined as the number of waves breaking at a fixed position in a given time divided by the number of waves of the dominant wave frequency that pass in the same period of time. The breaking frequency N_{br} is plotted in Fig. 4.2 as a function of wind speed V_{10} divided by dominant phase speed C_0. In particular, Thorpe and Humphries (1980) and Thorpe (1992) made observations of the frequency of breaking wind waves in a loch at a fetch of about 20 km for winds from 3 to 28 m/s, using a capacitance wire probe. Their results are denoted in this figure by circles and squares, respectively. In the same figure, the results of Longuet–Higgins and Smith (1983) (denoted by LH+S), Weissman et al. (1984) (denoted by W+A+K), Holthuijsen and Herbers (1986) (denoted by H+H) and Katsaros and Atakturk (1992) (denoted by points) are added for comparison.

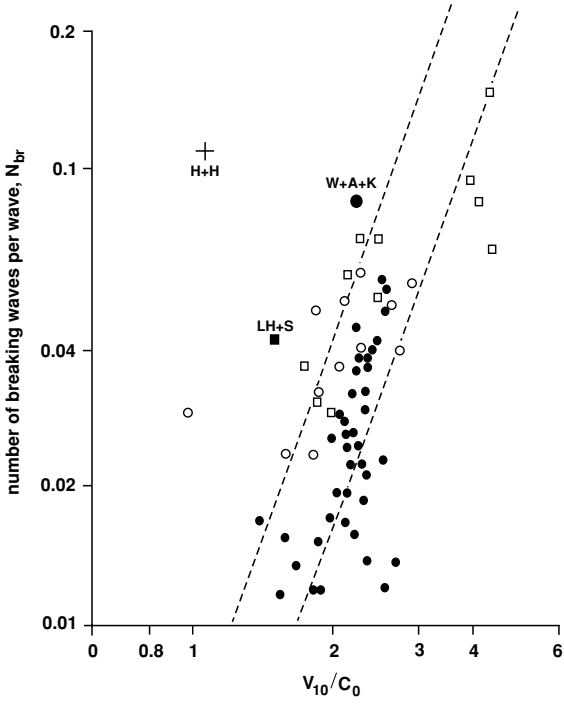

Figure 4.2: Number of breaking waves per wave, N_{br}, versus wind speed divided by wave speed of dominant waves (adapted from Thorpe, 1993).

Holthuijsen and Herbers data lie well above the others, possibly due to wave refraction in shallow water. On the other hand, Longuet–Higgins and Smith's data are slightly higher, maybe because they include steep but not breaking waves or are affected by the influence of swell. In general, the remaining data points satisfy the following relationship

$$N_{\mathrm{br}} = (4.0 \pm 2.0) \times 10^{-3} \left(\frac{V_{10}}{C_0}\right)^3, \tag{4.7}$$

denoted in Fig. 4.2 by dashed lines.

Myrhaug and Kjeldsen (1986) determined the wave steepness and wave asymmetry parameters, defined above, in 58 full-scale time series recorded during 22 gales in deep water on the Norwegian continental shelf. It should be noted that they considered a wave to be 'extreme' when $H > 5\,\mathrm{m}$, $\varepsilon_{\mathrm{f}} > 0.25$ and $\varepsilon_{\mathrm{H}} > 0.1$, and they showed that ε_{f} is larger than $2\varepsilon_{\mathrm{H}}$ for most extreme waves. For wave steepness in the range $0.1 < 2\varepsilon_{\mathrm{H}} < 0.25$, crest front steepness ε_{f} was between 0.2 and 0.32, with a mean value of about 0.26. Moreover, it was observed that $\lambda_{\mathrm{v}} > 1$ and $\lambda_{\mathrm{h}} > 0.5$ for most waves when $\varepsilon_{\mathrm{f}} > 2\varepsilon_{\mathrm{H}}$. In particular, the vertical asymmetry parameter λ_{v} showed a large scatter between 1.0 and 3.0, while the horizontal asymmetry parameter λ_{h} was concentrated around a value of 0.65. Therefore, the crests of extreme waves are usually asymmetric with shallow and relatively long troughs followed by high and relatively short crests.

It should be noted that for limiting second-order symmetric Stokes waves, ε_{f} equals 0.28. Cokelet (1977) using 120 Pade terms in his precise numerical calculations for the steepest monochromatic deep water waves obtained $\varepsilon_{\mathrm{f}} = 0.408$ and $\lambda_{\mathrm{h}} = 0.757$, when the mean water level is used as a reference level.

If we assume that the wave field is uniform, consisting of two-dimensional waves with the period of the dominant waves, we can regard N_{br}, given in Fig. 4.2, as an estimate of the fraction of the breaking crest length of any one wave. This result is consistent with the theoretical prediction of Phillips (1985), who showed that the number of breaking waves passing a fixed point per unit time is proportional to the cube of the friction velocity in the air, which is equivalent to the cube of the wind speed (see Section 6.3 for more details).

At present, there is no consensus on distinguishing between the extremes appearing in a homogeneous wave population and cases of exceptional high waves. These high waves result from totally different generation mechanisms. Kharif and Pelinovsky (2003) provided a review of physical mechanisms of rogue wave generation, such as focusing, wave–current interaction and modulational instability. These mechanisms have been supported by the classical nonlinear evolution equations, i.e. the nonlinear Schrödinger equation, the Davey–Stewartson system, the Korteweg–de Vries equation, the Kadomtsev–Petviashvili equation and the Zaharov equation. However, in order to distinguish between rogue waves and other extreme waves usually appearing in a random wave field, a simpler criterion should be applied.

The appearance of extreme, very rare wave events in the ocean, sometimes called *rogue waves* or *freak waves* is usually discussed in connection with damaging maritime structures as well as with sinking ships. However, extreme waves are also a demonstration of very severe ocean conditions and generation of intensive marine aerosol fluxes from the ocean surface to the atmosphere. A very comprehensive summary of extreme event statistics and numerical modelling of extreme waves was given by Massel (1996a) and Olagnon and Athanassoulis (2001). Moreover, Olagnon and van Iseghem (2001) recently provided a summary of characteristics of extreme waves recorded in the North Sea (Frigg field). Only sea states (9850 events) with significant wave height H_s, larger than 2 m were considered and a few selected extreme waves (128 events) were filtered out for $H_s > 2$ m and $\zeta_{c_{max}} > 5$ m, and these waves are classified as freak waves. Olagnon and Iseghem found that crest front steepness ε_f of 'normal' extreme waves is higher than that of the maximal waves but the difference is not significant. The same conclusion has been drawn for wave asymmetry parameters.

4.3.2 Visual method

Holthuijsen and Herbers (1986) using video technique observed whitecaps passing a fixed location in the North Sea at a water depth of 17.5 m. During observation the significant wave height, H_s, varied from 1.3 to 2.0 m with average peak period $T_p = 5s$ and significant wave steepness ranged from $\varepsilon_s = 0.0053$ to $\varepsilon_s = 0.0081$. Wave breaking events over a wide range of length scales, registered synchronously with the buoy signal, have been detected. Joint probability analysis of heights and periods of breaking and non-breaking waves showed considerable overlapping, and clear resolving of breakers on the basis of individual wave steepness was not possible. Ocean observations by Holthuijsen and Herbers (1986) suggest that none of the local wave geometry parameters ($\varepsilon_f, \lambda_v, \lambda_h$) should be used with confidence to discriminate spilling breakers from non-breaking steep waves. The steepness and asymmetry of waves in the ocean were smaller than those observed in laboratory experiments.

Holthuijsen and Herbers reported that the fraction of breaking waves during their field experiment varied from 10 to 16% within the observed range of wind speeds of 8–12 m/s. Two-thirds of breaking events were observed to occur in one-third of the wave groups, and breaking occurred most commonly in the centre of a group. The observed values of the fraction of breaking waves are consistent with the observations of Weissman et al. (1984), but they are much larger than those of Longuet–Higgins and Smith (1983), who used a different operational definition of a breaking wave. A comparison of Holthuijsen and Herbers data with the theoretical predictions is outlined in Chapter 5.

Katsaros and Atakturk (1992) used continuous video to record the breaking events together with registration at the wire wave probe on Lake Washington. A detailed analysis provided the number of plunging, spilling, and microscale breakers for each of the sixty-six 17-min records. They correlated the spilling and plunging breakers with five different atmospheric parameters and found

the following relationship for the probability of breaking F_{br} (ratio between the number of breaking waves and the total number of waves examined)

$$F_{\mathrm{br}} = -2.47 + 32.87u_*^2 + 42.37\frac{u_*}{C_{\mathrm{p}}}, \tag{4.8}$$

in which u_* is the friction velocity and C_{p} is the wave phase velocity at the spectral peak. The second term describes the influence of wind stress while the third one reflects the stage of wave development (wave age).

Banner et al. (2000) reported the results of observation of breaking waves in three geographically different water basins: the Black Sea, the Southern Ocean and Lake Washington. The collected data covered a wide range of dominant wavelengths from 3 m up to 300 m and wind speeds in the range 5-20 m/s. In all cases, the wave breaking events were detected visually. In particular, the Black Sea experiment involved visual surveillance of waves passing over a wave probe, with collected breaking events labelled electronically by an observer. In total, 16 records have been used in analysis with significant wave height up to 1.3 m and spectral peak period up to 6 s. During the Southern Ocean experiment, nadir video images of the ocean surface were recorded from a research aircraft flying at altitudes of 250 and 680 m. The video recorder images were processed and the number of breakers passing through a chosen point on the screen was counted. However, only breakers propagating with speeds close to the phase speed of the spectral peak were considered.

Banner et al. introduced a definition of dominant waves as waves of a frequency within the spectral band of $0.7f_{\mathrm{p}}$ to $1.3f_{\mathrm{p}}$, in which f_{p} is the peak wave frequency. Hence the dominant wave steepness ε_{d} becomes

$$\varepsilon_{\mathrm{d}} = \frac{H_{\mathrm{d}}k_{\mathrm{p}}}{2}, \tag{4.9}$$

in which k_{p} is the spectral peak wave number and wave height H_{d} is given by

$$H_{\mathrm{d}} = 4\sqrt{\int_{0.7f_{\mathrm{p}}}^{1.3f_{\mathrm{p}}} S(f)df}, \tag{4.10}$$

in which $S(f)$ is the frequency spectrum of wind waves and ε_{d} represents an average wave field parameter which determines the mean fraction of breaking waves in a defined frequency band. The authors found that ε_{d} varies from 0.040 up to 0.126, and threshold value of ε_{d} equal to or higher than 0.055 corresponds to breaking events. It should be noted that steepness ε_{d} is related to significant wave steepness ε_{s}, defined by (4.5) as

$$\varepsilon_{\mathrm{d}} = 2\pi^2\frac{H_{\mathrm{d}}}{H_{\mathrm{s}}}\varepsilon_{\mathrm{s}}. \tag{4.11}$$

Another method of visual observation of wave breaking was proposed by Jessup et al. (1997). It was found that a net upward heat flux from the ocean to the atmosphere is generated mainly by molecular conduction through the

skin layer at the ocean surface (see Section 1.3). The skin temperature of the ocean is less than the bulk temperature immediately below by a few tenths of a degree Celsius. However, when the cool skin layer is momentarily disrupted by a breaking wave, the skin temperature of the resulting turbulent wake is approximately equal to the bulk temperature. After that, when the wake subsides, the skin layer recovers and the skin temperature returns to its original, lower value. Jessup et al. showed that the time needed for the skin layer to recover is of the order of 10 s, depending on the ambient heat flux and strength of the wave breaking event. Therefore, basically infrared measurements of skin-layer recovery may provide a method for remotely monitoring free-surface turbulence under conditions of constant heat flux. The authors used an infrared imager and found that the time required for the skin layer within the wake to recover is proportional to the speed of the breaking crest. Faster-moving waves dissipate more energy, resulting in longer skin-layer recovery time τ. Moreover, experiments showed that the skin temperature deviation (normalized by its maximum) increases rapidly as the whitecap passes and then decays as the skin layer recovers. The skin-layer recovery time τ is usually defined as the time lapsed from the appearance of the maximum skin temperature deviation and the level of 0.3 of this deviation. Therefore the skin-layer recovery rate R_l can be expressed as follows

$$R_\mathrm{l} = \frac{\Delta T}{\tau}, \tag{4.12}$$

where ΔT is the temperature deviation.

The value of R_l is related to the rate of heat transfer per unit area required to establish the skin layer as $Q_\mathrm{r} = (\rho_\mathrm{w} c_\mathrm{p} \delta) R_\mathrm{l}$, in which ρ_w is the density of water, c_p is the specific heat of water, and δ is the thermal boundary layer thickness, usually taken as 0.5 mm for the observed wind conditions.

Jessup et al. (1997) showed that correlation between Q_r and the rate of energy dissipation per unit crest length for quasi-steady and unsteady breaking waves E is rather high. This implies that the skin-layer recovery rate R_l provides a measure of energy dissipation due to breaking. Such a conclusion was supported by field as well as by complementary laboratory measurements of individual, mechanically generated breaking waves, ranging in size from spilling to plunging breakers. It is expected that airborne applications of this technique should provide remote measurements of energy dissipation due to wave breaking, which are necessary to improve wave prediction models used for operational sea-state forecasting.

4.3.3 Air entrainment method

One the most obvious and characteristic features of wave breaking in the open sea is the entrainment of air by the breakers, which generates in turn a series of bubble plumes beneath and behind the breaking waves. Therefore, the presence of breaking waves can be detected by direct measurement of the near-surface void fraction, which is expressed as the percentage of air content in the water

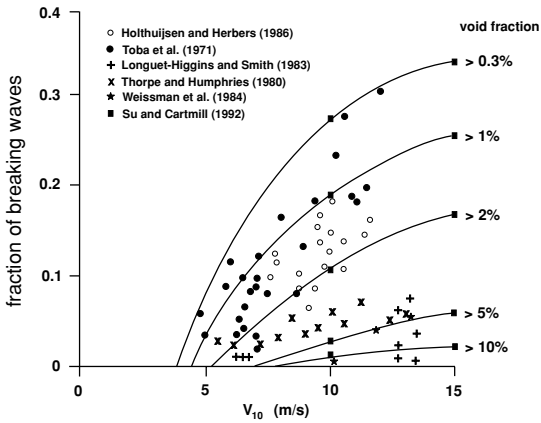

Figure 4.3: Fraction of breaking waves and void fraction as a function of wind speed (V_{10}) (adapted from Su and Cartmill, 1992).

by means of a floating vertical array on which several void fraction meters are usually installed at various depths. Such techniques have been used by Su and Cartmill (1992). They reported the results of void fraction measurements during the SWADE experiment (Weller et al., 1991). According to Su and Cartmill, each 'void fraction event' may be interpreted as one 'breaking wave event', under the assumption that a breaking wave is a wave which entrains air into the water that becomes a plume of bubbles with a measurable void fraction to a depth of about 30 cm below the surface. It is clear that this definition will exclude all micro-breaking by capillary waves and gravity-capillary waves with smaller wavelengths. In Fig. 4.3 the observed fraction of breaking waves and void fraction as a function of wind speed, V_{10}, collected by Su and Cartmill (1992), are shown. There is a surprisingly good overall agreement between the fraction of wave breaking and air entrainment due to breaking. This suggests that the quantitative measure of void fraction may serve as a reliable technique for detecting breaking waves and their intensity.

Gemmrich and Farmer (1999) presented observations of breaking frequency and scales of breaking waves using four 4-electrode conductivity cells measuring effective conductivity within a volume of roughly spherical shape and 0.09 m radius. The sensors followed the surface closely with the nominal depth of the shallowest sensor adjusted for deployments between 0.12 and 0.24 m. From the conductivity record an approximate air fraction due to air bubbles entraining into the top of the water column was calculated. Available theory relating conductivity to air fraction breaks down for large values (>0.5). However, calibrations in a tank suggest that for air fractions up to 0.25, the conductivity sensors can be used. A precise threshold is still arbitrary, depending on the precise depth of measurements and the vertical gradient of air fraction. As the instrument was equipped with flux-gate accelerometers and tilt meters, the surface elevation was estimated by double integration in frequency space. The experiments have been conducted at three different locations: the Strait

of Georgia, the Gulf of Alaska and the North-East Pacific at wind speeds up to 18 m/s.

To distinguish breaking waves, Gemmrich and Farmer defined a breaking event as an event in which the air fraction exceeds 0.08 at the top sensor. Analysis of experimental data showed that the average air fraction reaches a maximum value of 0.2 and it is higher than 0.08 for about 0.3 s. These higher values of volumetric fractions >0.2 are restricted to the upper layer ∼0.2 m. In general, in the open ocean ∼2% of breaking events showed deeper air penetration, presumably associated with plunging, while 98% of breaking waves are related to shallow air entrainment, characteristic for spilling type breaking waves.

Breaking waves exist over a wide range of scales, mostly being shorter than dominant waves, with median value $\frac{T_{\mathrm{br}}}{T_{\mathrm{p}}} \sim 0.54$, in which T_{p} is the period of the spectrum peak and T_{br} is the period of breaking waves. It should be noted that breaking waves are generally not the highest waves.

Even using a single breaking criterion – exceedance of 8% of the air fraction – the experiments did not confirm the dependence of the fraction of breaking waves per dominant wave on wind speed or wave age. On the other hand, the driving parameter for breaking is the energy transfer from the wind to the wave field. A roughly linear dependence was obtained for this energy transfer and breaking frequency, normalized by the effective frequency of waves associated with dissipation of wave energy. The air fraction value as an indicator of wave breaking was also suggested by Lamarre and Melville (1991) and Melville et al. (1992)– see Section 4.4.4.5.

4.3.4 Acoustic method

It is well known that breaking contributes significantly to the ambient underwater noise spectrum, which can be measured with hydrophones. Knudsen et al. (1948) in their pioneering measurements demonstrated that the ambient noise spectrum $N(f)$ in the 100–25 kHz range correlates with sea state, which can be expressed in the form

$$\log V = m(f)\, N(f) + n(f), \tag{4.13}$$

where V is the wind speed in m/s, f is the frequency in Hertz, $m(f)$ and $n(f)$ are coefficients, and the noise spectrum level in dB is given as follows

$$N(f) = 10 \log \left(\frac{p^2(f)}{p^2_{ref}} \right), \tag{4.14}$$

in which $p^2(f)$ is the ambient noise power spectrum, and $p^2_{\mathrm{ref}} = 1\,\mu\mathrm{Pa}^2/1\,\mathrm{Hz}$.

This technique is commonly known as weather observations through ambient noise (WOTAN). Felizardo and Melville (1995) collected the coefficients m and n obtained from various field measurements. Moreover they reported the results of the field experiment conducted off the coast of Oregon to measure ambient noise, wind speed and the wave field from the research platform FLIP.

The experiment suggests that the correlation between noise spectrum $N(f)$ and rms wave amplitude of the local wind sea is comparable to that between wind speed V and $N(f)$. Also a good correlation was found between the rms wave slope ε and N. Felizardo and Melville (1995) demonstrated that the mean square acoustic pressure $\overline{p^2}$, which is a measure of the radiated acoustic power, was found to be proportional to the total wave energy dissipation in some power, say $\sim E_{\mathrm{diss}}^n$, where $n = 0.5 - 0.8$. This relationship will be discussed in Chapter 6 in more detail.

Farmer and Vagle (1988) distinguished the ambient sound and fluctuations caused by wave breaking using moored WOTAN sensors. To obtain data in open ocean without being tied to a particular location, Farmer and Ding (1992) deployed drifting instruments equipped with four broad-band hydrophones, each one mounted at the end of a motor-driven arm which involves tracking of discrete sound sources associated with breaking waves in both space and time. Ding and Farmer (1994) showed that despite the limitations of this instrument, they were able to obtain an empirical relationship between breaking wave statistics and wind conditions such as duration, velocity, spacing and breaking probability. The wind dependence of breaking wave properties was shown to be very scattered, which implies that the observed breaking wave properties depend on more than just one or two parameters. The spectral and coherence properties of radiated sound allow detection of additional features of breaking events. However, to exploit fully the hydrophone records for development of a wave breaking model, information on wave directionality is required.

4.4 Laboratory experiments on wave breaking

To avoid the difficulties of field measurements, many studies on wave breaking have been carried out in laboratory wave flumes, aimed at duplicating, as closely as possible, the natural processes. Modelling of breaking phenomena in the laboratory tank allows accurate control over the input wave parameters. Also, more precise instrumentation can be used with direct control and maintenance during experiments. As the turbulent flow generated at breaking is non-stationary, turbulent statistics can only be determined by ensemble averages of many repeats of the experiment under identical initial and boundary conditions, which is impossible to obtain in the field. On the other hand, some disadvantages of laboratory simulations are reflections due to a finite-length channel and the problem of scaling the results to full natural scale. A large number of experiments on wave breaking have been reported in the professional literature, but only the most important will be discussed in this section.

4.4.1 Bonmarin's (1989) experiment

A very extensive laboratory study on a steep wave reaching breaking was reported by Bonmarin (1989). In the experiment, visualization and picture

acquisition techniques were applied to detect the evolution of a progressive mechanically generated wave of initial steepness equal to 0.28, near to but less than the value 0.29. As mentioned in Section 2.3, the steepness 0.29 is close to the upper limit of a regime where Benjamin–Feir instability dominates and the approach to breaking is essentially two-dimensional. Bonmarin determined the onset of breaking by means of an easily observed visual criterion: for a plunging breaker, it corresponds to the occurrence of a vertical crest front, and for a spilling breaker, it corresponds to foam occurrence. The reported results of the experiment are related to wave evolution to breaking, geometrical properties at breaking onset, crest evolution after breaking onset, including the overturning phenomenon, the splash-up phenomenon and degenerated forward flow.

In particular, the results on the water jet and splash-up phenomena are very worth mentioning as these phenomena play an important role in the generation of marine aerosol fluxes. Bonmarin observed that the elevation of the splash of water is as high as the original plunging crest. The first splash-up occurs after the collision between the falling water jet and the undisturbed water surface and forms two vortices, one revolving clockwise, the other anticlockwise. After the first splash-up, the flow can either directly degenerate into chaotic motion or displays successive splash-up cycles and less active vortices. The air trapped under the falling water jet and air trapped between the falling jet and the vortex occurring at the rear of the splash-up are the sources of the underwater noise.

Bonmarin found that the evolution of the wave from an initial symmetric form to an asymmetric one was clearly displayed by changes in the values of asymmetry parameters λ_{v} and λ_{h}. The observed evolution of the horizontal asymmetry λ_{h} results from the changing of the relative values of crest elevation and trough depth. Initially the horizontal asymmetry parameter λ_{h} was close to the value 0.50, and then it very quickly increased and reached a value close to 0.90. The vertical asymmetry results from the increase of the crest front steepness, and the time evolution of parameter λ_{v} is characterized by a strong increase before breaking after which it rapidly decreases within the breaking region. For the initial profile both above quantities, as well as the crest front steepness ε_{f}, have similar values.

Bonmarin observed that uniform or shear currents, at least at breaking onset, do not significantly affect wave asymmetry. Also, the observed breakers did not correspond exactly to the theoretical definitions of plunging breakers or of spilling breakers. Therefore, it will be useful to classify them into four categories: breakers that display very distinctly all the characteristics of the theoretical plunging definition are called 'typical plunging breakers' in contrast to breakers where the plunging effect is only distinctly dominating. A similar criterion was applied to spilling breakers. The values of the vertical and horizontal asymmetry parameters, as well as values of crest front steepness at breaking onset observed by Bonmarin, are summarized in Table 4.1.

Additionally, experimental values of λ_{v}, λ_{h} and ε_{f}, obtained by various authors, are compared with the theoretical values of Longuet–Higgins and Cokelet

Table 4.1: Values of parameters λ_v, λ_h and ε_f at breaking onset, according to Bonmarin (1989)

Breaker type	Min. value	Max. value	Mean value	Value for symmetric wave
(a) Horizontal asymmetry parameter λ_h				
typical plunging	0.65	0.93	0.77	0.5
plunging	0.62	0.93	0.76	0.5
spilling	0.59	0.91	0.75	0.5
typical spilling	0.60	0.80	0.69	0.5
(b) Vertical asymmetry parameter λ_v				
typical plunging	0.97	3.09	2.14	1.0
plunging	0.78	2.52	1.61	1.0
spilling	0.78	2.37	1.38	1.0
typical spilling	0.81	1.72	1.20	1.0
(c) Crest front steepness parameter ε_f				
typical plunging	0.31	0.85	0.61	–
plunging	0.29	0.77	0.47	–
spilling	0.24	0.68	0.41	–
typical spilling	0.31	0.51	0.38	–
(d) Crest front angle $\theta_f^{(\circ)}$				
typical plunging	17.22	40.36		
plunging	16.17	37.60		
spilling	13.49	34.21		
typical spilling	17.22	27.02		

(1976) in Table 4.2. The order of asymmetry of the theoretical profiles and the experimental one are very similar. The asymmetry depends on the type of breaking and it is more pronounced for a plunging than for a spilling breaker.

4.4.2 Rapp and Melville's (1990) experiment

The experiments reported by Bonmarin were mainly concentrated on plunging breakers (43% of all breakers) and only 27% of breakers have been classified as spilling breakers. The role of the growth rate of waves prior to breaking in predicting breaking was examined and a detailed survey of momentum and energy balance, as well as decay of turbulence and dissipation estimates, was made in the very extensive laboratory tests of Rapp and Melville (1990). Their tests on unsteady breaking were particularly concerned with simulation of breaking of

Table 4.2: Comparison of various experimental mean values of parameters λ_h, λ_v and ε_f with theoretical prediction by Longuet–Higgins and Cokelet (1976), according to Bonmarin and Kjeldsen (2001)

Parameters	λ_h	λ_v	ε_f
Theory ($ak_{initial} = 0.25$)	0.77	1.83	0.59
Bonmarin's (1989) experiment ($ak_{initial} \approx 0.28$)	0.76	1.87	0.54
Peltzer and Griffin (1992) experiment ($ak_{initial} = 0.24$)	0.76	1.43	0.50
Symmetric wave	0.5	1.0	0.28

waves with frequency around the peak of the wind-wave spectrum. Rapp and Melville argued that wind forcing is not important for waves near the peak of the spectrum. For these waves, breaking can be reproduced by simulation of the wave-wave interaction mechanism by generating a unidirectional frequency modulated wave packet, providing a focusing of wave energy at a predetermined time and location in the wave flume.

The technique used in the tests is based on linear reduction of the wave frequency and the resulting increase of group velocity, which leads to a dispersive focusing of the waves ('chirp' pulse technique). The direct effects of breaking were then confined to a finite region of the wave flume. Rapp and Melville (1990) used measurements of the free surface displacements to estimate the momentum and energy fluxes into and out of the breaking region. In particular, they found that the loss of excess momentum flux and energy flux is in the range of 10% for single spilling breakers to about 25% for plunging breakers. This loss of excess momentum flux was defined simply as the difference between the upstream and downstream levels where the momentum flux is nearly constant at x. A sharp rise of the loss of excess momentum flux was observed for steepness ak_c greater than 0.25. The wave number k_c corresponds to the central frequency $\omega_c = \frac{1}{2}(\omega_1 + \omega_N)$, in which ω_1 and ω_N are the frequencies of first and last components of the wave packet, respectively, and k_c value is defined by the linear dispersion relation

$$\omega_c^2 = gk_c \tanh(k_c h). \tag{4.15}$$

Studying the local wave parameters at breaking, Rapp and Melville found that the front steepness varied throughout the breaking process and the actual measure of crest front steepness at breaking depends upon how the break point is defined. They found that crest front steepness ε_f (see (4.1)) varied between 0.2 and 1.0. This scatter indicates that for such a very localized process, the horizontal length in ε_f is still too coarse to predict breaking, especially if there are short waves riding on long waves.

A substantial part of Rapp and Melville' experiment was dedicated to flow visualization of mixing in the breaking region. It was done by photographing the mixing of a dye patch floated on the water surface. The aerated region in spilling breaking waves was similar to a turbulent gravity current modelled by Longuet–Higgins and Turner (1974). In particular, the spatial evolution of mixing and the maximum depth, D, of dye excursion was determined. The mixing due to breaking carries the dye down $k_c D \approx 0.3$ for spilling and $k_c D \approx 0.5$ for plunging breakers within half wave period from breaking. The next passing waves carry the dye down additionally reaching a maximum depth of the order $k_c D \approx 1.1$ for spilling breakers and $k_c D \approx 1.7$ for plunging breakers. This corresponds to the depths of two to three wave heights and horizontal lengths of approximately one wavelength within five wave periods of breaking.

The detailed velocity measurements showed that the mean surface current is in the range $(0.02–0.03)\,C$, where C is the phase wave velocity. This current together with a deeper return flow forms a rotational region of approximately one wavelength where the observed horizontal velocity can be represented as

$$u = < u > + u', \tag{4.16}$$

in which u' is the fluctuation from the ensemble mean $< u >$. The same representation is valid for the vertical velocity w. Measurements showed that the volume integrated turbulent kinetic energy contribution from both velocities, i.e. u'^2 and w'^2 decay at t^{-1} power law, when the time origin is the time of observed breaking. Using this dependence, Rapp and Melville (1990) found that the dissipation rate per unit mass becomes

$$E_{diss} \approx t^{-5/2}, \tag{4.17}$$

and that 96–98% of the energy goes into turbulence being dissipated within four wave periods.

In the Rapp and Melville experiment, the presence of so-called 'radiant upstream waves' was noted. The laboratory measurements of this fine space-time structure phenomenon were performed by Rosenberg and Ritter (2005). It was found that the breaking splash is the main source of short surface wave generation and the main backscatter from breaking waves has a Doppler velocity close to the phase velocity of these waves.

4.4.3 Ocean Basin Experiment

Massel et al. (2001) carried out a control experiment on propagation of steep and breaking long- and short-crested waves in water of constant depth in the Ocean Basin in Trondheim (Norway). Regular waves and waves characterized by the JONSWAP spectrum with different directional spreadings were reproduced. Water depth was kept constant at 2.5 m. The main measuring profile,

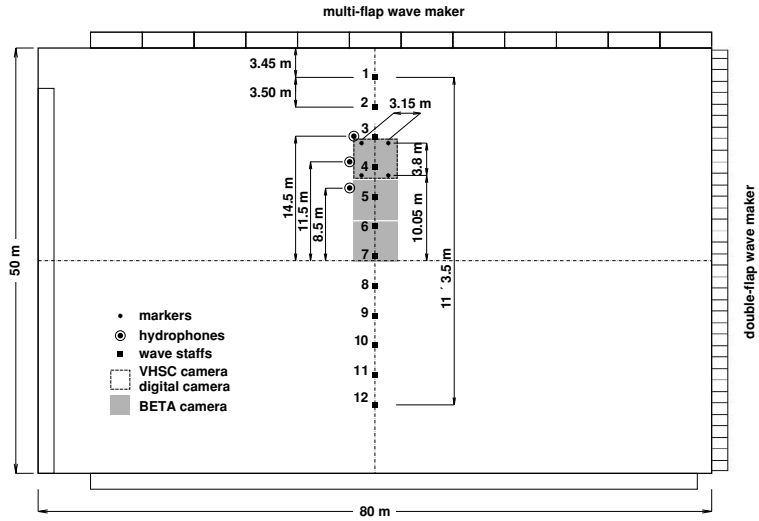

Figure 4.4: Arrangement of instruments during Ocean Basin Experiment in Trondheim (adapted from Massel et al., 2001).

consisting of 12 wave staffs, 4 video cameras (VHSC camera, 2 BETA cameras and digital camera) and 4 hydrophones, was located perpendicularly to the multi-flap wave-maker BM3 – see Fig. 4.4. The cameras situated 5 m above the still water level were synchronized with the wave staffs. Two cameras covered the same basic recording area of 3.8 m × 3.1 m and two other cameras covered the areas located further from the multi-flap wave-maker. The hydrophones were located at 0.5 and 1 m below still water level. The parameters of generated waves, generator type and recording time are listed in the Table 4.3. In this table the following notations are used: reg. – regular waves, irr – irregular waves, BM3 – multi-flap wave-maker and BM2 – double-flap wave-maker. It should be noted that the second double-flap wave-maker (BM2) was situated along the shorter side of the basin, being parallel to the main measuring profile. The methodology of the experiment and preliminary results were described by Massel et al. (2001).

Among the generated waves, three main groups can be distinguished depending on the initial significant wave steepness ε_s: in tests 4150–4500, a steepness of 0.0122 ($ak_p = 0.2408$) was used, while in tests 5100–5500, a steepness of 0.0104 ($ak_p = 0.2053$) was applied, and finally in tests 6100–6500, waves with lower steepness of 0.0091 ($ak_p = 0.1796$) were generated. Additionally five different directional spreadings were applied, ranging from a unidirectional wave train up to frequently observed directional distribution, proportional to $\cos^2 \Theta$.

The crest front steepness ε_f, vertical asymmetry λ_v and horizontal asymmetry λ_h, defined by Myrhaug and Kjeldsen (1986), have been calculated using the data recorded at particular wave staffs. In Table 4.4, the mean and maximal

Table 4.3: Wave parameters used in the Ocean Basin Experiment

	Test no.	Type of wave	Main direction of wave propagation	H_s (m)	T_p (s)	γ	Type of generator	Directional spreading	Record time (min)
1	4100	irr	0	0.11	1.0	7.0	BM3	unidir	23
2	4150	irr	0	0.12	1.0	7.0	BM3	unidir	23
3	4200	irr	0	0.12	1.0	7.0	BM3	$\sim \cos^{40}\Theta$	23
4	4300	irr	0	0.12	1.0	7.0	BM3	$\sim \cos^{20}\Theta$	23
5	4400	irr	0	0.12	1.0	7.0	BM3	$\sim \cos^{10}\Theta$	23
6	4500	irr	0	0.12	1.0	7.0	BM3	$\sim \cos^{2}\Theta$	23
7	5100	irr	0	0.16	1.25	7.0	BM3	unidir	23
8	5200	irr	0	0.16	1.25	7.0	BM3	$\sim \cos^{40}\Theta$	23
9	5300	irr	0	0.16	1.25	7.0	BM3	$\sim \cos^{20}\Theta$	23
10	5400	irr	0	0.16	1.25	7.0	BM3	$\sim \cos^{10}\Theta$	23
11	5500	irr	0	0.16	1.25	7.0	BM3	$\sim \cos^{2}\Theta$	23
12	6100	irr	0	0.20	1.5	7.0	BM3	unidir	23
13	6200	irr	0	0.20	1.5	7.0	BM3	$\sim \cos^{40}\Theta$	23
14	6300	irr	0	0.20	1.5	7.0	BM3	$\sim \cos^{20}\Theta$	23
15	6400	irr	0	0.20	1.5	7.0	BM3	$\sim \cos^{10}\Theta$	23
16	6500	irr	0	0.20	1.5	7.0	BM3	$\sim \cos^{2}\Theta$	23
17	7100	reg	0	0.16	1.0	–	BM3	unidir	23
18	7150	reg	0	0.25	1.25	–	BM3	unidir	23
19	7200	reg	0	0.35	1.5	–	BM3	unidir	23
20	7250	reg	0	0.19	1.0	–	BM3	unidir	23
21	7300	reg	0	0.30	1.25	–	BM3	unidir	23
22	7400	bichr	−15/+15	0.06/0.06	0.95/1.05	–	BM3	unidir	23
23	7425	bichr	−15/+15	0.08/0.08	0.95/1.05	–	BM3	unidir	23
24	7450	bichr	−15/+15	0.06/0.06	0.95/1.05	–	BM3	bi-dir	23
25	7600	reg	0	0.3	1.25	–	BM2	unidir	5
26	7650	reg	0	0.4	1.5	–	BM2	unidir	5
27	7700	reg	0	0.6	2.0	–	BM2	unidir	5
28	7725	reg	0	0.35	1.25	–	BM2	unidir	5
29	7800	irr	0	0.3	1.5	7.0	BM2	unidir	20
30	7850	irr	0	0.3	1.5	3.0	BM2	unidir	20

values of ε_f, λ_v and λ_h were collected for wave staffs 1, 5 and 12 and for three different wave steepnesses of the unidirectional wave trains. For short-crested waves, characterized by the directional spreading $\sim \cos^2\Theta$, these parameters are collected in Table 4.5.

It should be noted that when recording surface oscillations at a given point we are not able to estimate the local spatial steepness $\varepsilon_l = \frac{\partial\zeta}{\partial n}$, where n is a given direction. In order to avoid the difficulties with determining the local slope from a record at a given point, Myrhaug and Kjeldsen (1986) proposed the crest front steepness parameter ε_f. This parameter does not provide a local slope but a mean slope of the crest front considered as a straight line which joins

Table 4.4: Mean and maximum values of ε_f, λ_v and λ_h for unidirectional wave trains at wave staffs 1, 5 and 12

Parameters	Initial steepness (ε_s) 0.0122	0.0104	0.0091
Wave staff 1			
$\overline{\varepsilon}_f$	0.170	0.151	0.129
$\varepsilon_f^{(max)}$	0.812	0.663	0.408
$\overline{\lambda}_v$	1.115	1.150	1.161
$\lambda_v^{(max)}$	5.090	8.286	7.553
$\overline{\lambda}_h$	0.561	0.505	0.558
$\lambda_h^{(max)}$	0.987	0.995	0.998
Wave staff 5			
$\overline{\varepsilon}_f$	0.148	0.139	0.122
$\varepsilon_f^{(max)}$	1.018	0.915	0.462
$\overline{\lambda}_v$	1.104	1.109	1.193
$\lambda_v^{(max)}$	4.357	8.444	6.000
$\overline{\lambda}_h$	0.554	0.555	0.555
$\lambda_h^{(max)}$	0.947	0.989	0.987
Wave staff 12			
$\overline{\varepsilon}_f$	0.108	0.107	0.104
$\varepsilon_f^{(max)}$	0.569	0.639	0.619
$\overline{\lambda}_v$	1.064	1.124	1.152
$\lambda_v^{(max)}$	3.733	5.36	7.059
$\overline{\lambda}_h$	0.548	0.546	0.548
$\lambda_h^{(max)}$	0.999	0.999	0.999

a wave crest and the preceding zero crossing point (see Fig. 4.1). In Fig. 4.5, the probability of exceeding a particular crest front steepness is shown for three different initial wave steepnesses ε_s of short-crested waves recorded at the wave staff 5 of 17.5 m from the wave maker, and with directional spreading proportional to $\cos^2 \Theta$. The figure shows that the probability does not differ substantially for particular initial wave steepnesses. Tables 4.4 and 4.5 demonstrate that the $\overline{\varepsilon}_f$ values decrease with the distance from the wave maker, while its maximum value depends strongly on the initial wave steepness. It should be mentioned that the probability density of the local steepness ε_l has been developed theoretically in Section 3.2.5.

Two other parameters suggested by Myrhaug and Kjeldsen (1986), namely λ_v and λ_h, characterize the nonlinearity of wave motion. For linear waves being

Table 4.5: Mean and maximum values of ε_{f}, λ_{v} and λ_{h} for short-crested waves at wave staffs 1, 5 and 12

Parameters	Initial steepness (ε_{s}) 0.0122	0.0104	0.0091
Wave staff 1			
$\overline{\varepsilon}_{\mathrm{f}}$	0.181	0.174	0.141
$\varepsilon_{\mathrm{f}}^{(\max)}$	0.873	0.791	0.918
$\overline{\lambda}_{\mathrm{v}}$	1.127	1.185	1.235
$\lambda_{\mathrm{v}}^{(\max)}$	6.571	6.692	6.700
$\overline{\lambda}_{\mathrm{h}}$	0.546	0.549	0.546
$\lambda_{\mathrm{h}}^{(\max)}$	0.997	0.978	0.991
Wave staff 5			
$\overline{\varepsilon}_{\mathrm{f}}$	0.147	0.136	0.119
$\varepsilon_{\mathrm{f}}^{(\max)}$	0.743	0.708	0.495
$\overline{\lambda}_{\mathrm{v}}$	1.117	1.123	1.178
$\lambda_{\mathrm{v}}^{(\max)}$	5.300	6.889	7.273
$\overline{\lambda}_{\mathrm{h}}$	0.547	0.541	0.543
$\lambda_{\mathrm{h}}^{(\max)}$	0.992	0.998	0.995
Wave staff 12			
$\overline{\varepsilon}_{\mathrm{f}}$	0.120	0.115	0.097
$\varepsilon_{\mathrm{f}}^{(\max)}$	0.473	0.476	0.319
$\overline{\lambda}_{\mathrm{v}}$	1.122	1.122	1.173
$\lambda_{\mathrm{v}}^{(\max)}$	4.000	5.167	8.500
$\overline{\lambda}_{\mathrm{h}}$	0.555	0.541	0.540
$\lambda_{\mathrm{h}}^{(\max)}$	0.999	0.998	0.975

a superposition of simple sinusoidal components, the mean vertical asymmetry λ_{v} is usually equal to 1.0, while the horizontal asymmetry λ_{h} is very close to 1/2. As shown in Tables 4.4 and 4.5, the mean vertical asymmetry $\overline{\lambda}_{\mathrm{v}}$ becomes in all cases greater than one, while the mean horizontal asymmetry λ_{h} exceeds 1/2. Both these values indicate that the observed wave motion is nonlinear.

Tęgowski (2004) estimated the probability of breaking by comparying the results obtained from the algorithm, based on the limiting vertical acceleration and video observations during the Ocean Basin Experiment. The probability of breaking was defined as the ratio of the number of breaking waves and the total number of waves. This ratio, presented versus the significant wave height H_{s} and peak wave period T_{p}, did not exceed 10%. Video records exhibited

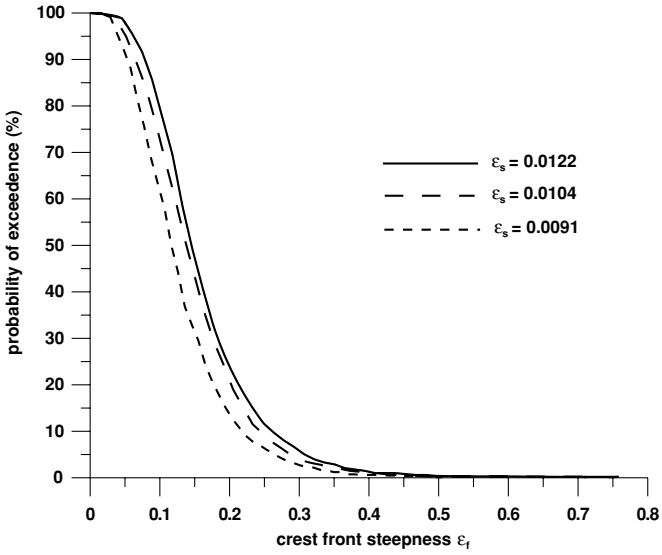

Figure 4.5: Probability of exceedance of crest front steepness for three initial wave steepnesses.

irregular spilling breakers appearing on the basin surface and wave energy slowly attenuated along the wave of propagation.

In Fig. 4.6 the energy variation along the main transect is shown for unidirectional wave trains of three different steepnesses ε_s. Similar energy attenuation

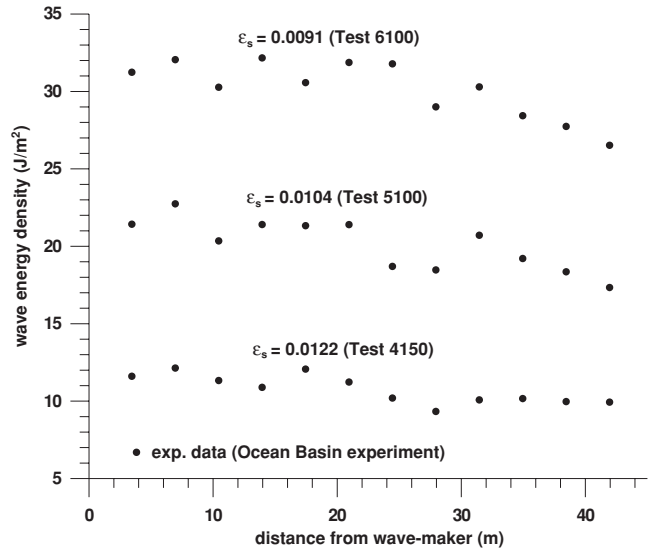

Figure 4.6: Wave energy attenuation along the transect for unidirectional wave train.

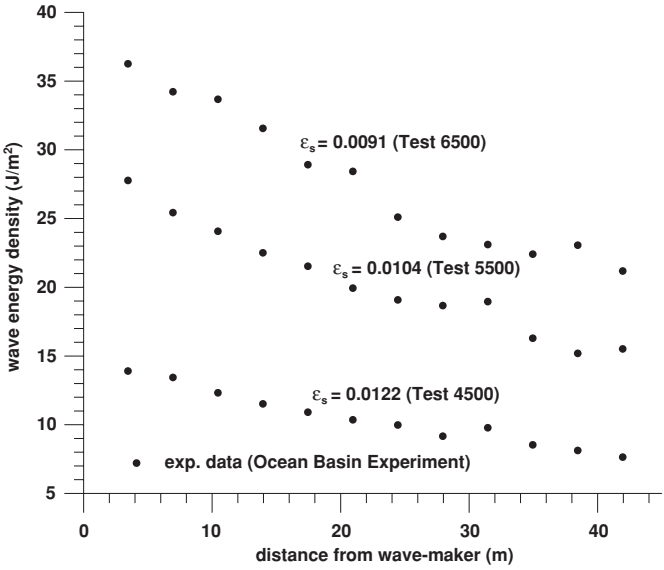

Figure 4.7: Wave energy attenuation along the transect for short-crested waves.

for wave trains characterized by directional spreading $\sim \cos^2 \Theta$ is illustrated in Fig. 4.7. Both figures demonstrate that attenuation of wave energy with distance is not uniform. For short-crested waves, the energy attenuation gradient varies from 0.162 to 0.387 J/(m^{2}m^{-1}), while for long-crested waves attenuation is much smaller, being in the range of 0.044–0.122 J/(m^{2}m^{-1}). A comparison of these results with theoretical ones is left to Chapter 6.

4.4.4 Other experiments

4.4.4.1 Simulation of steep random waves in wave tanks

Ochi and Tsai (1983) reproduced several series of irregular waves with different spectra in a wave tank using pre-programmed tapes yielding relatively high waves leading to breaking and corresponding to severe storms in the North Atlantic. The wave height-wave period relationship at time of breaking of irregular waves was obtained from measurements of over 40 incident waves about to break. Typical significant wave height was 8 cm and peak period was 0.95 s. They found that the probability of occurrence of breaking waves depends to a great extent on the shape of the wave spectrum, and that the fourth moment of the spectrum is a dominant parameter which influences the occurrence of breaking. The probability of breaking varied from 1.5 to 6.0%. The most probable probability of breaking increases from 1 to 13% when significant wave steepness $\varepsilon_s = \frac{H_s}{gT_p^2}$ varies from 3.9×10^{-3} to 4.75×10^{-3}. The wave height measured by Ochi and Tsai for the breaking of steep nonlinear waves

in a channel provides the following threshold value for the global limiting wave steepness ε_{g}

$$\varepsilon_{\mathrm{g}} = \frac{H}{gT^2} = 0.020. \tag{4.18}$$

Laboratory experiments on wave breaking in deep-water random seas, represented by the JONSWAP spectrum with enhancement factor $\gamma \simeq 7.0$, were reported by Dawson et al. (1993). Waves were generated at one end of a 116-m wave tank, and wave breaking was observed approximately 30 m from the wave-maker. Frequencies ranging from near zero to approximately twice the peak spectral frequency were considered in increments of $2\pi/100$ rad/s. In wave generation procedure, for each frequency, the corresponding spectral-density amplitude was used with a random phase chosen from a uniform distribution to define a sinusoidal component of the wave-maker command. While the wave-maker command was formed by linear superposition of sinusoidal components with random phase from a uniform distribution, the actual components comprising the sea state were different because of nonlinear effects, and final crest amplitudes become greater than trough amplitudes.

Breaking waves have been identified by correlating the time history with a video record of the test and with marker signals on the output from the wave probe. Observed relative number of crest amplitudes of non-breaking waves exceeding specified levels showed a good agreement with a modified Rayleigh distribution of crest amplitudes (see Section 5.5) that accounts approximately for nonlinear effects in seas with a narrow frequency band. It should be pointed out that the classical Rayleigh distribution predicts lower probability of specific amplitude threshold levels appearing. In the experiment, five independent records with the significant wave height H_{s} in the range 36.9–55.2 cm, and with the peak period about 2.83 s were obtained. Inspection of the time history shows the nonlinear effect of increased crest amplitude in comparison with trough values. It was also seen that the highest waves were not always the ones that broke on the probe. The observed probability of breaking was found to be a function of the significant wave steepness ε_{s}. For $0.005 < \varepsilon_{\mathrm{s}} < 0.011$, the probability of breaking F_{br} changes in the range $0.06\% < F_{\mathrm{br}} < 6\%$.

Caulliez (2002) reported the results of a statistical analysis of some geometric properties of breaking wind waves observed in the large Marseille-Luminy wind-wave facility. In particular, the relationship of the breaking events and the instantaneous slope was examined. The slope was defined as

$$\varepsilon(t) = -\frac{1}{C}\,\frac{\partial \zeta(t)}{\partial t}, \tag{4.19}$$

where C is the phase speed of the dominant frequency. A wave breaking was detected everywhere the water surface slope at the crest exceeded the value 0.586 in magnitude, i.e. when the time derivative signal had a value higher than $0.586\,C$ (see Eq. (2.21), resulting from the Longuet–Higgins and Fox (1977) theory.

Caulliez (2002) distinguished two types of breaking: waves at the inception of breaking ('near-breaking region') when waves are characterized by a well-defined single-value profile, and waves with a steep but corrugated wave front ('fully developed breaking') when $\frac{\partial \zeta(t)}{\partial t}$ presents several peaks crossing the threshold value and separated from each other by very short time intervals. For the 'near-breaking region' case, the wave front was inclined by about 45°, that is an angle much larger than 30.37°, predicted by Longuet–Higgins and Fox (1977). In the case of 'fully developed breaking', the wave front angle reaches about 32° only. However for both cases, the profiles of wind waves do not depend on wave scale and initial wave generation, which suggests that the physical mechanisms leading to breaking are universal and only weakly dependent on wind forcing at the wave crest.

Another interesting conclusion resulting from Caulliez's experiment is the linear relation between so-called wave breaking intensity I_{b} and breaking rate R_{d}. The breaking intensity I_{b} is defined as the average jump height over a time sequence weighted by the average breaking frequency (this is the average number of waves breaking per second). On the other hand, the breaking rate R_{d} is defined as the ratio of the sum of the breaking jump duration and the total duration of the time sequence. Above experimental findings will be compared with various theoretical developments in Chapters 5 and 6.

4.4.4.2 Chirp pulse generation approach

Griffin et al. (1996) in their laboratory experiments studied the spatial evolution of the crest front steepness ε_{f} and the vertical asymmetry parameter λ_{v} along the wave channel. The method of wave packet generation employed in the experiments was based on the chirp pulse generation technique for focusing the wave energy at a desired location in the channel. It was found that the crest front steepness ε_{f} evolves in space before the breaking point and the value of ε_{f} at breaking point depends on the initial wave steepness ak. The observed maximum crest front steepness for spilling breakers was equal to $\varepsilon_{\mathrm{f}} = 0.32$, while for plunging breakers ε_{f} reached a value of 0.62.

Vertical asymmetry parameter λ_{v}, initially very close to 1.0, varies moderately and decreases slightly when the spilling breaker is generated. For the plunging breaker, the λ_{v} parameter becomes larger with $\lambda_{\mathrm{v}} = 2$ just before breaking, and then decreases to about $\lambda_{\mathrm{v}} \approx 1.7$ at the breaking point. This value corresponds to $\lambda_{\mathrm{v}} = 1.83$, obtained by Longuet–Higgins and Cokelet (1976) in their numerical calculations for a plunging breaker. In Kjeldsen' (1990) experiments, λ_{v} was in the range (0.9–2.2). On the other hand Duncan et al. (1994b) found that λ_{v} varied between 1.3 and 1.7 at breaking, for spilling and plunging breakers, respectively, while the horizontal asymmetry parameter λ_{h} changed only slightly as the breaking evolved from the incipient stage towards fully plunging ($0.72 < \lambda_{\mathrm{h}} < 0.80$).

Moreover, Griffin et al. discussed the wave breaking associated with wave steepness in the absence of wind. The potential energy density averaged over

a wavelength, defined as follows

$$E_{\text{pot}} = \frac{1}{L}\left\{\frac{\rho g}{2}\int_0^L \zeta^2(x)dx\right\}, \tag{4.20}$$

was found to be approximately half of the potential energy of the highest symmetric Stokes wave as computed by Cokelet (1977), and approximately 75 to 90% of the total potential energy was concentrated in the crest region at breaking.

4.4.4.3 Image processing technique

Lader et al. (1998) published laboratory experimental data on breaking wave geometry using zero-downcrossing analysis as well as the image processing technique. Three different cases of two-dimensional deep water breaking waves were examined, namely plunging breaker, spilling breaker and an intermediate breaker. The last one was defined as a breaker that is initiated by a microscale plunging event, and evolves further as a spilling breaker. Experiments confirmed that the crest front steepness experiences a large increase up to breaking and the wave becomes vertically asymmetric for spilling breakers. Experiments demonstrated also that for the plunging breaker, horizontal asymmetry factor λ_{h} increases significantly.

Processing of the images obtained from camera records provides a good opportunity for more detailed description of wave surface steepness. In particular, it appears that at the front inflection point (where $\frac{\partial^2\zeta}{\partial x^2} = 0$), steepness $\varepsilon_{inf} = \left|\frac{\partial\zeta}{\partial x}\right|$ increases up to 1 and its evolution is similar for spilling and plunging breakers. The point on the wave crest with the highest second derivative was referred to as the maximum crest curvature point, at which $\text{cur}_{\max} = \left|\frac{\partial^2\zeta}{\partial \text{x}^2}\right|$. The $\text{cur}_{\max}$ value was equal to $10\,\text{m}^{-1}$ for spilling breakers and $20\,\text{m}^{-1}$ for plunging breakers. Moreover, observation indicated that for spilling breakers foam generation starts at the maximum crest curvature point.

Let us now assume that $dx = C\,dt$, where C is the phase velocity. Therefore, $\text{cur}_{\max}$ becomes

$$\text{cur}_{\max} = \left|\frac{\partial^2\zeta}{\partial \text{x}^2}\right| = \frac{1}{\text{C}^2}\left|\frac{\partial^2\zeta}{\partial \text{t}^2}\right| = \frac{1}{\text{C}^2}\,\text{a}_{\text{z}}^{(\text{E})} \tag{4.21}$$

and

$$a_z^{(E)} = C^2\,\text{cur}_{\max}, \tag{4.22}$$

in which $a_z^{(E)}$ is the Eulerian vertical acceleration (also called the apparent acceleration) at the maximum crest curvature point. Taking into account that phase velocity for plunging, intermediate and spilling breakers in the experiment were equal to 1.75, 1.51 and 1.62 m/s, respectively, and using values of $\text{cur}_{\max}$ resulting from the experiments, we can estimate values of the Eulerian

acceleration $a_z^{(E)}$ as:

$a_z^{(E)} \sim 5$ g for plunging breakers

$a_z^{(E)} \sim 6.6$ g for intermediate breakers

$a_z^{(E)} \sim 2.7$ g for spilling breakers.

All these values of $a_z^{(E)}$ are very high. More detailed discussion on the nature of Eulerian and Langrangian vertical accelerations at the breaking point are given in Chapter 5.

Stansell and MacFarlane (2002) performed laboratory experiments to obtain horizontal components of fluid particle velocity at the surface crests of breaking and non-breaking waves to examine the applicability of the kinematic breaking criterion. Waves were produced at one end of the flume by a computer-controlled wave paddle and surface elevation $\zeta(x,t)$ was composed as the sum of N linear waves, each of amplitude a_n, wave number k_n, frequency ω_n and initial phase φ_n as

$$\zeta(x,t) = \sum_{n=1}^{N} a_n \cos(k_n x - \omega_n t + \varphi_n). \tag{4.23}$$

A series of capacitance wave gauges were placed at intervals of 0.1 m along the wave flume and surface elevation was recorded at intervals of 1/16 s. In addition to the surface elevation measurements, fluid particles in the wave crests were measured using the particle image velocimetry (PIV) technique. The water was seeded with neutrally buoyant pollen grains that were illuminated by the pulsating light sheet. As the velocities were measured close to, but not at, the fluid surface, extrapolation of the measured velocities to the surface was needed. This was done by using a fitting function, and the phase speed was measured in the same reference frame as the fluid velocities.

The experiment included six tests with one plunging breaker, two spilling breakers and three non-breaking waves. Analysis of the experimental data shows that the greatest ratio of horizontal fluid particle velocity in the crest to local phase speed for the rounded crest of a plunging breaker is about 0.81, being significantly less than the common kinematic breaking criterion. For both of the spilling breakers the maximum horizontal fluid particle velocity at the tip of the crest is about 6% less than the local phase speed, implying that the kinematic breaking criterion is closer to being satisfied. In all waves analysed in the experiment, the local phase speed has its lowest minimum in the vicinity of the point of the wave where one would expect the surface velocity to be the greatest. The various definitions of phase speed used in the Stansell and MacFarlane experiment are discussed in Section 5.4.

4.4.4.4 Amplitude modulated wave packet approach

Kway et al. (1998) simulated a variety of deep water breaking waves through wave-wave interactions in frequency and amplitude modulated wave packets. Based on a study of single breaking events it was found that the amplitude of the wave crest ζ_c normalized by the characteristic wave number k varies from

$k\zeta_c = 0.4$ to 0.6 for plunging waves, which is higher than $k\zeta_c = 0.4432$ for limiting regular symmetric waves (see Section 2.2). The value of $k\zeta_c$ for spilling breakers was in the range of 0.5, suggesting that wave steepness alone was an unreliable indicator of the type of wave breaking.

4.4.4.5 Air entrainment method

Evolution of the entrained air and determination of whether the moments of the void-fraction field are related to wave parameters have been discussed by Melville et al. (1992) and Lamarre and Melville (1991). In their laboratory studies, the instrument enabled measurement of the void-fraction down to a threshold of 0.3% and to within 3 cm of the surface. The characteristic wavelength of the wave generated in the flume was 2 m. The authors computed the total volume of air V normalized by the initial volume of air entrained, V_0. Volume V_0 was determined from video images of a cylinder of air formed as the surface impacted on itself (Melville et al., 1992). The area of formed air bubble plume A within the 0.3% threshold was measured and the mean void-fraction $\overline{\alpha}$ was calculated by dividing the total volume of air by the area. The normalized air volume V/V_0 is shown in Fig. 4.8a as a function of normalized time lag $(t - t_{\mathrm{br}})/T$, when the breaking time t_{br} is taken as a reference. The three wave trains, with varying steepness ak, have been fitted by simple power law

$$\frac{V}{V_0} = 2.5 \exp\left[-3.9\,\frac{t - t_{\mathrm{br}}}{T}\right]. \tag{4.24}$$

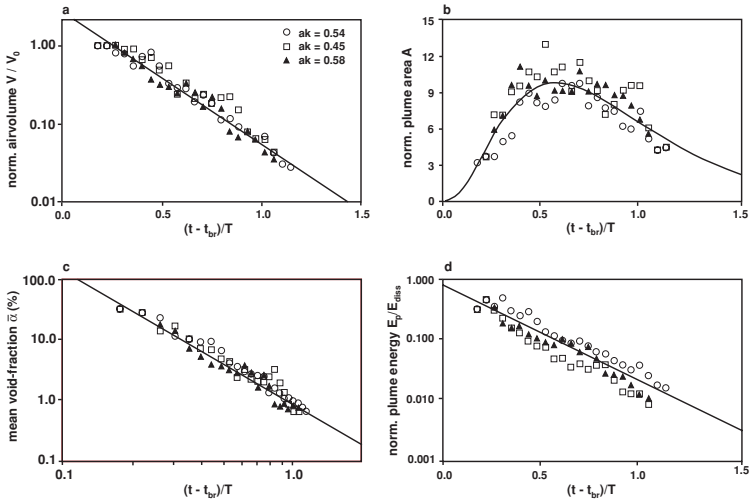

Figure 4.8: Air entrainment characteristics induced by wave breaking: (a) normalized air volume $\frac{V}{V_0}$; (b) bubble plume cross-sectional area A, normalized by $\frac{V}{V_0}$; (c) mean void-fraction $\overline{\alpha}$; (d) normalized bubble plume potential energy $\frac{E_{\mathrm{p}}}{E_{\mathrm{diss}}}$ (adapted from Melville et al., 1992).

From the figure it can be seen that only a few percent of the initial air entrainment remains in the water column after one wave period. In Fig. 4.8b, the normalized bubble plume cross-sectional area A is shown. The data for this figure are simply obtained from the relationship for V/V_0 in order to avoid extrapolation of the data for A directly. So, let us present the total volume of air as follows

$$V = Ab\overline{\alpha}, \tag{4.25}$$

in which A is the area of the bubble plume, b is the wave flume width and $\overline{\alpha}$ is the mean void-fraction of air. The normalized bubble plume cross-sectional area is given as

$$\frac{A}{\frac{V_0}{b}} = \frac{bA}{V_0}. \tag{4.26}$$

Melville et al. (1992) presented function $\frac{Ab}{V_0} = f\left(\frac{t-t_{\mathrm{br}}}{T}\right)$ in the form (see Fig. 4.8b)

$$\frac{A\,b}{V_0} = 325\left(\frac{t-t_{\mathrm{br}}}{T}\right)^{2.3}\exp\left[-3.9\,\frac{t-t_{\mathrm{br}}}{T}\right]. \tag{4.27}$$

It follows that the area of bubble plume increases rapidly and then decreases as bubbles are lost.

The interesting relationship between mean void fraction ($\overline{\alpha}$) and normalized time lag $\left(\frac{t-t_{\mathrm{br}}}{T}\right)$ is given in a double logarithmic scale in Fig. 4.8c. The $\overline{\alpha}$ value varies during about one period after breaking onset from 10% to 1%. The data are presented by a power law with $\overline{\alpha} = 100\%$ for $t \approx 0$, as one would expect for the initial air pocket.

The wave energy which goes into entraining the air is equal to the work done against buoyancy forces by the water in mixing down the air

$$E_{\mathrm{p}} = \rho_{\mathrm{w}} g b \int_A \alpha z\, dA, \tag{4.28}$$

in which α is the void fraction, z is the distance to the water surface.

The normalized $\frac{E_{\mathrm{p}}}{E_{\mathrm{diss}}}$, where E_{diss} is the total energy loss during breaking, gives the fraction of the dissipated energy which goes into entraining the air. The data given in Fig. 4.8d suggest that

$$\frac{E_{\mathrm{p}}}{E_{\mathrm{diss}}} = 0.7\exp\left[-3.6\,\frac{(t-t_{\mathrm{br}})}{T}\right]. \tag{4.29}$$

4.4.4.6 Acoustic method

Control laboratory experiments are specially suitable for examining the applicability of acoustic methods for detection of breaking waves. Passive acoustic detection of breaking is not a new technology and several papers have reported

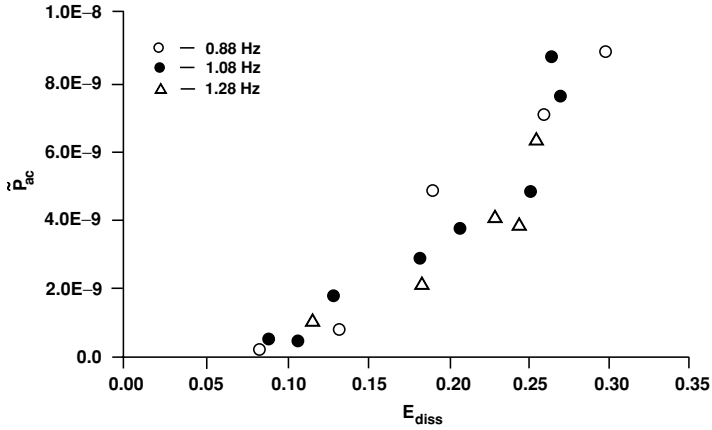

Figure 4.9: Relationship between mean square acoustic pressure $\tilde{p}_{ac}$ and the energy dissipation E_{diss} for three different incident wave frequencies (adapted from Melville et al., 1992).

on direct measurements of sound generation by breaking waves. The individual bubbles which break off from the initial volume of air entrained oscillate and generate sound. The departure of the acoustic signal above the background noise level was found to be strongly related to the onset of breaking. The duration of the hydrophone signal is compared to the wave period and the sound terminates at the same time as the air entrainment at the leading edge of the breaker.

Melville et al. (1992) showed that the dominant microwave signal occurs prior to wave breaking and it is not from the whitecapping but from the steepening unbroken wave just prior to impact. The relationship of dimensionless mean square acoustic pressure and energy dissipated due to wave breaking E_{diss} is shown in Fig. 4.9 when the dimensionless mean square acoustic pressure is defined as follows

$$\tilde{p}_{ac} = \frac{\overline{p_{ac}^2}}{(\rho_{\text{w}} C^2)}, \tag{4.30}$$

where p_{ac} is the acoustic pressure and C is the phase wave speed.

Dissipated energy is determined by the mean square surface displacement upstream and downstream of wave breaking. The proportionality between $\tilde{p}_{ac}$ and E_{diss} is clearly seen from the figure.

Tęgowski (2004) attempted to describe, using the spectral parameters, the consecutive phases of noise generated by breaking events and to estimate the mean radiated acoustic energy generated by breaking waves versus the rate of energy dissipation in a breaking wave. Noise generated by breaking waves was recorded by hydrophones located below the water surface (see Massel et al., 2001).

Spectral analysis of the noise signal showed strong dependence of spectral width and spectral skewness on the phase of the breaking event. In the initial phase, the decrease in spectral skewness is caused by oscillating bubbles created at the wave front. During fragmentation of the air cavity formed by the plunging jet, small bubbles are created by the division of large ones, and the group of small bubbles oscillates with low frequencies. These oscillations cause an increase in spectral skewness.

The relationship between the acoustic energy generated by a breaking wave and the energy dissipated during breaking is valuable information for predicting the whitecap percentage in a given sea state, and subsequently for estimating the aerosol fluxes (Loewen and Melville, 1991). Assuming the simple dipole model for the source emitting the noise of the breaking wave, the total acoustic energy obtained by integrating the radiated intensity over a hemisphere of radius R_0 becomes (Ding and Farmer, 1994)

$$E_{ac} = \frac{2\pi R_0^2}{\rho_{\mathrm{w}} C_s} \int_0^t p_{ac}^2(t)\, dt, \tag{4.31}$$

in which R_0 is the radius centred at the point where the dipole intersects the pressure release surface, p_{ac} is the acoustic pressure radiated by the breaking event, C_s is the sound speed in water and t is the time of the breaking event.

For the wave parameters used in the experiment (Massel et al., 2001), the acoustic energy of breaking waves varied between 9.0×10^{-7} and $1.2 \times 10^{-5}\, J$. Following Melville (1994), Tęgowski (2004) estimated the mean value of the rate of energy dissipation per unit length along the wave crest $\approx 9.6 \times 10^{-3}$, and obtained the ratio of acoustic energy to the dissipated energy in breaking waves varying from 1.0×10^{-7} to 4.1×10^{-7}. This value corresponds to the value of $(0.6 \times 10^{-8} - 4.0 \times 10^{-8})$ given by Ding and Farmer (1994) and the value of $(0.3 \times 10^{-8} - 2.3 \times 10^{-8})$ of Carey et al. (1993). Higher values of $(0.8 \times 10^{-7} - 1.09 \times 10^{-6})$ were obtained by Kolaini and Crum (1994).

4.5 Physical simulation of extreme ocean waves in large scale

The experiments described in the above sections are dedicated to mostly qualitative as well as quantitative observations of the shape evolution and instability mechanisms leading to wave breaking. However, they were not concerned particularly with the extreme wave environment. The prediction and reproduction of extreme ocean waves is a complex task as they are very rare events and difficult to observe in the real ocean. Also, fully nonlinear theoretical models for random extreme waves still do not exist, although there are several theoretical approaches that include many linear and nonlinear components and properties of ocean waves.

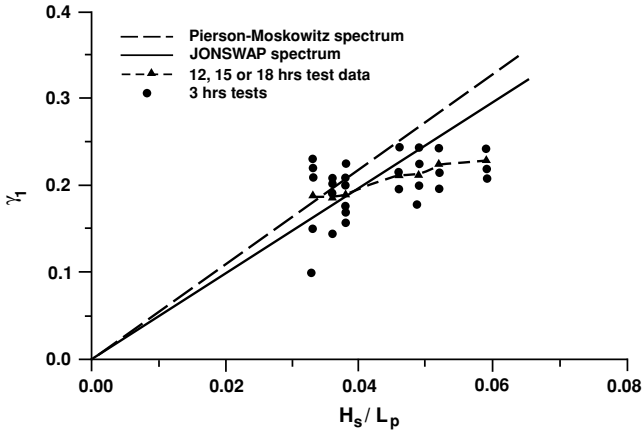

Figure 4.10: Skewness γ_1 as a function of the average wave steepness (adapted from Stansberg, 2000).

Therefore, the scale reproductions of ocean waves in laboratory basins are essential for better understanding of the extreme wave phenomena and the impact of the severe wave environment on ships and coastal and offshore structures. Usually in laboratory tests linear random signals (see simulation techniques described in Chapter 3) are given as the input to the wavemaker. After some wavelengths of propagation, nonlinear effects in the wave field appear, and extreme high waves can be formed. As the extremes are rare events, laboratory studies require rather long records. Stansberg (2000) indicate that although a 3 hour record may be sufficient for most standard testing purposes, data sets of 12, 15 or 18 h tests are required for the study of statistics of extremes. He reported results of experiments in the Ocean Basin at MARINTEK (Trondheim), in which typical Norwegian storm sea states ($H_\mathrm{s} \sim 8 - 16$ m, $T_\mathrm{p} \sim 10 - 18$ s) have been reproduced in model scale 1:55–1:70 with duration of 3 h as well as in the form of 4, 5 or 6 independent 3 h realisations. In Figs. 4.10 and 4.11 the statistical skewness γ_1 and excess of kurtosis $(\gamma_2 - 3)$ are shown as a function of wave steepness $\left(\frac{H_\mathrm{s}}{L_\mathrm{p}}\right)$ when L_p is the wavelength corresponding to the wave peak period T_p. For nonlinear second-order random waves, skewness γ_1 and excess of kurtosis $(\gamma_2 - 3)$ are no longer zero. Vinje and Haver (1994) for the Pierson–Moskowitz spectrum showed that

$$\gamma_1 = 5.41 \left(\frac{H_\mathrm{s}}{L_\mathrm{p}}\right) \tag{4.32}$$

and

$$\gamma_2 - 3 = 3\gamma_1^2. \tag{4.33}$$

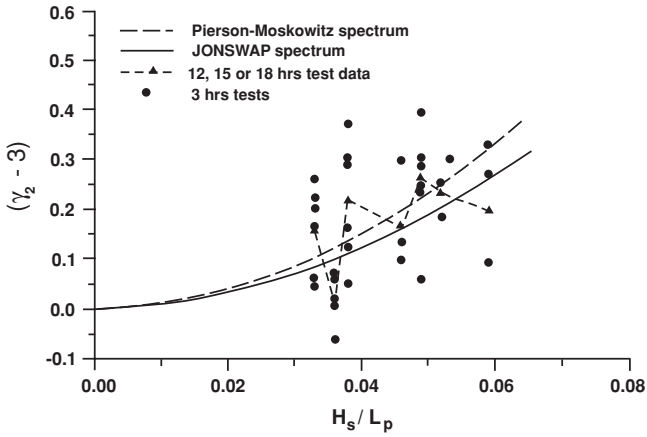

Figure 4.11: Excess of kurtosis $(\gamma_2 - 3)$ as a function of the average wave steepness (adapted from Stansberg, 2000).

It is observed that the theory predicts lower values of γ_1 and $(\gamma_2 - 3)$ for the narrow (JONSWAP) spectrum than for the broad-banded Pierson–Moskowitz spectrum. Experimental values of the statistical skewness γ_1 and theoretical ones resulting from second-order theory for steepness up to $\frac{H_s}{L_p} = 0.04$ are in good agreement. For higher steepnesses, skewness γ_1 remains almost constant and equal to $\gamma_1 \approx 0.2 - 0.23$. On the other hand, the excess of kurtosis $(\gamma_2 - 3)$ compares well with (4.33). It should be noted that lower kurtosis values are observed for multidirectional waves than for unidirectional waves.

From Fig. 4.12, the extreme crest heights ζ_c, normalized by the standard deviation σ_ζ of the process $\zeta(t)$, are higher than that resulting from nonlin-

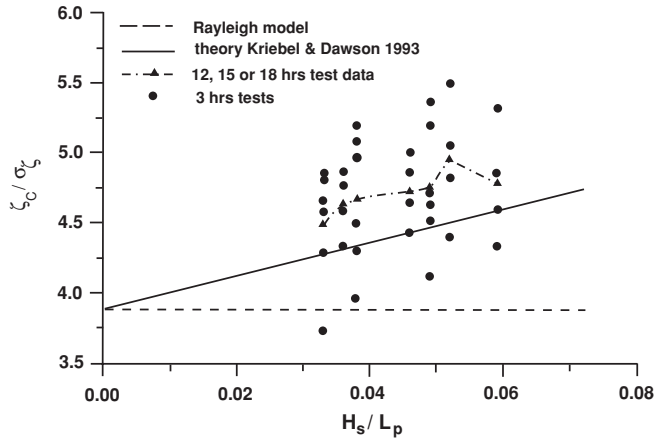

Figure 4.12: Normalized maximum crest heights ζ_c/σ_ζ as a function of the average wave steepness (adapted from Stansberg, 2000).

ear prediction of Dawson et al. (1993) (see Section 5.5). It is also clear that the Rayleigh distribution is unacceptable for prediction heights ζ_c. However, the experimental results, not shown here, indicate that a normalized extreme peak-to-peak wave height shows reasonable agreement with the Rayleigh distribution.

It can be shown that the expected maximum crest height $E[\zeta_{c_{\max}}]$ deducted under the second-order random wave assumption is (Stansberg, 2000)

$$E[\zeta_{c_{\max}}] = E[\zeta_{c_{\max}}]_{\text{Rayleigh}} \left\{1 + \frac{1}{2} k_p E[\zeta_{c\max}]_{\text{Rayleigh}}\right\}, \tag{4.34}$$

where

$$E[\zeta_{c_{\max}}]_{\text{Rayleigh}} = \left[(2\ln N)^{1/2} + 0.577\,(2\ln N)^{-1/2}\right], \tag{4.35}$$

in which N is the number of independent amplitudes in a record.

Experiments in the Ocean Basin Experiment showed that (4.35) provides lower values of $E[\zeta_{c_{\max}}]$ than experimental ones and the Rayleigh model is clearly again under-predicting.

4.6 Detection of breaking in a given wave record

4.6.1 Introduction

Wave breaking is an intermittent process in a wave field evolving in time. During breaking substantial modification in the spectral structure of surface waves appears. Traditional research on the statistics of ocean waves is limited to global quantities such as the Fourier spectra. These quantities provide very valuable information on the general properties of waves but give no insights into the initiation of breaking and its intensity. Particularly because of evolution in time and because of the intermittency of the breaking process, the common Fourier transform approach is not adequate for a description of a local wave. Although the Fourier spectrum is valid under extremely general conditions, there are some crucial restrictions of Fourier spectral analysis, namely the system must be linear and the data must be strictly periodic or stationary. In fact, the stationarity requirement is not particular to Fourier spectral analysis, but is a general one for most of the processing methods of available data.

Usually in practice we only have data for finite time spans and application of rigorous definitions of stationarity in the wide and narrow sense is not possible. It should be noted that Fourier spectral analysis requires linearity. Although many natural phenomena can be approximated by linear systems, the breaking event is a highly nonlinear which cannot be presented as a superposition of linear systems. In particular Fourier spectral analysis uses linear superposition of trigonometric functions and many harmonic components are needed to simulate the deformed profiles of breaking, nonlinear waves. Due to the fact that

the form of data on breaking waves deviates from a pure sine or cosine function, the Fourier spectrum will contain spurious harmonics that cause energy spreading. Therefore, Fourier spectral analysis is of limited use.

Recently, several approaches have been devised to process highly nonlinear and nonstationary signals. The most promising are wavelet transform analysis (WT) and the phase-time method (PTM) based on the Hilbert transform. These two time–frequency approaches, described below, present effective methods towards better understanding of nonlinear and nonstationary wave processes.

4.6.2 Wavelet transform approach (WT)

The wavelet transform (WT), developed during the last two decades, is an ideal tool for the study of measured time series data of nonstationary, transient phenomena such as breaking waves. Details on WT can be found in many books and articles. An introduction to WT and its application to wave phenomena was published recently by Massel (2001b) and a brief summary of the wavelet transform methodology is presented in Appendix B.

For a real time series, not necessarily stationary, the time localization cannot be extracted from a frequency spectrum. However, this can be done through the wavelet transform, which can be considered as a broadened extension of the commonly used Fourier transform. Both methods transform the function representing the process in one domain to some different domain. In the case of the wavelet transform, this domain is the frequency and the time domain. What new information is provided by the wavelet transform? First of all, this approach provides a better insight into the inherently nonstationary wave process governed by intermittent wave groups (Liu, 2000a,b). Spedding et al. (1993) found that the wavelet transform is a very useful tool to obtain a space-scale decomposition of a two-dimensional surface wave field resulting from the wave-wave interaction in an unsteady wave field. Although their analysis was preliminary in nature, the careful application of a two-dimensional complex wavelet transform allows a quantitative, whole-field, unsteady analysis to be performed. There are also some attempts to apply the wavelet transform to separate gravity waves generated by simultaneous forcing sources acting either at the same location but at different frequencies or at the same frequency but over different time periods and at different locations. In particular, Pairaud and Auclair (2005) applied so-called combined wavelet and principal component analysis (WEof) for the extraction of external gravity waves and internal gravity wave lower modes in the case of a flat bottom and constant Brunt-Väisälä frequency.

In contrast to the Fourier transform, wavelet transform analysis allows exceptional localization both in the time domain via translation τ of the wavelet, and in the frequency domain via dilation scales b of the mother wavelet (see Appendix B for definitions of both quantities). As was found by Massel (2001b), in wave mechanics Morlet's wavelet is a good candidate for the mother wavelet.

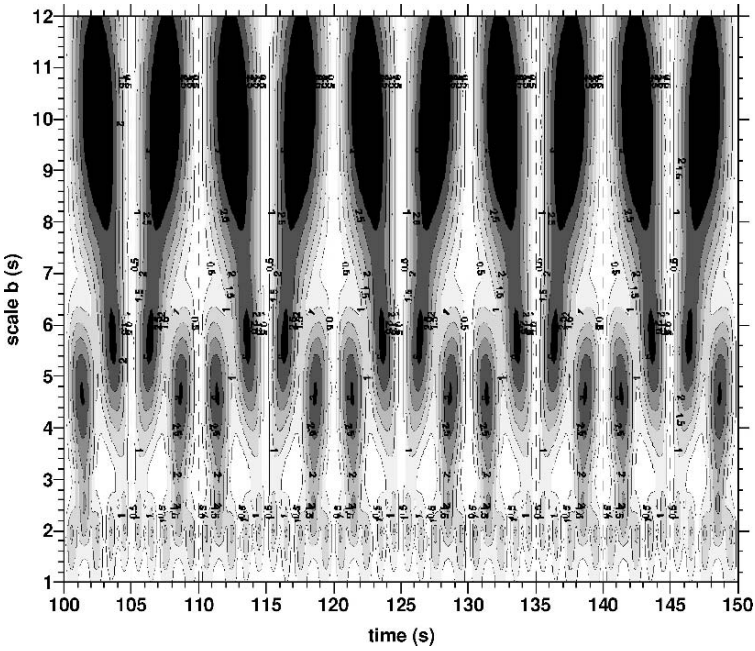

Figure 4.13: Contours of $|WT|$ for a superposition of three sinusoidal signals.

The final expression for wavelet transform of signal $\zeta(t)$ takes the form

$$WT(\tau, b) = \frac{1}{\sqrt{b}} \int_{-\infty}^{\infty} \exp\left[-\frac{1}{2}\left(\frac{t-\tau}{b}\right)^2\right] \exp\left[i\frac{2\pi}{b}(t-\tau)\right] \zeta(t)\, dt. \tag{4.36}$$

For illustration, in Fig. 4.13 the function $|WT(\tau, b)|$ is shown for a superposition of three sinusoidal signals

$$\zeta(t) = \sin\left(\frac{2\pi t}{2}\right) + \sin\left(\frac{2\pi t}{5}\right) + \sin\left(\frac{2\pi t}{10}\right). \tag{4.37}$$

The maxima of the absolute values of wavelet $|WT(\tau, b)|$ are concentrated in the periods of three components. Moreover, they are distributed in time according to the periodicity of the resulting wave field.

The relationship between the scale b and the Fourier period T is discussed in detail in a paper by Massel (2001b). It was shown that for the Morlet wavelet, used in this chapter, we have

$$b = \frac{c + \sqrt{c^2+2}}{4\pi}\, T \approx 1.0125\, T, \tag{4.38}$$

in which $c = 2\pi$.

In Fig. 4.14 a piece of random wave record (Test 4150 from the Ocean Basin Experiment – Massel et al., 2001) is shown. A corresponding Fourier spectrum

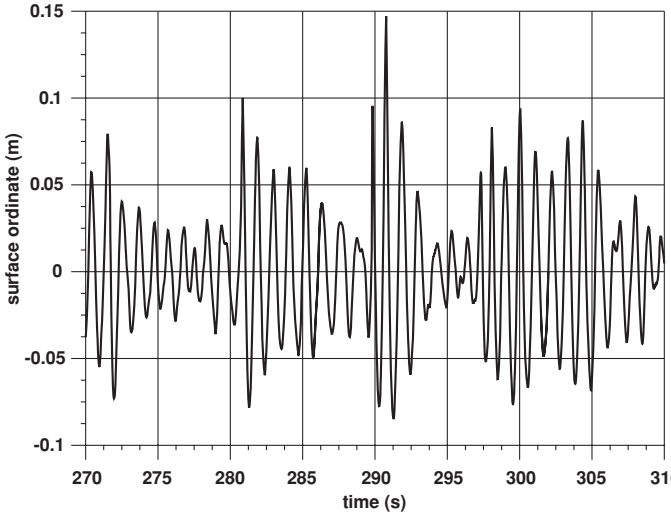

Figure 4.14: Part of a record of mechanically generated waves in the Ocean Basin Experiment (Test 4150).

is given in Fig. 4.15. The peak period T_p of the mechanically generated waves is equal to 1 s; however, due to imperfect mechanical generation and due to nonlinear wave interactions, the energy peak slightly shifted. In contrast to the Fourier spectrum, the wavelet shown in Fig. 4.16 provides good localization

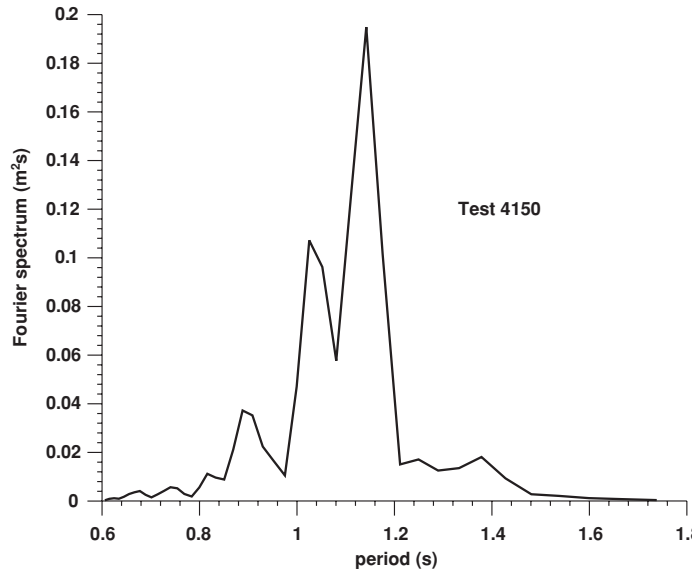

Figure 4.15: Fourier spectrum corresponding to wave record given in Fig. 4.14.

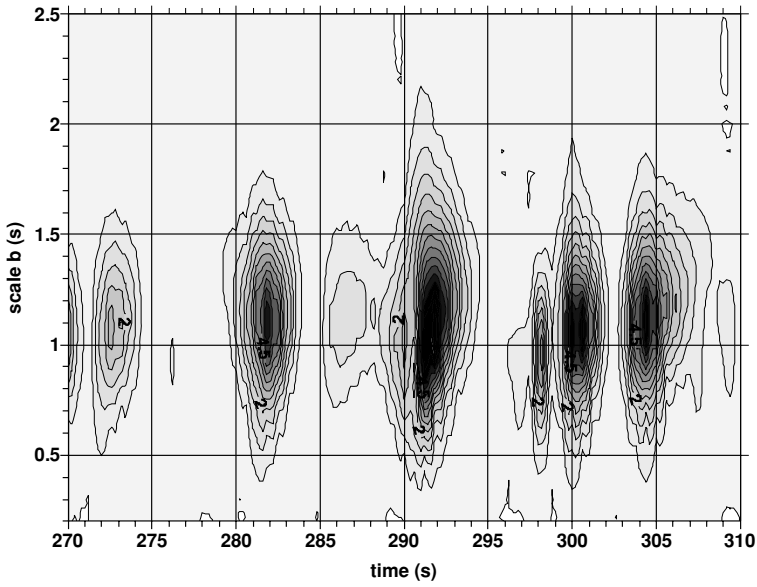

Figure 4.16: Contours of the $|WT(\tau, b)|$ for wave record given in Fig. 4.14.

of the wave energy in time. The highest energy for the high elevation around $t \sim 291\,\mathrm{s}$ is clearly seen. This energy corresponds to the wave component of period $\sim 1.16\,\mathrm{s}$. On the other hand, the second peak of the Fourier spectrum with the period $\sim 1.05\,\mathrm{s}$ corresponds to the group of high waves seen in Fig. 4.14 for time interval from 300 to 305 s, which is also confirmed in Fig. 4.16.

4.6.3 Phase-time method

Another method to better localize the wave breaking is the phase-time method (PTM) based on the Hilbert transform. As shown in Appendix C, the surface elevation $\zeta(t)$ and its Hilbert transform $\xi(t)$ form so called analytic signal

$$\eta(t) = \zeta(t) + i\xi(t), \tag{4.39}$$

where

$$\zeta(t) = \sum_{n=0}^{\infty} [a_n \cos(n\omega t) + b_n \sin(n\omega t)], \tag{4.40}$$

$$\xi(t) = \sum_{n=0}^{\infty} [a_n \sin(n\omega t) - b_n \cos(n\omega t)]. \tag{4.41}$$

Due to phase lag, equal to $(-\pi/2)$, between signal $\zeta(t)$ and its Hilbert transform, $\xi(t)$, can be interpreted as the 'horizontal' component of the surface elevation. The analytic signal $\eta(x, t)$ can be rewritten in the form

$$\eta(t) = A(t) \exp[i\theta(t)], \tag{4.42}$$

and

$$A(t) = \sqrt{\zeta^2(t) + \xi^2(t)} \quad \text{and} \quad \theta(t) = \arctan\left(\frac{\xi(t)}{\zeta(t)}\right), \tag{4.43}$$

where $A(t)$ is the local wave amplitude and $\theta(t)$ is the local phase function.

Representation (4.42) yields the local wave member $k_{\text{l}}(t)$ and instantaneous angular frequency $\omega_{\text{l}}(t)$ as follows

$$k_{\text{l}}(t) = \frac{\partial\theta(t)}{\partial x} \tag{4.44}$$

and

$$\omega_{\text{l}}(t) = \frac{\partial\theta(t)}{\partial t}. \tag{4.45}$$

Therefore, the local wave speed becomes

$$C_{\text{l}}(t) = \frac{\omega_{\text{l}}(t)}{k_{\text{l}}(t)}. \tag{4.46}$$

The above definitions indicate that in principle the local phase velocity can be obtained from the signal-point measurements.

Additionally, the local horizontal and vertical velocity components at the free surface can be approximated as follows

$$\left.\begin{array}{rcl} u(t) & = & \dfrac{\partial\xi(t)}{\partial t} \\ w(t) & = & \dfrac{\partial\zeta(t)}{\partial t} \end{array}\right\}. \tag{4.47}$$

As the original signal and its Hilbert transform are both time domain signals, we can decompose the phase function $\theta(t)$, given in (4.43), into its mean value $\overline{\theta}$ and time varying component $\delta(t)$ as

$$\theta(t) = \overline{\theta}(t) + \delta(t) \tag{4.48}$$

or

$$\theta(t) = \omega_0 t + \delta(t), \tag{4.49}$$

in which the mean phase $\overline{\theta}(t)$ is simply a product of the mean frequency ω_0 and time t. In the PTM approach, the phase is unwrapped and the varying part of the phase angle $\delta(t)$ is obtained by subtracting the linear component $\overline{\theta}(t)$ from total phase $\theta(t)$.

It should be noted that the instantaneous frequency ω_{l} can be derived directly from (4.43) as follows

$$\omega_{\text{l}} = \frac{\dfrac{\partial\xi}{\partial t}\zeta - \dfrac{\partial\zeta}{\partial t}\xi}{\zeta^2 + \xi^2}. \tag{4.50}$$

In a real situation, breaking events occur only at the crests of waves, where $\frac{\partial \zeta}{\partial t} \sim 0$ and ξ is small, due to 90° phase shift of $\xi(t)$. Therefore, (4.50) simplifies as follows

$$\omega_{\mathrm{I}} \approx \frac{1}{\zeta} \frac{\partial \xi}{\partial t} \tag{4.51}$$

or

$$\omega_{\mathrm{I}} \approx \frac{\sum_{n=0}^{\infty} (n\omega)[a_n \cos(n\omega t) + b_n \sin(n\omega t)]}{\sum_{n=0}^{\infty} [a_n \cos(n\omega t) + b_n \sin(n\omega t)]}. \tag{4.52}$$

For a single frequency wave train we have

$$\zeta(t) = a\cos(\omega_0 t), \quad \xi(t) = a\sin(\omega_0 t) \quad \text{and} \quad \omega_{\mathrm{I}} = \omega_0. \tag{4.53}$$

As the cosine and sine are smaller than one, the numerator of (4.52) increases rapidly with the frequency and ω_{I} will be large at any time when there is a concentration of high frequency components at the measurement point. Therefore, an increase in ω_{I} appears when wave breaking involves a nonlinear capture of high frequency components. This fact is a basis for the PTM method of detection of breaking.

Zimmermann and Seymour (2002) conducted a laboratory experiment to develop and validate a deep water breaking wave detection model based on the rapid growth of the instantaneous frequency. Experimental setup includes measurement of surface variations at 11 equally spaced wave staffs arranged in two parallel arrays and recording of breaking events by multiple video cameras. For every test, the time of each breaking wave was noted on the video record and corresponding wave gauge was notified where breaking occurred. The wave breaking detection model includes, as a first step, an elimination of extraneous large peaks in the frequency variation signal by removing the events associated with near-zero wave elevations as breaking never occur at these points. It was assumed that for $\zeta(t) < 1.5\sigma_\zeta \approx 0.38 H_{\mathrm{s}}$, the frequency variations are filtered out. This means that for surface elevation below threshold value of $0.38\,H_{\mathrm{s}}$ all frequency variations are set to zero. Inspection of the filtered record at each breaking event showed a consistent frequency variation pattern related to incipient breakers, namely a very high and sharp peak.

The important parameter for successful application of PTM is the sampling rate of the time series. The laboratory results as well as field data indicate that the method requires sampling the surface elevation at rates greater than typically employed. The best results are obtained at sampling rates of 25–50 times the peak frequency. Zimmermann and Seymour (2002) concluded that prediction of breaking in deep water by the PTM method is correct in about 95% of cases with false detection limited to about 5%.

Figure 4.17 illustrates a sharp increase in the instantaneous frequency for particularly steep waves which are very close to breaking. The dashed line denotes

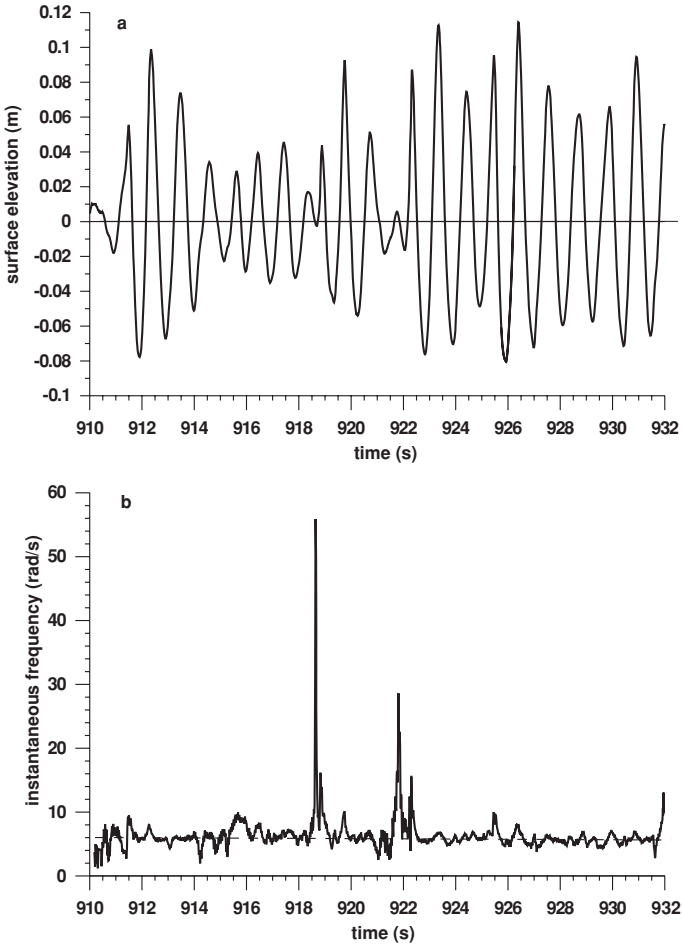

Figure 4.17: Part of a record of steep waves (a) and corresponding instantaneous frequency (b).

the wave-maker frequency. From the figure it follows that the highest departure of the frequency is not necessary related to the highest surface elevation, but rather with the highest slope.

Griffin et al. (1996) in their experiment found that the variation of the local frequency down the wave channel was nearly constant for steep but non-breaking waves, increasing slightly for spilling breakers and growing rapidly for fully plunging breakers. This conclusion is in contradiction with the results of Zimmermann and Seymour (2002). However, it should be noted that the experiment of Griffin et al. (1996) involved a coincident arrival of packets at one point in order to obtain breaking, whereas the experiments mentioned above are based on random waves which can break anywhere in the basin.

4.7 Summary of experimental data

4.7.1 Global breaking wave characteristics

Due to the complexity of the breaking process, robust and sufficiently precise threshold values determining the onset of breaking do not exist. However, the global as well as local wave breaking parameters are the most useful. In the previous sections it was shown that a wave approaching breaking point becomes highly asymmetric with an increasingly steeper crest front. Also, there are a number of investigations showing a wide range of critical wave heights at the onset of breaking (Ochi and Tsai, 1983; Bonmarin, 1989; Dawson et al., 1993). Schultz et al. (1987) and Ramberg and Griffin (1987) found that the global wave steepness at breaking is

$$\varepsilon_{\mathrm{g}} = \frac{H}{gT^2} = 0.021. \tag{4.54}$$

Tulin and Li (1992), reviewing the results of short wave tank experiments, confirmed that the average value of maximum wave steepness is 0.021, although the scatter in the data of these experiments was substantial. It should be noted that this value is smaller than the Stokes limiting steepness of 0.027. In Table 4.6 laboratory measurements of the limiting wave height H of paddle-generated deep water waves as a function of the gT^2 value are collected from the data of Bonmarin (1989) and Griffin et al. (1996). All experimental limiting wave heights are lower than that from the Stokes limit – see Fig. 4.18. The best fit to all data given in the figure provides the following value for limiting ε_{g}

$$\varepsilon_{\mathrm{g}} = \frac{H}{gT^2} = 0.019. \tag{4.55}$$

Table 4.6: Mean values of global limiting wave steepness $\varepsilon_{\mathrm{g}} = \frac{H}{gT^2}$ for paddle-generated waves.

	Legend	Breaker type	
Reference	for Fig. 4.18	Plunging	Spilling
Stokes (theoretical limits)		–	0.027
Ochi and Tsai (1983)	diamonds	0.020	–
Ramberg and Griffin (1987)	triangles	–	0.021 (1)
Bonmarin (1989)	half-solid squares	0.022 (2)	0.021 (4)
		0.020 (3)	0.020 (5)
Rapp and Melville (1990)	box area	–	0.017–0.21 (4)
Griffin et al. (1996)	box area	0.018-0.021(2)	0.017–0.018 (4)

The numbers in parentheses are defined as follow: 1 – spilling and slightly plunging, 2 – typical plunging, 3 – plunging, 4 – typical spilling, and 5 – spilling (adapted from Bonmarin, 1989 and Griffin et al., 1996).

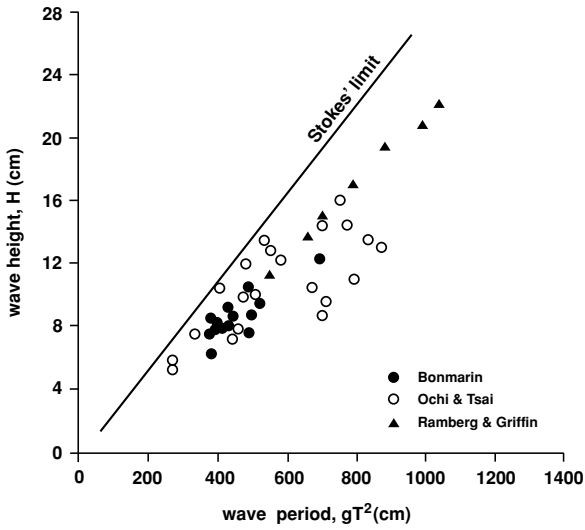

Figure 4.18: Global limiting wave height H of paddle-generated waves as a function of the period parameter gT^2 (adapted from Bonmarin, 1989 and Griffin et al., 1996).

The criterion resulting from the above experiments can be compared with Longuet–Higgins' (1985b) limiting wave steepness (see for example Table 5.1) $(ak)_{lim} = 0.4432$ what gives $\frac{H}{gT^2} = 0.022$ which is close to the estimates given in Table 4.6.

Moreover, the experimental data reported by Myrhaug and Kjeldsen (1986) indicate that wave front slope $\overline{\varepsilon}_{\rm f} \approx 0.26$. Therefore, approximately

$$\overline{\varepsilon}_{\rm f} = \frac{\zeta_{\rm c}}{C\,T'} \approx \frac{A_{br}}{C\,\frac{T}{4}} = \frac{4A}{CT}, \tag{4.56}$$

when the time $T^{'}$ was taken approximately as $\frac{T}{4}$. Thus

$$A = \frac{\overline{\varepsilon}_{\rm f}}{4}\,CT = \frac{\overline{\varepsilon}_{\rm f}\,gT^2}{8\pi} \approx 0.0103\,gT^2 \quad \text{and} \quad \frac{H}{gT^2} = 0.020, \tag{4.57}$$

which again is the same order as both above criteria.

The results of Xu et al. (1986) from wave channel experiments for wind-induced incipient breaking due to wind speed varying from 7 to 16 m/s are summarized in Fig. 4.19. The straight line corresponds to the best fit to the data and yields an identical expression as in (4.55). The scatter of the data about the line is about ±15%. Xu et al. found that the breaking probability, defined as the ratio between the number of breaking waves and the total number of waves recorded, increased rapidly with wind velocity as $\approx V_{10}^{2.2}$. The probability was defined as the mean passage rate past a fixed point of dominant wave breaking events per dominant wave period. The experimental results from the Black Sea

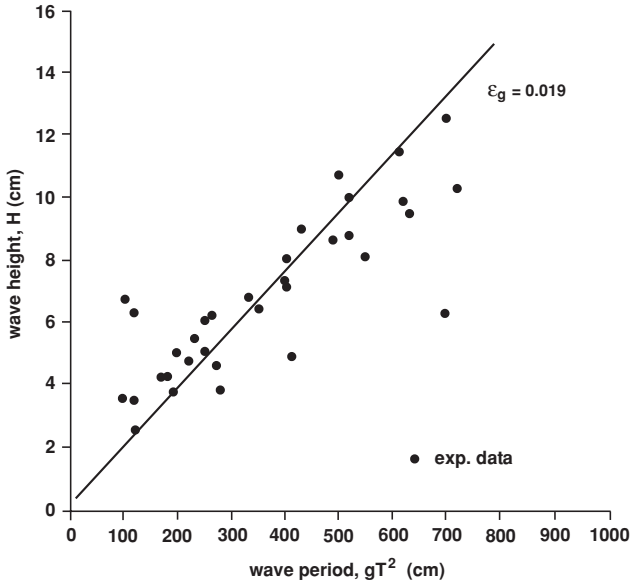

Figure 4.19: Global limiting wave height of wind-generated waves as a function of the period parameter gT^2 (adapted from Griffin et al., 1996).

Table 4.7: Local breaking threshold quantities based on numerical calculations

References	Threshold characteristics	Breaker type
Theory:2nd order Stokes wave	$\varepsilon_f = 0.28$; $\lambda_h = 0.50$	plunging
	$\lambda_v = 1.00$	plunging
Cokelet (1977)	$\varepsilon_f \geq 0.408$; $\lambda_h \geq 0.757$	plunging
Longuet–Higgins and Cokelet (1976)	$\lambda_v = 1.83$	plunging

Table 4.8: Local breaking threshold quantities based on field experiments

References	Threshold characteristics	Breaker type
Longuet–Higgins and Smith (1983)	surface inclination $\theta_{cr} \geq 30.37$	
Myrhaug and Kjeldsen (1986)	$0.2 < \varepsilon_f < 0.32$; $\overline{\varepsilon_f} = 0.26$	
	$1.0 < \lambda_v < 3.0$; $\overline{\lambda_v} \approx 0.65$	
Holthuijsen and Herbers (1986)	$0.0053 < \varepsilon_s < 0.0081$	
Kway et al. (1998)	$0.265 < \varepsilon_f < 0.304$	plunging
Gemmrich and Farmer (1999)	volumetric air fraction ≥ 0.08	

Table 4.9: Local breaking threshold quantities based on laboratory experiments

References	Threshold characteristics	Breaker type
Ochi and Tsai (1983)	$\varepsilon_{\mathrm{g}} = 0.020;\ 0.0039 < \varepsilon_{\mathrm{s}} < 0.00775$	plunging
Xu et al. (1986)	$\varepsilon_{\mathrm{g}} = 0.019$	spilling
Ramberg and Griffin (1987)	$\varepsilon_{\mathrm{g}} = 0.021$	spilling
Bonmarin (1989)	$0.65 < \lambda_{\mathrm{h}} < 0.93;\ \overline{\lambda}_{\mathrm{h}} = 0.77$	plunging
	$0.97 < \lambda_{\mathrm{v}} < 3.09;\ \overline{\lambda}_{\mathrm{v}} = 2.14$	plunging
	$0.31 < \varepsilon_{\mathrm{f}} < 0.85;\ \overline{\varepsilon}_{\mathrm{f}} = 0.61$	plunging
	$17.22^\circ < \theta_{\mathrm{f}} < 40.36^\circ$	plunging
	$0.60 < \lambda_{\mathrm{h}} < 0.80;\ \overline{\lambda}_{\mathrm{h}} = 0.69$	spilling
	$0.81 < \lambda_{\mathrm{v}} < 1.72;\ \overline{\lambda}_{\mathrm{v}} = 1.20$	spilling
	$0.31 < \varepsilon_{\mathrm{f}} < 0.51;\ \overline{\varepsilon}_{\mathrm{f}} = 0.38$	spilling
	$17.22^\circ < \theta_{\mathrm{f}} < 27.02^\circ$	spilling
Rapp and Melville (1990)	$0.017 < \varepsilon_{\mathrm{g}} < 0.021;\ k_{\mathrm{c}}D \approx 0.3$	spilling
	$0.2 \leq \varepsilon_{\mathrm{f}} \leq 1.0;$	spilling
	$k_cD \approx 0.5$	plunging
Kjeldsen (1990)	$0.9 < \lambda_{\mathrm{v}} < 2.2$	
Peltzer and Griffin (1992)	$\lambda_{\mathrm{h}} \approx 0.76\ \ \lambda_{\mathrm{v}} \approx 1.43$	
	$\varepsilon_{\mathrm{f}} \approx 0.50$	
Duncan et al. (1994a,b)	$\lambda_{\mathrm{v}} \approx 1.3$	spilling
	$\lambda_{\mathrm{v}} \approx 1.7$	plunging
	$0.72 < \lambda_{\mathrm{h}} < 0.80$	plunging
Griffin et al. (1996)	$0.018 < \varepsilon_{\mathrm{g}} < 0.021$	plunging
	$0.017 < \varepsilon_{\mathrm{g}} < 0.018$	spilling
	$\varepsilon_{\mathrm{f}} \approx 0.32;\ \lambda_{\mathrm{v}} \approx 1.0$	spilling
	$\varepsilon_{\mathrm{f}} \approx 0.62;\ 1.7 < \lambda_{\mathrm{v}} < 2.0$	plunging
Lader et al. (1998)	$\mathrm{cur}_{\max} = \left\lvert \frac{\partial^2 \zeta}{\partial x^2} \right\rvert \approx 10^{-1}$	spilling
	$\mathrm{cur}_{\max} = \left\lvert \frac{\partial^2 \zeta}{\partial x^2} \right\rvert \approx 20^{-1}$	plunging
	$a_z^{(E)} \approx 5g$	plunging
	$a_z^{(E)} \approx 6.6g$	intermediate
	$a_z^{(E)} \approx 2.7g$	spilling
Kway et al. (1998)	$k\zeta_{\mathrm{c}} \approx 0.4 - 0.6$	plunging
	$k\zeta_{\mathrm{c}} \approx 0.5$	spilling
Tulin and Waseda (1999)	$0.25 < \frac{H_m k}{2} < 0.35$	
	$0.05 < \frac{\delta\omega}{\omega} < 1.5$	
Massel et al. (2001)	$0.319 < \varepsilon_{\mathrm{f}}^{(max)} < 1.018;\ 0.097 < \overline{\varepsilon}_{\mathrm{f}} < 0.181$	spilling
	$3.733 < \lambda_{\mathrm{v}}^{(max)} < 8.500;\ 1.064 < \overline{\lambda}_{\mathrm{v}} < 1.235$	spilling
	$0.975 < \lambda_{h}^{(max)} < 0.999;\ 0.505 < \overline{\lambda}_{\mathrm{h}} < 0.561$	spilling
Bonmarin and Kjeldsen (2001)	$a_z^{(L)} \approx (1.5 - 2.2)g$	
	$\varepsilon_{\mathrm{f}} = 0.39;\ \lambda_{\mathrm{v}} = 1.20;\ \lambda_{\mathrm{h}} = 0.69$	fully spilling
	$\varepsilon_{\mathrm{f}} = 0.62;\ \lambda_{\mathrm{v}} = 2.13;\ \lambda_{\mathrm{h}} = 0.77$	fully plunging
Zimmermann and Seymour (2002)	$\omega_{\mathrm{l}} > \omega_{\mathrm{l}}^{(t)} \approx 0.85\omega_p$	

and Lake Washington (described in Section 4.3.2) showed that this breaking probability of dominant waves is well correlated with the steepness ε_{d}. The threshold value for ε_{d} around $0.055 - 0.06$ determines whether dominant wave breaking occurs or not. Up to the threshold value of $\varepsilon_{\mathrm{d}} = 0.055$, the probability of breaking is zero, but it increases quadratically for $\varepsilon_{\mathrm{d}} > 0.055$. This conclusion reflects the hypothesis that nonlinear hydrodynamic processes associated with wave groups are more important for the breaking process than wind speed or wave age (Banner et al., 2000). Moreover, Banner et al. (2002) confirmed that a similar threshold dependence in terms of an appropriate spectral parameter exists also for breaking probability of shorter wind waves of frequencies up to 2.48 times the spectral peak frequency. This correlation is characterized by robust threshold behaviour, similar to that existing for dominant waves. Thus also for high frequency waves, nonlinear wave hydrodynamics are more important than wind forcing for breaking wind waves.

4.7.2 Local breaking wave characteristics

To characterize the local behaviour of steep waves approaching breaking three main parameters have been suggested, namely crest front steepness ε_{f}, vertical asymmetry λ_{v} and horizontal asymmetry λ_{h}. Definitions of these quantities are given in (4.1), (4.2) and (4.3). Numerically and experimentally determined values of ε_{f}, λ_{v} and λ_{h} are summarized in Tables 4.7, 4.8 and 4.9.

The largest scatter is observed for the λ_{v} value, particularly for the plunging breaker, and the most stable behaviour is exhibited by the horizontal asymmetry λ_{h}. The crest front angle θ_{f} for a plunging breaker varies from 17.22° to 40.36° with mean value close to the Stokes angle 30°. However, for spilling breakers this angle is smaller than 30°, and varies from 17.22° to 27.02°.

Chapter 5

Wave breaking criteria and probability of breaking

5.1 Introduction

Breaking waves are usually associated with steep waves that occur in a given sea. Several criteria have been proposed for the detection of wave breaking events in the past with somewhat arbitrary thresholds. In general they can be divided into two classes, the first related to some characteristics of the surface elevation at a point, and the second to observations of air entrainment, whitecaps or ambient noise. The first set of simple criteria of the limiting form of wave motion was established by Stokes more than one hundred years ago (Stokes 1847, 1880). According to Stokes, the necessary criteria to start an individual wave breaking are:

(a) the particle velocity of fluid at the wave crest equals the phase velocity,
(b) the crest of the wave attains a sharp point with an angle of 120°,
(c) the ratio of wave height to wavelength is approximately 1/7,
(d) particle acceleration at the crest of the wave equals to $0.5\,g$.

The above criteria for breaking of regular waves in deep water have been addressed from various viewpoints in a series of papers by Longuet–Higgins (1969, 1976), Cokelet (1977) and others. A wave-breaking criterion based on crest-to-trough wave height was examined by Melville and Rapp (1988), Ochi and Tsai (1983), Huang et al. (1992), Xu et al. (1986), Bonmarin (1989), Dawson et al. (1993) and Griffin et al. (1996). Some of them questioned this criterion, in part because peak-to-peak wave heights vary significantly during breaking. However, probably no breaking criterion can be simple and precise.

In the previous chapter, a large variety of numerical calculations as well as field and laboratory experiments on the evolution and breaking of waves were

presented. They offer selected wave field characteristics, the threshold of which can serve as local indicators of wave breaking. All of these values have been collected in Tables 4.7–4.9. The tables indicate clearly that our present knowledge on the wave breaking phenomenon is based mostly on experimental insights and some threshold quantities have at present only theoretical value. They significantly expand our knowledge of the problem; however, some of them are not suitable for practical use, as they need many non-measurable factors for their determination.

In this chapter, the probability of breaking, F_{br}, appearing at a given point is discussed. When the surface of breaking waves passes a fixed point with varying speed, the probability of breaking will change, even for a two-dimensional stationary and homogeneous wave field. Therefore, there is a need for conversion of the temporal fraction of the breaking surface to the spatial one. Usually this conversion is based on linear wave theory. This theory provides some convenient measures of incipient wave breaking such as kinematic, geometric and dynamic criteria of wave breaking. In particular, a wave starts to break when the horizontal fluid velocity at the surface u exceeds the phase velocity C (kinematic criterion). In terms of the kinematic criterion, this position represents the stagnation point of the streamlines of fluid particles relative to the waves form. Downstream from this point, fluid particles tend to escape from the water surface. They can either be ejected into air to become droplets or curl down to trap air into water. Such events are associated with exchanges of mass, momentum and energy across the air–water interface. It should be noted that during breaking, the wave steepness ak, usually becomes $\mathcal{O}(1)$ and $\frac{u}{C} > 1$. Therefore, wave breaking should be considered as a strongly nonlinear process. It should be noted that detailed velocity measurements at the crest are quite limited in number and are difficult to obtain as well (Melville and Rapp, 1988; Kjeldsen, 1990; Stansell and MacFarlane, 2002).

In limiting regular waves, the crest attains a sharp point with an angle of 120° and the particle acceleration at the crest is equal to $0.5\,g$. However, near-limiting waves have rounded crests with a very small radius of curvature. It was shown (Longuet–Higgins and Fox, 1977) that the local crest profile of such waves approaches a self-similar form and the maximum surface slope can exceed the 30° slope of the limiting wave, ultimately reaching a value of about 30.37°, when the vertical acceleration at the crest is not $0.5\,g$. It should be pointed out there are two different vertical accelerations depending on the measurement procedure, i.e. the *apparent* acceleration measured by a fixed vertical probe, and the *real* acceleration of the fluid particles, as measured by a small, free-floating buoy following the sea surface (Longuet–Higgins, 1985b).

For irregular waves we apply the Snyder and Kennedy (1983) hypothesis, which states that the stability of the gravity wave flow is controlled by the level of some 'threshold' variable defined on the surface of the fluid. This 'threshold variable' is the vertical acceleration. The threshold acceleration criterion is applied at the wave crest for the one-dimensional case and everywhere on the sea surface for the two-dimensional case. In fact, Longuet–Higgins (1985b) and

Srokosz (1986) suggested to use the wave crest acceleration as global breaking criteria. Moreover, Schultz et al. (1994) proposed a simple potential energy criterion, although experimentally or computationally this criterion is a function of many parameters.

5.2 Limiting wave steepness criterion

5.2.1 Global and local limiting wave steepness

Breaking criteria based on global or local wave steepness seem to be very logical and appropriate for such phenomena as sea surface wave motion. As was shown in Chapter 4, wave steepness can be expressed in terms of global or local wave parameters. Global steepness usually involves characteristic wave height and wavelength, while local steepness depends on the spatial (time) derivative of the sea surface ordinates. In oceanology practice, breaking criteria are usually expressed in terms of global wave steepness when a crest-to-preceding-trough value for wave height is used. On the other hand, studies on the local wave steepness threshold indicate that this approach is not robust when applied to the onset of wave breaking at sea when the separation between breaking and non-breaking is not sharp, but rather diffuse. For an irregular wave field, the most complete representation of breaking criteria, based on limiting wave steepness, is that in the form of the probability density. It is our aim to use this methodology for global as well as for local criteria.

5.2.2 Probability of wave breaking based on the global limiting wave steepness criterion

Under the assumption that low steepness swell waves have little effect on the dynamics of breaking of dominant local wind waves, so-called dominant steepness ε_{d} was defined by (4.9) in the form

$$\varepsilon_{\mathrm{d}} = \frac{1}{2} H_{\mathrm{d}} k_{\mathrm{p}}, \tag{5.1}$$

where

$$H_{\mathrm{d}} = 4\left\{ \int_{0.7\omega_{\mathrm{p}}}^{1.3\omega_{\mathrm{p}}} S(\omega) d\omega \right\}^{\frac{1}{2}}, \tag{5.2}$$

in which ω_{p} is the peak frequency. In order to determine wave height H_{d}, the integral in (5.2) should be calculated from a known spectral density $S(\omega)$. If we use the JONSWAP spectrum (3.19), from (5.2) we obtain

$$H_{\mathrm{d}} = \frac{4g}{\omega_{\mathrm{p}}^2} \sqrt{\beta} \sqrt{I_{\mathrm{d}}}, \tag{5.3}$$

in which

$$I_{\mathrm{d}} = \int_{0.7}^{1.3} \hat{\omega}^{-5} \exp\left(-\frac{5}{4}\hat{\omega}^{-4}\right) \gamma^{r} d\hat{\omega}. \tag{5.4}$$

For typical peak enhancement factors the integral I_{d} is

$$I_{\mathrm{d}} = \begin{cases} 0.1280 & \text{for } \gamma = 1.0 \\ 0.2330 & \text{for } \gamma = 3.3 \\ 0.3730 & \text{for } \gamma = 7.0 \end{cases} \tag{5.5}$$

Therefore, the dominant steepness ε_{d} becomes

$$\varepsilon_{\mathrm{d}} = \frac{2g}{\omega_{\mathrm{p}}^2}\sqrt{\beta I_{\mathrm{d}}}k_{\mathrm{p}} = 2\sqrt{\beta I_{\mathrm{d}}}, \tag{5.6}$$

where

$$k_{\mathrm{p}} = \frac{\omega_{\mathrm{p}}^2}{g}. \tag{5.7}$$

Using (3.22), the steepness ε_{d} can now be rewritten in the form

$$\varepsilon_{\mathrm{d}} = a_{\gamma}\left(\frac{gX}{V_{10}^2}\right)^{-0.11}, \tag{5.8}$$

where

$$a_{\gamma} = \begin{cases} 0.1973 & \text{for } \gamma = 1.0 \\ 0.2661 & \text{for } \gamma = 3.3 \\ 0.3367 & \text{for } \gamma = 7.0 \end{cases} \tag{5.9}$$

Parameter ε_{d} reflects not only the mean steepness of dominant waves, but also the fundamental role of nonlinear group dynamics in determining breaking onset. In particular, wave breaking appears when (Banner et al., 2000)

$$\varepsilon_{\mathrm{d}} \geq 0.055, \tag{5.10}$$

or

$$\varepsilon_{\mathrm{d}} = a_{\gamma}\left(\frac{gX}{V_{10}^2}\right)^{-0.11} \geq 0.055. \tag{5.11}$$

Hence, the probability of breaking for the wave field modelled by the JONSWAP spectrum is non-zero when

$$\frac{gX}{V_{10}^2} \leq \begin{cases} 1.1 \times 10^5 & \text{for} \quad \gamma = 1.0 \\ 1.7 \times 10^6 & \text{for} \quad \gamma = 3.3 \\ 1.4 \times 10^7 & \text{for} \quad \gamma = 7.0 \end{cases} \tag{5.12}$$

The breaking probability F_{br} for dominant waves is defined as the mean passage rate past a fixed point of dominant wave breaking events per dominant wave period. As dominant waves are taken within the spectral band of $0.7\,\omega_{\mathrm{p}}$ to

$1.3\,\omega_{\mathrm{p}}$, they contain the spectral components determining the group structure of the dominant wave field. Large values of ε_{d} can be reached for restricted fetch when wind velocity is relatively small. Such a situation is usually reproduced in wave tank experiments. In field conditions, fetches and wind velocity are larger than in laboratory experiments, and the resulting limiting dominant wave steepness ε_{d} is smaller. It should be noted that the threshold (5.11) is not a criterion for breaking of individual waves, but it represents an average wave field parameter for determination of the mean fraction of breaking waves in the appropriate frequency band.

Additionally, Banner et al. (2000) showed that the probability of breaking of dominant waves increases close to quadratically for $\varepsilon_{\mathrm{d}} > 0.055$ when

$$F_{\mathrm{br}} = a\,(\varepsilon_{\mathrm{d}} - 0.055)^b, \tag{5.13}$$

in which a is in the range $(13.0 \div 37.2)$, with mean value of 22.0 and b is in the range $(1.78 \div 2.30)$, with mean value of 2.01.

5.2.3 Probability of wave breaking based on the local limiting wave steepness criterion

The slope criterion of wave breaking requires that the surface wave will break when the local surface slope in the n-direction exceeds the threshold slope $\varepsilon_{\mathrm{th}}$, i.e.

$$\frac{\partial \zeta}{\partial n} \geq \varepsilon_{\mathrm{th}}. \tag{5.14}$$

Longuet–Higgins and Fox (1977) showed that $\varepsilon_{\mathrm{th}} = 0.586$ and the critical local angle θ of the sea surface with the horizontal plane is $\theta = 30.37^{\circ}$. Hence the probability of breaking waves propagating in n-direction becomes

$$F_{\mathrm{br}} = \int_{\varepsilon_{\mathrm{th}}}^{\infty} f(\varepsilon_{\mathrm{l}})\, d\varepsilon_{\mathrm{l}}. \tag{5.15}$$

Let us consider first the case of laboratory waves generated in the wave channel when all spectral components propagate along the x-axis (long-crested waves case). Then the probability density $f(\xi)$ for non-dimensional slope $\xi = \frac{g\varepsilon_{\mathrm{l}}}{\sqrt{m_4}}$ is given by (3.131). After substituting this equation into (5.15) and integrating, we obtain

$$F_{\mathrm{br}} = 2Q(\xi_{\mathrm{th}}), \tag{5.16}$$

where $\xi_{\mathrm{th}} = \frac{\varepsilon_{\mathrm{th}}}{\sqrt{\tilde{m}_4}} = \frac{g\varepsilon_{\mathrm{th}}}{\sqrt{m_4}}$ and $Q(\xi_{\mathrm{th}})$ is given by (Abramowitz and Stegun, 1975)

$$Q(x) = \frac{1}{\sqrt{2\pi}} \int_x^{\infty} e^{-\frac{t^2}{2}}\, dt = 1 - \Phi(x), \tag{5.17}$$

in which $\Phi(x)$ is given by (3.88). Therefore, we have

$$F_{\mathrm{br}} = 2Q(\xi_{\mathrm{th}}) = 2\left[1 - \Phi(\xi_{\mathrm{th}})\right]. \tag{5.18}$$

The limiting crest front steepness ε_{f} can serves as a good approximation of the real limiting steepness $\varepsilon_{\mathrm{th}}$. As was shown in Chapter 4, the crest front limiting steepness in laboratory tests varied in the range of $0.31 < \varepsilon_{\mathrm{f}} < 0.51$ (with a mean value of $\overline{\varepsilon}_{\mathrm{f}} = 0.38$) for spilling breakers, and in the range of $0.31 < \varepsilon_{\mathrm{f}} < 0.85$ (with a mean value of $\overline{\varepsilon}_{\mathrm{f}} = 0.61$) for plunging breakers. Thus, let us assume that

$$\xi_{\mathrm{th}} = \begin{cases} \dfrac{0.38}{\sqrt{\tilde{m}_4}} & \text{for spilling breakers} \\ \dfrac{0.61}{\sqrt{\tilde{m}_4}} & \text{for plunging breakers} \end{cases} \tag{5.19}$$

In Fig. 5.1 the probability F_{br} is shown as a function of normalized spectral moment $\tilde{m}_4$ for long-crested spilling and plunging breakers, when threshold steepness $\overline{\varepsilon}_{\mathrm{f}} = 0.38$ and $\overline{\varepsilon}_{\mathrm{f}} = 0.61$ are used, respectively. From the figure it follows that at the same wave intensity, expressed by the moment $\tilde{m}_4$, the probability of spilling breakers is higher than the probability of plunging breakers. This is a consequence of the higher threshold of the limiting steepness for plunging breakers. In Fig. 5.2, the influence of the limiting steepness of long-crested spilling breakers on the probability of breaking is shown. The lower and

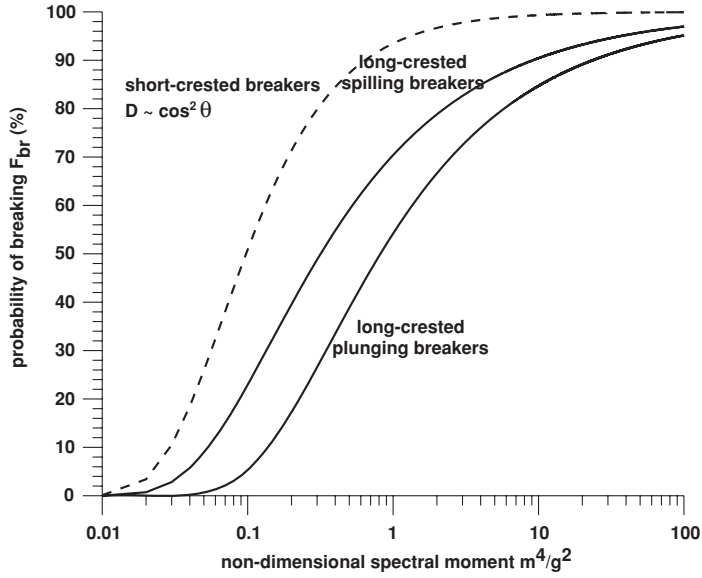

Figure 5.1: Probability of breaking as a function of normalized spectral moment $\tilde{m}_4 = \frac{m_4}{g^2}$ for long-crested spilling and plunging breakers (solid lines). Dashed line – short-crested waves.

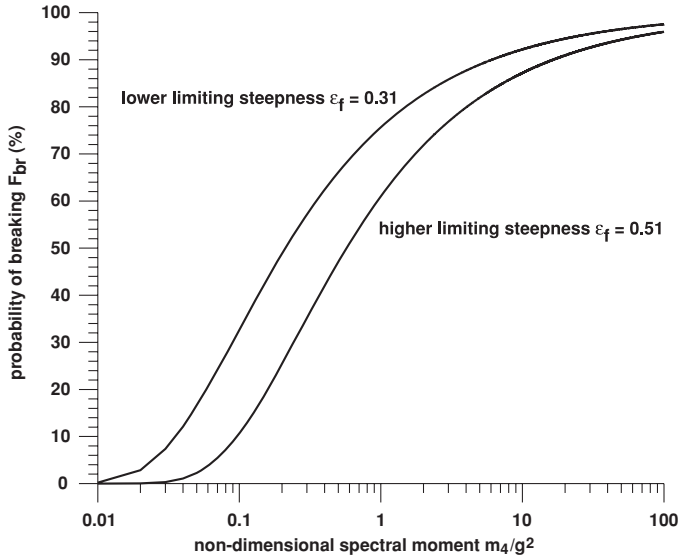

Figure 5.2: Probability of breaking of long-crested spilling breakers as a function of normalized spectral moment $\tilde{m}_4 = \frac{m_4}{g^2}$ for two limiting steepnesses.

higher limiting wave steepnesses $\varepsilon_{\rm f}$, obtained in laboratory tests, i.e. $\varepsilon_{\rm f} = 0.31$ and $\varepsilon_{\rm f} = 0.51$, have been used in this figure.

To describe the probability of breaking of short-crested ocean waves we use the standard directionality function $D(\Theta) = \frac{2}{\pi}\cos^2\Theta$, when the integrals $I_{\rm c} = I_{\rm s} = \frac{1}{2}$ and the probability density function $f(\xi)$ is given by (3.127). After substituting this equation into (5.15) and integrating we obtain

$$F_{\rm br} = \exp\left(-\xi_{\rm th}^2\right) = \exp\left(-\frac{\varepsilon_{\rm th}^2}{\tilde{m}_4}\right). \tag{5.20}$$

The function (5.20) is also shown in Fig. 5.1 for $\overline{\varepsilon}_{\rm f} = 0.26$ (see Table 4.8), indicating that probability of breaking of short-crested waves becomes higher than for long-crested waves for the same wave field intensity.

To express the formulae (5.18) and (5.20) in terms of spectral density, we assume that surface waves are characterized by the JONSWAP spectrum (3.19) and its moments. Let us first discuss the case of wind blowing along a narrow sea basin when the waves can be considered long-crested. Using the relationship (D.7) for $\gamma = 3.3$, we get probability of breaking given by (5.18), where

$$\xi_{\rm th} = 2.778\varepsilon_{\rm th}\left(\frac{gX}{V_{10}^2}\right)^{0.11} \tag{5.21}$$

Probability of breaking (5.18) is shown in Fig. 5.3 versus non-dimensional fetch $\left(\frac{gX}{V_{10}^2}\right)$ for threshold steepness equal to $\varepsilon_{\rm th} = \overline{\varepsilon}_{\rm f} = 0.38$ for spilling breakers.

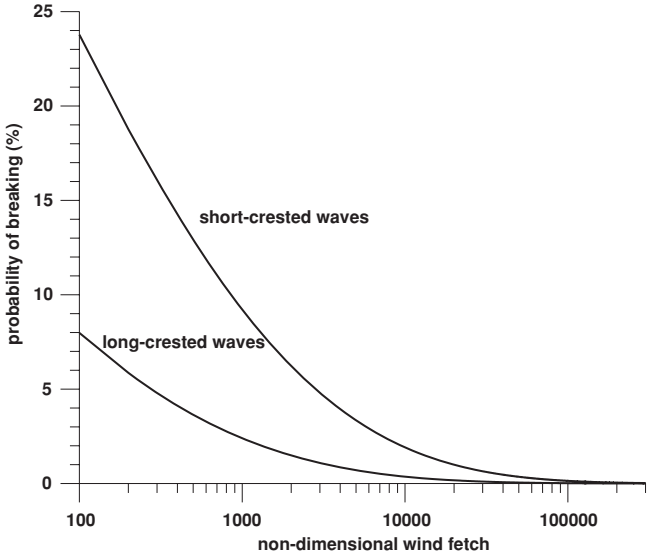

Figure 5.3: Probability of breaking as a function of non-dimensional wind fetch for long- and short-crested waves.

In a similar way, after substituting (D.7) into (5.20) we get the probability of breaking for short-crested waves, when $D(\Theta) = \frac{2}{\pi}\cos^2\Theta$, in the form

$$F_{\mathrm{br}} = \exp\left[-7.714\varepsilon_{\mathrm{th}}^2\left(\frac{gX}{V_{10}^2}\right)^{0.22}\right]. \tag{5.22}$$

Function (5.22) is added in Fig. 5.3 for $\varepsilon_{\mathrm{th}} = \overline{\varepsilon}_{\mathrm{f}} = 0.26$.

5.3 Limiting vertical acceleration criterion

5.3.1 Definition of particle accelerations in the wave field

Before carrying out a discussion on the vertical acceleration criterion, a distinction should be made between two vertical accelerations of water particles (Longuet–Higgins, 1985b, 1986). The first one is known as the apparent (or Eulerian) vertical acceleration and it is related to recording of the water surface oscillations by a fixed vertical probe

$$a_z^{(E)} = \frac{\partial^2\zeta(x,t)}{\partial t^2} = \frac{\partial w(x,\zeta,t)}{\partial t}, \tag{5.23}$$

in which $\zeta(x,t)$ is the surface wave profile and w is the vertical component of velocity. The above equation shows that the acceleration is a measure of the curvature of the free surface.

On the other hand, the real (or Lagrangian) acceleration is measured ideally by a small, free-floating buoy. In particular, for plane waves propagating in x

direction we obtain:

$$a_z^{(L)}(x,\zeta,t) = \frac{Dw}{Dt} = \frac{\partial w}{\partial t} + u\frac{\partial w}{\partial x} + w\frac{\partial w}{\partial z} = \frac{\partial w}{\partial t} + u\frac{\partial u}{\partial z} - w\frac{\partial u}{\partial x} \text{ at } z = \zeta, \quad (5.24)$$

where horizontal and vertical velocity components u and w are given at the sea surface. In the linearized theory both acceleration definitions are equal, but in steep waves of finite amplitude they are different.

5.3.2 Limiting vertical acceleration for regular waves

5.3.2.1 Fenton's fifth-order Stokes theory

We consider now the accelerations for purely theoretical wave profiles resulting from two theoretical solutions. The first result follows from the Stokes expansion method. So, let us assume that a regular, plane wave is propagating over constant water depth in x-direction. The corresponding velocity potential $\Phi(x,z,t)$ of the fifth-order takes the form (Fenton, 1985)

$$\Phi(x,z,t) = C_0\left(\frac{g}{k^3}\right)^{1/2}\sum_{i=1}^{5}\varepsilon^i\sum_{j=1}^{i}A_{ij}\,\cosh[jk(z+h)]\,\sin[j(kx-\omega t)], \quad (5.25)$$

in which the dimensionless wave amplitude $\varepsilon = k\left(\frac{H}{2}\right)$, ω is the wave frequency and h is the water depth. The coefficients A_{ij}, and C_0 can be found in Fenton (1985).

From potential $\Phi(x,z,t)$, the following formulae for wave parameters result:

– surface elevation

$$\begin{aligned}\zeta(x,t) \;=\; & \frac{1}{k}\Big\{\varepsilon\cos\psi + \varepsilon^2 B_{22}\cos 2\psi + \varepsilon^3 B_{31}(\cos\psi - \cos 3\psi)\\ & +\varepsilon^4(B_{42}\cos 2\psi + B_{44}\cos 4\psi) + \varepsilon^5[-(B_{53}+B_{55})\cos\psi\\ & + B_{53}\cos 3\psi + B_{55}\cos 5\psi]\Big\} + 0(\varepsilon^6), \end{aligned} \quad (5.26)$$

in which coefficients B_{ij} are also given by Fenton (1985).

– horizontal velocity component

$$u(x,z,t) = C_0\left(\frac{g}{k^3}\right)^{1/2}\sum_{i=1}^{5}\sum_{j=1}^{i}A_{ij}\,\varepsilon^i\,jk\cosh[jk(z+h)]\cos(j\psi) \quad (5.27)$$

– vertical velocity component

$$w(x,z,t) = C_0\left(\frac{g}{k^3}\right)^{1/2}\sum_{i=1}^{5}\sum_{j=1}^{i}A_{ij}\,\varepsilon^i\,jk\sinh[jk(z+h)]\sin(j\psi), \quad (5.28)$$

where

$$\psi = kx - \omega t. \quad (5.29)$$

The wave number k is given by the formula

$$-\frac{2\pi}{T\sqrt{gk}} + C_0(kh) + \varepsilon^2 C_2(kh) + \varepsilon^4 C_4(kh) = 0. \quad (5.30)$$

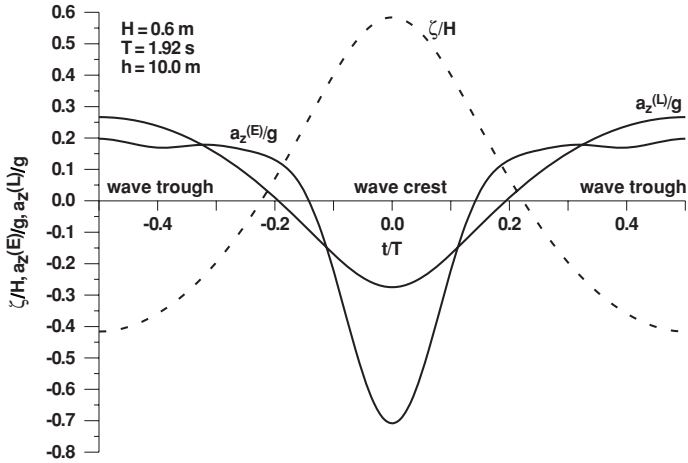

Figure 5.4: Surface elevation, Eulerian and Lagrangian accelerations for regular waves.

For deep water, (5.25)–(5.28) simplify considerably and in particular for the velocity potential we obtain

$$\Phi(x,z,t) = \left(\frac{g}{k^3}\right)^{1/2} \sum_{i=1}^{5} \varepsilon^i \sum_{j=1}^{i} A_{ij}^{(d)} \exp(jkz) \sin[j(kx-\omega t)]. \tag{5.31}$$

Now the coefficients $A_{ij}^{(d)}$ are not functions of (kh) but constants – see Fenton (1985).

In particular for surface elevation we have

$$\begin{aligned} \zeta(x,t) &= \frac{1}{k}\left\{\varepsilon\cos\psi + \frac{1}{2}\varepsilon^2\cos 2\psi + \frac{3}{8}\varepsilon^3(\cos 3\psi - \cos\psi)\right. \\ &\quad + \frac{1}{3}\varepsilon^4(\cos 2\psi + \cos 4\psi) \\ &\quad \left. + \frac{1}{384}\varepsilon^5(-422\cos\psi + 297\cos 3\psi + 125\cos 5\psi)\right\}. \end{aligned} \tag{5.32}$$

From (5.31) we obtain two components of velocity as follows

$$u(x,z,t) = \left(\frac{g}{k^3}\right)^{1/2} \sum_{i=1}^{5} \varepsilon^i \sum_{j=1}^{i} (jk)\, A_{ij}^{(d)} \exp(jkz) \cos[j(kx-\omega t)], \tag{5.33}$$

$$w(x,z,t) = \left(\frac{g}{k^3}\right)^{1/2} \sum_{i=1}^{5} \varepsilon^i \sum_{j=1}^{i} (jk)\, A_{ij}^{(d)} \exp(jkz) \sin[j(kx-\omega t)]. \tag{5.34}$$

After substitution of all required functions into (5.23) and (5.24), we are able to determine the accelerations $a_z^{(E)}$ and $a_z^{(L)}$. In Fig. 5.4, the apparent $a_z^{(E)}$ and real $a_z^{(L)}$ accelerations at the wave surface are compared for a regular wave

of height $H = 0.6$ m and period $T = 1.92$ s propagating in water of depth $h = 10.0\,\mathrm{m}$. From (5.30), wavelength becomes equal to $L = 6.3\,\mathrm{m}$. Therefore, we have $\frac{L}{h} = 0.63$ (almost deep water wave) and $\varepsilon = k\frac{H}{2} = 0.30$. It should be noted that minimum apparent acceleration at the wave crest is much lower than minimum real acceleration, namely $a_z^{(E)}/g = -0.708$ and $a_z^{(L)}/g = -0.275$, respectively. On the other hand, the positive accelerations change only slightly for points lying in the wave trough. It should also be noted that both accelerations are symmetric against the wave crest profile, which should be expected for a symmetric wave profile.

5.3.2.2 Longuet–Higgins' solution for steep waves

The second method results from the parametric equations for a free surface written by Longuet–Higgins (1985a) in the form

$$\left.\begin{aligned} k\zeta &= \tfrac{1}{2}a_0 + \sum_n^\infty a_n \cos(n\,\theta) \\ kx &= \theta + \sum_n^\infty a_n \mathit{sin}(n\,\theta) \end{aligned}\right\}, \tag{5.35}$$

where $\theta = k\Phi/C$.

In contrast to standard methods, when the coefficients a_n are expanded in powers of a small parameter being a measure of wave steepness ε, Longuet–Higgins showed that it is much simpler to determine coefficients a_n by direct solution of the quadratic relations between the Fourier coefficients as

$$\left.\begin{aligned} a_0 + a_1\,a_1 + 2a_2\,a_2 + 3a_3\,a_3 + \cdot\cdot &= -C^2 \\ a_1 + a_0\,a_1 + 2a_1\,a_2 + 3a_2\,a_3 + \cdot\cdot &= 0 \\ a_2 + a_1\,a_1 + 2a_0\,a_2 + 3a_1\,a_3 + \cdot\cdot &= 0 \\ a_3 + a_2\,a_1 + 2a_1\,a_2 + 3a_0\,a_3 + \cdot\cdot &= 0 \end{aligned}\right\}, \tag{5.36}$$

According to Longuet–Higgins (1985a), to find numerical solution to equation (5.36) it is convenient to manipulate the first of above equations, the only one containing C^2, and then use Newton's method of approximation. After calculating the coefficients a_n, all wave parameters can be given. In particular, the minimum values of apparent and real accelerations for the case shown in Fig. 5.4 equal $a_z^{(E)}/g = -0.779$ and $a_z^{(L)}/g = -0.278$, which are very close to the fifth-order Stokes solution.

5.3.2.3 Relationship between Eulerian and Langrangian acceleration

As follows from (5.23), the Eulerian acceleration can be easily determined by twice differentiating in time the sea surface ordinate. On the other hand, determination of the Lagrangian acceleration requires full knowledge not only of the surface elevation but also both components of orbital velocities. Therefore for practical prediction of the true Lagrangian acceleration it will be useful to

Table 5.1: Maximum (at wave trough) and minimum (at wave crest) values of non-dimensional apparent (Eulerian) acceleration $a_z^{(E)}/g$

		Maximum		Minimum	
$\frac{H}{gT^2}$	$\varepsilon = ak$	accor. Stokes V	accor. Longuet–Higgins (1985b)	accor. Stokes V	accor. Longuet–Higgins (1985b)
0.0051	0.1	0.0830	0.0833	−0.1244	−0.1251
0.0105	0.2	0.1430	0.1420	−0.3303	−0.3357
0.0166	0.3	0.1977	0.1831	−0.7082	−0.7795
0.0200	0.35	0.2338	0.1971	−1.0127	−1.2814
0.0237	0.40	0.2860	0.2050	−1.4304	−2.6753
0.0268	0.4432	0.3464	0.2032	−1.8660	$-\infty$

examine the relationships of both accelerations. To establish these relationships we use the data published by Longuet–Higgins (1985b), as well as the formulae resulting from the fifth-order Stokes expansion.

We are mostly interested here in the almost-highest waves. According to Cokelet (1977) and Williams (1981), the highest wave in deep water has steepness $\varepsilon = k\frac{H}{2} = 0.4432$. Longuet–Higgins and Fox (1977) showed that in this case, the minimum real acceleration of a particle at the crest equals $-0.388g$, while the maximum real acceleration (at wave trough) becomes $+0.3011g$.

In Tables 5.1 and 5.2, the comparison of maximum and minimum values of the apparent and real accelerations, calculated from fifth-order Stokes approximation and by Longuet–Higgins (1985b) method, is shown. It is interesting to note that a better agreement between both approaches exists for real

Table 5.2: Maximum (at wave trough) and minimum (at wave crest) values of non-dimensional real (Lagrangian) acceleration $a_z^{(L)}/g$

		Maximum		Minimum	
$\frac{H}{gT^2}$	$\varepsilon = ak$	accor. Stokes V	accor. Longuet–Higgins (1985b)	accor. Stokes V	accor. Longuet–Higgins (1985b)
0.0051	0.1	0.0986	0.0989	−0.0988	−0.0991
0.0105	0.2	0.1903	0.1908	−0.1923	−0.1931
0.0166	0.3	0.2664	0.2662	−0.2748	−0.2784
0.0200	0.35	0.2944	0.2930	−0.3057	−0.3175
0.0237	0.40	0.3128	0.3073	−0.3183	−0.3548
0.0268	0.4432	0.3188	0.3011	−0.2976	−0.388

Table 5.3: Ratio of the minimum (at wave crest) values of real and apparent accelerations $\left(\frac{a_z^{(L)}}{a_z^{(E)}}\right)_{\min}$

		$\left(\frac{a_z^{(L)}}{a_z^{(E)}}\right)_{\min}$	
$\frac{H}{gT^2}$	$\varepsilon = ak$	accor. Stokes V	accor. Longuet–Higgins (1985b)
0.0051	0.1	0.7942	0.7922
0.0105	0.2	0.5822	0.5752
0.0166	0.3	0.3880	0.3571
0.0200	0.35	0.3019	0.2478
0.0237	0.40	0.2225	0.1326
0.0268	0.4432	0.1595	0.0000

acceleration, maybe except for the almost-highest waves. For the apparent acceleration, differences between the two solutions are greater, again especially for very steep waves. The above discrepancies for very steep waves result from the fact that the accuracy of fifth-order Stokes wave theory is insufficient to reproduce properly the kinematics and dynamics of the flow close to the wave crest of the highest waves.

In Tables 5.3 and 5.4, the ratios $\left(\frac{a_z^{(L)}}{a_z^{(E)}}\right)_{\min}$ at the wave crest and $\left(\frac{a_z^{(L)}}{a_z^{(E)}}\right)_{\max}$ at the wave trough, resulting from the fifth-order Stokes approximation and Longuet–Higgins' (1985b) methods are shown. For the minimum acceleration, at the wave crest, both methods provide very similar results except for the steepest waves. The Longuet–Higgins method yields infinite value of the apparent acceleration and the ratio $\left(\frac{a_z^{(L)}}{a_z^{(E)}}\right)_{\min}$ is equal to 0. For maximum accelerations at the wave trough, there is a substantial difference between predictions resulting from the Stokes fifth-order approximation and Longuet–Higgins's

Table 5.4: Ratio of the maximum (at wave trough) values of real and apparent accelerations $\left(\frac{a_z^{(L)}}{a_z^{(E)}}\right)_{\max}$

		$\left(\frac{a_z^{(L)}}{a_z^{(E)}}\right)_{\max}$	
$\frac{H}{gT^2}$	$\varepsilon = ak$	accor. Stokes V	accor. Longuet–Higgins (1985b)
0.0051	0.1	1.1879	1.1873
0.0105	0.2	1.3307	1.3437
0.0166	0.3	1.3475	1.4538
0.0200	0.35	1.2592	1.4865
0.0237	0.40	1.0937	1.4990
0.0268	0.4432	0.9203	1.4818

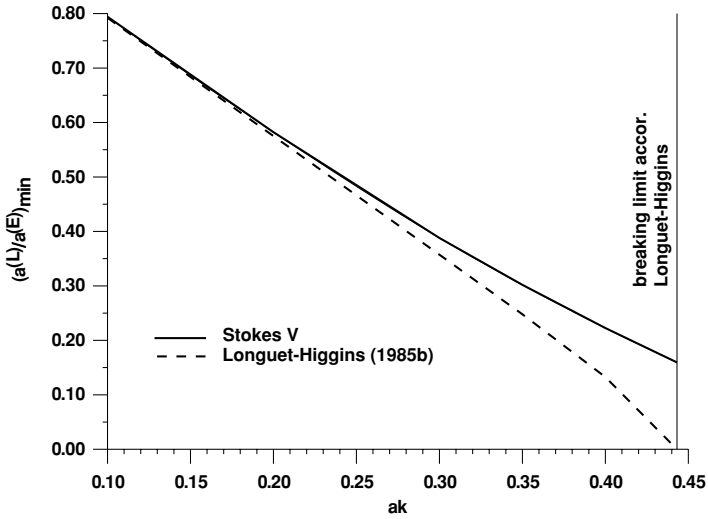

Figure 5.5: Ratio of real and apparent minimum accelerations at the wave crest in terms of ak.

approach. The ratios are also illustrated in Figs. 5.5 and 5.6. These figures have some practical value as they provide a way to calculate the real acceleration at the wave crest and wave trough using a known value of the apparent acceleration which is easy to obtain from double time differentiation of the surface ordinates.

5.3.3 Limiting vertical acceleration for irregular waves

5.3.3.1 Experimental data on Lagrangian acceleration

Experimental data on true Langrangian acceleration are very rare. In one such experiment, Kjeldsen (1990) used a special wave-follower system consisting of a carriage perfectly synchronised with the wave, which kept a current meter submerged in the crest while the wave propagated over a distance of 15–20 m, becoming more asymmetric and finally breaking as a plunging breaker. Altogether 225 experimental runs were performed. Moreover, a Lagrangian technique has been used to simulate wave crest kinematics at the free steep wave surface. This technique took advantage of the Hilbert transform approach (see Appendix C) and showed reasonable agreement with the observations.

Bonmarin and Kjeldsen (2001) reported results of measurements of acceleration on the surface of a plunging crest using small floating tracers. Acceleration up to $-1.5g$ was measured when the plunging crest met the floating tracer, and maximum acceleration of the order of $-2.2g$ was measured in the overturning region. Due to the finite size of the tracers the true acceleration of the fluid particles will probably be slightly higher.

5.3.3.2 Best fit of the fifth-order Stokes profile to the experimental profile

For a wave profile which is not very different from a regular one, all wave parameters can be determined through the best fitting selected theoretical profile to the initial one. We illustrate this approach for the almost regular wave profile obtained in the experiment carried out in the Ocean Basin Experiment (see Section 4.4.3). In the experiment the mechanically generated regular waves were periodic; however, their profile was not exactly regular for many reasons. In particular, nonlinear interaction between elementary wave components, disturbances in mechanical generation, and irregularities in the wave flume geometry result in a wave profile which can be regarded as 'almost' regular only.

In Fig. 5.7, a steep wave profile is shown. The recorded wave has a height $H = 0.378\,\mathrm{m}$ and period $T = 1.25\,\mathrm{s}$. Thus, the global wave steepness becomes $\varepsilon_\mathrm{g} = 0.0247$. Wave profile is asymmetric with a steep front slope. Surprisingly, the resulting Eulerian apparent acceleration (normalized against gravity acceleration g) is unrealistically high. The unrealistically high value of the acceleration probably results from very irregular, small ripples propagating on the crest of the almost breaking wave. These ripples are clearly seen in the record as the sampling frequency was very high, namely $f_\mathrm{s} = 80\,\mathrm{Hz}$. With such a fast sampling rate, not only is the rising and falling sea surface recorded; also foam, aerated water portion and any, sometimes random, water particles are marked by wave staff. All these facts demonstrate water instability, namely whitecaps or bubbly roller formation, particular on the forward face of a progressive gravity wave. At wavelengths less than about 10 cm, a capillary-gravity wave can

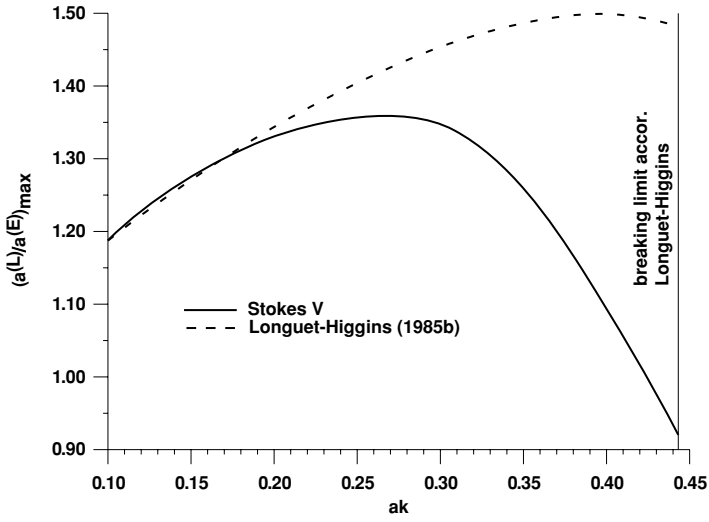

Figure 5.6: Ratio of real and apparent maximum accelerations at the wave trough in terms of ak.

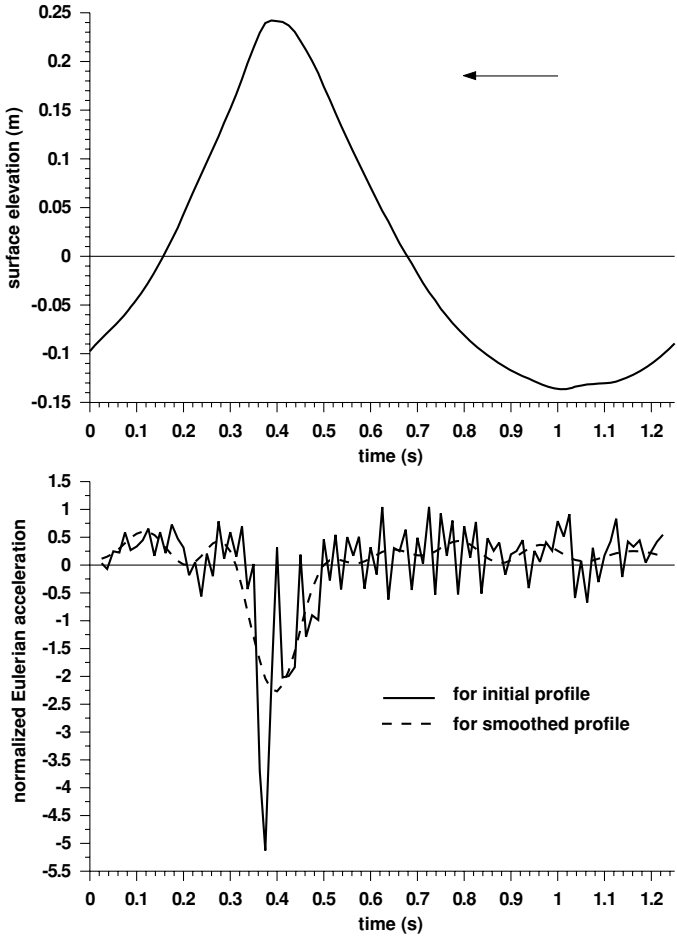

Figure 5.7: Profile of steep, breaking 'almost' regular experimental wave and Eulerian accelerations.

trap pockets of air in the wave troughs. Practical criteria of wave breaking cannot be based on the instantaneous records of such a multiphase medium producing a very noisy signal.

Therefore, it is useful to filter out all random, chaotic components by suitable smoothing technique. For example, an almost regular wave, as given in Fig. 5.7, can be simply represented in the form of the Fourier series when high harmonics are neglected. In our case, when $T = 1.25\,\mathrm{s}$ ($\omega = 1.6\pi\,\mathrm{rad/s}$), only the first eight harmonics were retained. This means that the components with frequencies $\omega_n > 8\omega = 12.8\pi$ (or with wave periods $T_\mathrm{n} < 0.16\,\mathrm{s}$ and wavelengths $L_\mathrm{n} < 0.04\,\mathrm{cm}$) were filtered out. In Fig. 5.7, the normalized Eulerian acceleration corresponding to such a smoothed profile is shown. It is found that the filtration of very high frequencies yields a substantial reduction

of the apparent acceleration. The minimum acceleration is now of the order of $-2.26g$, which is much smaller than the acceleration for incident raw data, equal to $-5.13g$.

To determine the real Lagrangian acceleration we fit the adopted theoretical profile $\zeta_s(t)$, for which this acceleration can be calculated, to the experimental profile $\zeta(t)$ as close as possible. To achieve the best fit, we have to minimize the quadratic error of fitting γ as follows

$$\gamma = \sum_{i=1}^{N} [\zeta(i) - \zeta_s(i)]^2 = \min, \tag{5.37}$$

where $i = 1, 2, \ldots, N$ are points equally distributed over the selected wave period. The profile $\zeta_s(t)$ is represented by the fifth-order Stokes profile (5.26) with phase $\psi = \varphi - \omega t$, where phase lag φ corresponds to the shifting of the experimental wave profile with respect to time $t = 0$. Requirement (5.37) results in two equations

$$\frac{\partial \gamma}{\partial \varphi} = 0 \quad \text{and} \quad \frac{\partial \gamma}{\partial \varepsilon} = 0. \tag{5.38}$$

After calculation for the profile given in Fig. 5.7, we obtain $\varphi = 2.073$ and $\varepsilon = 0.4096$. In Fig. 5.8, a comparison of the best-fit fifth-order Stokes expansion and initial profile $\zeta(t)$ is given. In the same figure, the Eulerian and Lagrangian accelerations corresponding to the best-fit fifth-order Stokes profile are shown. The Eulerian acceleration is still high, equal to about $-1.5g$, while the Lagrangian acceleration at the wave crest is equal to $-0.326g$. Such high values of the accelerations indicate that a given wave is about to break, which was confirmed by the very high value of global wave steepness, $\varepsilon_g = 0.0247$, and video film.

The best fit of the fifth-order Stokes profile to the experimental profile provides an effective and reliable method to calculate the values of local wave parameters, in particular the vertical accelerations at the wave crest of a breaking wave, only when the initial profile is almost regular. In the case of a very irregular wave profile, the multi-scale methodology described in the next section may be useful.

5.3.3.3 Two-scale methodology for short wave components riding on the surface of long waves

As was mentioned in Section 4.3.2, Holthuijsen and Herbers (1986) observed breaking at much lower wave steepness than that observed in laboratory tanks. The fact that under field conditions waves break at low steepness was also confirmed by Su and Green (1985). They showed that less steep initial waves require a larger fetch to evolve to breaking. On the other hand, the limited laboratory fetch would require relatively steep waves to be generated in order to observe breaking near the end of the wave flume. The low steepness associated with wave breaking in field conditions may be explained by superimposing

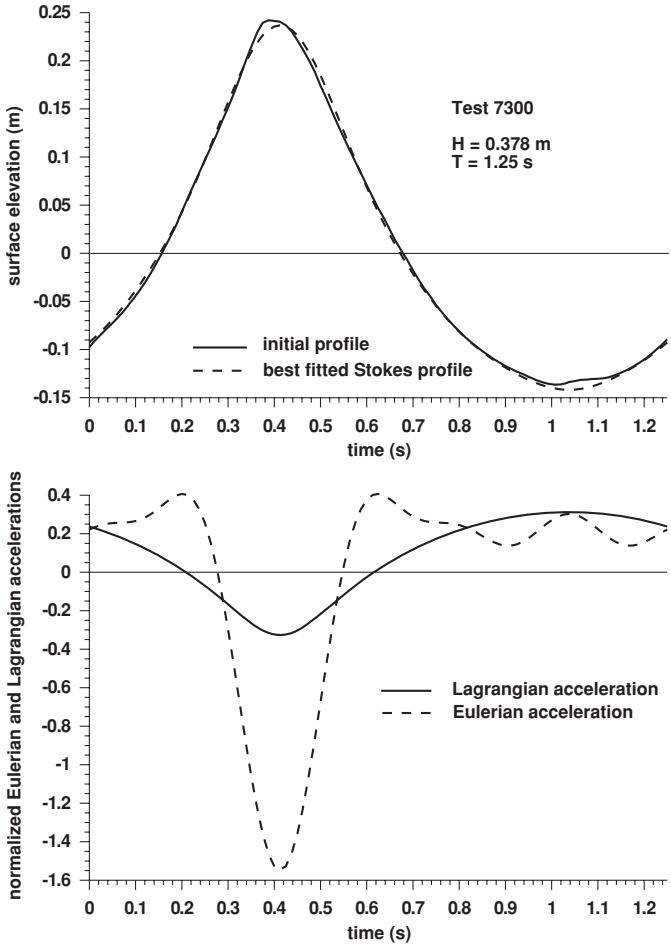

Figure 5.8: Fifth-order Stokes profile fitted to the experimental profile $\zeta(t)$ and corresponding accelerations.

a sequence of a relatively short gravity waves riding on the back of a longer wave. Longuet–Higgins (1985b) pointed out that such superposition may induce a high downwards acceleration which causes the waves to break at a lower value of steepness than do steady waves.

In general, any experimental profile can be treated as a result of superposition of two types of harmonics, namely bound waves and free waves. This partition is very clearly seen when a wave train is mechanically generated in the wave flume (Massel, 1981). The bound harmonics do not follow the dispersion relation and all harmonics propagate with the same speed as the first basic harmonic. A fifth-order Stokes wave profile (5.26) is a good example of the superposition of bound wave harmonics. In contrast to bound harmonics, each free harmonic satisfies the dispersion relation and propagates with different speed.

We use the distinguishing between the bound and free components to calculate the required accelerations at the crest of the observed wave profile, assuming that relatively short gravity waves ride on the back of a longer wave. The longer wave is represented by the best-fit fifth-order Stokes profile $\zeta_s(t)$, while the remaining residual profile $\zeta_{\rm rez}(t) = \zeta(t) - \zeta_s(t)$ is given by a sequence of short harmonics. Due to the fact that the shorter waves have phases different to that of the longer Stokes profile, it is expected that minimum Lagrangian acceleration is not associated with the crest of the incident wave profile $\zeta(t)$. Therefore, let us calculate the required acceleration for the profile section $t_{\max} - \Delta t < t < t_{\max} + \Delta t$ around the maximum of the longer component $\zeta_s(t_{\max})$. The real (Lagrangian) acceleration at the surface of the longer wave segment can be represented as follows:

$$a_z^{(L)}(t) = a_1^{(L)}(t) = \alpha_1(t)\, g \quad \text{or} \quad \mathrm{a_z^{(L)}(t)/g} = \alpha_1(\mathrm{t}), \tag{5.39}$$

where $a_1^{(L)}(t)$ is the Lagrangian acceleration associated with the longer wave and the effective value of gravity becomes

$$g_e'(t) = [1 + \alpha_1(t)]\, g. \tag{5.40}$$

Therefore, the real acceleration at the surface of the short wave (when only one harmonic is taken into account) is

$$a_{s,1}^{(L)} = \alpha_{s,1}\, g_e'(t) = \alpha_{s,1}[1 + \alpha_1(t)]\, g. \tag{5.41}$$

The relative real acceleration $\alpha_{s,1}(t)$ for simple harmonic can be calculated from (5.24), in which the velocity gradients are calculated from the linear theory. Thus, the resulting total normalized real acceleration at the surface of the short wave becomes

$$a_z^{(L)}(t)/g = [a_1^{(L)}(t) + a_{s,1}^{(L)}(t)]/g = \alpha_1(t) + \alpha_{s,1}(t)[1 + \alpha_1(t)]. \tag{5.42}$$

It should be added that the effective value of gravity at the surface of the shorter wave now becomes

$$g_e''(t) = [1 + \alpha_{s,1}(t)]\, g_e' = [1 + \alpha_1(t)][1 + \alpha_{s,1}(t)]\, g. \tag{5.43}$$

Suppose now that on the surface of the short wave there is an even shorter one. Analysis similar to that given above yields

$$a_{s,2}^{(L)}(t) = \alpha_{s,2}(t)\, g_e'' = \alpha_{s,2}(t)[1 + \alpha_1(t)][1 + \alpha_{s,1}(t)]\, g. \tag{5.44}$$

Therefore, resulting real acceleration becomes

$$\begin{aligned} a^{(L)}(t) &= a_1^{(L)} + a_{s,1}^{(L)} + a_{s,2}^{(L)} \\ &= \{\alpha_1(t) + \alpha_{s,1}(t)[1 + \alpha_1(t)] + \alpha_{s,2}(t)[1 + \alpha_1(t)][1 + \alpha_{s,1}(t)]\}\, g \end{aligned} \tag{5.45}$$

and

$$g_e'''(t) = [1 + \alpha_{s,2}(t)]\, g_e'' = [1 + \alpha_1(t)][1 + \alpha_{s,1}(t)][1 + \alpha_{s,2}(t)]\, g. \tag{5.46}$$

The above methodology can be extended to a sequence of similar gradually decreasing wavelengths, namely

$$\begin{aligned} a^{(L)}(t) &= \alpha_1(t)\, g + \{\alpha_{s,1}(1+\alpha_1)\, g + \\ &\quad \alpha_{s,2}(1+\alpha_1)(1+\alpha_{s,1})\, g + \\ &\quad \alpha_{s,3}(1+\alpha_1)(1+\alpha_{s,1})(1+\alpha_{s,2})\, g + \\ &\quad \alpha_{s,4}(1+\alpha_1)(1+\alpha_{s,1})(1+\alpha_{s,2})(1+\alpha_{s,3})\, g + \cdots\}\,. \end{aligned} \tag{5.47}$$

Similar analysis can also be applied for Eulerian acceleration.

Due to the fact that the effective value of gravity increases with the superposition of short waves, breaking waves can exist under less stringent conditions than needed for breaking initiation (Ramberg and Griffin, 1987). Therefore, it may be stated that the Longuet–Higgins criterion (2.14) represents an upper bound to the actual value. In the case of random seas, wave components can combine and instantaneously produce a high breaking wave having an associated value greater than this critical threshold.

5.3.3.4 A local Fourier approximation

In the methods discussed above, the accelerations resulting from regular wave theory are used to approximate the unknown acceleration at the surface of irregular waves. The usefulness of such an approach is strongly dependent on the level of 'irregularity' of wave profile. When the irregular profile can be approximated by a regular profile closely, the resulting acceleration can be estimated with reasonable accuracy (see Section 5.3.3.2). Otherwise the calculated acceleration is only a crude approximation of the real one.

An alternative method to determine the accelerations at the wave surface is to formulate the boundary value problem for wave motion and subsequently calculate the accelerations. However, there is no existing method that can accommodate the complete problem. Usually such a boundary value problem is formulated assuming wave periodicity in time and in space.

A review of the available approximate theories to represent a complete irregular wave, from crest (through) to following crest (through) or from zero-crossing to following zero-crossing is given by Sobey (1992). From this review it follows that a full solution of the Laplace equation under periodic lateral boundary conditions is numerically possible but time-consuming. However, in fact we are not interested in wave parameters at any time within the wave period. Instead we are interested in the wave characteristics at the wave crest where most likely breaking can occur. This region of our interest coincides with the region of maximum uncertainty in wave theory predictions. Therefore, it will be more useful to concentrate on methodologies that seek only to represent the local (close to the wave crest) behaviour of waves. Such local methodology compromises applicability in a global sense to achieve as exact as possible a representation of wave motion in a local sense. In particular, in a local Fourier approximation methodology, the field equation throughout the fluid domain, the bottom boundary condition at the bed and the free surface boundary conditions at the

water surface should be satisfied within a time window of duration τ, which is small in comparison with the local zero-crossing period. The description of the local Fourier approximation method given below is mainly due to Sobey (1992).

So, let us consider the irrotational motion of a homogeneous, incompressible and inviscid fluid under a free surface in a constant water depth h. The origin is located at the mean water level and the vertical axis z is positive upward. The flow can be described by a velocity potential $\Phi(x, z, t)$ satisfying the Laplace equation with kinematic and dynamic boundary conditions at the wave surface and at the sea bottom, i.e.

$$\nabla^2\Phi(x, z, t) = 0, \tag{5.48}$$

$$w - \frac{\partial\zeta}{\partial t} - u\frac{\partial\zeta}{\partial x} = 0 \quad \text{at} \quad z = \zeta(x, t), \tag{5.49}$$

$$\frac{\partial\Phi}{\partial t} + \frac{1}{2}(u^2 + w^2) + g\zeta = 0 \quad \text{at} \quad z = \zeta(x, t), \tag{5.50}$$

$$\frac{\partial\Phi}{\partial z} = 0 \quad \text{at} \quad z = -h, \tag{5.51}$$

where u and w are the horizontal and vertical components of wave velocity, and ζ is the wave surface ordinate.

It is convenient to represent locally the unknown velocity potential Φ in the following form

$$\Phi(x, z, t) = \sum_{j}^{M} A_j \frac{\cosh[jk(z + h)]}{\cosh(jkh)} \sin[j(kx - \omega t)], \tag{5.52}$$

in which A_j are the unknown amplitudes, k and ω are the wave number and wave frequency, accordingly.

Usually in laboratory experiments only time series of wave oscillations at a given point are available. To estimate the unknown spatial gradient of the surface elevation ζ in (5.49), local phase velocity $\left(\frac{\omega}{k}\right)$ was applied to relate the spatial and temporal gradients, i.e.

$$\frac{\partial\zeta}{\partial t} + \frac{\omega}{k}\frac{\partial\zeta}{\partial x} = 0. \tag{5.53}$$

Thus, the surface boundary conditions take the form

$$\left.\begin{aligned} w + \left(\frac{k}{\omega}\right) u\frac{\partial\zeta}{\partial t} &= \frac{\partial\zeta}{\partial t} \\ \frac{\partial\Phi}{\partial t} + \frac{1}{2}\left(u^2 + w^2\right) + g\zeta &= 0 \end{aligned}\right\}. \tag{5.54}$$

It should be noted that the following quantities are unknown in the system (5.48–5.51): A, k, ω and x of which there are M. For calculation, the variable kx was chosen because the wave number k and horizontal coordinate x appear in the equations only in the form of product kx. These unknowns are valid only locally in a small segment of the wave profile, and Sobey (1992) suggested that the length of the segment is typically equal to $\tau \approx 0.1\,T$. In his paper he presented examples of practical implementation of above approach.

5.3.4 Limiting vertical acceleration criterion in presence of surface drift

When a wave breaks, the crest of the wave rolls forward at the phase velocity. Thus, the breaking crest contributes greatly to the mass and momentum transport. Phillips and Banner (1974) modelled this effect and found the wind-induced drift current to have a influence on the incipient breaking

$$A_{\mathrm{br}} = \frac{\alpha g}{\omega^2}\left(1 - \frac{C_{\mathrm{dr}}}{C}\right)^2, \tag{5.55}$$

where A_{br} is the maximum wave amplitude, C is the phase velocity, C_{dr} is the velocity of the surface drift at the point where the wave profile crosses the mean water level. Coefficient α accounts for the fact that magnitude of the downward crest acceleration of the breaking wave is not exactly $\frac{1}{2}g$. After neglecting the drift, (5.55) becomes

$$A_{\mathrm{br}} = \frac{\alpha g}{\omega^2}. \tag{5.56}$$

When $\alpha = 0.5$, this result agrees with Stokes' criterion of wave breaking. Thus, for a regular wave of amplitude A and frequency ω we have

$$A\omega^2 \sim \frac{1}{2}g \tag{5.57}$$

and the maximum amplitude A_{br} becomes

$$A_{\mathrm{br}} = \frac{g}{2\omega^2}. \tag{5.58}$$

For an irregular wave, the frequency ω is characterised by the root-mean-square frequency $\omega_0 = \left(\overline{\omega^2}\right)^{1/2}$ and from (5.55) we obtain

$$A_{\mathrm{br}} = \frac{\alpha g}{\omega_0^2}\left(1 - \frac{C_{\mathrm{dr}}}{C_0}\right)^2, \tag{5.59}$$

where C_0 is the characteristic phase velocity of the wave corresponding to the characteristic frequency ω_0. Velocity of the Eulerian mean surface drift C_{dr} is usually fixed at one half of the friction velocity of the wind u_*, namely

$$C_{\mathrm{dr}} \approx 0.5u_*, \tag{5.60}$$

where

$$u_* = \sqrt{C_{10}}\, V_{10}, \tag{5.61}$$

in which C_{10} is the drag coefficient.

Precise and systematic insight into the dependence of C_{10} can be obtained through the similarity approach (Massel, 1996a). However, for the purpose of

our analysis we use the following simpler expression for C_{10}, suggested by Wu (1980, 1982)

$$C_{10} \approx (a + bV_{10})\, 10^{-3}, \tag{5.62}$$

where $a = 0.8$ and $b = 0.065$. Therefore, we get

$$C_{\mathrm{dr}} = 0.5\sqrt{C_{10}}V_{10} = \alpha_2 V_{10}, \tag{5.63}$$

in which $\alpha_2 = 0.5\sqrt{C_{10}}$. In the wind velocity range $6\,\mathrm{m/s} < V_{10} < 20\,\mathrm{m/s}$, the coefficient α_2 varies from 0.0172 to 0.023.

Hence (5.59) now becomes

$$A_{\mathrm{br}} = \frac{\alpha g}{\omega_0^2}\left(1 - \alpha_2 \frac{V_{10}}{C_0}\right)^2 = \frac{\alpha g}{\omega_0^2}\left(1 - \alpha_2 \frac{\omega_0 V_{10}}{g}\right)^2. \tag{5.64}$$

To find the value of the coefficient α, let us use the experimental results of Ochi and Tsai (1983) when the maximum breaking wave height for the random mechanically generated wave train ($V_{10} = 0$) satisfied the condition

$$H_{\mathrm{br}} \geq 0.020\, gT^2. \tag{5.65}$$

Combining (5.64) and (5.65) for $V_{10} = 0$, we obtain

$$0.010\, T_0^2 = \frac{\alpha g}{\omega_0^2} \tag{5.66}$$

and

$$\alpha = 0.04\,\pi^2 \approx 0.395. \tag{5.67}$$

The above value predicts that the downward acceleration at the wave crest is $\approx 0.395g$, which is very close to the theoretical value of $0.388g$ given by Longuet–Higgins (1985b).

Using this α value in (5.64) we obtain

$$A_{\mathrm{br}} = \frac{0.04\,\pi^2 g}{\omega_0^2}\left(1 - \alpha_2 \frac{V_{10}}{C_0}\right)^2, \tag{5.68}$$

or

$$A_{\mathrm{br}} = \frac{0.04\,\pi^2 g}{\omega_0^2}\left(1 - \alpha_2 \frac{V_{10}\omega_0}{g}\right)^2. \tag{5.69}$$

In Table 5.5, the maximum breaking wave amplitude A_{br} for selected wind velocities V_{10} and wind fetches X is given. The frequency ω_0 is calculated under the assumption that the wave field is described by the JONSWAP spectrum (Hasselmann et al., 1973) and $\omega_0 = \omega_{\mathrm{p}}$ given by (3.23) and the coefficient $\alpha_2 = 0.02$. In the brackets, maximum amplitudes for the non-wind case are given. Reduction of breaking amplitude due to surface drift is of the order of (3–10)%, and the limiting wave steepness ka equals $\approx 0.35 - 0.37$.

Table 5.5: Maximum breaking wave amplitude $A_{\rm br}$ for peak frequency $\omega_{\rm p}$

	Wind velocity V_{10} (m/s)			
X (km)	6	8	10	16
10	0.52 (0.55)	0.62 (0.67)	0.71 (0.78)	0.95 (1.08)
20	0.83 (0.88)	1.00 (1.06)	1.15 (1.24)	1.54 (1.71)
100	2.45 (2.53)	2.97 (3.08)	3.44 (3.59)	4.65 (4.94)

Phillips and Banner (1974) observed that short wind generated waves are also suppressed when a train of long, mechanically generated waves propagate in the wind direction. The corresponding reduction of the spectral energy density can be as high as 60% when the steepness of long waves is $(ak)_{\rm l} = 0.05$ (Mitsuyasu, 1966). The spectral energy density can even be reduced by a factor of about 2.5 when the slope $(ak)_{\rm l} = 0.105$ (Donelan, 1987). Phillips and Banner attributed this fact to enhanced short wave breaking due to modulation by the long wave. Some discussion of this mechanism can be found in a paper by Wright (1976). Recently Chen and Belcher (2000) made an attempt to explain the observed phenomena through the analysis of the partition between long wave-induced $\tau_{\rm l}$ stresses and turbulent $\tau_{\rm t}$ stresses, when

$$\tau_{\rm tot} = \tau_{\rm l} + \tau_{\rm t} = {\rm const} = \rho_{\rm a}\, {\rm u}_*^2. \tag{5.70}$$

The following relationship for turbulent wind stress has been obtained

$$\frac{\tau_{\rm t}}{\tau_{\rm tot}} = 1 - \frac{\tau_{\rm l}}{\tau_{\rm tot}} \approx \frac{1}{1 + \frac{1}{2}(a_{\rm l}\, k_{\rm l})^2 \alpha_{\rm p}}, \tag{5.71}$$

in which $\alpha_{\rm p}$ is the asymmetric pressure coefficient. Recalling some empirical relations for the development of pure wind waves (with no long waves) under steady wind, the ratio of energy density of wind waves with (E) and without long waves (E_0) becomes

$$\frac{E}{E_0} = \left(\frac{\tau_{\rm t}}{\tau_{\rm tot}}\right)^{1.36}, \tag{5.72}$$

and the corresponding ratio of the wind wave growth rates at the spectral peak frequency is

$$\frac{\gamma(\omega_{\rm p})}{\gamma_0(\omega_{0\rm p})} = \left(\frac{\tau_{\rm t}}{\tau_{\rm tot}}\right)^{0.571}. \tag{5.73}$$

A higher exponent in (5.72), larger than the exponent in (5.73), yields strong reduction in the energy density. For a long wave steepness of $\approx$0.1, the energy density of wind waves is reduced by up to 40%, while the growth rate at the peak frequency is reduced only by up to 20%. To compare the theoretical results with the experiments of Phillips and Banner (1974) and Mitsuyasu (1966), the value of the asymmetric pressure coefficient $\alpha_{\rm p} = 80$ and $\alpha_{\rm p} = 160$ was

selected, respectively. The model showed a reasonable agreement with both sets of laboratory data. However, the implementation of the results for ocean waves showed that the reduction of spectral wind wave energy in the presence of swell is very weak and therefore very difficult to observe. This is mostly because the ratio $\frac{C_1}{u_*}$ (C_1 is the phase velocity of long waves) in natural conditions is usually larger than 25 and the asymmetry coefficient becomes small, typically $\alpha_p \approx 1.0$. This value yields a reduction in the spectral energy density of less than 5%.

5.3.5 Probability of wave breaking based on the limiting vertical acceleration criterion

As was shown in Section 2.2, near-limiting waves have rounded crests with a small radius of curvature, while the vertical acceleration at the crest is smaller than $0.5\,g$, but equals $0.39\,g$ approximately. To extend this result to the case of breaking of irregular waves, let us assume that the downward acceleration at the crest of the wave is greater than αg for breaking to occur, i.e.

$$\left|\frac{d^2\zeta}{dt^2}\right| > \alpha g, \tag{5.74}$$

in which α is a constant. According to Snyder et al. (1983), α varies from 0.4 to 0.52, while the laboratory experiments of Ochi and Tsai (1983) provide the value $\alpha \approx 0.4$.

The starting point for calculation of probability of wave crests breaking in a given wave train is the probability density function of maxima (crests) with a downward acceleration greater than αg, which can be expressed as follows (Cartwright and Longuet–Higgins, 1956; Massel, 1996a)

$$f_{\max}(\zeta_{\max}) = \frac{\int_{-\infty}^{-\alpha g} f_3\left(\zeta_{\max}, 0, \ddot{\zeta}\right)\ddot{\zeta}\,d\ddot{\zeta}}{\int_0^{\infty}\int_{-\infty}^{-\alpha g} f_3\left(\zeta_{\max}, 0, \ddot{\zeta}\right)\ddot{\zeta}\,d\ddot{\zeta}\,d\zeta}, \quad 0 \le \zeta \le \infty, \tag{5.75}$$

in which

$$f_3\left(\zeta_{\max}, \dot{\zeta}, \ddot{\zeta}\right) = \frac{1}{(2\pi)^{3/2}\sqrt{m_2\tilde{\Delta}}}\exp\left\{-\frac{1}{2\tilde{\Delta}}\left[m_4\,\zeta_{\max}^2 + 2m_2\,\zeta_{\max}\,\ddot{\zeta} + m_0\,\ddot{\zeta}\right] - \frac{1}{2m_2}\dot{\zeta}^2\right\}, \tag{5.76}$$

where $\tilde{\Delta} = m_0 m_4 - m_2^2$. The dots over variables denote differentiation in time. Integration of (5.75) with respect to vertical acceleration $\ddot{\zeta}$ yields the probability density for a breaking wave crest of elevation ξ (Srokosz, 1986; Massel, 1998)

$$f_{\max}(\xi; |\ddot{\zeta}| > \alpha g) = \frac{1}{\sqrt{2\pi}}\left\{\epsilon\exp\left[-\frac{1}{2}\gamma^2 - \frac{1}{2\epsilon^2}\left(\xi - \sqrt{1-\epsilon^2}\,\gamma\right)^2\right] + \sqrt{1-\epsilon^2}\,\xi\exp\left(-\frac{1}{2}\xi^2\right)\int_u^{\infty}\exp\left(-\frac{1}{2}x^2\right)dx\right\}, \tag{5.77}$$

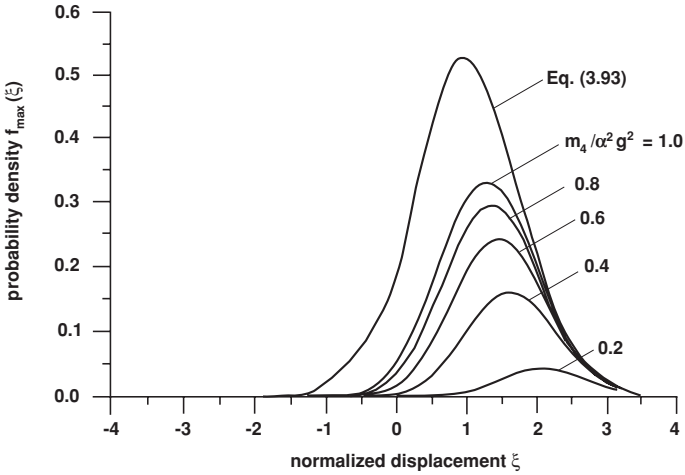

Figure 5.9: Probability density function of wave crests that are breaking when acceleration is greater than αg (adapted from Massel, 1996a).

in which

$$\xi = \frac{\zeta}{\sqrt{m_0}};\ \gamma = \frac{\alpha g}{\sqrt{m4}};\ \ u = \frac{1}{\epsilon}\left(\gamma - \sqrt{1-\epsilon^2}\xi\right). \tag{5.78}$$

The probability (5.77) is illustrated in Fig. 5.9 as a function of the non-dimensional moment $\frac{m_4}{\alpha^2 g^2}$. The α and ϵ values were taken as 0.4 and 0.6, respectively. For comparison in the same figure, the probability density (3.93) is shown for the value of $\epsilon = 0.6$. Equation (3.93) corresponds to a value of $\alpha = 0\,(m_4/\alpha^2 g^2 = \infty)$ and implies that all the crests reach breaking conditions.

The probability that a crest of any height will break is simply an integral of probability $f_{\max}(\xi; |\ddot{\zeta}| > \alpha g)$, i.e.

$$F_{\rm br}^{(1)} = \int_0^\infty f_{\max}(\xi; |\ddot{\zeta}| > \alpha g) d\xi. \tag{5.79}$$

After substitution of (5.77) into (5.79) we obtain (Srokosz, 1986)

$$F_{\rm br}^{(1)} = \exp\left(-\frac{(\alpha g)^2}{2m_4}\right). \tag{5.80}$$

Function $F_{\rm br}^{(1)}$ represents the probability that breaking will occur at a crest point on the sea surface. It can be shown that as $m_4 \to \infty$, $F_{\rm br}^{(1)} \to 1$ (see Fig. 5.10). The formula (5.80) is of practical importance for the two-dimensional case of waves propagating in a wave flume as it determines the relative number of breaking wave crests in the wave train. Probability $F_{\rm br}^{(1)}$ is independent of any assumption on the spectral width, assuming that moment m_4 exists.

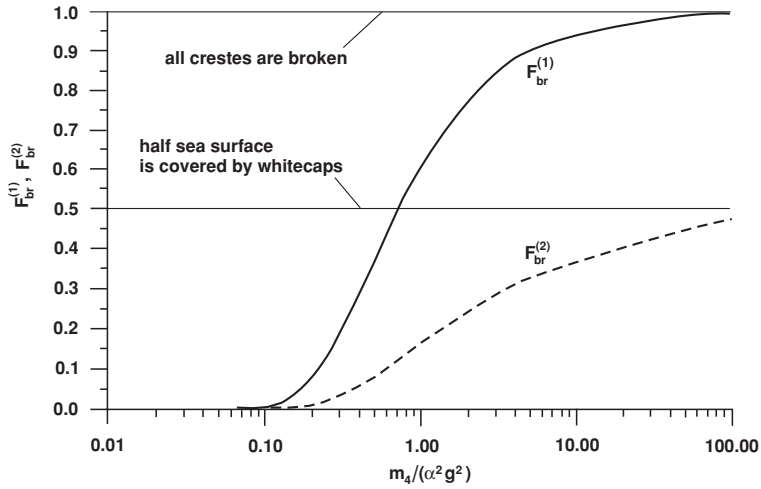

Figure 5.10: Probability of breaking crests $F_{\rm br}^{(1)}$ and breaking wave coverage of sea surface $F_{\rm br}^{(2)}$as a function of $m_4/\alpha^2 g^2$.

The probability that at least one wave in a record of time duration t and number of waves equal to N becomes unstable and starts to break is (Massel, 1998)

$$F_{\rm br}^{(1)} = \frac{1}{N} \approx \frac{\overline{T}}{t}, \tag{5.81}$$

in which $\overline{T}$ is the mean wave period. In low energy regimes all observed waves are stable and the probability $F_{\rm br}^{(1)}$ is equal to zero. However, for a sufficiently long time t, there will be some non-zero chance that the maximum wave will become unstable and start to break. The corresponding spectral moment m_4 becomes

$$m_4 = -\frac{\alpha^2 g^2}{2\ln(F_{\rm br}^{(1)})} \tag{5.82}$$

and

$$\int_0^\infty \omega^4 S(\omega) d\omega = -\frac{\alpha^2 g^2}{2\ln(F_{\rm br}^{(1)})}, \tag{5.83}$$

or

$$\int_0^\infty \omega^4 S(\omega) d\omega = -\frac{\alpha^2 g^2}{2[\ln \overline{T} - \ln t]}. \tag{5.84}$$

Equations (5.83) and (5.84) represent necessary conditions for spectral density $S(\omega)$ to provide a moment m_4 sufficient to initiate wave instability and breaking for a given value of α.

The probability $F_{\rm br}^{(1)}$ should be distinguished from that of Snyder and Kennedy (1983), which deals with the fraction of the sea surface covered by breaking water. According to this concept, wave breaking occurs in regions of fluid where the surface motion (not only in the wave crest vicinity) requires the downward acceleration to exceed the dynamical threshold αg. Snyder and Kennedy (1983) found that this definition of breaking yields the percentage of sea surface covered by whitecaps in the form

$$F_{\rm br}^{(2)} = 1 - \Phi\left(\frac{\alpha g}{\sqrt{m_4}}\right), \tag{5.85}$$

where Φ is the probability integral given by (3.88). For very small waves, $m_4 \to 0$ and $F_{\rm br}^{(2)} \to 0$. During a strong storm, $m \to \infty$ and $F_{\rm br}^{(2)} \to 1/2$. This means that half of the sea surface, where acceleration of the water elements is directed downwards and is greater than the critical one, is covered by breaking waves – see Fig. 5.10.

To illustrate the dependence of probability of breaking $F_{\rm br}^{(1)}$ on wind conditions, let us substitute a value for the moment m_4 following from the JONSWAP spectrum. Hence after substituting (D.7) into (5.80) and using (3.22) we obtain the probability of breaking in the form

$$F_{\rm br}^{(1)} = \exp\left[-3.858\alpha^2\left(\frac{gX}{V_{10}^2}\right)^{0.22}\right]. \tag{5.86}$$

Function (5.86) for a few values of parameter α was illustrated in Fig. 5.11. The fetch dependence of probability of breaking is substantial. For a given fetch X, a small value of $\left(\frac{gX}{V_{10}^2}\right)$ is associated with a higher wind velocity and a higher

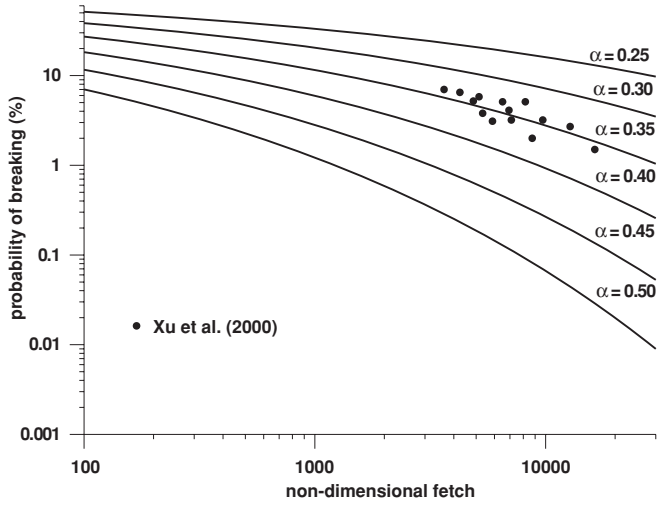

Figure 5.11: Probability of breaking (in %) against the non-dimensional wind fetch.

value of the Phillips constant β. The small value of $\left(\frac{gX}{V_{10}^2}\right)$ also provides a high value of ω_{p} (or small T_{p} value). This finally yields a higher value of moment m_4 and higher probability of breaking. In this figure, experimental data collected by Xu et al. (2000) in the Bohai Bay were added. The close agreement between experimental data and theoretical formula (5.86) exists for $\alpha \approx 0.35$.

The probability of breaking resulting from the downward threshold acceleration principle can also be presented as a function of significant wave steepness (4.5)

$$\varepsilon_{\mathrm{s}} = \frac{H_{\mathrm{s}}}{gT_{\mathrm{p}}^2}. \tag{5.87}$$

After substituting $H_{\mathrm{s}} = 4\sqrt{m_0}$ we obtain

$$\varepsilon_{\mathrm{s}} = \frac{4\sqrt{m_0}}{gT_{\mathrm{p}}^2}. \tag{5.88}$$

The m_0 moment resulting from the JONSWAP spectrum becomes (see (D.4))

$$m_0 = 0.3048\beta g^2 \omega_{\mathrm{p}}^{-4}. \tag{5.89}$$

After substituting the Phillips constant β, the resulting significant wave steepness is

$$\varepsilon_{\mathrm{s}} = 0.01542 \left(\frac{gX}{V_{10}^2}\right)^{-0.11}. \tag{5.90}$$

Combining (5.86) and (5.90) yields

$$F_{\mathrm{br}}^{(1)} = \exp\left[-9.1733 \cdot 10^{-4} \left(\frac{\alpha}{\varepsilon_{\mathrm{s}}}\right)^2\right]. \tag{5.91}$$

Function (5.91) for various values of constant α is presented in Fig. 5.12. These curves represent the relationship between the probability of breaking of a wave of any height and sea state characterised by the significant wave steepness. The resulting probability of breaking $F_{\mathrm{br}}^{(1)}$ increases with the significant wave steepness ε_{s}, and lower value of α produces more rapid growth of the probability $F_{\mathrm{br}}^{(1)}$. In the figure the range of significant wave steepnesses observed by Holthuijsen and Herbers (1986), namely $0.0053 < \varepsilon_{\mathrm{s}} < 0.0081$, is given. It should be noted that for this steepness range, the calculated probability of breaking varies from 2% to 12% when $\alpha = 0.4$ is assumed. This result is in full agreement with the Holthuijsen and Herbers observation (see Section 4.3.2).

5.4 Kinematic breaking criterion

The kinematic breaking criterion finding that the horizontal water velocity exceeds the speed of the crest is the traditional and most natural breaking

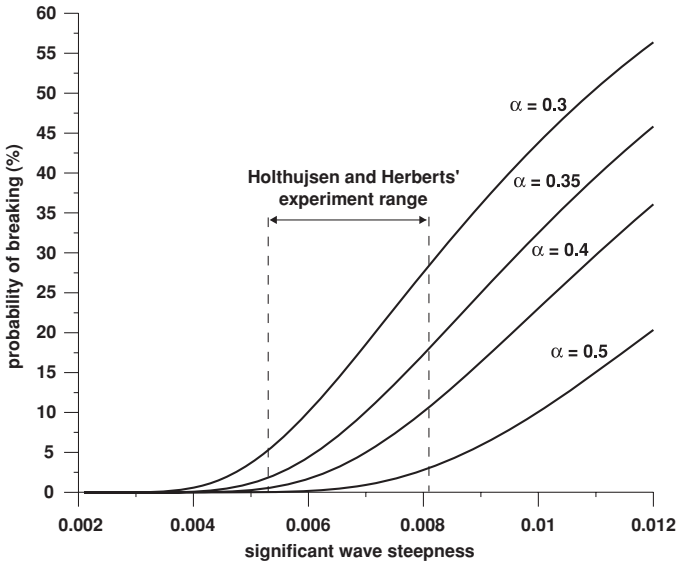

Figure 5.12: Dependence of probability of breaking on significant wave steepness for four values of α.

criterion. The equivalence of horizontal particle velocity at the wave crest and phase speed is a logical conjecture for a limiting periodic wave with a sharply pointed crest. Viewing the wave from a reference frame in which the surface profile is stationary, the flow at the tip of the crest must be a stagnation point, and the velocity of a fluid particle at the tip must be equal to the speed of the wave profile. However, the numerical calculations cited in Section 2.4 lead to the conclusion that a Stokes wave becomes unstable before it reaches its limiting form where the equivalence of phase speed and fluid particle speed appears. The existence of crest instabilities is essentially a local property of the wave crest. Therefore, the previously global phase speed of the wave will be replaced by the local phase speed.

However, the relationship between the local phase speed and the fluid particle velocities on the surface of an unstable wave is not well understood. Therefore, the application of the kinematic criterion for irregular breaking crests, changing their shape in time, appears to be very difficult as we need proper definitions of particular wave parameters, local in space and time. Below we present a methodology for determining these parameters following mainly Stansell and MacFarlane (2002). According to the simplest approach, the phase speed of an irregular wave is approximately equal to an equivalent linear regular wave as follows

$$C = \frac{\omega}{k}. \tag{5.92}$$

Application of this definition requires that the values of wave period T and wave length L are constant over the time and space scale of any particular wave of interest. As usually only the time series of the surface profile is known, the wave number k should be obtained from the dispersion relation

$$\omega^2 = gk. \tag{5.93}$$

Thus, the phase speed is totally defined by the wave frequency as

$$C = \frac{g}{\omega}. \tag{5.94}$$

Using the definition (5.94) for a wave that is about to break is not satisfactory as the phase speed is identical at all points between consecutive zero-down-crossings of the wave. On the contrary, when the wave starts to break and its front face becomes vertical, the speed of the breaking crest is usually greater than the speed of the trough preceding it. In other words, the phase speed of an evolving wave is a local quantity.

A slightly improved definition of phase speed can be based on the speed of the position of the surface elevation maximum associated with the wave crest of interest. So we have

$$C(t) = \frac{dx_{\mathrm{c}}(t)}{dt} \tag{5.95}$$

in which $x_{\mathrm{c}}(t)$ denotes the x-coordinate of the surface maximum of the crest. This phase speed is only valid at the locus of the crest maximum. Therefore, it is instantaneous only in time, not in space.

The desired local phase speed can be obtained as a ratio of an instantaneous frequency $\omega(x,t)$, with an instantaneous wave number $k(x,t)$, i.e.

$$C(x,t) \equiv \frac{\omega(x,t)}{k(x,t)}. \tag{5.96}$$

A convenient way to define $\omega(t,x)$ and $k(x,t)$ is provided by the theory of analytic functions and the technique of the Hilbert transform. This method, described in Appendix C in detail, has been used in Section 4.6.3 to detect waves breaking in a given wave record, when the incipient breakers are associated with consistent instantaneous frequency variations. However, to obtain the phase speed according to (5.96) we have to extend the definition of the Hilbert transform for a two-dimensional wave $\zeta(x,t)$ as follows (Stansell and MacFarlane, 2002)

$$\xi_t(x,t) = \mathcal{H}_t[\zeta(x,t)] = P \int_{-\infty}^{\infty} \frac{\zeta(x,t_1)}{\pi(t-t_1)}\, dt_1 \tag{5.97}$$

and

$$\xi_x(x,t) = \mathcal{H}_x[\zeta(x,t)] = P \int_{-\infty}^{\infty} \frac{\zeta(x_1,t)}{\pi(x-x_1)}\, dx_1. \tag{5.98}$$

Now the corresponding analytical signals take the forms

$$\eta_x(x,t) = \zeta(x,t) + i\,\xi_x(x,t) = A_x(x,t)\exp(i\,\theta_x(x,t)) \tag{5.99}$$

and

$$\eta_t(x,t) = \zeta(x,t) + i\,\xi_t(x,t) = A_t(x,t)\exp(i\,\theta_t(x,t)), \tag{5.100}$$

where

$$A_x(x,t) = \sqrt{\zeta^2(x,t) + \xi_x^2(x,t)} \text{ and } \theta_x(x,t) = \arctan\left(\frac{\xi_x(x,t)}{\zeta(x,t)}\right) \tag{5.101}$$

and

$$A_t(x,t) = \sqrt{\zeta^2(x,t) + \xi_t^2(x,t)} \text{ and } \theta_t(x,t) = \arctan\left(\frac{\xi_t(x,t)}{\zeta(x,t)}\right). \tag{5.102}$$

The local frequency $\omega(x,t)$ now becomes

$$\omega(x,t) = \frac{\partial\theta_t(x,t)}{\partial t} \tag{5.103}$$

or

$$\omega(x,t) = \frac{1}{\zeta^2(x,t) + \xi_t^2(x,t)}\left[\zeta(x,t)\,\frac{\partial\xi_t(x,t)}{\partial t} - \xi_t(x,t)\,\frac{\partial\zeta(x,t)}{\partial t}\right]. \tag{5.104}$$

As shown in Appendix C, application of the Hilbert transform for definition of the instantaneous frequency should be done with care, particularly with wideband spectra. For such cases, sometimes the obtained frequency becomes zero or even negative, which should be regarded as an unphysical result. Usually such cases are associated with maxima in $\zeta(x,t)$ occurring below, or minima occurring above mean water level. To avoid such unwanted frequencies, Huang et al. (1998) proposed a methodology based on so-called intrinsic mode function (IMF) – see Appendix C.

The local wave number $k(x,t)$ can obtained in a similar way. Thus, we have

$$k(x,t) = \frac{\partial\theta_x(x,t)}{\partial x} \tag{5.105}$$

or

$$k(x,t) = \frac{1}{\zeta^2(x,t) + \xi_x^2(x,t)}\left[\zeta(x,t)\,\frac{\partial\xi_x(x,t)}{\partial x} - \xi_x(x,t)\,\frac{\partial\zeta(x,t)}{\partial x}\right]. \tag{5.106}$$

Substitution (5.104) and (5.106) into (5.96) yields the phase speed as

$$C(x,t) = \frac{\zeta^2(x,t) + \xi_x^2(x,t)}{\zeta^2(x,t) + \xi_t^2(x,t)}\left\{\frac{\zeta(x,t)\frac{\partial\xi_t(x,t)}{\partial t} - \xi_t(x,t)\frac{\partial\zeta(x,t)}{\partial t}}{\zeta(x,t)\frac{\partial\xi_x(x,t)}{\partial x} - \xi_x\frac{\partial\zeta(x,t)}{\partial x}}\right\}. \tag{5.107}$$

It can be shown that for linear waves

$$\xi_x(x,t) = \mathcal{H}_x[\zeta(x,t)] = -\xi_t(x,t) = -\mathcal{H}_t[\zeta(x,t)]. \tag{5.108}$$

Substitution of the above relationship into (5.107), results in a simplified form for phase velocity as follows:

$$C(x,t) = \frac{\zeta(x,t)\,\frac{\partial \xi_t(x,t)}{\partial t} - \xi_t(x,t)\,\frac{\partial \zeta(x,t)}{\partial t}}{\xi_t(x,t)\,\frac{\partial \zeta(x,t)}{\partial x} - \zeta(x,t)\,\frac{\partial \xi_t(x,t)}{\partial x}}. \tag{5.109}$$

Stansell and MacFarlane (2002) performed experiments to test the breaking criterion, stating that the horizontal fluid particle velocity at the surface of a crest exceeds the local phase speed of the crest prior to breaking. For each of the waves studied (plunging breakers, spilling breakers and nonbreaking waves) they found that the phase speeds calculated from linear waves give poor approximation to the values obtained by using any of the local phase speed definitions. The observed ratio of $u(\zeta, x, t)/C(x, t)$ was at all times smaller than one. Thus, the kinematic breaking criterion was not satisfied for all three definitions used for phase speed. In particular, the criterion is far from satisfied for plunging breakers. For spilling breakers, the criterion is closer to being satisfied. Moreover, it should be concluded that the condition $u(\zeta, x, t)/C(x, t) > 1$ in a wave crest, at or before the first occurrence of a vertical tangent to the forward face, may be a sufficient condition for breaking but it is not a necessary condition.

5.5 Probability of wave breaking for modulated second-order Stokes waves

Dawson et al. (1993) considered seas with narrow-banded frequencies and narrow distribution for nonlinear crest amplitudes to derive an expression for the probability of breaking. The narrow-banded random sea can be conveniently represented approximately by a modulated second-order Stokes wave with slowly varying amplitude and phase. According to Tayfun (1980, 1981), the expression for the free-surface elevation $\zeta(t)$ at time t and at a given point takes the form

$$\zeta(t) = A\cos(\overline{\omega}t + \varphi) + \frac{\overline{k}}{2}A^2\cos 2(\overline{\omega}t + \varphi), \tag{5.110}$$

where $A = A(t)$ is the modulated amplitude, $\varphi = \varphi(t)$ is the phase, and $\overline{\omega}$ and $\overline{k}$ are the mean frequency and wave number, respectively. For breaking waves we are particularly interested in the amplitude or envelope function for nonlinear wave crests $r(t)$ when

$$r = A + \frac{\overline{k}}{2}A^2 \quad \text{and} \quad A \approx r - \frac{\overline{k}}{2}r^2. \tag{5.111}$$

To obtain the probability density function for the nonlinear amplitude $f(r)$, the following transformation of random variables is applied:

$$f(r) = f(A)\frac{dA}{dr}\Big|_{A=f(r)}, \tag{5.112}$$

in which $f(A)$ is the Rayleigh probability density of amplitude for a Gaussian wave field

$$f(A) = \frac{A}{\sigma_\zeta^2} \exp\left(-\frac{A^2}{2\sigma_\zeta^2}\right) = \frac{16A}{H_\mathrm{s}^2} \exp\left(-8\frac{A^2}{H_\mathrm{s}^2}\right). \tag{5.113}$$

Using (5.111) and (5.113) in (5.112), Dawson et al. (1993) obtained

$$f(r) = 16\frac{r}{H_\mathrm{s}^2}\left(1 - \frac{3}{2}\frac{\varepsilon_k r}{H_\mathrm{s}}\right) \exp\left[-8\frac{r^2}{H_\mathrm{s}^2}\left(1 - \frac{\varepsilon_k r}{H_\mathrm{s}}\right)\right], \tag{5.114}$$

where ε_k is the characteristic steepness parameter for the narrow-band sea

$$\varepsilon_k = \frac{H_\mathrm{s}\overline{\omega}^2}{g} = \overline{k} H_\mathrm{s}, \tag{5.115}$$

in which $\overline{\omega}$ is the mean frequency.

In (5.114), the Rayleigh distribution is retained and the additional term represents a correction that includes explicitly a measure of the average wave steepness defined by the parameter ε_k. For $r = A$ and $\varepsilon_k = 0$, the Rayleigh probability density $f(a)$ for linear waves appears. On the other hand, when $\frac{r}{H_\mathrm{s}} = \frac{2}{3}\varepsilon_k^{-1}$, the function $f(r) = 0$. The probability of occurrence of crest elevations equal to or greater than some threshold level r_th is given by

$$F_{r_\mathrm{th}} = B\left\{\exp\left[-8\left(\frac{r_\mathrm{th}}{H_\mathrm{s}}\right)^2\left(1 - \frac{\varepsilon_k r_\mathrm{th}}{H_\mathrm{s}}\right)\right] - \exp\left(-\frac{32}{27}\frac{1}{\varepsilon_k^2}\right)\right\}, \tag{5.116}$$

in which

$$B = \left[1 - \exp\left(-\frac{32}{27}\frac{1}{\varepsilon_k^2}\right)\right]^{-1}. \tag{5.117}$$

The coefficient B is the normalization factor for the distribution of (5.114). It should be noted that for ε_k of 0.35 or less it is essentially equal to unity and the last term in (5.116) is also negligible for this range of values of ε_k. Therefore, (5.116) simplifies as follows

$$F_{r_\mathrm{th}} = \exp\left[-8\left(\frac{r_\mathrm{th}}{H_\mathrm{s}}\right)^2\left(1 - \frac{\varepsilon_k r_\mathrm{th}}{H_\mathrm{s}}\right)\right], \tag{5.118}$$

Let us now express the breaking criterion in terms of the downward acceleration threshold

$$\left|\frac{d^2\zeta_c}{dt^2}\right| \geq A\overline{\omega}^2 = \alpha g, \tag{5.119}$$

where α is constant. As was shown above in this chapter, the experimental value for α is equal to about 0.4 and the value of 0.5 given by Stokes may represent an upper bound to the actual value. Using the above breaking criterion in

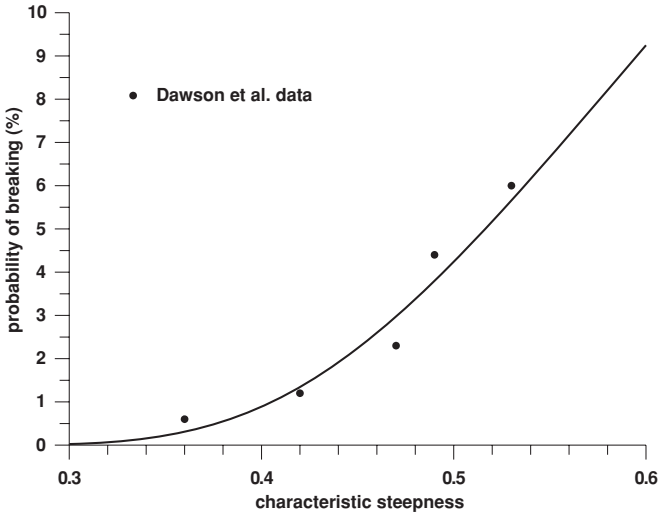

Figure 5.13: Comparison of the theoretical probability of breaking with the experimental Dawson et al. (1993) data.

terms of the critical threshold level for nonlinear crest elevation, $r_{\rm th} = \frac{g\alpha}{\bar{\omega}^2}$, the probability of breaking $F_{\rm br}$ becomes (Dawson et al., 1993)

$$F_{\rm br} = B\left\{\exp\left[-8\left(\frac{\alpha}{\varepsilon_k}\right)^2(1-\alpha)\right] - \exp\left(-\frac{32}{27}\varepsilon_k^{-2}\right)\right\}. \tag{5.120}$$

When the characteristic steepness ε_k is equal to 0.35 or less, probability of breaking $F_{\rm br}$ simplifies as follows

$$F_{\rm br} \approx \exp\left[-8\left(\frac{\alpha}{\varepsilon_k}\right)^2(1-\alpha)\right]. \tag{5.121}$$

In contrast to Srokosz's (1986) solution (5.80), result (5.121) depends indirectly only on the zero and first spectral moments through dependence of ε_k on the significant wave height and mean wave frequency. By visual inspection, the relative number of wave breaking events recorded on the wave probe in laboratory experiments, using a JONSWAP-type sea, has been counted for various characteristic wave steepnesses ε_k, and the value of α was estimated as 0.391. The value of $\alpha = 0.391$ is interpreted as an average condition for active breaking rather than the condition for impending breaking.

Function (5.120) is presented in Fig. 5.13. In the same figure the experimental Dawson et al. (1993) values are shown. These data correspond to the five cases studied. In particular, for the significant wave height $H_{\rm s} = 0.552\,{\rm m}$ and frequency $\omega = 3.08\,{\rm rad/s}$, ($\varepsilon_k = 0.53$), 95 waves of a total 1580 waves were broken, resulting in the probability of breaking equal 6%. For the smallest waves ($H_{\rm s} = 0.369\,{\rm m}$, $\bar{\omega} = 3.91\,{\rm rad/s}$, $\varepsilon_k = 0.36$) only seven breakers of total 1180 waves were observed, and the probability of breaking is equal 0.6%.

Chapter 6

Energy dissipation due to wave breaking

6.1 Introduction

Despite great efforts, present knowledge of breaking wave statistics and the related energy dissipation is fragmentary. Our ability to quantify wave breaking processes is inhibited by the absence of good quantitative measures of the distribution of breaking. Numerical models developed during the last 30 years on wind wave mechanics have been based on the transport or spectral balance equation incorporating three dynamical processes: energy input from the wind, wave–wave interactions and dissipation by wave breaking. The first two are distinct dynamical processes that have attracted considerable theoretical, experimental and observational attention, and they are considered in principal calculable. In contrast, dissipation still remains a problem. In his pioneering work, Hasselmann (1974) proposed a dissipation source function that incorporated only some general physical constraints together with many empirical data modified over the years. He argued that although wave breaking is locally a highly nonlinear process, it is in general weak in mean and the spectral dissipation should be a quasi-linear function of $S(\omega)$ with a damping coefficient proportional to the square of the frequency ω. Another approach taken by Kitaigorodskii (1983, 1992), Zakharov and Zaslavskii (1982, 1983) and others, was based on the weak turbulence theory of wind waves. It was assumed that energy input from the wind occurs to the largest waves and that dissipation is concentrated at the smallest scales. This theory provides spectral shapes close to those observed, except for shapes over frequencies that are large compared with those of the spectral peak. Komen et al. (1984) revised the Hasselmann solution and developed an expression for the damping coefficient by numerical simulations on the form of this coefficient to reproduce the characteristics of the Pierson–Moskowitz spectrum in the high frequency range.

Phillips (1985) proposed the equilibrium range theory for wind-generated gravity waves in which all three processes are comparable. Under steady wind

conditions, a quasi-equilibrium develops at high frequencies. The net energy supplied by the other processes determines the number density and distribution characteristics of the breaking events. Phillips based his theory on Toba's spectrum form $S(\omega) \approx u_* g \omega^{-4}$ and rates of momentum and energy loss from the wave field by breaking. The resulting amount of energy lost was found to be proportional to the integral of the function $\approx \omega^{11} S^3(\omega)$ over the high frequency range.

The physical arguments suggest that the loss of energy during breaking should be equal to the difference between the square of the current wave amplitude and square of the limiting wave amplitude which corresponds to the stable condition after breaking. This rationale is behind the Longuet–Higgins (1969) solution for the energy loss during wave breaking for a very narrow frequency spectrum. In Section 6.3 this approach was extended to the two-dimensional probability density function $f(A, \omega)$.

6.2 Experiments on the rates of energy dissipation in breaking waves

The experiments on wave breaking reported in Chapter 4 provide several estimates of rates of energy dissipation due to breaking. In particular, Bonmarin (1989) in his measurements of breaking shows the wavelength decreasing by approximately 20%, the wave height decreasing by approximately 50%, and the steepness of the forward face of the wave decreasing by approximately 75% during breaking. Rapp and Melville (1990) concluded that more than 90% of the total energy lost from the wave field is dissipated within four wave periods after the inception of breaking, and the active breaking itself lasted for a time comparable to the wave period.

Here we give some additional experimental data on the rate of energy dissipation in breaking waves obtained from a different perspective. Thus, let us consider a section of length L of the crest of one wave. The rate of energy loss associated with this section of the simplified two-dimensional wave field is ELN_{br}, where N_{br} is the number of breaking waves per wave given by (4.7). If L_0 is the wavelength of the dominant wave, the rate of energy loss per unit surface area becomes (Thorpe, 1993)

$$E_{\mathrm{dissrate}} = \frac{ELN_{\mathrm{br}}}{LL_0} = \frac{EN_{\mathrm{br}}}{L_0} = (1.9 \pm 1.1) \times 10^{-4} \rho_{\mathrm{w}} \left(\frac{V_{10}}{C_0}\right)^3 \frac{C_{\mathrm{br}}^5}{gL_0} \tag{6.1}$$

or

$$E_{\mathrm{dissrate}} = (3.0 \pm 1.8) \times 10^{-5} \rho_{\mathrm{w}} \left(\frac{C_{\mathrm{br}}}{C_0}\right)^5 V_{10}^3 \quad [\mathrm{J/m^2\,s}], \tag{6.2}$$

in which C_{br} is the phase speed of the breaking waves measured relative to the underlying flow. The characteristic phase speed of the breaking waves C_{br} has been estimated in a few laboratory experiments. Oakey and Elliot (1982)

concluded that if the energy lost from a breaking wave supports the turbulence in the mixed layer, $C_{\rm br}/C = 0.25$. A similar value was obtained by Thorpe (1993). If we use the estimates of dissipation rates for spilling unsteady waves, there is a surface layer an order of magnitude shallower than the mixed layer in which the dissipation rates are one to two orders of magnitude higher and $C_{\rm br}/C \approx 0.40 - 0.63$.

Duncan (1981) found that the velocity of the breaking front provides a useful tool to define the energy loss from the waves to turbulence per unit length of front. In a continuing active breaker in deep water, the breaking zone extends down the forward face of the wave over a fixed fraction of its amplitude and its shape is geometrically similar for waves of different scales, which implies that the breaking waves themselves are geometrically similar. In particular, the wavelength, the crest-to-trough amplitude and the vertical extent of the breaking region were all proportional to the phase-speed squared, i.e.

$$L_{\rm br} = 5.765\,\frac{C_{\rm br}^2}{g}, \tag{6.3}$$

$$a_{\rm br} = 0.6\frac{C_{\rm br}^2}{g}, \tag{6.4}$$

$$L\,\sin\theta = \frac{a_{\rm br}}{1.6} = 0.375\,\frac{C_{\rm br}^2}{g}. \tag{6.5}$$

It should be noted that the inclination of a breaking wave's forward face θ ranges from 10 to 14.7°. The breaking region thickness, divided by its length, was found to be the same for all conditions, and the cross-sectional area of the breaking zone was proportional to the square of the local wavelength, or to $\left(\frac{C_{\rm br}^2}{g}\right)^2$.

The measurements on breaking waves produced by towing a submerged, two-dimensional hydrofoil showed that the breaking region produced a shearing force along the forward face of the wave. The force was equal to the component of the region's weight in the direction of the stress. The weight of the breaking zone per unit length of the front exerts a tangential force per unit length which is proportional to $\frac{C_{\rm br}^4}{g}$. This force acts on the incoming stream of the speed of $C_{\rm br}$. Therefore, the rate of energy loss per unit length of front becomes $b\rho_{\rm w}\left(\frac{C_{\rm br}^5}{g}\right)$, where b is a numerical constant. In particular Duncan (1981) found

$$E_{\rm dissrate} \sim 0.009\rho_{\rm w}\,\frac{C_{\rm br}^5}{g\sin\theta} \quad [{\rm J/m\,s}], \tag{6.6}$$

where θ is the angle of inclination of the breaking region to the horizontal. The inclination θ of the breaking region was in the range $12.5 \pm 2.5°$. Therefore (6.6) can be rewritten as

$$E_{\rm dissrate} = (0.044 \pm 0.008)\,\frac{\rho_{\rm w} C_{\rm br}^5}{g}. \tag{6.7}$$

Moreover, Duncan (1983) in his measurements of 1983 showed that the inclination of the forward face of the breaking wave changes significantly with changes in the depth of submergence of the hydrofoil and the dissipation rate per unit length becomes

$$E_{\text{dissrate}} = 0.0075\,\frac{\rho_{\text{w}} C_{\text{br}}^5}{g\sin\theta}. \tag{6.8}$$

Melville and Matusov (2002) by their measurements of wave breaking using aerial imaging found that the distribution of the length of a breaking front per unit area of sea surface is proportional to the cube of the wind speed and decays exponentially with C_{br} and proportionality constant b is in the range $\mathcal{O}(10^{-3} - 10^{-2})$, being dependent on the steepness of the waves. They argue that breaking can be measured by remote techniques, and that the distribution of the average length of a breaking crest is directly relevant for ocean-surface processes. In particular, wave dissipation is proportional to V_{10}^3 and dominated by intermediate scale waves. On the other hand, the fraction of the ocean mixed by breaking waves per unit time, being also proportional to V_{10}^3, is dominated by the shorter breaking waves.

In general, surface waves are characterized by an amplitude as well as a phase speed and dispersion relationship. Therefore, the rate of dissipation would not depend only on the phase speed of the wave. To get some insight into the rate of dissipation due to unsteady breaking, Rapp and Melville (1990) examined the relationship between the total energy dissipated and an integral slope parameter. Their dye measurements (see Section 4.4.2) showed that there is a layer of enhanced dissipation at the surface having a thickness D of the order of wave height and a length comparable to the wavelength L and the dissipation rate per unit length of crest E_{dissrate} is given by

$$E_{\text{dissrate}} \approx \frac{\rho_{\text{w}}\tilde{u}^3}{l}\,\frac{DL}{2}, \tag{6.9}$$

in which l is some integral length scale. Scaling all the lengths and velocities with the wave variables $\tilde{u} = \chi C_{\text{br}}$ and $L = 2\pi\frac{C^2}{g}$, (6.9) can be rewritten as follows (Melville, 1994)

$$E_{\text{dissrate}} \approx \frac{\rho_{\text{w}}\pi}{g}(\chi C_{\text{br}})^3\, C_{\text{br}}^2. \tag{6.10}$$

Rapp and Melville (1990) estimated a numerical constant χ to be in the range 0.1–0.17. Therefore, the dissipation rate per unit length of crest becomes

$$E_{\text{dissrate}} \approx (3.2\times 10^{-3} \div 1.6\times 10^{-2})\,\frac{\rho_{\text{w}} C_{\text{br}}^5}{g}, \quad \chi = 0.1,\ 0.17 \tag{6.11}$$

Also Phillips et al. (2001) suggested using the velocity of breaking waves as a measure of breaking scale. The speed of breaking events as determined by Ding and Farmer (1994) was in the range 0.4–0.7 of the wind speed. As in a fully

developed sea the dominant wave phase speed C is close to the wind speed, it means that the mean breaking event speed C_{br} is considerably smaller than C. This result implies the importance of higher frequency components which are those components propagating at lower speed than the dominant waves. They reported the results of a set of X-band radar measurements, backscattered from the sea surface with very high spatial and temporal resolution when radar cross sections were of the order of $1\,\mathrm{m}^2$. They found that the observed fastest breaking events had line-of-sight speeds of about 0.6 of the dominant wave speed. Phillips et al. (2001) determined the distribution of wave energy dissipation by breaking and momentum flux to the water by breaking waves. In particular, using the experimental data on the average shape of broken area, the distribution $\Lambda(C)$ of the length of breaking front per unit area of surface with respect to speed was determined. The analysis was based on the assumption that a single breaking event, being initiated at some point on the wave crest, spreads laterally so that its average length is of an order of half its ultimate length, which is equal to the width of the broken patch. According to Thorpe (1993), the expected ultimate length is about $0.7\,C\tau$, where C is the speed of wave crest and τ is duration. Therefore, the expected length of breaking front to be observed at an arbitrary instant is $\alpha C\tau(\tau/T)$, in which T is the total observation time and α is the numerical constant. If we now consider all events in the speed range $C, C + \Delta C$, then the expected total length of breaking fronts at any instant of the observation time period becomes $\alpha\Sigma C\tau(\tau/T)$, where the summation is over all events in that speed interval. Moreover, if A represents the swath area of the sea surface under observation, then the average length of breaking front per unit area per unit speed interval is (Phillips et al., 2001)

$$\Lambda(C) \approx \alpha C(\Sigma\tau^2)/(AT\Delta C). \tag{6.12}$$

This function plays an important role in the statistical mechanics of breaking waves controlling the generation of turbulence in the upper mixed layer, the momentum flux from waves to the upper layer and the rate of exchange of gases across the air–sea interface. The function $\Lambda(C)$ has been calculated by Phillips et al. (2001) from the measured statistics of breaking events with use of (6.12). They showed that faster, generally larger breaking events make smaller contributions to the total length of a breaking front than do slower, smaller events. This is due to the increased frequency of the latter. However, the most interesting result of the Phillips et al. experiment is related to the distribution of wave energy lost by wave breaking. As was shown above, the rate of energy loss per unit length of breaking front is proportional to $b\rho_{\mathrm{w}}\frac{C^5}{g}$. Making use of the data on $\Lambda(C)$, Phillips et al. (2001) argued that the distribution of wave energy dissipation by breaking can be expressed as follows:

$$\frac{E_{\mathrm{diss}}}{b} \approx \alpha\rho_{\mathrm{w}}\frac{C^5}{g}\Lambda(C). \tag{6.13}$$

The resulting distribution is broadbanded over the range of event speeds above about 3 m/s. Therefore, there is no support for the basic assumption of the

weak turbulence theory of wind waves that the energy dissipation from waves is concentrated at the smallest scales.

Wave energy at a given frequency, reduced due to wave breaking, may also change because of the input from wind and possible energy transfer to or from waves of different frequencies. These facts complicate the direct measurements of energy dissipation due to wave breaking in nature. On the other hand, the measurements in the laboratory flumes provide an alternative to get some insights into the energy lost during wave breaking. When no wind is present in the wave flume and the energy transfer among different wave frequencies is negligible due to the small length scale of the wave breaking, the differences in energy before and after an isolated breaker can be viewed as the dissipation due to wave breaking. Rapp and Melville (1990) by comparing the spectra measured before and after an isolated breaker found that major energy loss occurs at the 'second harmonic' band and the low-frequency waves propagate through breaking without significant loss of energy. They reported that even though the wave was not breaking, the spectra at different locations changed significantly at high and low frequencies. Melville (1996) pointed out that spectra at low frequency displayed a slight increase downstream of the breaking region. He suggested that this fact may be a result of change in the gradients of the radiation stress accompanying breaking. This means that breaking is not just a sink of wave energy, but can also be a source for waves of low frequencies. A similar conclusion has been obtained by Kway et al. (1998).

Meza et al. (2000) conducted laboratory studies to quantify the energy dissipation as a function of wave frequency, caused by various types of isolated breakers. They found that significant changes in both high- and low-frequency bands of the wave spectra, measured at different locations along a wave staffs, even in the absence of wave breaking, are possibly due to the presence of bound-wave components which interfere with the changes due to wave breaking in the same frequency bands. Due to the nonlinear nature of surface waves, the free-wave components interact among themselves. In particular, when relatively low-frequency free-wave components overtake relatively high-frequency free-wave components near the location of breaking, the interaction among them produces bound-wave components and energy at very high and low-frequency bands significantly increases just before breaking (Rapp and Melville, 1990; Kway et al., 1998). However, when the low-frequency free-wave components surpass the high-frequency components downstream of breaking, the interactions between free-wave components disappear and so do the corresponding bound-wave components. Thus, occurrence and disappearance of bound-wave components along the wave flume can make the spectra at different locations quite different. Moreover, because the phase velocities of a free-wave and bound-wave component of the same frequency are different, the resultant amplitude and spectra change from one location to another.

In other words, the presence of bound-wave energy contaminates the measurements of energy loss and gain due to wave breaking through a direct comparison

of the wave spectra measured before and after breaking. Therefore it is desirable to decouple the contributions of the bound-wave components from the measured elevation. Meza et al. decoupled the bound-wave components using the hybrid wave model developed by Zhang et al. (1996). In the absence of bound-wave components, the free-wave spectra of steep wave trains become almost steady when no wave breaking appears. The dependence of energy dissipation on wave frequency can now be more accurately determined simply by comparing the free-wave amplitude spectra before and after an isolated breaker. The authors found that wave breaking in the irregular wave train mainly consumes energy of frequencies significantly higher than the spectral peak frequency. The wave components of frequencies close to the spectral peak frequency lose or gain an insignificant amount of energy during breaking, although their energy is the greatest among all wave components. Wave components of frequencies below the spectral peak gain a small portion of energy lost by the wave components of high frequencies.

Ding and Farmer (1994) reported the statistics of breaking surface waves in the open ocean obtained from observations during the Surface Wave Processes Program with a novel acoustic instrument tracking individual breaking events. The observations confirm the fact that wave breaking occurs at multiple scales. The mean breaking event speed C_{br} is found to be in the order of 45%–75% of the phase speed of the dominant wind wave due to the contribution of breaking of small scale waves. Their data were also used to obtain statistical insights into breaking event density, duration and velocity. Event density is defined here as the number of events per unit time, and experiments showed that the event density lies in the range $0.2 \div 1.1\,(\times 10^{-3}\mathrm{m}^{-2}/\mathrm{s})$ for these data. Moreover, the dominant breaking wave scale increases with increasing wind, resulting in a decrease in the total number of breaking waves detected per unit area. However, the data show no significant dependence on wave age, possibly because the sea states were essentially fully developed.

To quantify the whitecap coverage, Ding and Farmer introduced so-called active acoustic coverage, the fraction of the sea surface swept by active acoustic events during their lifetime. The mean area swept by each individual event is given by $\overline{L_{\mathrm{D}}L_{\mathrm{c}}} \approx 2\bar{L}_{\mathrm{D}}^2$, in which L_{D} is the distance a breaking event travels and L_{c} is the cross dimension $\approx 2\,L_{\mathrm{D}}$. Therefore, the active acoustic coverage AC becomes

$$AC = \frac{2\bar{L}_{\mathrm{D}}^2}{\bar{l}_{\mathrm{s}}^2}, \tag{6.14}$$

where $\bar{l}_{\mathrm{s}}$ is the mean spacing of the breaking events. Ding and Farmer found that AC is a function of the inverse fourth moment m_4^{-1} of the frequency spectrum. This dependence appears to agree closely with the Snyder and Kennedy (1983) model when we choose the proportionality coefficient α to the gravity acceleration to be 0.082. However, this value is extremely low compared with that found in the laboratory by Ochi and Tsai (0.40) and that of Snyder et al. (1983) when $0.25 < \alpha < 0.40$. The low value of α is due to the sensitivity of

the acoustic system to detection of breaking events that do not show up for the same duration, and due to underestimation of moment m_4.

The rate of turbulent kinetic energy dissipation E_{dissrate} in the upper oceanic layers is of great importance for mixing of near surface waters, mass transfer across the interface, dispersal of buoyant pollutants and the thermocline development. Measurements of dissipation close to the surface obtained in a large lake, under conditions of strong wind, were reported by Terray et al. (1996). They found that the conventional estimates of the dissipation rate of turbulent kinetic energy, based on the wall layer analogy, i.e. $\frac{u_*^3}{\kappa z}$, where u_* is the friction velocity in the water, z is the depth, and κ is von Kármán constant 0.4, are too small by an order of magnitude in moderate and strong winds. Instead they propose a wave-dependent scaling of dissipation in the form

$$\frac{E_{\text{dissrate}} H_{\text{s}}}{u_*^2 \overline{C}} = 0.3 \left(\frac{z}{H_{\text{s}}} \right)^{-2}, \tag{6.15}$$

in which H_{s} is the significant wave height and $\overline{C}$ is the effective phase speed related to wind input in terms of this speed and the wind stress τ_a, namely

$$\frac{\tau_a \overline{C}}{\rho_{\text{w}}} \approx u_*^2 \overline{C}. \tag{6.16}$$

This scaling confirms that energy flux from the wind depends on the wave spectrum and its development.

6.3 Theoretical models of wave energy dissipation

As we showed in the preceding chapters, direct measurements of the total dissipation due to wave breaking in the field are not yet feasible. Also there have been several attempts to explore the wave breaking process in the laboratory tests and by mathematical modelling. In Chapter 2, theoretical and numerical works were discussed. However, those attempts were focused on the breaking of a single wave. If we are dealing with a random wave field, the energy dissipation potentially would be estimated from the energy budget expressed in the wind-wave evolution models. In this section, three different approximate methods are considered, namely: equilibrium range model, whitecap model for fully developed wind sea and probability model.

6.3.1 Equilibrium range model

In this approach, the fundamental assumption is that the whitecapping process is essentially local in the wave number space. The wave breaking process is highly nonlinear in wave steepness, but this nonlinearity has no effect until some limiting steepness is achieved. At that time waves become unstable

and break, producing a whitecap and inducing a substantial energy loss. For a wave spectrum which is smooth and continuous, the breaking energy loss may be associated at a particular wave number or at a range of wave numbers surrounding it. The evolution of the surface wave field can be represented in the form of an energy balance equation as follows (Phillips, 1985)

$$\rho_{\mathrm{w}} g \left(\frac{\partial S}{\partial t} + C_{\mathrm{g}} \frac{\partial S}{\partial x} \right) = S_{\mathrm{w}} + S_{\mathrm{nl}} - S_{\mathrm{diss}}. \tag{6.17}$$

The components with wave numbers, large compared with that of the spectral peak, approach a state of statistical equilibrium determined by a balance among the wave-wave interactions, action input from the wind and energy loss by breaking, i.e.

$$S_{\mathrm{w}} + S_{\mathrm{nl}} - S_{\mathrm{diss}} = 0, \tag{6.18}$$

where S_{w} is the rate of spectral input from the wind, S_{nl} denotes the net spectral flux of energy action through the wave numbers $\vec{k}$ by resonant wave-wave interactions and S_{diss} is the energy loss by breaking. With an assumption that all of these processes are important in the equilibrium range, and that the wave number and wave frequency spectra take the forms suggested by Toba (1973), we obtain (Hanson and Phillips, 1999)

$$\Psi(\vec{k}) = \beta_1 (\cos \Theta)^s \, u_* g^{-1/2} k^{-7/2}, \tag{6.19}$$

and

$$S(\omega) = \alpha_1 g u_* \omega^{-4} = 4 \beta_1 I(s) u_* g \omega^{-4}, \tag{6.20}$$

in which u_* is the friction velocity in the air, $I(s)$ is a spreading function given by

$$I(s) = \int_{-\pi/2}^{\pi/2} (\cos \Theta)^s d\Theta = B\left(\frac{1}{2}, \frac{1}{2}(s+1) \right), \tag{6.21}$$

in which $B(m, n)$ is the beta function (Abramowitz and Stegun, 1975), the Θ is the angle between the wave number and the wind and value of s may be deduced from observational data. The numerical constant β_1 is related to Toba's constant α_1 and $I(s)$ as follows

$$\beta_1 = \frac{\alpha_1}{4 I(s)}. \tag{6.22}$$

Phillips (1985) argued that the lower and upper bounds of the directional spreading parameter s are 0.5 and 2, respectively, while the α_1 value ranged from 0.06 to 0.11 in experimental data reviewed by Phillips. The above assumptions result in the spectral energy dissipation term in (6.17) as follows

$$S_{\mathrm{diss}}(\omega) = \frac{\gamma_1 I(3s) \rho_{\mathrm{w}}}{16 [I(s)]^3 g^3} \omega^{11} \, S^3(\omega) \quad [\mathrm{J/m^2}]. \tag{6.23}$$

Integration of the above equation provides the total energy dissipation rate as (Hanson and Phillips, 1999)

$$E_{\text{dissrate}} = \frac{\gamma_1 I(3s)\rho_{\text{w}}}{16[I(s)]^3 g^3} \int_{\omega_{\text{p}}}^{\infty} \omega^{11}\, S^3(\omega) d\omega \quad [\text{J/m}^2\text{s}], \tag{6.24}$$

in which

$$\gamma_1 \approx \frac{0.04}{\beta_1^2} = 0.04 \left(\frac{\alpha_1}{4I(s)}\right)^{-2}. \tag{6.25}$$

It should be noted that as the directional distributions are now routinely measured, the terms $I(s)$ and $I(3s)$ could be replaced with observational data. The integral in (6.24) will converge as long as the spectral slope of $S(\omega)$ is steeper than ω^{-4} as $\omega \to \infty$. Hence when we apply the equilibrium range spectrum form (6.20), we obtain the total energy dissipation rate expressed in terms of wind and wave parameters (Hanson and Phillips, 1999)

$$E_{\text{dissrate}} = 4\gamma_1 \beta_1^3 I(3s)\rho_{\text{w}} u_*^3 \int_{\omega_{\text{p}}}^{\infty} \omega^{-1} d\omega \quad [\text{J/m}^2\text{s}]. \tag{6.26}$$

The lower limit of the equilibrium range was assumed to be the spectral peak frequency. In order to avoid the infinite value of the above integral, we introduce the upper frequency limit ω_{u}. Then, integrating in (6.26) yields

$$E_{\text{dissrate}} = 4\gamma_1\, \beta_1^3 I(3s)\rho_{\text{w}}\, u_*^3 \ln\left(\frac{\omega_{\text{u}}}{\omega_{\text{p}}}\right) \quad [\text{J/m}^2\text{s}] \tag{6.27}$$

As the dynamic processes controlling wave breaking are specific to gravity waves, the influence of surface tension should be neglected and frequency ω should be restricted to the range $\omega_{\text{u}} \ll \left(\frac{4g^3}{\gamma}\right)$, where γ is the ratio of surface tension to water density. However, Phillips (1985) argued that this upper limit should be determined by the presence of wind drift which suppresses the formation of high frequency waves travelling at the same velocity. Using this argument, the upper limit of frequency becomes $\omega_{\text{u}} = \sqrt{r}_1 \frac{g}{u_*}$, where r_1 is a constant of order one. The total rate of wave energy dissipation is controlled largely by the coefficient $\gamma_1\, \beta_1^3 I(3s)$. Felizardo and Melville (1995) indicate that the value of this coefficient is in the range $(3.7 - 8.0) \times 10^{-4}$.

In Fig. 6.1, the total energy dissipation rate, according to (6.27), is shown for wind speed $2 < V_{10} < 20$ m/s and two wind fetches $X = 20$ and 100 km. For calculation the following values of parameters were used: $s = 2$, $\alpha_1 = 0.08$, $\gamma_1\, \beta_1^3 I(3s) = 0.000498$ and $r = 0.16$. The set of two lines shows almost linear dependence of the total dissipation rate on the wind speed in the log–log scales scheme. The influence of the wind fetches is very weak and the rate is almost identical for the chosen fetches.

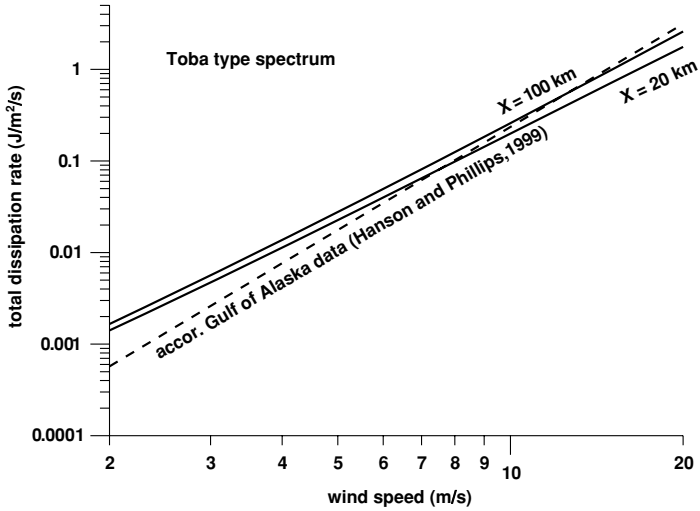

Figure 6.1: Dependence of the total dissipation rate E_{dissrate} on the wind speeds and wind fetches according to Phillips' (1985) model. Toba's type spectrum assumed.

Hanson and Phillips (1999) estimated the total rate of wave energy dissipation in the equilibrium range directional spectra in the Gulf of Alaska and found that these estimates were fairly well correlated with the wind speed as follows

$$E_{\text{dissrate}} = 4.28 \times 10^{-5}\, V_{10}^{3.74}, \tag{6.28}$$

with a correlation coefficient of $r = 0.82$. The function (6.28) was added in Fig. 6.1 for comparison showing a reasonably good agreement. However, Hanson and Phillips stressed that wind history, expressed in terms of wind speed acceleration and attenuation, can significantly influence wind sea growth and its substantial dissipation.

Additionally in Fig. 6.2 the total energy dissipation rate resulting from (6.24) is shown for the JONSWAP spectrum (3.19) for wind fetches $5 < X < 300$ km and for four wind speeds $V_{10} = 5$, 10, 15, 20 m/s. The directional spreading was assumed to be proportional to $\cos^2\Theta$, while parameters $\alpha_1 = 0.08$ and $\gamma_1 = 248$. In the log–log reference scheme, the dependence of total energy dissipation rate on the wind fetch for a given wind speed is almost linear.

The total energy dissipation rate for the Donelan et al. (1985) spectrum (3.24), which exhibits ω^{-4} behaviour at high frequencies, is shown in Fig. 6.3 for comparison. It should be noted that all spectra provide similar energy dissipation rates and exhibit similar dependence on wind speed.

Let us now consider the energy balance equation for a stationary wave field characterized by a one-dimensional spectrum (Komen et al., 1994)

$$\rho_{\text{w}} g C_{\text{g}} \frac{\partial S}{\partial x} = S_{\text{w}} + S_{\text{nl}} - S_{\text{diss}}. \tag{6.29}$$

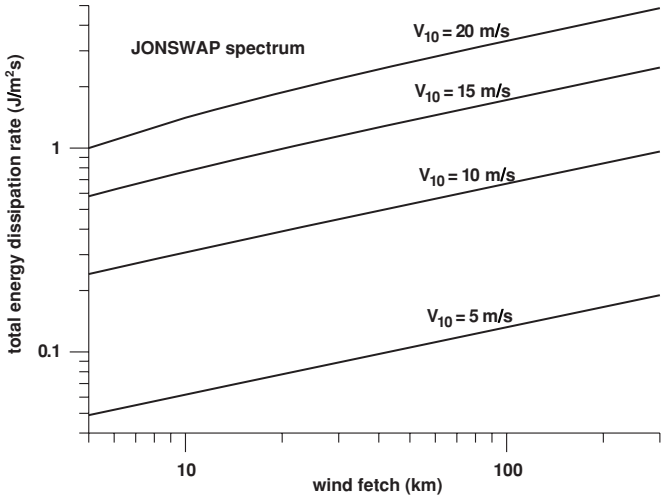

Figure 6.2: Dependence of the total dissipation rate E_{dissrate} on wind speeds and wind fetches according to Phillips (1985) model. JONSWAP spectrum assumed.

In particular we assume that waves are generated by wind in some restricted water basin or by a wave-maker in a wave tank, and subsequently propagate outside. The energy generation factor is absent and the nonlinear interactions between wave components are weak when dimensions of the water basin are limited or when the time of wave propagation is restricted. Therefore, the energy

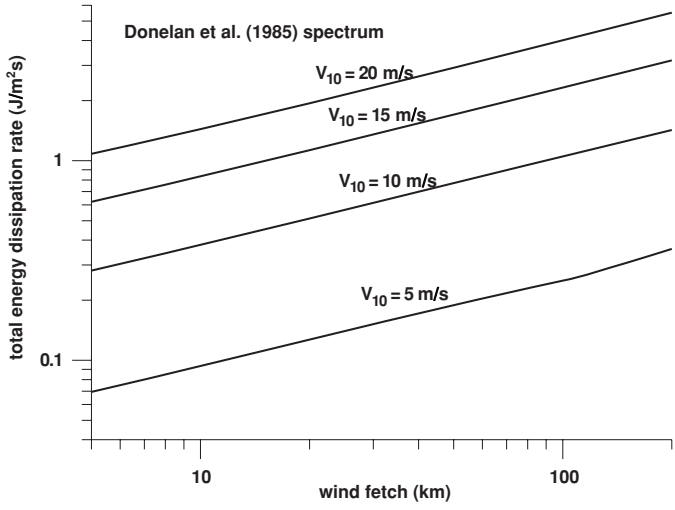

Figure 6.3: Dependence of the total dissipation rate E_{dissrate} on wind speeds and wind fetches according to Phillips (1985) model. Donelan et al. (1985) spectrum assumed.

balance in the region outside the generation area can be further simplified as follows:

$$\rho g C_{\mathrm{g}} \frac{\partial S}{\partial x} = -S_{\mathrm{diss}}(\omega). \tag{6.30}$$

Thus, the spectral energy density gradient takes the form

$$\rho g \frac{dS(\omega)}{dx} = -\frac{2\omega_{\mathrm{p}}}{g} S_{\mathrm{diss}}(\omega). \tag{6.31}$$

Substitution of (6.23) in (6.31) and integration against ω, yields the linear energy attenuation with a distance x

$$E(x) = E_0 - bx = E_0 \left(1 - \frac{b}{E_0} x\right), \tag{6.32}$$

in which E_0 is the wave energy at point $x = 0$ and b is the energy attenuation gradient given as

$$b = \frac{\gamma_1 I(3s) \rho_{\mathrm{w}} \omega_{\mathrm{p}}}{8[I(s)]^3 g^4} \int_{\omega_{\mathrm{p}}}^{\omega_{\mathrm{u}}} \omega^{11} S^3(\omega) d\omega \tag{6.33}$$

Equation (6.32) indicates that the energy attenuation along the x axis due to breaking depends totally on the wave parameters at the initial point $x = 0$. For illustration, the energy attenuation gradient, b, for wind fetch $X = 50\,\mathrm{km}$ and the wind speed in the range $2 < V_{10} < 20$ m/s for two different wave spectra, namely the JONSWAP and Toba's type spectra, is shown in Fig. 6.4. In Fig. 6.5,

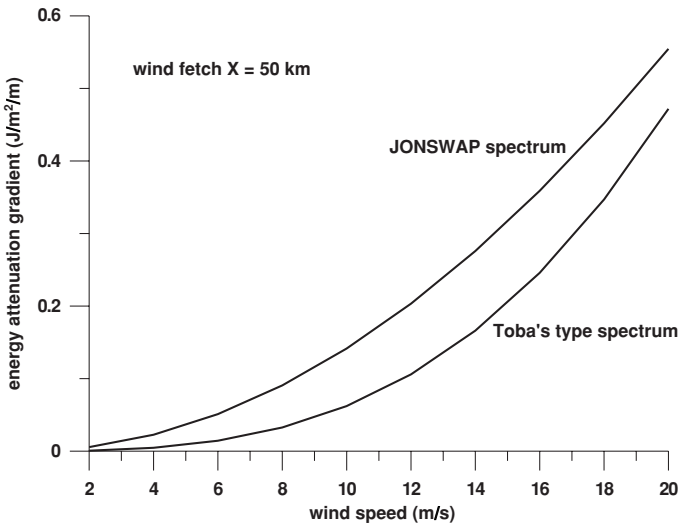

Figure 6.4: Energy attenuation gradient versus wind speed for the JONSWAP and Toba's type spectra.

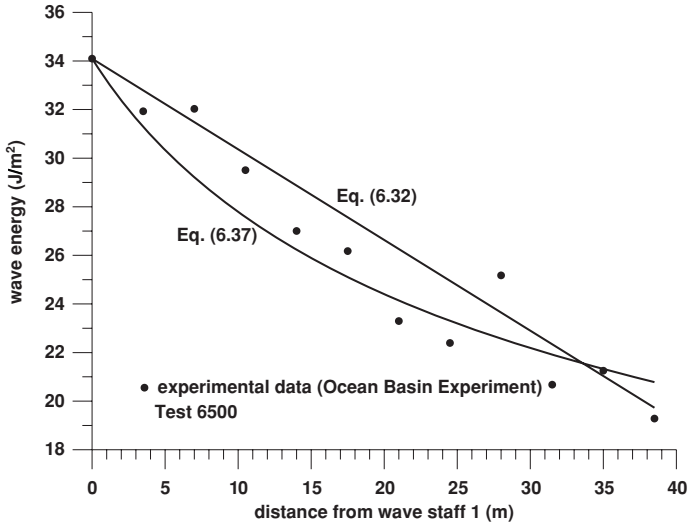

Figure 6.5: Comparison of experimental wave energy attenuation with theoretical solutions (6.32) and (6.37).

the comparison of function (6.32) with experimental data collected during the Ocean Basin Experiment (Massel et al., 2001) is shown. Test 6500 with the following parameters at the initial wave staff 1 (see Fig. 4.4) was chosen: $H_s = 0.23, \omega_p = 4.08$ rad/s and $E_0 = 34.09$ J/m^2. Mechanically generated waves corresponded closely to the JONSWAP spectrum with peak enhancement $\gamma = 7.0$, and directional energy spreading was characterised by function $\cos^2\Theta$. The approximate solution, exhibiting linear wave energy attenuation, agrees well with the observed energy attenuation. However, it should be noted that the approximate solution (6.32) is a local solution when energy attenuation depends on the energy E_0 at some reference point. Still, it can serve as a predictive tool for energy distribution in the breaking wave field of the spatial scale, say of a dozen wavelengths, corresponding to the spectral peak frequency.

Let us now assume that the energy attenuation depends on the local frequency spectrum which due to energy dissipation is a function of distance x too. Using (6.23), equation (6.31) takes the form

$$\frac{\partial S(\omega;x)}{\partial x} + b_1 S^3(\omega;x) = 0, \tag{6.34}$$

in which

$$b_1 = \frac{\gamma_1 I(3s)\omega_p \omega^{11}}{8[I(s)]^3 g^5}. \tag{6.35}$$

Solution of (6.34) becomes

$$S(\omega;x) = \frac{S(\omega;x_0)}{\sqrt{1 + 2b_1(x-x_0)S^2(\omega;x_0)}}, \tag{6.36}$$

where $S(\omega; x_0)$ is the known spectrum at initial location $x = x_0$. Integration of (6.36) against frequency ω provides the wave energy dependence on distance x as follows

$$E(x) = \rho_{\mathrm{w}} g \int S(\omega; x) d\omega \tag{6.37}$$

Function (6.37) was included in Fig. 6.5 for comparison. The solution (6.37) results in nonlinear energy attenuation with distance x. However, when comparing the equilibrium model with experimental data it should be noted that there is some uncertainty about proper selection of parameters α_1, β_1 and γ_1 which correspond to the frequency spectrum with ω^{-4} dependence in the equilibrium range.

6.3.2 Whitecap model of wave energy dissipation for fully developed wind-sea spectrum

The whitecap model, originally developed by Hasselmann (1974), was used in the wave prediction model WAM (Komen et al., 1994). The starting point of the model is the assumption that the space and time scales of the whitecapping process are small compared with the characteristic wavelengths and periods of the waves, which implies that the whitecapping process is highly local in physical space and time. Moreover, from Duncan's (1981) experiments (see Chapter 4) it follows that the whitecaps and underlying waves are in geometric similarity. This similarity implies that a combination of the pressure exerted by the whitecap on the surface of the waves and induced energy decay as well as the attenuation of short waves by passage of large whitecaps yields the dissipation function in the form (Komen et al., 1984)

$$S_{\mathrm{diss}} = C_{\mathrm{diss}} \rho g \left(\frac{\hat{\alpha}}{\hat{\alpha}_{PM}} \right)^m \left(\frac{\omega}{\overline{\omega}} \right)^n \overline{\omega} S(\omega), \tag{6.38}$$

in which C_{diss}, m, and n are fitting parameters, $\overline{\omega}$ is the mean radian frequency and $\hat{\alpha}/\hat{\alpha}_{PM}$ is a measure of the overall steepness of the wave field. It should be noted that for $m = 0$ and $n = 1$, the expression (6.38) agrees with Hasselmann's (1974) result.

Komen et al. (1984) showed that quasi-stationary solutions of the energy transfer equation can exist, provided the dissipation parameters lie in a certain region of the parameters' space. In particular, they suggested the following values: $C_{\mathrm{diss}} = 3.33 \times 10^{-5}$ and $m = n = 2$. Additionally, two functions $\hat{\alpha}$ and $\hat{\alpha}_{PM}$ in (6.38) were assumed to have the forms

$$\hat{\alpha}_{PM} = 4.57 \times 10^{-3}, \quad \hat{\alpha} = \frac{m_0 \, \overline{\omega}^4}{g^2}. \tag{6.39}$$

After substituting (6.39) into (6.38) we obtain

$$S_{\mathrm{diss}} = 1.59 \rho g \left(\frac{m_0 \overline{\omega}^4}{g^2} \right)^2 \left(\frac{m_0}{m_1} \right) \omega^2 S(\omega) \quad [\mathrm{J/m^2}] \tag{6.40}$$

or

$$S_{\text{diss}} = 1.59\rho g \left(\frac{m_1^4}{g^2 m_0^3}\right)^2 \left(\frac{m_0}{m_1}\right) \omega^2 S(\omega). \tag{6.41}$$

Therefore, the energy dissipation rate due to wave breaking can be expressed as follows

$$E_{\text{dissrate}} = \rho g \int S_{\text{diss}}(\omega)\, d\omega \quad [\text{J/m}^2\,\text{s}]. \tag{6.42}$$

Substitution of (6.41) into (6.42) and integration gives

$$E_{\text{dissrate}} = 1.59\rho g \left(\frac{m_1^4}{g^2 m_0^3}\right)^2 \left(\frac{m_0 m_2}{m_1}\right) \quad [\text{J/m}^2\,\text{s}] \tag{6.43}$$

or

$$E_{\text{dissrate}} = 1.59\rho g \left(\frac{m_0 \overline{\omega}^4}{g^2}\right)^2 \left(\frac{m_0 m_2}{m_1}\right). \tag{6.44}$$

Using that $m_0 = \dfrac{H_{\text{s}}^2}{16}$ and $\overline{\varepsilon} = \dfrac{H_{\text{s}}}{g\overline{T}^2}$, equation (6.44) can be rewritten as follows

$$E_{\text{dissrate}} = 1.59\pi^8 \rho g\, \overline{\varepsilon}^4 \left(\frac{m_0 m_2}{m_1}\right). \tag{6.45}$$

Applying the definition for the spectral width parameter ν (see (3.7)), we can present the above relationship as

$$E_{\text{dissrate}} = 1.59\rho g(\nu^2 + 1) m_1 \left(\frac{m_1^4}{g^2 m_0^3}\right)^2. \tag{6.46}$$

It should be noted that for extremely narrow spectra, when $\nu \to 0$ and $S(\omega) \approx \sigma_\zeta^2 \delta(\omega - \omega_{\text{p}})$, in which $\delta(\,)$ is Dirac's delta function and σ_ζ^2 is the variance of the spectrum, (6.46) becomes

$$E_{\text{dissrate}} = 1.59\rho g m_1 \left(\frac{m_1^4}{g^2 m_0^3}\right)^2. \tag{6.47}$$

On the other hand for storm waves, the value of ν is usually of the order of $0.3 \div 0.4$. Thus, (6.46) can be presented in the form

$$E_{\text{dissrate}} \approx (1.73 \div 1.84)\rho g\, m_1 \left(\frac{m_1^4}{g^2 m_0^3}\right)^2. \tag{6.48}$$

In Fig. 6.6, the total dissipation rate resulting from (6.44) is shown for wind speeds $5 < V_{10} < 20$ m/s and for wind fetch in the range $5 < X < 300$ km, when the wave field is represented by the JONSWAP spectrum. Comparison of this figure with Fig. 6.2 showed that Komen et al.'s (1984) approach provides a smaller dissipation rate than that resulting from Phillips' (1985) model.

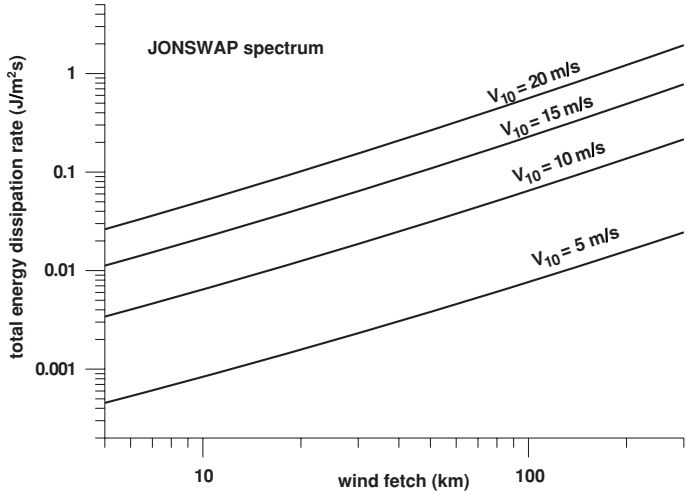

Figure 6.6: Dependence of the total dissipation rate E_{dissrate} on wind speeds and wind fetches according to Komen et al. (1984) model. JONSWAP spectrum assumed.

Komen et al.'s (1984) formulation can also be applied for prediction of energy dissipation of waves escaping from generation area. Using the arguments given above, we obtain

$$\frac{\partial S(\omega;x)}{\partial x} + b_2 S(\omega;x) = 0, \tag{6.49}$$

in which

$$b_2 = \frac{3.18\omega_{\text{p}}\omega^2}{g\overline{\omega}}\left(\frac{m_0\overline{\omega}^4}{g^2}\right)^2. \tag{6.50}$$

Solution of (6.49) becomes

$$S(\omega;x) = S(\omega;x_0)\,\exp[-b_2(x-x_0)], \tag{6.51}$$

where $S(\omega;x_0)$ is the known spectrum at initial location $x = x_0$. From equation (6.50) it follows that the energy attenuation gradient b_2 depends on the mean wave steepness $\overline{\varepsilon}$ and on the peak frequency ω.

Integration of (6.51) against frequency ω provides the wave energy dependence on distance x as follows

$$E(x) = \rho g \int S(\omega;x)d\omega. \tag{6.52}$$

6.3.3 Probability model of wave energy dissipation for very narrow frequency spectrum

This model is a consequence of the philosophy of the limiting wave amplitude which is reached close before breaking. The particular wave breaks in such

a way that its amplitude decreases from the present A value to A_{br} value, representing the critical saturation level. For a narrow frequency spectrum, when all energy is concentrated around one frequency $\omega = \omega_{\mathrm{p}}$, the distribution of wave amplitude A is the Rayleigh distribution, namely

$$f(A) = \frac{2A}{A_{\mathrm{rms}}^2} \exp\left[-\frac{A^2}{A_{\mathrm{rms}}^2}\right], \tag{6.53}$$

in which A_{rms} is the root-mean-square amplitude. Therefore, the current wave energy density is

$$E = \frac{1}{2}\rho g A_{\mathrm{rms}}^2 = \rho g \int_0^\infty S(\omega) d\omega. \tag{6.54}$$

Let us assume now that all waves of amplitude greater than the critical amplitude A_{br} will break. Therefore, the mean local loss of energy per wave cycle and per unit horizontal area becomes (Longuet–Higgins, 1969)

$$E_{\mathrm{diss}} = \int_{A_{\mathrm{br}}}^\infty \frac{1}{2}\rho g \left(A^2 - A_{\mathrm{br}}^2\right) f(A) dA = \frac{1}{2}\rho g A_{\mathrm{rms}}^2 \exp\left(-\frac{A_{\mathrm{br}}^2}{A_{\mathrm{rms}}^2}\right). \tag{6.55}$$

The integral (6.55) is schematically presented in Fig. 6.7 in which E_{diss} represents energy dissipated and converted into turbulence, locally around the sea surface point, at which the amplitudes A_{rms} and A_{br} are known. The limiting wave amplitude A_{br} can be determined from the threshold vertical acceleration at the crest of breaking waves. Using (5.64) and neglecting the influence of surface drift we obtain

$$A_{\mathrm{br}} = \frac{\alpha g}{\omega_0^2}, \tag{6.56}$$

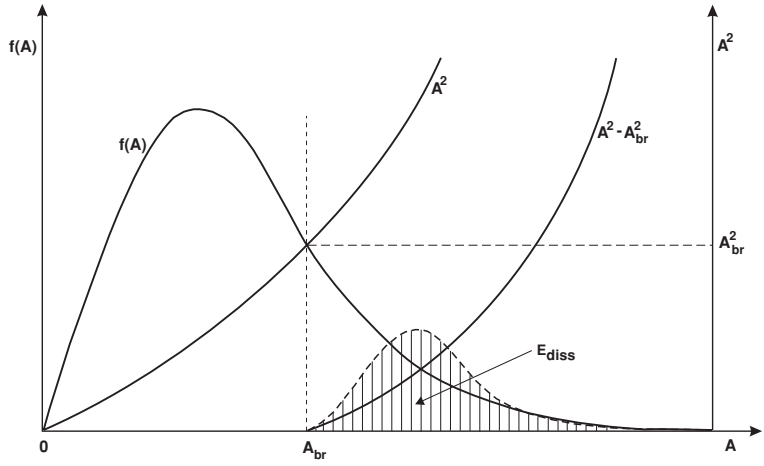

Figure 6.7: Schematic representation of energy dissipation for narrow spectrum.

in which ω_0 is the root-mean-square frequency. Therefore, if the frequency spectrum $S(\omega)$ is known, we have

$$\omega_0^2 = \frac{\int_0^\infty \omega^2 S(\omega) d\omega}{\int_0^\infty S(\omega) d\omega} = \frac{m_2}{m_0}. \tag{6.57}$$

Let us express the root-mean-square amplitude A_{rms} in the form

$$A_{\text{rms}} = \sqrt{2}\sigma_\zeta = \sqrt{2m_0}. \tag{6.58}$$

After substituting (6.56), (6.57) and (6.58) into (6.55), we obtain the mean local loss of energy per wave cycle and per unit horizontal area in the form

$$E_{\text{diss}} = \rho g m_0 \exp\left(-\frac{b_3}{\rho g m_0}\right), \tag{6.59}$$

in which

$$b_3 = \frac{1}{2}\rho g \left(\frac{\alpha g}{\omega_0^2}\right)^2. \tag{6.60}$$

Let us now consider the energy dissipation along the main wave direction. Equation (6.59) provides the local energy dissipated per wave cycle and per unit horizontal area. However, as during one wave cycle the wave moves a distance of one wavelength $\overline{L}_0 = \frac{2\pi g}{\overline{\omega}^2}$, the loss of energy per unit distance along the wave propagation (6.59) becomes

$$E_{\text{dissrate}} = \frac{\overline{\omega}^2}{2\pi g}\rho g m_0 \exp\left(-\frac{b_3}{\rho g m_0}\right), \tag{6.61}$$

Therefore the governing equation for the spectral energy density gradient is

$$\frac{dE(x)}{dx} + \frac{\overline{\omega}^2}{2\pi g} E(x) \exp\left(-\frac{b_3}{E(x)}\right) = 0. \tag{6.62}$$

It should be noted that in equation (6.62) the attenuation of energy due to wave breaking is explicitly taken into account. However, equation (6.62) does not have a closed solution and therefore we solve it numerically. If we know the energy at some point x_i, the predicted energy at point x_{i+1} becomes

$$E_{i+1} = E_i \left[1 - a_i \exp\left(-\frac{b_i}{E_i}\right)\Delta x\right], \tag{6.63}$$

in which $a_i = \left(\frac{\overline{\omega}^2}{2\pi g}\right)$, $b_i = \frac{1}{2}\rho g \left(\frac{\alpha g}{\omega_0^2}\right)^2$ and Δx is a distance between points x_i and x_{i+1} in metres.

In Fig. 6.8, the comparison of wave energy observed at the particular wave staffs distributed along the main profile during the Ocean Basin Experiment (Massel et al., 2001) with theoretical results expressed in (6.63) is shown. In all tests mechanically generated waves correspond to the JONSWAP spectrum

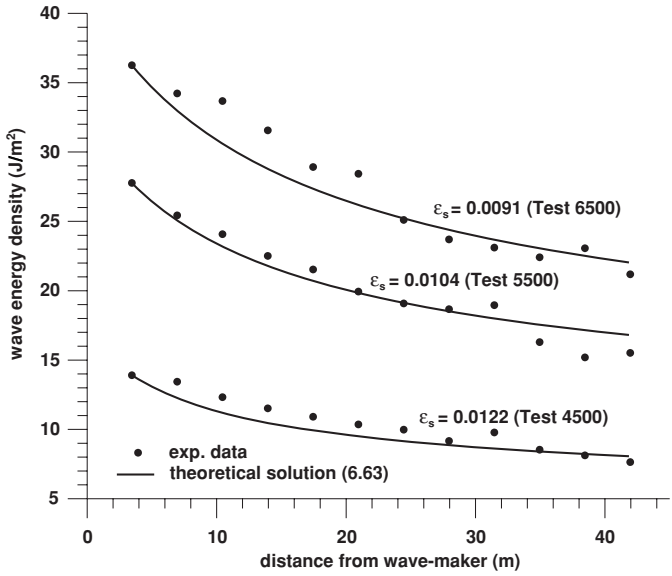

Figure 6.8: Comparison of experimental energy attenuation with theoretical attenuation resulting from Longuet–Higgins' approach.

with enhancement parameter $\gamma = 7.0$ and directional distribution $\approx \cos^2 \Theta$. The initial wave train characteristics were assumed at the wave staff 1 located at 3.45 m from the wave generator (see Fig. 4.4).

As was shown in Section 5.3.3.3, the presence of shorter waves riding on the surface of a long wave results in less stringent conditions for wave breaking initiation. To illustrate this fact, we examined the data from the Ocean Basin Experiment (Test 6500). The root-mean-square wave period T_{rms} increases along the main transect, being equal to 1.391 s at wave staff 1 and increasing up to 1.447 s at wave staff 12. Using the methodology described in Section 5.3.3.3 we first calculated the Eulerian and Lagrangian accelerations, assuming that the 'longer' components can be identified with regular waves of root-mean-square wave height and period. The results of calculations are collected in Table 6.1, which shows that resulting accelerations of the 'longer' component are much lower than the limiting ones, associated with breaking. On the other hand, the best fitting of (6.63) to the experimental data indicates that the mean Eulerian acceleration corresponding to the observed wave breaking along the transect is equal to $0.281\, g$. Comparing this value with accelerations given in Table 6.1 yields the conclusion that the onset of wave breaking appears in spite of lower acceleration of the fundamental wave components. Therefore, as was argued in Section 5.3, generation of additional accelerations due to high frequency components riding on the longer waves may be responsible for irregular wave breaking with smaller downward acceleration.

Table 6.1: Eulerian and Lagrangian accelerations corresponding to the longer wave component of the root-mean-square wave height and period

Wave staff no	Distance from wave-maker	$T_{\rm rms}$ (s)	$H_{\rm rms}$ (m)	$\lvert a_1^{(E)}\rvert/g$	$\lvert a_1^{(L)}\rvert/g$
1	3.45	1.391	0.1720	0.266	0.169
2	6.95	1.395	0.1671	0.253	0.164
3	10.45	1.405	0.1657	0.245	0.160
4	13.95	1.422	0.1604	0.226	0.152
5	17.45	1.409	0.1535	0.219	0.149
6	20.95	1.411	0.1523	0.215	0.147
7	24.45	1.394	0.1431	0.205	0.142
8	27.95	1.412	0.1390	0.190	0.135
9	31.45	1.424	0.1387	0.185	0.133
10	34.95	1.419	0.1352	0.181	0.131
11	38.45	1.446	0.1371	0.175	0.128
12	41.95	1.447	0.1314	0.166	0.123

6.3.4 Probability model for wave energy dissipation based on two-dimensional probability density function $f(A,T)$

For wider wave spectra, the dependence of the limiting amplitude $A_{\rm br}$ on frequencies other than the frequency corresponding to spectrum peak should be taken into account. Therefore instead of (6.55) it should be

$$E_{\rm diss} = \frac{1}{2}\int_0^\infty \int_{A_{\rm br}(T)}^\infty \rho g(A^2 - A_{\rm br}^2(T))\, f(A,T)\, dA\, dT. \tag{6.64}$$

When wave amplitude A, corresponding to the particular period T, is greater than the critical value $A_{\rm br}(T)$, wave energy is dissipated in an amount proportional to the difference $(A^2–A_{\rm br}^2)$ for a given wave period. If $A \le A_{\rm br}(T)$ at a given period, no energy is dissipated. This formulation is an extension of the Longuet–Higgins (1969) approach for a very narrow spectrum concentrated around peak period $T_{\rm p}$ when $f(A,T) = f(A)\,\delta(T–T_{\rm p})$, where $\delta()$ is Dirac's function. To evaluate the amount of energy dissipated during breaking, we apply the two-dimensional probability density $f(A,T)$ proposed by Longuet–Higgins (1983b). After transferring function (3.172) into (A,T) coordinate space we obtain

$$f(A,T) = a_1(T)\, A^2 \exp\left[-b_1(T)\, A^2\right], \tag{6.65}$$

in which

$$a_1(T) = \frac{\overline{T}\, L(\nu)}{\sqrt{2\pi}\,\nu\, m_0^{3/2} T^2} \tag{6.66}$$

and

$$b_1(T) = \frac{1 + \left(1 - \frac{\overline{T}}{T}\right)^2 / \nu^2}{2m_0}. \tag{6.67}$$

Substitution of (6.65) into (6.64) gives

$$E_{\rm diss} = \frac{\rho g}{2} \int_0^\infty a_1(T) \int_{A_{\rm br}(T)}^\infty \left[A^2 - A_{\rm br}^2(T)\right] A^2 \, \exp\left[-b_1(T) A^2\right] dA\, dT. \tag{6.68}$$

To evaluate the integral against amplitude A, let us rewrite it as follows

$$I_A(T) = \int_{A_{\rm br}(T)}^\infty A^4 \exp[-b_1(T)A^2] dA - A_{\rm br}^2(T) \int_{A_{\rm br}(T)}^\infty A^2 \exp[-b_1(T)A^2] dA. \tag{6.69}$$

Substituting $x = A^2$ and $dA = \frac{dx}{2\sqrt{x}}$, we obtain (Gradshteyn and Ryzhik, 1980)

$$\begin{aligned} I_A(T) \;&=\; \frac{1}{2} \int_{A_{\rm br}^2}^\infty x^{3/2} \exp\left[-b_1(T)x\right] dx - \frac{A_{\rm br}^2(T)}{2} \int_{A_{\rm br}^2}^\infty x^{1/2} \exp[-b_1(T)x] dx \\ &= \frac{1}{2} b_1(T)^{-5/2}\, \Gamma\left(\frac{5}{2}, b_1(T) A_{\rm br}^2\right) \\ &\quad - \frac{1}{2} A_{\rm br}^2\, b_1(T)^{-3/2}\, \Gamma\left(\frac{3}{2}, b_1(T)\, A_{\rm br}^2(T)\right), \end{aligned} \tag{6.70}$$

in which $\Gamma(\alpha, x)$ is the incomplete gamma function (Abramowitz and Stegun, 1975)

$$\Gamma(\alpha, x) = \int_x^\infty e^{-t}\, t^{\alpha-1}\, dt. \tag{6.71}$$

The energy dissipated due to breaking per unit horizontal surface area now becomes

$$E_{\rm diss} = \int_0^\infty E_{\rm diss}(T) dT = \frac{\rho g}{2} \int_0^\infty a_1(T)\, I_A(T)\, dT \quad [\mathrm{J/m^2}]. \tag{6.72}$$

Before we take integration in (6.72), let us consider first the expression for $E_{\rm diss}(T)$. This is the amount of energy dissipated due to breaking per unit time and unit horizontal area for a particular wave period T. To evaluate the limiting wave amplitude $A_{\rm br}(T)$ we can use the Phillips and Banner (1974) criterion for onset of breaking in presence of drift current. From Section 5.3.4 we find

$$A_{\rm br}(T) = 0.01\, gT^2 \left(1 - 2\pi\alpha_2\, \frac{V_{10}}{gT}\right)^2. \tag{6.73}$$

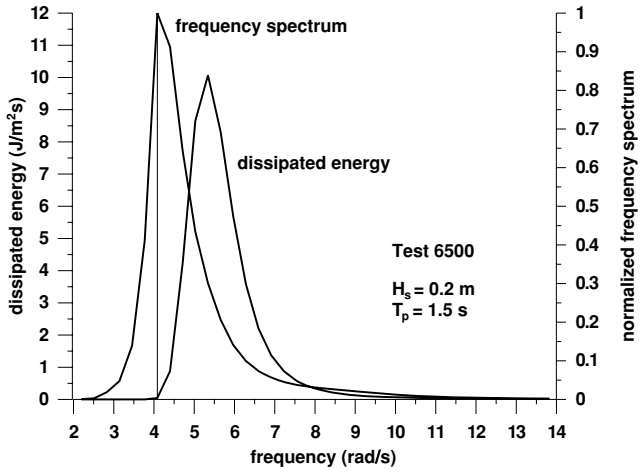

Figure 6.9: Energy dissipated for particular frequencies at wave staff 1 in Test 6500.

In the wind speed range $6 < V_{10} < 20$, the coefficient α_2 varies from 0.0172 to 0.023. Assuming that wind velocity V_{10} is known, and substituting (6.73) into (6.72), we get a final expression for the energy dissipated due to breaking. The function $E_{\text{diss}}(T)$ is illustrated in Fig. 6.9 versus frequency ω for Test 6500 (wave staff 1) of the Ocean Basin Experiment when $V_{10} = 0$. From the figure it follows that the energy loss is almost exclusively from wave components at frequencies higher than the spectral peak frequency. This conclusion is in full agreement with results of experiments conducted by other investigators. Integration in (6.72) yields the energy dissipated per unit horizontal area. If should be noted that the above approach can also be applied to the two-dimensional probability density for a finite bandwidth wave field (see Section 3.3.10).

6.4 Summary of formulae for wave energy dissipation

As demonstrated above, wave dissipation is the most important dynamic factor in breaking waves. On the other hand, the estimating the amount of energy lost during breaking is a very difficult task despite the many experimental and theoretical efforts described above. In Tables 6.2 and 6.3 a summary of known experimental data and theoretical results is provided. The tables indicate that basically we have distinguished two approaches to estimate the energy loss due to breaking of random surface waves. The equilibrium Phillips' estimate and Komen et al. estimate are based on measurements of the surface wave spectrum. As pointed out by Felizardo and Melville (1995), this approach has the weakness that at low wind speeds where there is no breaking, the value

Table 6.2: Summary of experimental data on wave energy dissipation due to wave breaking

Quantity	Mathematical expression	Source
Number of breaking waves/wave	$N_{\mathrm{b}} = (4.0 \pm 2.0) \times 10^{-3} \left(\frac{V_{10}}{C_0}\right)^3$	Eq. (4.7) Thorpe (1993)
Rate of energy loss per unit surface [J/m^2 s]	$E_{\mathrm{dissrate}} = (3.0 \pm 1.8) \times 10^{-5} \rho \left(\frac{C_{\mathrm{br}}}{C_0}\right)^5 V_{10}^3$	Eq. (6.2) Thorpe (1993)
Rate of energy loss per unit crest length [J/m^2 s]	$E_{\mathrm{dissrate}} \sim 0.009 \rho_{\mathrm{w}} \frac{C_{\mathrm{br}}^5}{g \sin\theta}$	Eq. (6.6) Duncan (1981)
	$E_{\mathrm{dissrate}} \sim 0.0075 \rho_{\mathrm{w}} \frac{C_{\mathrm{br}}^5}{g \sin\theta}$	Eq. (6.8) Duncan (1983)
	$E_{\mathrm{dissrate}} \sim (3.2 \times 10^{-3} \div 1.6 \times 10^{-2}) \rho_{\mathrm{w}} \frac{C^5}{g}$	Eq. (6.11) Rapp and Melville (1990)
Rate of total energy dissipation in the equilibrium range [J/m^2 s]	$E_{\mathrm{dissrate}} = 4.28 \times 10^{-5} V_{10}^{3.74}$	Eq. (6.28) Hanson and Phillips (1999)

Table 6.3: Summary of theoretical formulae for wave energy dissipation due to wave breaking

Quantity	Mathematical expression	Source
Rate of total energy dissipation in the equilibrium range [J/m^2/s]	$E_{\mathrm{dissrate}} = \frac{\gamma_1 \rho_{\mathrm{w}} I(3s)}{16[I(s)]^3 g^3} \times \int_{\omega_{\mathrm{p}}}^{\infty} \omega^{11} S^3(\omega) d\omega$	Eq. (6.23) Hanson and Phillips (1999)
	$E_{\mathrm{dissrate}} = 1.59 \rho g \frac{m_0 m_2}{m_1} \left(\frac{m_1^4}{g^2 m_0^3}\right)^2$	Eq. (6.43) based on Komen et al. (1984)
Rate of energy dissipation for extremely narrow spectrum [J/m^2/s]	$E_{\mathrm{dissrate}} = 1.59 \rho g m_1 \left(\frac{m_1^4}{g^2 m_0^3}\right)^2$	Eq. (6.47)
Energy dissipation for very narrow spectrum [J/m^2/s]	$E_{\mathrm{diss}} = \frac{1}{2} \rho g A_{\mathrm{rms}}^2 \exp\left(-\frac{A_{\mathrm{br}}^2}{A_{\mathrm{rms}}^2}\right)$	Eq. (6.55)
Energy dissipation for two-dimensional probability density $f(A,T)$ [J/m^2/s]	$E_{\mathrm{diss}} = \frac{1}{2} \rho g \int_0^{\infty} a_1 I_A(T) dT$	Eq. (6.72)

of the wave spectrum is still nonzero. Therefore, these models provide nonzero estimates of dissipation from wave breaking even in the absence of breaking waves. However, after rearranging the governing relationships of both models, the total dissipation of the wave field can be computed from integral wind wave field characteristics. This fact will be used extensively in Chapter 10 where the linkage between sea state and aerosol fluxes will be discussed.

The third estimate discussed above follows from the idea of limiting wave amplitude being reached close before breaking. The dissipated energy is simply the difference between current wave energy and that corresponding to the limiting wave amplitude. However, it should be noted that this model developed by Longuet–Higgins (1969) is valid for a very narrow frequency spectrum.

Chapter 7

Whitecap coverage of the sea surface

7.1 Introduction

Breaking waves appearing in the form of whitecaps represent a very familiar yet poorly understood feature of the wind-driven sea surface. They are formed when large numbers of bubbles produced by a wave rise to the surface, and the bright white area of a whitecap arises from multiple light scattering by elements of size comparable to or greater than the wavelength of visible light. These elements are clusters of proximate, closely packed bubbles at or near the surface. In this book, the concept of statistically steady fractional coverage, i.e. the percentage of the sea surface covered by whitecaps at a given time, with a close relationship between the wave breaking area and whitecap coverage, is used. It includes the determination of the energy dissipation rate at breaking and the relationships between energy loss and gas and aerosol transfer.

The percentage of whitecap coverage is usually parameterized in terms of the wind speed when this speed is greater than about 4 m/s. Below this speed, whitecaps are not observed. As the wind blows over the water surface, at any instant of time the fronts of the breaking waves define a distribution of isolated line or segments of the wave surface. The scales of breaking waves may cover a very wide range, from very short gravity waves in which the breaking is unsteady and turbulent, to actual whitecaps in which the breaking waves generate turbulence and extensive patches of foam. There is clearly some association of the breaking events with waves of different scales, but it is difficult to make the association in an unambiguous way if we consider only the surface configurations at one given instant. A breaking crest may indeed be a local maximum in the instantaneous surface configuration but there is no guarantee that a local wavelength of the breaking wave can be defined precisely.

There is no doubt that a correlation between wind speed and whitecap coverage exists, but the premise that whitecaps are a function of wind speed alone is unacceptable. Whitecaps are generated by wave breaking, but there are other

processes that contribute to wave breaking, for example wave–wave interactions, current–wave interactions and others. Moreover, numerous meteorological and environmental factors affect wind energy input, sea state, and frequency of breaking waves, which in turn influence the extent and lifetime of whitecaps (Wu, 1979). Therefore, wind speed alone cannot fully parameterize the complex event of wave breaking, either explicitly or implicitly.

There is an extensive body of research on whitecaps, as they have been investigated due to their importance for a variety of geophysical processes such as marine aerosol production, gas exchange between the oceans and the atmosphere, air–sea exchange of heat and moisture, transport and transformation of organic matter (Lewis and Schwartz, 2004). In this chapter we provide the experimental and theoretical arguments for the necessity of including more complex mechanisms controlling wave breaking and the resulting whitecap coverage. For the purpose of our analysis, we define whitecap coverage F_{cov} as the spatial fraction of sea surface covered by whitecaps, i.e.

$$F_{\mathrm{cov}} = \frac{S_{\mathrm{w}}}{S_{\mathrm{ref}}}, \tag{7.1}$$

where S_{w} is the sum of individual areas covered by whitecaps formed within the reference sea surface S_{ref} at an instant of time. The area S_{ref} should be sufficiently large to contain a sufficient number of whitecaps, and it should be sufficiently restricted to satisfy the requirement of spatial uniformity of the wave field. It should be noted that F_{cov} may be different from the dominant wave breaking probability because it integrates whitecap contributions of all wave scales and may include residual foam cover. This is different to more common point measurements such as obtained by Longuet–Higgins and Smith (1983) and Hwang et al. (1989). Also this methodology differs from observations of whitecap coverage which is in fact an indirect measure of breaking waves.

7.2 Experimental data on whitecap coverage

Whitecap coverage F_{cov} has been reported as a function of wind speed and other meteorological quantities by several investigators. Usually the whitecap coverage ratio is determined from photographs of the sea surface taken from aircraft, towers and ships. A typical method for determination of F_{cov} from video tapes involves digitizing videos and determining the fraction of pixels that exceed a given threshold for brightness. However, there is some inconsistency over the terms used to describe the various whitecap structures. For example, Ross and Cardone (1974) distinguished 'actively forming whitecaps and large new foam patches' from 'thin foam and foam streaks'. Similarly, Koepke (1984, 1986) distinguished 'whitecaps (foam patches)' and 'foam streaks'. The division of whitecaps into the categories proposed by Monahan and Woolf (1988, 1989) is examined in more detail below in this section.

Thus, there are some difficulties in determining F_{cov} objectively. In particular they include the oblique angle at which the photograph was taken, shadowing

of sea surface by large waves, inability of the measurement system to resolve all white areas, lack of contrast because of sea colour and variable sky reflectance, and small number statistics arising from the measurement data. As was mentioned by Lewis and Schwartz (2004), whitecap coverage determined by photographs typically is greater than that determined by video by one or two orders of magnitude. An important factor which influences F_{cov} strongly is the sampling methodology. Unfortunately, this problem is not usually discussed by the authors. There is some possibility of bias due to taking pictures only when whitecaps are present. On the other hand, some investigators took pictures at fixed intervals, without regard to the instantaneous presence or absence of whitecaps. The obvious bias is introduced due to the fact that photographs and videos are restricted to daytime and to conditions where visibility is not substantially reduced. Finally, some questions may arise regarding the representativeness of measurements due to limited areas of observation and restricted meteorological conditions.

Key studies are those of Toba and Chaen (1973), Wu (1979), Koepke (1984), Marks (1987), Bortkovskii (1987), Stramska and Petelski (2003) and Monahan et al. (1988) in several large-scale studies (BOMEX+, JASIN, STREX, MIZEX83, MIZEX84, HEXPILOT, and HEXMAX). In particular, Monahan (1971) collected 71 observations of whitecapping at locations on the Atlantic Ocean and adjacent salt water basins. The basic motivation for this study was to obtain observations suitable for direct comparison with the several existing contradictory descriptions of wind dependence of salt water whitecaps. The optimal power-law expression for the dependence of oceanic whitecap coverage fraction F_{cov} on 10 m elevation wind speed V_{10} is usually given in the form

$$F_{\text{cov}} = a\, V_{10}^{b}. \tag{7.2}$$

The least squares fitting method based on Monahan (1971) data suggests that $a = 1.35 \times 10^{-5}$, $b = 3.4$ for 4 m/s $< V_{10} <$ 10 m/s. Cardone (1970) using the results from fresh-water whitecap observations and assuming that the fraction of the water surface covered by whitecaps is directly related to the rate of energy transfer from the air flow to the fully developed sea, obtained $a = 1.2 \times 10^{-5}$, $b = 3.3$ for 4 m/s $< V_{10} <$ 10 m/s. Toba and Chaen's (1973) observations of the whitecaps in the East China Sea and the coastal waters of Japan yield the following values of coefficients: $a = 1.55 \times 10^{-6}$, $b = 3.75$. Combining the Atlantic Ocean data collected by Monahan (1971), and the Pacific Ocean data of Toba and Chaen (1973), Wu (1979) found that: $a = 1.7 \times 10^{-6}$, $b = 3.75$.

Monahan and O'Muircheartaigh (1981) reanalysed the previous data using the ordinary least squares fitting (OLS) and robust weight fitting (RWF) methods and they found

$$F_{\text{cov}} = 2.95 \times 10^{-6}\, V_{10}^{3.52} \qquad \text{for OLS method} \tag{7.3}$$

and

$$F_{\text{cov}} = 3.84 \times 10^{-6}\, V_{10}^{3.41} \qquad \text{for RWF method} \tag{7.4}$$

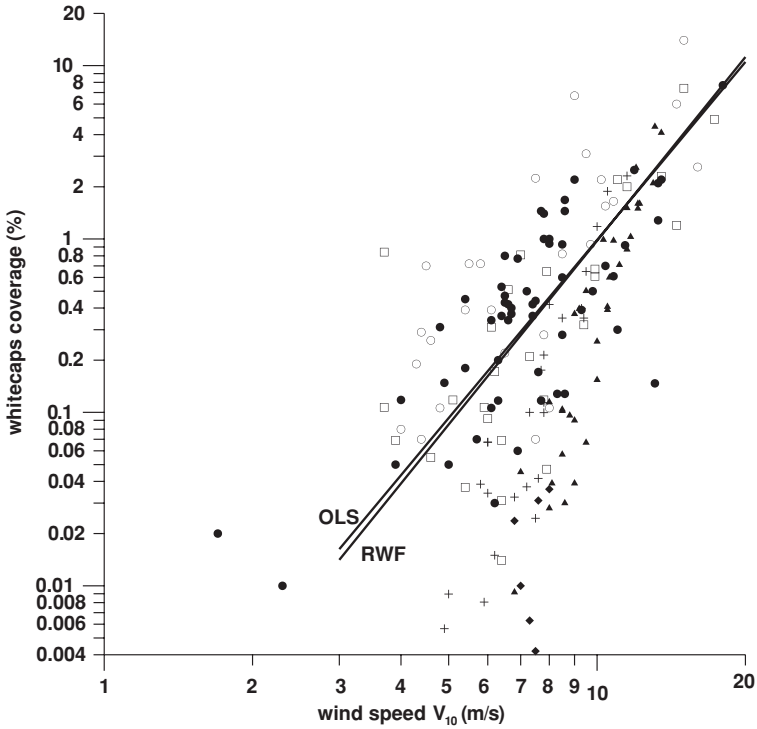

Figure 7.1: Fraction $F_{\rm cov}$ of the ocean covered by whitecaps as a function of wind speed V_{10}. Explanation of the symbols is given in the text (adapted from Monahan and O'Muircheartaigh, 1981).

These expressions fit the combined data set better than any of the previously published fittings – see Fig. 7.1. It should be noted that in the figure the open circles represent whitecap coverage values from the 1978 JASIN experiment, the filled circles mean whitecap coverage from specific observations of Monahan (1971), while the open squares denote whitecap coverage values from Toba and Chaen (1973). However, the proposed parameterization requires some comments. Fitting the data to the expression (7.2) in a least square sense results in the fit being dominated by the largest values of $F_{\rm cov}$ (or V_{10}). For example, if the uncertainty in $F_{\rm cov}$ is proportional to the mean value, then for $b = 3.52$, the value of $F_{\rm cov}$ corresponding to $V_{10} = 15.0\,{\rm m/s}$ would be nearly 48 times greater than that for $V_{10} = 5.0$ m/s, and its contribution to the total error

$$\text{error}^2 = \sum \left[F_{\rm cov}^{\rm exp} - aV_{10}^{b}\right]^2 \tag{7.5}$$

would be more than about 2000 times greater. Therefore, it seems to be quite appropriate that high values of $F_{\rm cov}$ should be weighted more than low values of $F_{\rm cov}$. The whitecap coverage value of 10^{-5} or 10^{-6} makes little difference in the

existing aerosol concentration, whereas the aerosol production corresponding to F_{cov} will probably dominate the marine aerosol concentration.

If we restrict the fit to F_{cov} greater than a certain minimum value, the final result will be affected considerably. For example, fitting only data with $F_{\text{cov}} > 10^{-4}$ to the expression (7.2) yields an exponent $b = 3.3$, whereas fitting all nonzero values yields $b = 4.7$. A similar difference was observed by Hanson and Phillips (1999). They examined the video data of Monahan and obtained $b = 3.6$ for $F_{\text{cov}} > 5 \times 10^{-5}$, whereas for the complete data set the value $b = 5.2$ was obtained.

Marks (1987) considered the data collected during a cruise on the research vessel 'Polarstern' in the North Atlantic and Greenland Sea (polar expedition Arkis–III). The whitecap coverage was recorded by a modern video camera system mounted about 15 m above the sea surface. The final result is given by the following relationship

$$F_{\text{cov}} = 2.54 \times 10^{-6}\, V_{10}^{3.58}. \tag{7.6}$$

The rate of energy supplied by the wind is closely related to the wind stress and the atmospheric stability conditions. Consequently, the percentage of sea surface covered by breaking waves should be related to the energy flux from the wind as (Wu, 1988b)

$$F_{\text{cov}} \sim \frac{dE}{dt} \sim \tau V_{10} \sim (\rho u_*^2)\, u_* \sim u_*^3, \tag{7.7}$$

in which $\frac{dE}{dt}$ is the rate of energy supplied by the wind per unit area of the sea surface. Using Eq. (5.61) we can rewrite Eq. (7.7) in the form

$$F_{\text{cov}} \sim \left(\sqrt{C_{10}}\, V_{10}\right)^3 \sim C_{10}^{1.5}\, V_{10}^3. \tag{7.8}$$

Wu (1979) suggested that $C_{10} \sim V_{10}^{0.5}$; therefore, Eq. (7.8) yields

$$F_{\text{cov}} \sim V_{10}^{3.75}. \tag{7.9}$$

As was noted by Lewis and Schwartz (2004), the hypothesis of proportionality between F_{cov} and the energy flux from wind has not been well established. These two quantities may be related but any such relation involves not only the fraction of the energy flux that goes into wave breaking but also the relation between F_{cov} and the energy expended in wave breaking. Also it should be noted that the power in (7.9) is based on the proportionality of the wind stress coefficient C_{10} and the square root of the wind speed.

Wu (1982) proposed a linear relationship between C_{10} and V_{10} – see equation (5.62). However, this function would result in the relationship $F_{\text{cov}} = f(V_{10})$, which is not a power law. When the drag coefficient C_{10} from numerous experiments is fitted to power laws (Wu, 1980), exponents between 0.08 and 0.74 are obtained, and these values would result in exponents for the wind speed dependence of whitecap coverage $F_{\text{cov}} = f(V_{10})$ ranging from 3.1 to 4.1.

The wind-stress coefficient C_{10} varies with atmospheric stability conditions. Therefore the use of the wind friction velocity u_*, rather than wind speed V_{10}, can be considered as an upgrade of analysing the whitecap data. Using this argument, Wu (1988b) averaged the sets of data from BOMEX, JASIN, STREX and MIZEX experiments and proposed an empirical law in the form

$$F_{\mathrm{cov}} = 0.2\, u_*^3 \quad \text{and} \quad F_{\mathrm{cov}} = 2.0\, V_{10}^{3.75}, \tag{7.10}$$

in which F_{cov} is expressed in ppm, V_{10} in m/s and u_* in cm/s. Observations indicated that there were no systematic variations of the whitecap coverage with water temperature for other than near-zero temperatures.

A very similar result was obtained by Hanson and Phillips (1999). They excluded very small coverage ($F_{\mathrm{cov}} < 10^{-5}$), when scatter becomes very large and unsystematic, and found the following relationship for the Gulf of Alaska

$$F_{\mathrm{cov}} = 2.04 \times 10^{-7} \times V_{10}^{3.61}. \tag{7.11}$$

Xu et al. (2000) conducted field measurements at the oil platform in Bohai Bay. The whitecaps were observed by photography from the top of the platform at about 46 m above the sea level covering an area of $80 \times 89\,\mathrm{m}^2$ of sea surface. The fraction of whitecap coverage from 10 pictures, taken at intervals of 30 s, was averaged to give one whitecap coverage value corresponding to a given wind speed and wind fetch. The wind speed varied from 9 to 18 m/s, and wind fetch ranged from 60 to 170 km. The observed whitecap coverage was greater than 1.5% and smaller than 7.0%.

Stramska and Petelski (2003) reported results of recording of whitecaps in the north polar waters of the Atlantic. Field data were collected during three cruises on the R/V *Oceania* operated by the Institute of Oceanology in Sopot (Poland). The study area extended between the northern part of the Norwegian coast (Tromsø) and Svalbard. Field data for the polar regions are very scarce despite the frequent periods of strong winds and storms. To group them in a coherent series, the co-authors followed Monahan and distinguished two types of whitecaps, stage A (young) and stage B (older) whitecaps. Stage A whitecaps are the crests of actively breaking waves with an albedo of 0.5 or greater, lasting only a few seconds, after which they decay into stage B whitecaps. Stage B whitecaps are of lower albedo with foam that is visible on the sea surface for some short time after the wave breaks. Knowledge of stage A whitecaps is relevant to the study of wave evolution and energy dissipation by breaking waves. On the other hand, information on total whitecap coverage (including stage A and B whitecaps) is of interest for studies on global albedo, global climate models, and on the atmospheric corrections for satellite ocean colour remote sensing. Some investigators postulate that videos record only stage A whitecaps, whereas photographs detect both stage A and stage B whitecaps. In particular, Monahan et al. (1988) reported that the ratio $\frac{F_{\mathrm{cov,A}}}{F_{\mathrm{cov,B}}}$ for various wind speeds falls within an estimated range of 0.001–0.2.

Stramska and Petelski (2003) pointed out that although their estimates of the total whitecap coverage were dominated by type B whitecaps, it was not

possible to objectively classify the photographs into type A or B. Therefore, the total whitecap coverage was considered. The regression line for data points for the total fraction of whitecap coverage satisfies the following relationship

$$F_{\text{cov}} = 4.18 \times 10^{-5}(V_{10} - 4.93)^3 \tag{7.12}$$

and

$$F_{\text{cov}} = 8.85 \times 10^{-7}(u_* - 15.34)^3. \tag{7.13}$$

The use of u_* instead of V_{10} did not significantly reduce the scatter of data points. Moreover, Stramska and Petelski (2003) concluded, comparing the results on whitecap coverage in cold and warm waters, that there is no evidence to support the notion that the differences between their data and the data of Monahan (1971) and Toba and Chaen (1973) can be explained by the effect of sea surface temperature on F_{cov}. This conclusion was supported by Lewis and Schwartz 2004). They summarized available data and noted that although there is some indication that F_{cov} is generally greater at high sea temperatures than at low sea temperatures, due to the large scatter in data it is difficult to quantify the dependence of F_{cov} on sea temperature, and little is known about the physical basis for this dependence.

A very important conclusion resulting from Stramska and Petelski's (2003) observations is that whitecap coverage depends on the history of wave field development. They distinguished three sea states, namely developed sea, undeveloped sea and decreasing sea. In terms of mechanics of wave generation, all of these states are related to the wind fetch X and wind duration t, or more precisely to non-dimensional quantities such as $\frac{gX}{V_{10}^2}$ and $\frac{gt}{V_{10}}$. As was shown in Fig. 7.2, at any given wind velocity V_{10}, the fully developed seas (denoted by crests) are generally characterized by greater whitecap coverage than undeveloped seas (denoted by closed triangles), and seas corresponding to decreasing winds (denoted by diamonds). Examples of fully developed seas are the regions of trade winds, where winds vary on smaller time scales. On the other hand, highly variable atmospheric conditions, as in the north polar regions, result in lower whitecap coverage. The least squares fitting provides the following relationships (in %) for whitecap coverage for developed and undeveloped seas, respectively (see Fig. 7.2)

$$F_{\text{cov}}^{(\text{dev})} = 0.005 \times (V_{10} - 4.47)^3 \tag{7.14}$$

and

$$F_{\text{cov}}^{(\text{undev})} = 0.00875 \times (V_{10} - 6.33)^3. \tag{7.15}$$

The data reported by Stramska and Petelski (2003) were also added in Fig. 7.1 for comparison.

As mentioned above, Cardone (1970) argued that wave dissipation estimates resulting from modelled wind seas were better correlated with whitecap fraction

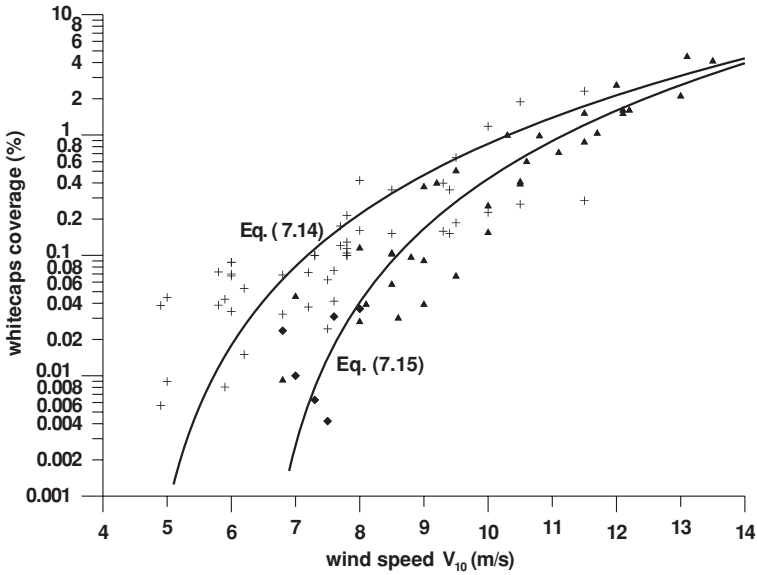

Figure 7.2: Oceanic whitecap coverage as a function of wind speed in the north polar waters: crests – developed sea, closed triangles – undeveloped sea, diamonds – decreasing wind (adapted from Stramska and Petelski, 2003).

estimates than with wind speed only. This suggestion is also supported by the fact that the V_{10} exponent of 3.74 in Eq. (6.28), reported by Hanson and Phillips (1999) and relating the energy dissipation and wind speed, is nearly identical to that given by Wu (1988b) in (7.10) for the experimental relationship between $F_{\rm cov}$ and wind speed. Therefore we can write

$$F_{\rm cov} \sim E_{\rm dissrate} \sim u_*^3 \sim V_{10}^{3.75}. \tag{7.16}$$

The above sequence of relationships suggests that $F_{\rm cov} \sim E_{\rm dissrate}$. However, examination of the dependence of experimental whitecap coverage $F_{\rm cov}$ with the rate of energy dissipation shown by Hanson and Phillips (1999) yields the conclusion that the best fit is obtained for the whitecap power-law model when

$$F_{\rm cov} = 3.4 \times 10^{-3} \times E_{\rm dissrate}^{1.5}. \tag{7.17}$$

The authors noted that scatter of $F_{\rm cov}$ with $E_{\rm dissrate}$ is much smaller than that with V_{10}. Moreover, the use of wave dissipation rate in place of wind speed removes the uncertainty caused by atmospheric forcing variability. The reason that the power of 1.5 on $E_{\rm dissrate}$ was used, rather than a power of unity, as implied by Eq. (7.16), is that not all of dissipation is represented by $F_{\rm cov}$, especially for breaking at very small scales. These open ocean results support the laboratory findings of Lamarre and Melville (1991) – see Section 4.4.4.5.

Anguelova et al. (2005) argued that existing measurements of whitecap coverage from photographs do not provide enough information to quantify the dependence of $F_{\rm cov}$ on other variables, in addition to wind speed, environmental and meteorological factors. They propose a method using passive microwave satellite measurements to retrieve $F_{\rm cov}$ on a global scale under various conditions encountered in world oceans. This method relies on changes of ocean surface emission at microwave frequencies induced by the presence of whitecaps. Ocean surface emissivity, e, is a composite of two contributions: emissivity due to the rough sea surface, $e_{\rm r}$, in places free of whitecaps, and emissivity due to foam, $e_{\rm f}$, in foam-covered areas. Thus we have (Anguelova et al., 2005)

$$e = e_{\rm r}(1 - F_{\rm cov}) + e_{\rm f} F_{\rm cov} \tag{7.18}$$

Assuming that all emissivities can be calculated, we obtain for whitecap coverage as

$$F_{\rm cov} = \frac{e - e_{\rm r}}{e_j - e_{\rm r}}. \tag{7.19}$$

The composite ocean emissivity, e, is retrieved from satellite-measured brightness temperature, $T_{\rm B}$, while emissivities of rough surface and foam, $e_{\rm r}$, and $e_{\rm f}$, are computed using theoretical or empirical expressions. In particular, the recent launch of the polarimetric microwave radiometer WindSat provides a possibility to obtain more precise value of the surface emissivity e. The emissivity of rough sea surface, $e_{\rm r}$, can be obtained from a so-called two-scale model describing the changes of ocean emissivity for winds up to 10–12 m/s due to Bragg scattering from short gravity and capillary waves riding on long waves with a Gaussian distribution of slopes. Moreover, emissivity of foam, $e_{\rm f}$, is obtained from the full radiative transfer model for the emission of a foam layer with depth profile of the void fraction.

Kerman and Szeto (1994), using the modern geometrical concepts of Mandelbrot, showed that the cumulative probability function of the intensity is self-similar for sufficiently large intensities occupying about 10% of an imaged area. They applied a box-counting technique to images obtained from flights and they found that the estimated fractal dimension decreases from about 2.25 for a 10% areal coverage to about 1.7 for 0.1% coverage.

For further work, it will be of interest to compare oceanic and fresh water whitecap coverage. Therefore following Monahan (1971), let us assume that under identical meteorological conditions the rate R of whitecap production per unit area of water surface and the initial area A_0 of individual whitecaps are the same for salt and fresh water. Thus, the whitecap area formed per unit time and unit area becomes $A_0 R$. The whitecap area $A(t)$, at time t from its formation is given by

$$A(t) = A_0 \exp\left(-\frac{t}{\tau}\right), \tag{7.20}$$

where τ is the time constant. Hence the rate at which individual area decay per unit and unit area becomes

$$\frac{dA(t)}{dt} = -\frac{A(t)}{\tau}, \tag{7.21}$$

and for the whitecap area decay (per unit time and unit area) we obtain $\frac{F_{\text{cov}}}{\tau}$, where F_{cov} is the total area of whitecaps per unit area of sea surface.

In steady state conditions, the rate of whitecap area formation is equal to the rate of whitecap area decay, i.e.

$$A_0 R = \frac{F_{\text{cov}}}{\tau} \tag{7.22}$$

and

$$F_{\text{cov}} = A_0 R \tau \tag{7.23}$$

Monahan and Zieltow (1969) found that the time constant τ for salt water is about 1.5 times the time for fresh water. This means that for the same meteorological conditions, the fraction of sea surface covered by whitecaps should be 1.5 times the fraction of a fresh water surface covered by whitecaps.

Little systematic investigation of lifetimes and sizes of oceanic whitecaps has been reported, and known results vary significantly. Maximum areas of individual whitecaps of up to $40\,\text{m}^2$ at $V_{10} = 14\,\text{m/s}$ were observed, although mean areas were generally smaller, namely 1.4 and $2.2\,\text{m}^2$ for wind speeds of 5–11 m/s and 11–14 m/s, respectively (Lewis and Schwartz, 2004). On the other hand, the mean areas of individual crests and foam strips increased from 0.5 to $1.2\,\text{m}^2$ and from 20 to $30\,\text{m}^2$, respectively as wind speed increased over this range.

It is generally recognised that whitecap coverage is negligibly small for wind speeds less than 3 m/s. For wind speed above 9 m/s, the mechanical tearing away of wave crests, resulting in the formation of spume lines, becomes an important, additional mechanism of white water formation. All these facts suggest strongly that the use of a more complex form for function $F_{\text{cov}}(V_{10})$ than a simple power law is required to describe precisely the dependence of F_{cov} upon V_{10}.

During Ocean Basin Experiment (Massel et al., 2001), the whitecaps coverage due breaking waves (without wind) was estimated using image processing methods applied to video records. Whitecaps were observed as a separate region in the picture after thresholding and eliminating individual pixels. In particular, the 'saturation' component of the film frame enhances the whitecap area in the most effective way. Video recordings were first converted from RGB to HSV (High-Saturation-Value) format, and substantially whitecaps were determined as proportional to the nnmber of black pixels in the converted picture. This method applied to all frames of the video stream (25 frames per second) provided the average whitecaps area in the measured time period of about 10 minutes. The resulting whitecaps coverage was no greater than 0.1%, and only for highest waves it exceeds 1% (Tęgowski, 2004).

7.3 Theoretical models of whitecap coverage

7.3.1 Whitecap coverage model based on the Phillips theory for equilibrium range

Estimation of the wave breaking area and resulting whitecap coverage is a complicated task as our present understanding of most aspects of wave breaking remains fragmentary. In this section we present theoretical models based on various breaking criteria. Most of them exhibit close links between whitecap coverage and wave breaking probability.

In particular, expressions on the spectral properties of wind generated waves, proposed by Phillips (1985) – see Section 6.2 – provide a way to determine the degree of whitecap coverage or the fraction of surface area covered by bubbles. Only breaking zones with a rate of energy release bC^5/g exceeding some threshold value will contribute to formation of whitecaps. If we assume that the bubbles, once generated, persist for an average time, T, on the surface, then the whitecap coverage becomes

$$F_{\mathrm{cov}} = \int C\Lambda(C)T d\,C, \tag{7.24}$$

in which $\Lambda(C)$ is the average length of breaking front per unit area and per unit speed interval given in (6.12). Using the formula for expected number of breaking waves passing a given point proposed by Phillips (1985), the whitecap coverage from (7.24) yields

$$F_{\mathrm{cov}} \approx \beta^3 b^{-1} I(3p) T\, C_T^{-4}\, g\, u_*^3, \tag{7.25}$$

in which the speed C_T is the slowest speed of fronts capable of producing whitecaps, b is the numerical constant estimated by Duncan from his experiments as approximately 0.06 and function $I(3p)$ is given by (6.21). It should be noted that the above estimate exhibits the whitecap coverage dependence on wind speed, which is close to that found empirically by Wu (1988b) and by Stramska and Petelski (2003).

7.3.2 Whitecap coverage model based on the limiting steepness criterion

Let us assume for a moment that long-crested waves propagate in one direction, along the x-axis, and l_{cov} is the sum of the individual lengths occupied by whitecaps at some instant of time. If we consider a square sea area with a side of length equal l_{cov}, then for a two-dimensional wave field, the ratio l_{cov}/l (l is the length of a sufficiently long line oriented in the x direction) becomes a measure of the whitecap surface coverage, i.e.

$$\frac{l_{\mathrm{cov}}}{l} \approx F_{\mathrm{cov}}. \tag{7.26}$$

The slope criterion of wave breaking requires that the surface wave will break when the local surface slope ε_{l} exceeds the threshold slope $\varepsilon_{\mathrm{th}}$, i.e.

$$\varepsilon_{\mathrm{l}} = \frac{\partial \zeta}{\partial x} \geq \varepsilon_{\mathrm{th}} \tag{7.27}$$

Thus the probability of breaking, identified with the spatial fraction of sea surface covered by whitecaps F_{cov}, becomes

$$F_{\mathrm{cov}} = \int_{\varepsilon_{\mathrm{th}}}^{\infty} f(\varepsilon_{\mathrm{l}})\, d\varepsilon_{\mathrm{l}}. \tag{7.28}$$

In Chapters 2 and 4 theoretical and experimental data on the limiting surface slope were collected, and in Chapter 5 the probability density of the surface slope was given for two different wave regimes, i.e. long-crested and short-crested waves, when breakers can be of the spilling and plunging form. Here we assume that fully developed sea short-crested waves are characterized by the Pierson–Moskowitz spectrum (3.17) and spilling breakers predominate. Therefore, substituting (3.122) into (7.28) and taking into account the relationship (D.7), we obtain

$$F_{\mathrm{cov}} = \exp\left[-8.265\varepsilon_{\mathrm{th}}^2\left(\frac{gX}{V_{10}^2}\right)^{0.22}\right] = \exp\left[-0.5587\left(\frac{gX}{V_{10}^2}\right)^{0.22}\right], \tag{7.29}$$

when $\varepsilon_{\mathrm{th}} = \overline{\varepsilon}_{\mathrm{f}} = 0.26$ (see Table 4.8) and $a_4 = 1.5919$ (see Table D.1) are used. In a similar way, for fetch limited areas, when the JONSWAP spectrum ($\gamma = 3.3$) applies, we get

$$F_{\mathrm{cov}} = \exp\left[-7.714\varepsilon_{\mathrm{th}}^2\left(\frac{gX}{V_{10}^2}\right)^{0.22}\right] = \exp\left[-0.5215\left(\frac{gX}{V_{10}^2}\right)^{0.22}\right], \tag{7.30}$$

Functions (7.29) and (7.30) are illustrated in Fig. 7.3. Higher whitecap coverage is associated with lower values of the non-dimensional fetch $\frac{gX}{V_{10}^2}$. However, the influence of the spectral form is not substantial. In Fig. 7.3, experimental data reported by Xu et al. (2000) are added. Values of experimental whitecap coverage are slightly higher than those predicted by (7.29) and (7.30).

Assuming for a moment that the wind fetch in formula (7.29) is known, F_{cov} becomes a function of wind speed only. This function is shown in Fig. 7.4 for wind fetches $X = 10, 25, 50, 100, 200, 300, 500$ and 1000 km. In the same figure, the experimental data, reanalysed by Monahan and O'Muircheartaigh (1981), as well as the data reported by Stramska and Petelski (2003), are given. Despite scattering, the computed whitecap coverage provides realistic values under the assumption of an adopted wind fetches range as the true fetches are unknown. A closer comparison shows that small whitecap coverage appears only for the case of decreasing winds in the north polar waters (Stramska and Petelski, 2003).

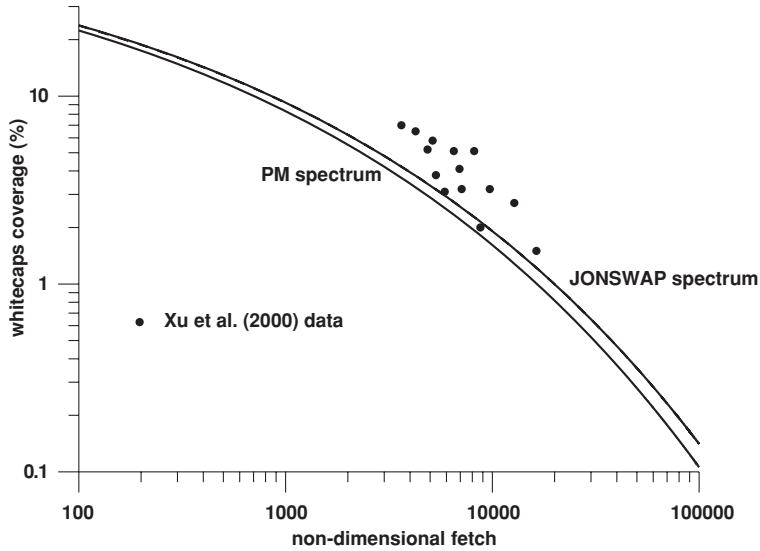

Figure 7.3: Dependence of whitecap coverage, based on the limiting steepness criterion, on the non-dimensional fetch for the Pierson–Moskowitz and JONSWAP spectra.

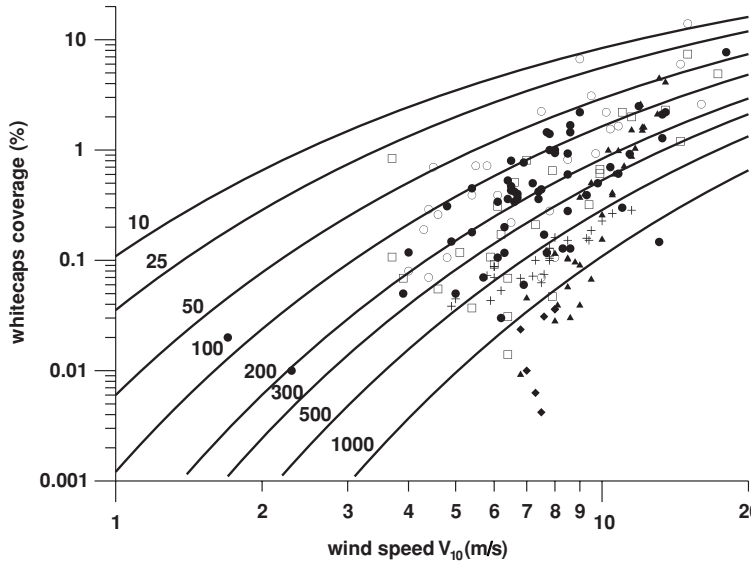

Figure 7.4: Whitecap coverage, based on the limiting steepness criterion, as a function of wind speed for chosen wind fetches. Experimental data from Figs. 7.1 and 7.2 are added for comparison.

7.3.3 Whitecap coverage model based on the vertical acceleration criterion

Let us now examine another breaking criterion and assume that for breaking to occur the downward acceleration at the crest of the wave has to be greater than αg, i.e.

$$\left|\frac{d^2\zeta}{dt^2}\right| > \alpha g, \tag{7.31}$$

in which α is a constant. In particular, Snyder et al. (1983) have found that α varies from 0.4 to 0.52, and laboratory experiments of Ochi and Tsai (1983) provided the value $\alpha \approx 0.4$. According to the Snyder and Kennedy (1983) philosophy, wave breaking occurs on the sea surface everywhere the downward acceleration exceeds the dynamic threshold value αg. Therefore the occurrence of breaking coincides with the occurrence of whitecaps. Therefore from (5.85) we have

$$F_{\text{cov}} = 1 - \Phi(x) = 1 - \frac{1}{\sqrt{2\pi}} \int_{-\infty}^{x} \exp\left(-\frac{1}{2}t^2\right) dt, \tag{7.32}$$

in which the argument x is given by

$$x = \frac{\alpha g}{\sqrt{m_4}}. \tag{7.33}$$

After substituting a moment m_4 for the Pierson–Moskowitz spectrum (D.7) and using β, given by (3.22), the equation (7.32) yields

$$F_{\text{cov}} = 1 - \Phi\left\{2.8373\alpha\left(\frac{gX}{V_{10}^2}\right)^{0.11}\right\}. \tag{7.34}$$

The whitecap coverage given by Eq. (7.34) depends on the α value which should be determined a priori. To estimate the range of α value variation, we use the Monahan (1971) data in which the tests with negligible whitecap coverage (data noted as $F_{\text{cov}} = 0.0$) have been neglected. For the remaining data, the α values giving the optimal agreement of the theoretical F_{cov} value with the experimental ones were determined (Fig. 7.5). It was found that the α values are in the range of $0.21 < \alpha < 0.44$, with the mean value of 0.27, which supports the conclusion that relationship (7.34) is capable of representing the whitecap coverage under the condition that the α value is known (Massel, 2001a).

In general the coefficient α is not constant and it depends on the intensity and type of breaking. Therefore, it should be considered as a function of local hydrodynamic and meteorological conditions. In Fig. 7.6 the whitecap coverage is given as a function of the non-dimensional fetch with $\alpha = 0.27$. Experimental data reported by Xu et al. (2000) were added for comparison. Values of experimental whitecap coverage are higher than those predicted by (7.34). Additionally in Fig. 7.7, the comparison of the theoretical formula (7.34) with experimental data for particular fetches is given. In all cases, the coefficient $\alpha = 0.32$ was assumed. This value is slightly greater than the mean value $\alpha = 0.27$, resulting from Monahan's data, in order to take into account Stramska and Petelski' data.

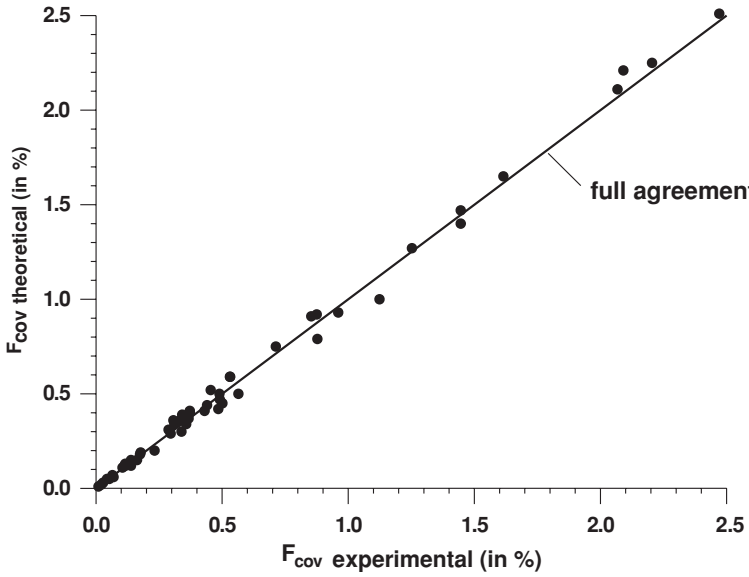

Figure 7.5: The best fitting α value based on Monahan's data.

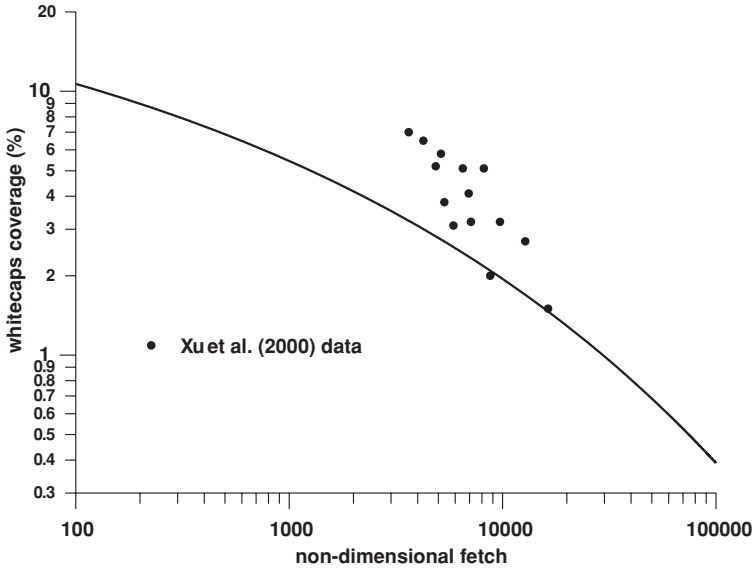

Figure 7.6: Whitecap coverage, based on the threshold downward acceleration criterion, as a function of non-dimensional fetch for the Pierson–Moskowitz spectrum.

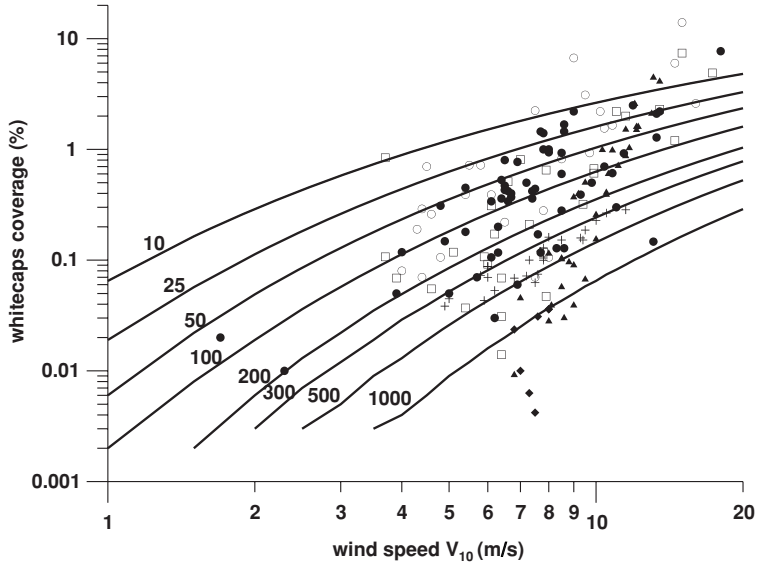

Figure 7.7: Whitecap coverage based on the threshold downward acceleration criterion as a function of wind speed for chosen wind fetches. Experimental data from Figs. 7.1 and 7.2 are added for comparison.

7.3.4 Whitecap coverage model based on the geometry of spilling breakers

The whitecaps appear at the wave crest, usually in the form of spilling breakers. Sometimes a so-called roller is formed on the top of the wave crest. The roller is represented by a rotating mass of water, moving with phase speed in the direction of wave propagation (Massel, 1996a). According to Monahan's (1971) classification, the whitecaps for fresh and young seas are concentrated in the small section of the wave crests. They belong to so-called class A of whitecaps. A schematic representation of the breaking crest is given in Fig. 7.8.

Using the rationale presented in Section 6.3.3, we assume that due to breaking, wave amplitude decreases to the value $A_{\rm br}$ representing the critical saturation level. Thus, the portion of the amplitude loss in a unit cycle becomes (Huang, 1981)

$$\Delta A = \int_{A_{\rm br}}^{\infty} (A - A_{\rm br}) f(A)\, dA = \frac{2}{A_{\rm rms}^2} \int_{A_{\rm br}}^{\infty} A(A - A_{\rm br}) \exp\left(-\frac{A^2}{A_{\rm rms}^2}\right) dA \qquad (7.35)$$

or

$$\Delta A = 2A_{\rm rms}\, I_1\left(\frac{A_{\rm br}}{A_{\rm rms}}\right), \qquad (7.36)$$

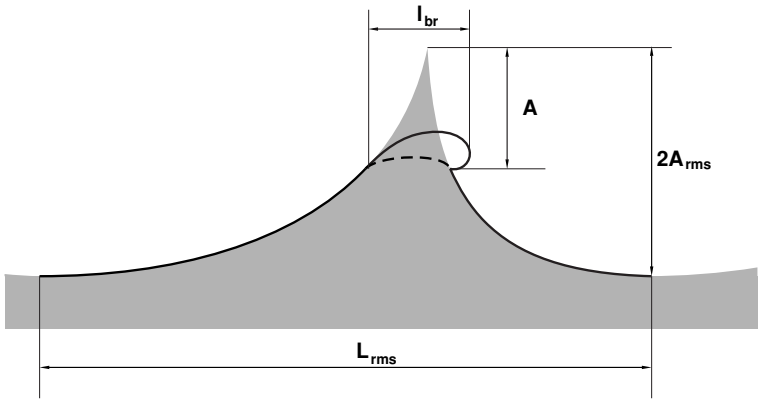

Figure 7.8: Schematic representation of the breaking wave crest.

where

$$I_1\left(\frac{A_{\rm br}}{A_{\rm rms}}\right) = \int\limits_{\frac{A_{\rm br}}{A_{\rm rms}}}^{\infty} x\left(x - \frac{A_{\rm br}}{A_{\rm rms}}\right)\exp(-x^2)\,dx. \tag{7.37}$$

After integration we obtain

$$\begin{aligned}\Delta A = 2A_{\rm rms}\, I_1\left(\frac{A_{\rm br}}{A_{\rm rms}}\right) = \\ = 2A_{\rm rms}\left\{\frac{1}{2}\,\Gamma\left(\frac{3}{2}, \frac{A_{\rm br}^2}{A_{\rm rms}^2}\right) - \left(\frac{A_{\rm br}}{A_{\rm rms}}\right)\,\Gamma\left(1, \frac{A_{\rm br}^2}{A_{\rm rms}^2}\right)\right\},\end{aligned} \tag{7.38}$$

in which $\Gamma(\alpha, x)$ is the incomplete gamma function (Abramowitz and Stegun, 1975).

Now let us use a simple geometrical argument that

$$\frac{\Delta A}{\frac{l_{\rm br}}{2}} \approx \frac{2A_{\rm rms}}{\frac{L_{\rm rms}}{2}} \tag{7.39}$$

or

$$\frac{l_{\rm br}}{L_{\rm rms}} \approx \frac{\Delta A}{2A_{\rm rms}} = I_1\left(\frac{A_{\rm br}}{A_{\rm rms}}\right). \tag{7.40}$$

Assuming for a moment a narrow directional wave spreading when almost all waves propagate in one direction, we find that the whitecap coverage per metre square becomes

$$F_{\rm cov} = \frac{l_{\rm br}}{L_{\rm rms}} = I_1\left(\frac{A_{\rm br}}{A_{\rm rms}}\right). \tag{7.41}$$

Thus, the whitecap coverage depends totally on the ratio of the amplitude at breaking $A_{\rm br}$ and $A_{\rm rms}$ amplitude. From the relationship (6.56), (6.57) and

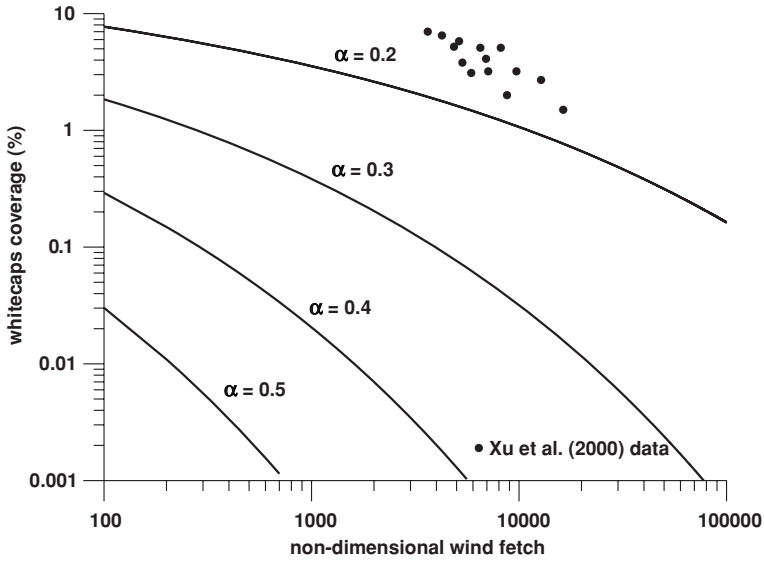

Figure 7.9: Dependence of whitecap coverage, resulting from the geometry of spilling breakers, on the non-dimensional fetch for the Pierson–Moskowitz spectrum. Four different values of α are selected.

(6.58), this ratio takes the form

$$\frac{A_{\rm br}}{A_{\rm rms}} = \frac{\alpha g}{\sqrt{2}} \frac{\sqrt{m_0}}{m_2}. \tag{7.42}$$

Using the moments m_0 and m_2 for the Pierson–Moskowitz spectrum (D.5) and expression for β (3.22) we obtain

$$\frac{A_{\rm br}}{A_{\rm rms}} = 2.8945\alpha \left(\frac{gX}{V_{10}^2}\right)^{0.11}. \tag{7.43}$$

In Fig. 7.9 the whitecap coverage is given as a function of the non-dimensional fetch for four different values of the coefficient α. Experimental data reported by Xu et al. (2000) are added for comparison. These data indicate that the α coefficient in the Bohai Bay experiment (Xu et al., 2000) was even smaller than 0.2 when the argument of the geometry of spilling breakers is used. The dependence of whitecap coverage on the α value is very strong. In particular, changing the α value from 0.2 to 0.5 for $\frac{gX}{V_{10}^2} = 500.0$ results in a decrease in whitecap coverage by 1000 times, from about 8% to 0.002%. Fig. 7.10 illustrates the comparison of the theoretical formula (7.43) with experimental data for particular fetches, when in all cases the coefficient $\alpha = 0.27$ is assumed. The predicted values of whitecap coverage for wind fetches varying from 10 km to 1000 km are smaller than those observed reported by Monahan, and Stramska and Petelski.

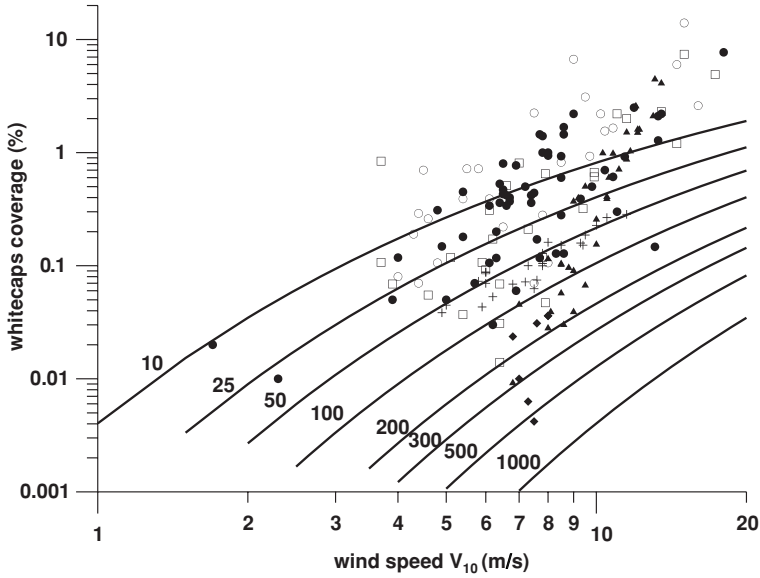

Figure 7.10: Whitecap coverage, based on the geometry of spilling breakers, as a function of wind speed for selected wind fetches. Experimental data from Figs. 7.1 and 7.2 are added for comparison.

7.3.5 Whitecap coverage model for the non-Gaussian wave field

For any waves with an amplitude greater than $A_{\rm br}$, breaking will occur and whitecaps appear at the sea surface. Hence the probability of whitecap coverage can be presented as follows

$$F_{\rm cov} = \int_{A_{\rm br}}^{\infty} f(A)\, dA. \tag{7.44}$$

Surface waves which are very steep, close to breaking, are characterized by the probability density function $f(a)$ for wave amplitude which is different from the Rayleigh distribution. This difference is attributed to the presence of nonlinearities in the wave motion. To include the effects of nonlinearities, Tayfun and Al-Humond (2002) proposed the distribution $f(A)$ as was given by (3.159). Let us rewrite it as follows

$$f(A) = B_3 \exp(-B_2^2), \tag{7.45}$$

where

$$B_2 = \frac{g\sqrt{m_0}}{\sqrt{2}\, m_2}(B_4 - 1), \tag{7.46}$$

$$B_3 = \frac{g}{m_2}\,\frac{B_4 - 1}{B_4}, \tag{7.47}$$

$$B_4 = \sqrt{1 + \frac{2m_2}{gm_0}\,A}. \tag{7.48}$$

For waves of small amplitudes, the nonlinear effects can be neglected. Thus when $\frac{2m_2}{gm_0}A \to 0$, functions B_2, B_3 and B_4 become

$$B_4 \approx 1 + \frac{m_2}{gm_0}\,A, \tag{7.49}$$

$$B_2 \approx \frac{A}{\sqrt{2m_0}} = \frac{A}{A_{\mathrm{rms}}}, \tag{7.50}$$

$$B_3 \approx \frac{g}{m_2}\,\frac{\frac{m_2 A}{gm_0}}{1 + \frac{m_2 A}{gm_0}} = \frac{A}{m_0} = \frac{2A}{A_{\mathrm{rms}}^2}. \tag{7.51}$$

After substituting (7.49), (7.50) and (7.51) into (7.45) we obtain

$$f(A) = \frac{2A}{A_{\mathrm{rms}}^2} \exp\left[-\left(\frac{A}{A_{\mathrm{rms}}}\right)^2\right], \tag{7.52}$$

which is the Rayleigh distribution.

In general, if the moments m_0 and m_2 are determined for the Pierson–Moskowitz spectrum, we obtain

$$B_2 = 2.894(B_4 - 1)\left(\frac{gX}{V_{10}^2}\right)^{0.11}, \tag{7.53}$$

$$B_3 = \frac{25.65\,g}{V_{10}^2}\left(\frac{gX}{V_{10}^2}\right)^{0.22}\frac{B_4 - 1}{B_4}, \tag{7.54}$$

$$B_4 = \sqrt{1 + 3.062\,\frac{Ag}{V_{10}^2}}. \tag{7.55}$$

To determine the whitecap coverage in (7.44), let us estimate the limiting amplitude A_{br} from the vertical acceleration criterion, i.e.

$$A_{\mathrm{br}} = \frac{\alpha g}{\omega_0^2} = \frac{\alpha g m_0}{m_2} = \frac{0.653\,\alpha V_{10}^2}{g}, \tag{7.56}$$

when the Pierson–Moskowitz spectrum is taken into account. After substituting (7.45) into (7.44) we get the whitecap coverage induced by a nonlinear wave field. In Fig. 7.11 the whitecap coverage (7.44) is presented as a function of the wind speed and wind fetch. In the calculations, the Pierson–Moskowitz

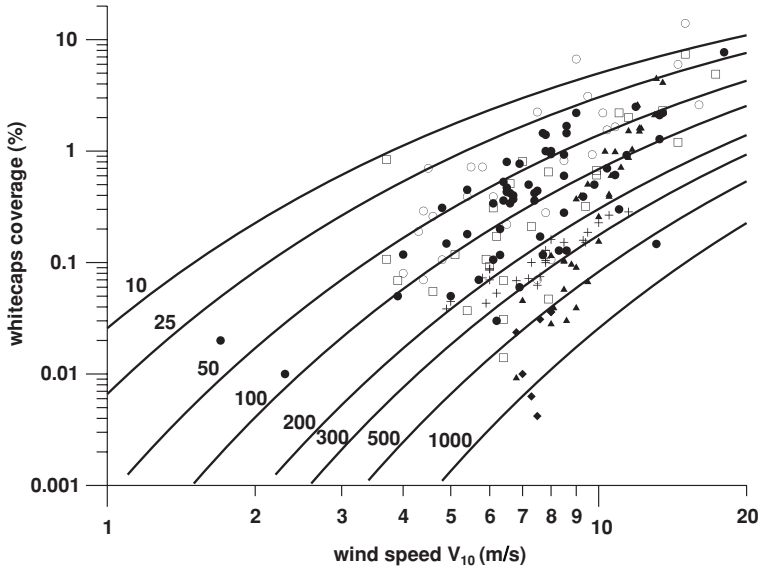

Figure 7.11: Whitecap coverage as a function of wind speed for selected wind fetches based on the non-Gaussian wave amplitude distribution. Experimental data from Figs. 7.1 and 7.2 are added for comparison.

spectrum and the coefficient $\alpha = 0.32$ were assumed. The predicted whitecap coverage for a broad range of wind speeds and wind fetches realistically encompasses all experimental data.

In Section 5.5, the probability of breaking for modulated second-order Stokes waves, developed by Dawson et al. (1993), was presented. The resulting formula (5.120) on the probability of breaking depends on the characteristic steepness parameter ε_k and normalized threshold acceleration parameter α. Applying the arguments for a narrow directional wave field, we can argue that the percentage of surface covered by whitecaps identifies the probability of breaking given by (5.120). To examine the implementation of this formula for prediction of wave breaking for real field conditions, we represent the characteristic steepness parameter ε_k in terms of the non-dimensional fetch $\left(\frac{gX}{V_{10}^2}\right)$. From (3.3) and (3.156) we obtain the characteristic breaking parameter ε_k in terms of the spectral moments as follows

$$\varepsilon_k = \frac{H_s\,\bar{\omega}^2}{g} = \frac{4}{g}\,m_0^{-3/2}\,m_1^2. \tag{7.57}$$

After evaluating moments m_0 and m_1 for the JONSWAP spectrum with the peak enhancement factor $\gamma = 7.0$, formula (7.57) becomes

$$\varepsilon_k = 3.406\,\beta^{1/2} = 0.939\left(\frac{gX}{V_{10}^2}\right)^{-0.11}. \tag{7.58}$$

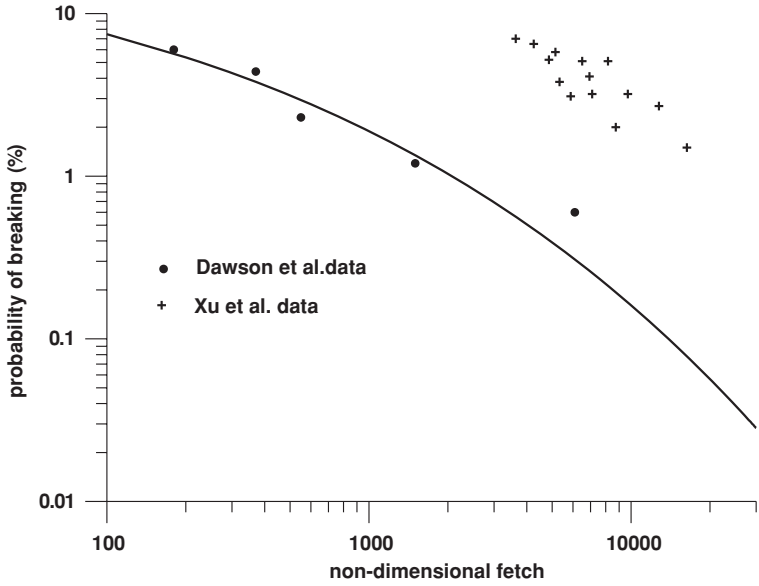

Figure 7.12: Whitecap coverage as a function of non-dimensional wind fetch resulting from the Dawson et al. solution. Experimental data from Dawson et al. and Xu et al. are added for comparison.

Application of (5.120) and (7.58) yields the opportunity to represent the probability of breaking as a function of the non-dimensional fetch $\left(\frac{gX}{V_{10}^2}\right)$. The resulting function is illustrated in Fig. 7.12. The experimental data show a good agreement with the theoretical function (5.120). The field data reported by Xu et al. (2000) were also added for comparison.

7.4 Summary of data and theoretical formulae on whitecap coverage

In Table 7.1, available experimental data on whitecap coverage and proposed parameterizations are collected. These parameterizations are based on the relationships between whitecap coverage and wind speed. In general, the whitecap coverage is approximately proportional to the power cube of the wind speed. The comparison of the observed whitecap coverage with the theoretical predictions developed in this chapter and shown in Figs. 7.4, 7.7, 7.10, 7.11 and 7.12 indicates that all used breaking criteria, i.e. limiting steepness criterion, threshold downward acceleration criterion and criterion resulting from the non-Gaussian wave amplitude distribution, provide rather good approximation to the experimental whitecap coverage. The approach based on the geometry of spilling breakers resulted in whitecap coverage slightly smaller than the observed coverage (see Fig. 7.10). However, due to the lack of precise knowledge

Table 7.1: Summary of experimental data on whitecap coverage and their parameterisation

Relationship	Mathematical expression	Source
Whitecap coverage as a function of wind speed V_{10}	$F_{\rm cov} = a \times V_{10}^b$:	
	$a = 1.35 \times 10^{-5}$, $b = 3.4$	Monahan (1971)
	$a = 1.2 \times 10^{-5}$, $b = 3.3$	Cardone (1970)
	$a = 1.55 \times 10^{-6}$, $b = 3.75$	Toba and Chaen (1973)
	$a = 1.70 \times 10^{-6}$, $b = 3.75$	Wu (1979)
	$a = 2.95 \times 10^{-6}, b = 352$ $a = 3.84 \times 10^{-6}, b = 3.41$	Monahan and O'Muircheartaigh (1981)
	$a = 2.54 \times 10^{-6}$, $b = 3.58$	Marks (1987
	$a = 2.0$, $b = 3.75$	Wu (1988b)
	$a = 2.04 \times 10^{-7}$, $b = 3.61$ (for $F_{\rm cov}$ in ppm, V_{10} in m/s)	Hanson and Phillips (1999)
Whitecap coverage as a function of friction velocity u_*	$a = 0.2$, $b = 3.0$ (for $F_{\rm cov}$ in ppm, u_* in cm/s)	Wu (1988b)
Whitecap coverage as a modified function of wind speed V_{10} or friction velocity u_*	$F_{\rm cov} = a(V_{10} - c)^b$ $a = 4.18 \times 10^{-5}, b = 3, c = 4.93$ $F_{\rm cov} = a(u_* - c)^b$ $a = 8.85 \times 10^{-7}, b = 3, c = 15.34$	Stramska and Petelski (2003)
Whitecap coverage as a function of the rate of energy dissipation	$F_{\rm cov} = a \times E_{diss}^b$ $a = 3.4 \times 10^{-3}$, $b = 1.5$	Cardone (1970) Hanson and Phillips (1999)

of wind fetch, it is not possible to match the theoretical prediction with particular experimental data. Xu et al. (2000) examined the whitecap coverage for wind fetches of 60, 120 and 170 km, and found that the $F_{\rm cov}$ value decreases with increasing fetch at a given wind speed. Reported values were appreciably lower than most values reported by other investigators at similar wind speeds. They also showed that at a given wind speed the values of $F_{\rm cov}$ decrease with wind fetch, although even for very large fetches the whitecap coverage becomes very small but not zero.

The theoretical solutions based on the limiting steepness criterion, threshold downward acceleration and non-Gaussian wave amplitude distribution approach cover almost all experimental data for $V_{10} > 4\,{\rm m/s}$ and $10\,{\rm km} < X < 1000\,{\rm km}$ – see Figs. 7.4, 7.7, 7.11 and 7.12. In all these solutions, some 'free' coefficients exist which should be assumed 'a priori'. In particular, for the limiting steepness criterion, the limiting crest front steepness $\varepsilon_{\rm f} = 0.26$ was assumed, while the threshold downward acceleration was estimated as $\alpha g = 0.32\,g$. It should be noted that all above theoretical solutions are very sensitive to the selection of the $\varepsilon_{\rm f}$ and α values. In Fig. 7.13 all four attempts to determine the whitecap coverage are presented in the form of function $\left(\frac{gX}{V_{10}^2}\right)$. Despite

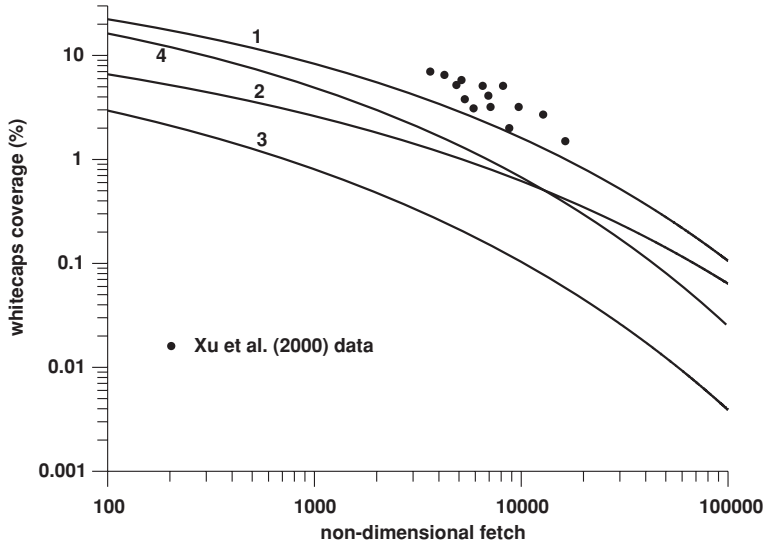

Figure 7.13: Whitecap coverage as a function of nondimensional wind fetch for four different methods: 1 – limiting steepness criterion, 2 – threshold acceleration criterion, 3 – geometry of spilling breakers approach, 4 – non-Gaussian amplitude distribution approach.

some scattering, all methods show the same decreasing trends with the nondimensional wind fetch.

The ocean whitecaps coverage is closely linked with the environmental impact of bubbles and spray. Blanchard (1963) published a distribution of this coverage for both hemispheres and for particular seasons. Figures in his papers clearly demonstrate the dominant role of the southern hemisphere in bubble and spray production. In particular, they indicate that the most extensive whitecap coverage appears during winter seasons, i.e. during December–February in the Northern Hemisphere and during June–August in the Southern Hemisphere. In both areas, whitecap coverage is about 6–8%. However, the absolute value of the whitecap coverage within 10° zonal strips in both hemispheres is quite different. In the Southern Hemisphere, due to the absence of continents and large wind fetches, the total whitecap area is much larger. For example, in June–August at the latitudes 40–50° S, this area is as large as about $30 \times 10^5\,\mathrm{km}^2$. It should be noted at these latitudes also during the 'southern summer' the whitecap coverage remains large, about $22 \times 10^5\,\mathrm{km}^2$. On the other hand, in the Northern Hemisphere, the total whitecap area becomes smaller and reaches about $10 \times 10^5\,\mathrm{km}^2$ during December–February at the latitudes 50–60° N.

Chapter 8

Fundamentals of marine aerosols

8.1 Introduction

All non-gaseous particles suspended in the atmosphere are called aerosols. Aerosols are mainly composed of droplets and crystals but also organic matter particles and large ions. These constituents can be both natural and anthropogenic, such as liquid seawater drops, dry sea salt particles, dust transport from the deserts by wind, as well as particles resulting from human activities related to industrial processes and agriculture, volcanic eruptions and meteorite destruction in the atmosphere. Particles forming aerosols attain sizes from nanometres to several micrometres. Particle size classes are traditionally named 'modes', namely: ultrafine, Aitken, accumulation and coarse mode. Aerosol emission from the global ocean is one of the major natural sources of aerosols in the atmosphere. Because approximately 71% of the Earth's surface is covered by oceans, marine aerosols play an important role for various geochemical and geophysical processes and for the Earth's climate as a whole. It is estimated that annual marigenic aerosols' contribution varies from 0.3×10^{12} to 30×10^{12} kg, corresponding to sea aerosol mass flux over the oceans of 0.03×10^{-3} kg/(m^2 s^1) to 3×10^{-3} kg/(m^2 s^1) (Lewis and Schwartz, 2004).

Marine aerosol composition is formed in the planetary boundary layer of the atmosphere over the open ocean. However, even in locations very distant from land, marine aerosols are seldom composed solely of marigenic aerosols. The reason for this fact is that the lifetime of the majority of aerosols in the atmosphere is long enough to allow long-distance transport. In fact, aerosol transport has to be considered on a global scale. However, there is a coarse mode of aerosols, frequently called sea salt mode, that can be of local origin.

Two types of aerosol of oceanic origin are distinguished in the atmosphere. In particular, marine primary aerosol is an aerosol directly emitted from the sea surface, while secondary aerosol defines aerosol formed from gases emitted from the ocean, which undergoes chemical transformation in the atmosphere. Emission of primary aerosol is completely determined by the dynamics and physical parameters of the sea surface. Contrary to that, emission of secondary aerosol is influenced also by biological and chemical processes in the sea, not

only by its dynamics. Marine aerosol particles interact with other atmospheric gaseous and aerosol constituents by acting as sinks for a considerable number of gases and by suppressing new particle formation. In this way they influence the geochemical cycles of substances with which they interact. Presence of aerosols affects the physics and chemistry of the marine atmosphere. Marine aerosols also play a very important role for visibility, remote sensing and air quality. In a global dimension, marine aerosols influence climate through scattering and absorbing solar radiation, and serving as seed particles for cloud drops and development of precipitation.

In this chapter we discuss the fundamentals of aerosol fluxes emitted from the sea surface and their climate connection. To get a better understanding of the mechanisms of aerosol production, it is useful to start with a discussion of the basic physical mechanisms of air bubble production and their entrainment in breaking waves. For the convenience of later analysis, the definitions of aerosol particle sizes, concentration and spray generation functions are given. Moreover, the characteristics of the basic types of aerosol droplets, namely jet drops, film drops and spume drops, are discussed in detail. Finally, comments on air–sea gas exchange enhanced by wave breaking and their connection with climate formation are added.

8.2 Bubble entrainment in breaking waves

Breaking waves dissipate up to 40% of their energy and up to 50% of the energy loss is expended in entraining air bubbles and in creating a dense plume of bubbles (Rapp and Melville, 1990). Laboratory and field measurements have shown that bubbles are concentrated within clouds formed during breaking and they are forced downward by turbulence. Bubbles penetrate to a depth about a factor $6\left(\frac{C}{V_{10}}\right)^{-1}$ times the significant wave height H_s, and their concentration is typically coherent over a depth scale of $H_\mathrm{s}/2$. Moreover, the measured mean bubble radius decreases weakly with depth, being in the range from 30 to 80 µm. This value is typically about two thirds of the radius contributing most to the void fraction. Moreover, the total surface area of the bubbles is on average comparable to that of the sea surface above them (Graham et al., 2004a,b). From models simulating the generation of bubble clouds by sporadically breaking wind waves it follows that growing bubble clouds release entrained air back to the surface at rates dependent on the largest of the eddies generated. The estimated rate of bubble generation per unit sea surface is about $50\,\varepsilon^2\left(\frac{g}{L_p^5}\right)^{1/2}$, where ε is the ratio of the significant wave height H_s to energetically dominant wavelength L_p. Bubbles are distributed over a volume equivalent to hemisphere of radius $R = 2H_\mathrm{s}$. Moreover, the persistent bubble clouds contribute to the active whitecap fraction in a factor $500\,\varepsilon^4$.

The most important property of the bubbles is their size distribution, which is a controlling factor for air–sea gas flux, aerosol production, generation of

ambient noise and scavenging of biological surfactants. Experimental data (Monahan and Lu, 1990; Spiel, 1992; Cartmill and Su, 1993; Loewen et al., 1996; Deane and Stokes, 2002; Leifer and de Leeuw, 2002; de Leeuw and Cohen, 2002; Stokes et al., 2002) have shown that the bubble spectrum evolves quite rapidly in the first second or so after the active phase of air entrainment ceases. This rapid evolution was denoted by Monahan and Lu (1990) as dense 'alpha' plumes in contrast to more diffuse 'beta' plumes.

Bubble formation generates sound during the so-called acoustic phase. The recording of sound provides useful information on the mechanism of bubble formation and their dimension distributions. Two primary mechanisms determine the bubble size distribution during the acoustic phase when newly created bubbles produce pulses of sound. The first is jet and drop entrainment, which is active during the entire acoustic phase and determines the slope of the size distribution for bubbles smaller than the Hinze scale. The second mechanism is related to the bubble fragmentation in turbulent and sheared flow. This mechanism operates when the wave cavity collapses and it determines the slope of the distribution for bubbles larger than the Hinze scale. The Hinze scale is determined by the turbulent dissipation rate within the breaking wave crest as follows (Deane and Stokes, 2002)

$$a_{\mathrm{H}} = 2^{-8/5} E_{\mathrm{dissrate}}^{-2/5} \left(\frac{\gamma We}{\rho_{\mathrm{w}}} \right)^{3/5}, \tag{8.1}$$

in which γ is the fluid surface tension, ρ_{w} is the fluid density, E_{dissrate} is the energy dissipation rate, and We is the Weber number

$$We = \left(\frac{\rho_{\mathrm{w}}}{\gamma} \right) u^2 d, \tag{8.2}$$

where u is the turbulent velocity field on the scale of the bubble and d is the bubble diameter. Deane and Stokes (2002) examined video images of a breaking wave crest and distinguished two slopes corresponding to the two mechanisms mentioned above. For larger bubbles ($r > 1\,\mathrm{mm}$) they found that the bubble density per 1 µm radius increment and per m^3 is proportional to $r^{-10/3}$, while for smaller bubbles, a $r^{-3/2}$ power-law scaling with radius r results.

The multimode character of the bubble size distribution was also confirmed during the LUMINY Wind-Wave Experiment (Leifer and de Leeuw, 2002). Large variability was observed between bubble plumes in terms of density, dynamics, size and penetration depth. To take into account these factors, a special bubble plume classification system was proposed by the authors. Bubble distribution for radii <0.05 mm is proportional to $r^{-2/3}$, while for radii $r > 1.5\,\mathrm{mm}$ the relationship has a form proportional to $\sim r^{-5/3}$.

Typical oceanic bubble size spectra observed 30 cm below whitecaps, off the coast of southern California, also disclosed a two-slope pattern. For smaller bubbles ($r < 1\,\mathrm{mm}$), the slope varies from (−1.8) to (−2.9), and for larger bubbles this slope is in the range from (−4.9) to (−5.5) (Deane and Stokes, 2002; Stokes

et al., 2002). The bubbles of radii less than 300 µm are at least 10 times more numerous in open ocean whitecaps than in the laboratory. The differences between oceanic and laboratory bubble plumes have important implications for air–sea gas flux estimation. As the smaller bubbles are more numerous in the open sea, CO_2 transport is actually dominated by these bubbles and the soluble gas flux may be 2 to 4 times greater than that resulting from earlier estimates (Stokes et al., 2002).

An open-ocean experiment on bubble size distributions was also reported by de Leeuw and Cohen (2002). Their bubble measuring system, deployed from buoys, provides bubble size distribution in the diameter range from 30 to 1000 µm. The resulting spectra possessed peaks at diameter of 50–80 µm while the spectrum slope varied from (−1.8) to (−5). Often a second peak appeared at diameter 200–300 µm. Moreover, some differences between deployments in the North Sea and in the North Atlantic were observed, probably due to seasonal variations.

It should be expected that the chemical composition of water alters the process of microbubble formation. This problem is of special importance when we try extrapolating the freshwater experimental results to the ocean environment. Cartmill and Su (1993) showed experimentally that the salinity changes the nature of the bubbles produced and their evolution. For bubble radii greater than 100 µm, there is an order of magnitude difference in the number of bubbles at a depth of 0.3 m. This difference is much smaller for bubble radii less than 100 µm. However, at water depth 0.73 m, the difference in the number of bubbles is of an order of magnitude over the entire range of observed radii. On the other hand, bubble density spectrum slope, with (−3) power, fits the data reasonably well in the 100–1200 µm range. The authors argued that observed difference in the number of bubbles produced by saltwater versus freshwater breaking waves is attributed to the coalescence of small bubbles in fresh water.

The size distributions of large bubbles entrained by mechanically generated breaking waves in freshwater and saltwater were measured by Loewen et al. (1996). They found that there were no significant differences observed between the depth and size distribution of the bubbles in saltwater and freshwater. Moreover, in both cases the size distribution was well represented by a power law equation of the form $N \sim r^{-3.7}$.

8.3 Definitions of aerosol particle size, concentrations, fluxes and spray generation functions

8.3.1 Size-dependent number concentrations

In this section we summarize briefly the basic definitions used in the literature to describe the fundamental parameters of marine aerosol production, removal

and transportation. The size of particles and their concentration are central to all aspects of aerosol behaviour. In particular, the number of aerosol particles per unit volume at a given location and time in a unit linear interval for radius r $(r,\ r + dr)$ is given by

$$n(r) = \frac{dN(r)}{dr}, \tag{8.3}$$

in which $N(r)$ denotes the number concentration of all particles with radius r less than the value of the argument. Therefore, the total number concentration of all aerosol particles is

$$N(r_0) = \int_0^{r_0} n(r)dr, \tag{8.4}$$

in which $N(r)$ is the cumulative distribution of the aerosol particles. Sometimes the size-dependent number concentration $n(r)$ is expressed in terms of the unit logarithmic interval of radius r $(\log r,\ \log r + d\log r)$ – see for example Lewis and Schwartz (2004). Therefore, we have

$$n_l(r) = \frac{dN(r)}{d\log r} = \ln 10\, r\, n(r). \tag{8.5}$$

Several functional forms have been proposed to parameterize size distributions of marine aerosol concentration. The most popular are three formulae, namely power law type formula, gamma or modified gamma distribution, and lognormal distribution. The power law type distribution takes the form proposed by Junge (1953)

$$\frac{dN(r)}{dr} = \frac{a}{\ln 10} r^{-(b+1)}, \tag{8.6}$$

in which $b > 0$. This distribution is also presented in the form

$$dN(r) = N_0 \left(\frac{r}{r_0}\right)^{-s} d\log r. \tag{8.7}$$

Junge distribution yields a monotonic decrease in increasing radius, r, and cannot describe the size distribution for all particle sizes. Thus, it is necessarily restricted in its radius range of applicability.

The popular gamma distribution and modified gamma distribution are

$$\frac{dN(r)}{dr} = ar^b \exp\left(-cr^d\right), \tag{8.8}$$

where $a > 0$, $c > 0$ and $d > 0$. The coefficients a, b, c and d are independent of r but they may depend on some meteorological quantities. It should be noted that for $d = 1$, the above distribution becomes the ordinary gamma distribution. Some widely used distributions such as those proposed by Nukiyama and

Tanasawa (1938), when $b = 2$ and $0.33 < d < 0.50$, and the popular Weibull (1951) distribution can be fitted to the same form.

A similar distribution was proposed by Bortkovskii (1987) for droplets size distribution in the near water atmospheric layer

$$\frac{dN(r)}{dr} = 4\frac{r^2}{r_{\mathrm{m}}}\exp\left(-2\frac{r}{r_{\mathrm{m}}}\right), \tag{8.9}$$

where r_{m} is the average drop radius, being in the range $30.0\,\mu\mathrm{m} < r_{\mathrm{m}} < 60.0\,\mu\mathrm{m}$.

Fairall and Larsen (1984) reported that the density of number of sea salt particle distribution may be presented by the following function

$$\frac{dN(r)}{dr} = C_1\left(\frac{r}{a}\right)\exp\left(-C_2(r/a)^b\right), \tag{8.10}$$

where r is the particle radius in μm, C_1 is the parameter depending on wind speed and on altitude above sea level, C_2 is the numerical constant, b is the parameter depending on wind speed and a is the coefficient depending on relative humidity.

Finally, lognormal distributions of the form

$$\frac{dN(r)}{dr} = \frac{1}{ar}\exp\left\{-\frac{1}{2}\left(\frac{\ln r}{b}\right)^2\right\} \tag{8.11}$$

were used for a wide variety of applications, including marine and atmosphere aerosol distribution, cloud drop size distribution and others.

8.3.2 Size-dependent mass concentrations

To distinguish one aerosol particle from another in a given set of conditions, the mass of solute it contains, m_{dry}, is used. In this way sea aerosol particle is described solely by its solute mass. Hence the number concentration can be presented in the form of dry particle mass, m_{dry}, as follows (Lewis and Schwartz, 2004)

$$\frac{dN(m_{\mathrm{dry}})}{dm_{\mathrm{dry}}} = \left(\frac{r_{80}}{r_{\mathrm{dry}}}\right)^3 \frac{n(r_{80})}{4\pi\rho_{\mathrm{ss}}r_{80}^2} \approx \frac{8n(r_{80})}{4\pi\rho_{\mathrm{ss}}r_{80}^2}, \tag{8.12}$$

in which

$$m_{\mathrm{dry}} = \frac{4\pi}{3}\rho_{\mathrm{ss}}r_{\mathrm{dry}}^3, \tag{8.13}$$

where ρ_{ss} is the density of dry sea salt and the radius r_{80} denotes the radius of the particle in equilibrium with the atmosphere at a given ambient relative humidity of 80%.

Sea water droplets are hygroscopic, and therefore they change their equilibrium water content and radii under different atmospheric conditions; particularly they depend on the ambient relative humidity. The mass fraction of sea

salt, corresponding to this relative humidity in a sea water drop, is about 23%, and the density is near $1.2\,\mathrm{g/cm^3}$. The ratio r_{80}/r_{dry} becomes nearly equal to 2.0, which was used in (8.12). It should be noted that for simplicity in the following text, the radius r_{80} is presented simply as r.

The mass of solute contained in the particle now becomes

$$m_{\mathrm{dry}} = \frac{4\pi}{3}\rho_{\mathrm{ss}}\, r_{\mathrm{dry}}^3 \approx \frac{1}{8}\,\frac{4\pi}{3}\,\rho_{\mathrm{ss}}\, r^3 = \frac{\pi}{6}\,\rho_{\mathrm{ss}}\, r^3. \tag{8.14}$$

It should be noted that the equivalent dry radius is not a physical quantity because dry particles of aerosol have various shapes, not necessarily spheres.

The dry particle mass can be used to define the size-dependent number concentration. Using relationships (8.3) and (8.13) we obtain

$$\frac{dN(r)}{dm_{\mathrm{dry}}} = \frac{2n(r)}{\pi\rho_{\mathrm{ss}}\, r^2}. \tag{8.15}$$

In a similar way, the size-dependent aerosol dry mass concentration $m(r)$ takes the form

$$m(r) = \frac{dM(r)}{dr} = \frac{\pi}{6}\,\rho_{\mathrm{ss}}\, r^3 n(r). \tag{8.16}$$

Zhang et al. (2005) noted that the dry sea-salt particle size is not well defined because water is present in sea-salt particles even at very low relative humidity (RH). Therefore, it will be more appropriate to use the particle size at formation as the reference state rather than the 'dry' particle size. They showed that the ratio of the particle size at the local (RH) relative to the particle size at formation is a function of relative humidity only. Assuming that there is thermodynamic equilibrium of water between sea-salt particles and the ambient environment and the effect of particle-surface curvature on water equilibrium is negligibly small, conservation of solute within each particle exists. Under these assumptions, the following relationships were obtained (Zhang et al., 2005)

$$\frac{r_0}{r_{\mathrm{RH}}} = \sum_{i=0}^{5} p_i\,(\mathrm{RH})^i \quad \text{for} \quad 45\% < \mathrm{RH} < 99\%, \tag{8.17}$$

in which r_0 and r_{RH} are the radii at formation and at ambient (RH), respectively, p_i are the fitting coefficients as follows

	Coefficients p_i					
i	0	1	2	3	4	5
p_i	28.376	−205.44	653.37	−1031.7	803.18	−247.08

Applying the above formula, we obtain for RH = 80%, $r_0/r_{80} = 1.97$. In general, values of the ratio r_0/r_{RH} match those from Fitzgerald's (1975) results when $\mathrm{RH}_0 = 98\%$ for $r_{\mathrm{dry}} \approx 30\,\mu\mathrm{m}$. Zhang et al. (2005) demonstrated an

application of the correction factor (8.17) to several spray generation functions which are discussed in Chapter 9.

We note that Andreas (1992) proposed the relationship between the particle radius at its formation, r_0, and at a relative humidity of 80%, r_{80}, in the form

$$r_{80} = 0.518 r_0^{0.976}, \tag{8.18}$$

where both radii are in micrometres. Roughly speaking, we can say that r_0 is approximately twice r_{80}.

8.3.3 Aerosol fluxes

The rate of upward transport of marine aerosol particles from the ocean to the atmosphere is one of the fundamental quantities of air–sea interaction processes. This transport, averaged over temporal and spatial scales much greater than those characterizing individual breaking waves and whitecaps, is known as the size-dependent production flux $f_{\text{prod}}(r, z)$. Function $f_{\text{prod}}(r, z)$ depending on a set of meteorological and environmental conditions denotes one-way flux of particles from the ocean to the atmosphere at a given level z. The production size-dependent flux differs from the size-dependent net vertical flux of marine aerosol particles $f(r, z)$ by the size-dependent flux of marine aerosol particles deposited, $f_{\text{dep}}(r, z)$. Thus we have (Lewis and Schwartz, 2004)

$$f(r, z) = f_{\text{prod}}(r, z) - f_{\text{dep}}(r, z), \tag{8.19}$$

when $f(r, z)$ and $f_{\text{prod}}(r, z)$ are taken as positive upward, and $f_{\text{dep}}(r, z)$ is taken as positive downward.

Function $f_{\text{dep}}(r, z)$ describes removal of aerosols by gravitational sedimentation, turbulent eddy diffusion, Brownian diffusion and removal through precipitation. It should be noted that processes responsible for the formation of aerosol particles and the processes responsible for the removal of aerosol particles to the sea surface through dry deposition are fundamentally different and controlled by different mechanisms. Therefore, it is essential to distinguish between the size-dependent flux $f_{\text{prod}}(r, z)$ and the size-dependent net flux $f(r, z)$, and to treat them separately. All above fluxes are related to a given horizontal reference plane at an arbitrary elevation z. In particular, size-dependent dry deposition flux $f_{\text{dep}}(r, z)$ is defined as the net downward flux through a horizontal reference plane at elevation z in the absence of a surface source. On the other hand, size dependent aerosol production flux through the level z is the number of aerosol particles produced at the sea surface that attain level z above mean sea level. For many purposes, the size-dependent net flux $f(r, z)$ rather than size-dependent production flux $f_{\text{prod}}(r, z)$ is desired. It is the measurable quantity describing the rate, per unit area of the sea surface, at which the number of aerosol particles of a given size above the level of measurement is changing. On the other hand, the aerosol size-dependent production flux $f_{\text{prod}}(r, z)$ constitutes a source of aerosol particles to the atmosphere, and it represents the

effect of marine aerosols on climate change and atmospheric chemistry (Lewis and Schwartz, 2004).

Beside the size-dependent production flux $f_{\text{prod}}(r, z)$, related to some reference level above the sea surface, another flux is frequently discussed. It is the so-called interfacial size-dependent production flux $f_{\text{prod}}(r, 0)$ defined as the rate of upward transport of aerosol particles per unit area from the ocean surface to the atmosphere. Therefore, similarly to (8.19) we have for the net flux at $z = 0$

$$f(r, 0) = f_{\text{prod}}(r, 0) - f_{\text{dep}}(r, 0). \tag{8.20}$$

The function $f_{\text{dep}}(r, 0)$ denotes now removal of aerosol particles at $z = 0$. Let us form a ratio (Lewis and Schwartz, 2004)

$$\Psi(r, z) = \frac{f_{\text{prod}}(r, z)}{f_{\text{prod}}(r, 0)}. \tag{8.21}$$

It is obvious that $0 \leq \Psi(r, z) \leq 1$. The quantity $\Psi(r, z)$ is equal to the probability that an aerosol particle of a given radius r produced at the sea surface attains a level z. In particular, for small particles, Ψ is near unity as nearly all of these particles formed at the sea surface attain a level z (say standard height of 10 m above sea surface). For increasing particle size, r, the ratio Ψ decreases as many particles cannot attain level z.

The ratio Ψ is required to relate the aerosol fluxes produced due to bursting of bubbles from whitecaps formed by breaking waves and those produced due to higher wind speed tearing of drops from wave crests. There are formulations in the literature, reviewed by Lewis and Schwartz (2004), showing that for aerosol particles less than several micrometres, $\Psi \approx 1.0$. When $r \geq 25\,\mu\text{m}$, the ratio $\Psi \approx 0.0$. For the particle size range $5\,\mu \geq \text{mr} \geq 25\,\mu\text{m}$, the ratio Ψ increases with increasing wind speed.

8.3.4 Spray generation functions

As mentioned above, the size-dependent interfacial marine aerosol production flux $f_{\text{prod}}(r)$ is defined as the rate of upward transport of aerosol particles per unit area and unit time from the ocean to the atmosphere. Knowledge of $f_{\text{prod}}(r)$ permits calculation of the total production fluxes, volume and mass of aerosols. Some investigations (Andreas et al., 1995; Andreas, 1998; Petelski and Piskozub, 2006) denote flux $f_{\text{prod}}(r)$ as the sea spray generation function f_{sgf}, quantifying the rate at which spray droplets of a given size are produced at the sea surface. This notation will also be used here to distinguish the fluxes from the size-dependent number concentrations. Thus, the sea spray generation function f_{sgf} in terms of a unit linear interval of radius r takes the form

$$f_{\text{sgf}}(r) = \frac{dF(r)}{dr}, \tag{8.22}$$

where $F(r)$ denotes the cumulative distribution of the total size-dependent production flux. In a similar way we define the size-dependent sea spray generation function in a unit logarithmic interval of radius r as follows

$$f_{\mathrm{sgf}}(r) = \frac{dF(r)}{d\log r} = \ln 10\, r\, \frac{dF(r)}{dr} = \ln 10\, r\, f_{\mathrm{sgf}}(r). \tag{8.23}$$

Now the total flux of dry sea salt mass f_{dmass} becomes

$$f_{\mathrm{dmass}}^{(\mathrm{tot})} = \int f_{\mathrm{dmass}}(r)dr \ \ [\mathrm{kg/m^2/s}], \tag{8.24}$$

in which the size-dependent dry mass flux $f_{\mathrm{dmass}}(r)$ is

$$f_{\mathrm{dmass}}(r) = \frac{\pi}{6}\rho_{\mathrm{ss}} r^3 f_{\mathrm{sgf}}(r). \tag{8.25}$$

Andreas (1998) argues that to study the spray heat and moisture transfer, so-called volume flux is more relevant and he defined it as follows

$$f_{\mathrm{vol}}(r) = \frac{4\pi r^3}{3} f_{\mathrm{sgf}}(r). \tag{8.26}$$

The volume flux is given in cubic metres per square metre of surface per second per increment in droplet radius.

8.4 Mechanisms of aerosol production

8.4.1 Introduction

The presence of aerosol particles in the atmosphere has long been known. But the exact processes by which aerosol particles are introduced into the atmosphere from the ocean have only recently been established. Among several aerosol production mechanisms, currently only two are believed to play a major role in aerosol production. The first one is the *bursting of bubbles* formed primarily by breaking waves (Blanchard, 1954; Wu, 1973, 1988a; Reinke et al., 2001) – see Fig. 8.1. When the wind speed is sufficiently high, typically ≈ 5 m/s or greater at 10 m above the ocean surface, the stress of the wind on the ocean causes the water near the surface to move faster than the underlying water and form a wave that breaks under the influence of gravity. This breaking wave entrains bubbles into the ocean, and these bubbles subsequently rise, forming a whitecap, and burst at the surface. Bursting bubbles, entrained by the breaking of waves, play a crucial role in global air–sea gas exchange, and mediate various physical, chemical and biological fluxes.

The other aerosol emission mechanism, also commonly regarded as an important factor in mass exchange between the ocean and atmosphere, is the direct driving of droplets by wind from the spume off the wave crests. The droplets generated by this mechanism are named *spume droplets* or sometimes they are also called spindrift or chop droplets (see Fig. 8.2). We have also to mention the

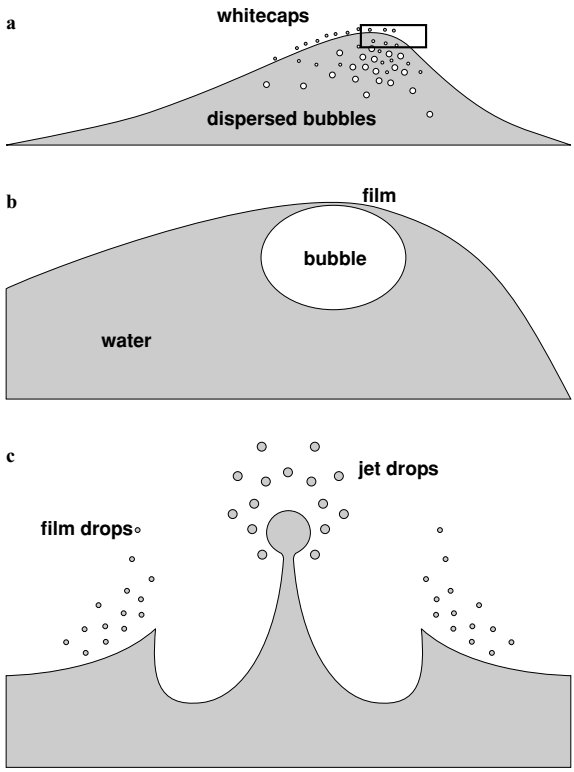

Figure 8.1: Scheme of aerosol production: (a) bubbles dispersed in the water body, (b) bubble approaching the water surface, (c) jet and film drop generation.

mechanism of aerosol generation based on droplets hitting the sea surface and throwing out in the form of so-called *splash droplets*. This mechanism is particularly intensive within the surf zone. Because splash droplets are secondary to bubble droplets or spume droplets, they are usually included in one of these categories.

A number of authors indicate atmospheric precipitation as a potential source of aerosol emission from the sea. However, at the same time atmospheric

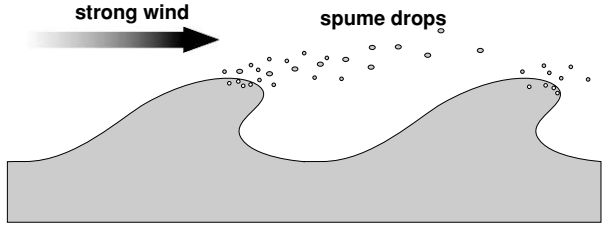

Figure 8.2: Scheme of spume drop generation.

precipitation is intensively removing aerosols from the atmosphere; hence its role in aerosol transport from the sea is ambiguous. In this context, there are some reports on an increase in sea salt concentration in the near water atmospheric layer under rainfall (Marks, 1990). Fortunately it is not continuously raining over the seas and the effect of rain can be easily eliminated from the results of studies on aerosol generation from the sea surface.

8.4.2 Drops from bursting bubbles

Droplets emission from gas bubbles bursting on the surface of a liquid is a process well recognised and extensively studied in laboratory experiments (Lewis and Schwartz, 2004). However, a coherent theory has not been formulated and this fact presents a primary obstacle in quantitative expression of the emission flux from the sea. Gas bubble bursting results in two types of droplets emitted into the atmosphere, namely: *jet droplets* – emitted in the form of a water jet from bubble bottom, and *film droplets* – formed from the bubble membrane, which extended over the sea surface. The process of bursting bubbles and producing jets and film droplets, schematically presented in Fig. 8.1, can be described as follows (Lewis and Schwartz, 2004): when a bubble arrives at the liquid surface, it initially overshoots its equilibrium position. As the sea surface is always covered by surface-active substances, the bubble relaxes within several milliseconds to its equilibrium position. A portion of the bubble – the bubble cavity – is situated below the equilibrium level of the surface due to internal pressure within the bubble, induced by the surface tension of the film. During relaxation time, the bubble film becomes thinner and ultimately bursts. Bursting may yield fragments, known as film droplets, which are projected at various angles with respect to the surface. Time of bursting is an order of tens of microseconds and velocity of the produced film droplets may be of an order of 10 m/s. The cavity formed by the bubble fills with water, due to surface tension, with accelerations being 10^3 and 10^6 times the acceleration due to gravity. This results in formation of a small vertical column, or jet, in the centre of the cavity left by the bubble. The jet is composed of a thin water layer on the cavity surface. The thickness of this layer is of the order 5–10% of the bubble diameter. The jet rises roughly one bubble diameter above the surface and becomes unstable. Drops ejected above the viscous boundary layer entrain upward into the atmosphere by turbulent eddies and contribute to the marine aerosols. It is believed that bubbles with radius $r_{\mathrm{bub}} \leq 0.5\,\mathrm{mm}$ produce only jet droplets and bubbles with $r_{\mathrm{bub}} \geq 3.0\,\mathrm{mm}$ only film droplets. For intermediate size bubbles, both jet and film droplets can be produced; however, jet droplets are generally larger than film droplets but film droplets are more numerous.

Woolf et al. (1987) used four properties of the aerosol production process to indirectly classify film droplets and jet droplets, namely:

(1) elapsed time from wave breaking to droplets,

(2) site of production of the droplets relative to the active whitecap plume,

(3) electrostatic charge per droplet and

(4) dependence of the number of droplets produced on seawater temperature.

The authors found that the bulk of the droplets produced in the radii range $0.25\,\mu m < r < 2\,\mu m$ are film droplets, while the majority of the droplets with radii greater than $2\,\mu m$ belong to the jet droplets type. However, both mechanisms contribute equally to $2\,\mu m$ radius droplets population.

8.4.2.1 Jet droplets

The detailed dynamics of a bursting bubble is very complicated from the physical and mathematical point of view. In consequence, there is almost a complete absence of any theoretical descriptions of aerosol particle production in the literature. One such attempt is the approximated analytical model for dynamics of bubble-mediated jet droplet production, developed by Dekker and de Leeuw (1993). The initial stage of the process is formation of a capillary surface wave by a bursting bubble. Determination of the evaluation in time of this initial capillary wave profile provides information on the local amplitude, vertical velocity and acceleration of particles at the sea surface. Theoretical analysis showed that the droplet is ejected just prior to the instant of maximum local acceleration. Moreover, energy balance allowed a prediction of the droplet size and the ejection velocity. The authors reported a good agreement with experimental data.

Current understanding on jet droplet generation is derived mostly from laboratory experiments involving droplets from a stream of monodispersive bubbles bursting individually at a calm water surface (Spiel, 1994). Laboratory tests showed that the number of jet droplets produced per bubble N_{jet} decreases toward zero as the radius of bubble r_{bub} increases. For bubbles of radius r_{bub}, in the range $0 < r_{\text{bub}} < 3.0\,\text{mm}$, the number N_{jet} can be parameterized by the Blanchard (1983) formula

$$N_{\text{jet}} = 7\exp(-0.65 r_{\text{bub}}). \tag{8.27}$$

Moreover, the majority of experimental data summarized by Levis and Schwartz (2004) are best fitted as

$$N_{\text{jet}} = 10\exp(-1.4 r_{\text{bub}}). \tag{8.28}$$

Loss of energy to friction during jet droplet production implies that a lower limit of the radius r for very small jet droplets, below which there would be insufficient energy left to produce a droplet (MacIntyre, 1968), should exist. This means that the relation (8.28) may not be valid for $r_{\text{bub}} \to 0$, and probably the mean number of jet droplets produced per bubble N_{jet} first increases with decreasing r_{bub}, and then it decreases for very small r_{bub} due to lack of sufficient energy available for jet droplet production.

There are some data on the temperature and salinity dependence showing that the number N_{jet} decreases with increasing water temperature. This

dependence is manifested through the viscosity, surface tension and density which control the behaviour and shape of the jet. At lower temperature, due to higher viscosity and higher surface tension, a longer jet is formed. In particular, Mårtensson et al. (2003) reported the results of laboratory experiments on the submicrometer particles production by bursting bubbles. When the water temperature increases, the number concentration decreases for $D_\mathrm{p} < 0.07\,\mu\mathrm{m}$ (D_p is the dry diameter), wheras for $D_\mathrm{p} > 0.35\,\mu\mathrm{m}$, this number increases. On the other hand , the salinity effect suggests different droplet formation process for droplets smaller and larger than $0.2\,\mu\mathrm{m}$.

Lewis and Schwartz (2004) summarized available dependence of radii of jet droplets r on bubble radius r_bub for experiments when jet droplets were produced by single bubbles bursting at a calm liquid surface. Size of jet droplets vary over a wide range, from $r = 0.5$ to $200\,\mu\mathrm{m}$. Almost all data are concentrated within the radius band

$$0.025 r_\mathrm{bub} < r < 0.1 r_\mathrm{bub}. \tag{8.29}$$

In particular, for the top and second droplets (i.e. for the first and second droplets produced) when $r_\mathrm{bub} \geq 0.1\,\mathrm{mm}$, the following relationship results

$$r = 0.075 r_\mathrm{bub}^{1.3}, \tag{8.30}$$

when r and r_bub are expressed in mm.

Jet droplets produced by bubbles bursting in calm water or sea water reach maximum heights up to 20 cm in still air for $r_\mathrm{bub} \approx 0.7{-}1\,\mathrm{mm}$, which corresponds to the jet droplets radii $r \approx 50 - 80\,\mu\mathrm{m}$. For further increasing bubble radius r_bub, the ejection height decreases to zero for very large bubbles which do not produce jet droplets. In a sequence of jet droplets produced by the burst of a single bubble, the maximum height reached by later droplets are significantly less than that of the top droplet. The maximum height h attained by a jet droplet is determined by its radius, ejection velocity v_0 and forces acting on the droplet, i.e. gravity and drag forces. To reach maximum height, jet droplets require very large velocity, up to tens of metres per second. There is some experimental evidence that jet droplets with $r \approx 50\,\mu\mathrm{m}$ reached an ejection velocity of at least $3\,\mathrm{m/s}$ (Kientzler et al., 1954).

Several relationships between the maximum height h attained by a jet droplet and r_bub have been proposed. In particular, Stuhlman (1932) found that

$$h \approx 36.79 r_\mathrm{bub}^{1.5} \quad \text{for} < 0.05\,\mathrm{mm}. \tag{8.31}$$

In the above formula height h is given in cm and r_bub in mm. When we use (8.30), we can rewrite (8.31) as follows

$$h \approx 730.65 r^{1.15}. \tag{8.32}$$

Spiel (1992) presented evidence that air bubbles bursting at the surface of water are Helmholtz resonators when the trapped gas tries to escape through the hole in the top of the bubble. The size of the artificially produced single

bubble was measured by determining the resonance frequency of the pulsating bubble at the moment of pinch-off from the capillary according to the formula (Longuet–Higgins et al, 1991)

$$r = \sqrt{\frac{3\gamma p}{\rho_{\mathrm{w}}}}\omega^{-1}, \tag{8.33}$$

where ω is the frequency, p is the ambient pressure and $\gamma = 1.4$ is the ratio of specific heats of the bubble gas when the process is assumed to be adiabatic. The estimated radius of jet droplets for the 491 µm radius bubbles ranged from 35 to 60 µm, while the vertical velocity ranged from 2.2 to 6.65 m/s. The estimated size of jet droplets is in good agreement with that obtained by Blanchard (1989).

In two companion papers, Spiel (1995, 1997) reported the results of his comprehensive laboratory experiments on the parameters of the birth of jet droplets originating from bubbles bursting on the water surface. The results are valid for bubble sizes r_{bub} from 350 to 1500 µm. He found that the dependence of the average jet droplet speed on bubble size is an exponential function of the form

$$v_{e_i} = a_i \exp(b_i\, r_{\mathrm{bub}}), \tag{8.34}$$

where r_{bub} is given in µm, v_{e_i} is in m/s and i is droplet number in the sequence when the top droplet is denoted by $i = 1$. Coefficients a_i and b_i depend on the water temperature. Typical values of a_i and b_i are given in Table 8.1.

From Table 8.1 it follows that for the top drop $v_{e_i} \approx 12.3 \exp(-0.0016\, r_{\mathrm{bub}})$. Extrapolating to small bubble size, we find that the maximum droplet ejection speed approaches 12 m/s as bubble size vanishes. On the other hand, for very large bubbles, say $r_{\mathrm{bub}} = 1500$ µm, the ejection speed will be only 1.1 m/s. The time t for the top droplet to separate from the rising jet depends also on the bubble radius in a similar exponential manner. Moreover, the variation of average break-off height of the jet droplets with bubble size shows strong dependence with r_{bub}, although no fits to the data were possible.

The time for a jet droplet of a given radius to attain its maximum height and to fall back to the sea surface determines the time period in which the jet droplet may be taken upward by the moving eddies contributing to marine aerosol production. Experiments have shown that jet droplets attain their maximum heights before they undergo some change due to evaporation. The time required for top jet droplets with radii $r = 10, 15, 20$ and 25 µm to reach their maximum

Table 8.1: Ejection velocity parameters (adapted from Spiel, 1997)

Droplet	a_i	$b_i \times 10^{-3}$
1	12.12 ± 0.33	-1.39 ± 0.041
2	9.64 ± 0.39	-2.806 ± 0.080
3	6.53 ± 0.84	-2.916 ± 0.260

heights 5, 8, 10 and 12 cm and fall back to the sea surface in still air equals approximately 1, 0.7, 0.6 and 0.5 s, respectively. However, in real conditions with nonzero wind speed, the maximum height attained by jet droplets becomes lower, and therefore the time during which the droplets can be moved upward becomes shorter. As a result, the mean number of jet droplets per bubble that are taken upward and remain airborne contributing effectively to aerosol production and formation of aerosol fluxes is much less than that given by the formulae (8.27) and (8.28).

According to Cipriano et al. (1983) and Lewis and Schwartz (2004) there are three basic factors providing a lower limit to the size of jet droplets which have any appreciable probability of being entrained upward into the atmosphere, namely: size of bubbles that burst at the surface, maximum height attained by the droplet and energy available for jet droplet production. It should be noted that small bubbles rise extremely slowly and frequently dissolve before they arrive at the surface. Thus only a few such bubbles would arrive at the surface to produce jet droplets. Moreover, jet droplets that are not ejected above the height of the viscous sublayer are unlikely to be further entrained upward by turbulence eddies. As follows from (8.31) and (8.32), the maximum ejection height decreases with decreasing r_{bub}, as does jet droplet size. The lower limit of the size of top jet droplets that attain a given height can be presented as follows (Lewis and Schwartz, 2004)

$$h \sim 0.3r, \tag{8.35}$$

in which h is given in cm, and r in μm. If bubbles produce more than one droplet, heights of later droplets are considerably smaller than those of the top droplet. Hence, they are less likely to be entrained upward.

8.4.2.2 Film droplets

In contrast to jet droplet generation, mechanisms producing film droplets still remain unresolved. Several different approaches have been reported, including a cloud of droplets, a single vertical line of droplets, a segment of a spherical cap, and a family of droplets projected at a low angle (Lewis and Schwartz, 2004). Some film droplets, presumably formed by the shattering of the film itself, are ejected vertically, while others, induced by the collision of the collapsing film with the water surface, are ejected at a low angle to the horizon. Experiments have shown that the radii of produced film droplets vary from the very small value of 0.01 to 170 μm in distilled water (Afeti and Resch, 1990). A large fraction of the number of film droplets from bursting bubbles have radii less than 1 μm. In particular, Cipriano et al. (1983) found experimentally that a lot of bursting bubbles in sea water produced film droplets of $r < 0.02$ μm.

Most of the experimental data suggest that number N_{film} generally increases with increasing r_{bub}. However, there are large discrepancies between the data,

some of which are attributed to the experimental techniques used, for example condensation chamber or diffusion chamber. Blanchard (1963) detected up to over 100 droplets with radius r at least as small as 0.01 μm. Moreover, a large peak in N_{film} (about 75) for sea water bubbles near $r_{\text{bub}} \sim 1$–$1.5\,\text{mm}$ has been observed (Blanchard and Syzdek, 1988; Resch and Afeti, 1992). Such peaks support the suggestion that multiple mechanisms are involved in the production of film droplets. Comprehensive observations on film droplets were carried out by Spiel (1998), especially for large bubbles.

Several formulae have been proposed to relate N_{film} with r_{bub} and other quantities such as the film area, A_{film}, and radius, r_{film}. However, sometimes the utility of these expressions is questionable because of the extremely large range of N_{film} for a given r_{bub}. This is probably due to a number of factors affecting film droplets production from the bubbles including temperature, contents of solutions in water, surface-active materials, residence time of the bubble on the liquid surface before it bursts, relative humidity and the speed of the air over the surface, and used experimental techniques. The data on sizes and maximum ejection heights of film droplets show that these heights are considerably smaller than those attained by jet droplets. Probably most aerosol droplets with $r < 1\,\mu\text{m}$ belong to the film droplets category.

Wu (2001) parameterized the data of film droplets produced by individual bubbles bursting at the surface of sea water by Blanchard and Syzdek (1988), Resch and Afeti (1991) and Spiel (1998). These data cover four different but overlapping size ranges. To represent the number of film droplets produced, Wu suggested the power law representation

$$N = b\, r_{\text{bub}}^{n}, \tag{8.36}$$

in which r_{bub} is the bubble radius in millimetres. The data collected by particular authors provide the best fit when $n = 2$ and the coefficients b of the particular data set are summarized in Table 8.2.

Beside the approximation (8.36) for total film droplets radii range, Wu (2001) attempted to quantify the production of film droplets over specific radius ranges. Assuming that formula (8.36) is valid in each subrange of film droplet

Table 8.2: Radii of bubbles and film droplets produced for three sets of data (adapted from Wu, 2001)

Source of data	bubble radius (mm)	film droplet radius (μm)	coefficient b
Blanchard and	0.71–3.14	0.01–4.0	1.96
Syzdek (1988)		0.4–20	1.65
Resch and Afeti (1991)	0.52–5.0	20–250	2.16
Spiel (1998)	1.47–6.29	9.0–250	2.85

radius he obtained

$$N(r) = \begin{cases} 1.96\, r_{\text{bub}}^2 & \text{for} \quad 0.01 < r < 0.4 \\ 0.96\, r_{\text{bub}}^2 & \text{for} \quad 0.4 < r < 9.0 \\ 0.69\, r_{\text{bub}}^2 & \text{for} \quad 9.0 < r < 20.0 \\ 2.16\, r_{\text{bub}}^2 & \text{for} \quad 20.0 < r < 250.0 \end{cases} \tag{8.37}$$

In the above expressions, the radius r is given in μm. Hence, the probability density of occurrence $f(r)$ for film droplets having radius r can be parameterized as follows

$$f(r) = \begin{cases} 0.066\, r^{-1/2} & \text{for} \quad 0.01 < r < 30 \\ 10.9\, r^{-2} & \text{for} \quad 30 < r < 100 \\ 1.09 \times 10^5 \times r^{-4} & \text{for} \quad 100 < r < 250 \end{cases} \tag{8.38}$$

From the above expression it follows that the mean radius for the entire size range 0.01–250 μm is 24.9 μm. It is interesting to note that only a very small fraction (about 1%) of the film cap of a bubble is used to produce film droplets.

8.4.3 Spume droplets

When the wind stress is sufficiently strong, wave breaking can directly produce droplets without the mediation of bubbles. This is in contrast to production by bubble bursting which occurs away from the crest after the wave has broken. This type of droplets, denoted as spume droplets, results from the mechanical tearing of the sharpened wave crests by the wind. The wind speed threshold for spume production is 7–11 m/s and corresponds to Beaufort Force 5. The particular value of the wind speed depends on water temperature, the wave field, and the turbulent intensity in the near-surface air. Spume droplets are usually projected nearly horizontally and their radii range up to several hundred micrometres. The formation of spume droplets has been little studied and does not appear to be well understood (Anguelova et al., 1999).

Koga (1982) investigated the spume droplets formation process using multicolour photography. He observed that during very high winds the water surface become irregular and small isolated projections occur, forming droplets with radius up to 750 μm. Koga attributed the formation of these projections to Kelvin-Helmholtz instability. However, Bortkovskii (1987) argued that this mechanism does not play a major role in typical oceanic conditions.

Wu (2000) discussed two sets of measurements of de Leeuw (1986) and Smith et al. (1993). In particular, the measurements of Smith et al. reflect two production mechanisms: one component represents the production of film and jet droplets by bursting bubbles, and the other of spume droplets by the wind tearing of wave crests. The measured production for spume droplets compares favourably in magnitude with that suggested by Wu (1993) on the basis of spray measurements in a wind-wave tank and in the field. Averaging these data Wu obtained that spectra were narrowly peaked at large radii and proportional to r^{-8}. The lower bound for this relationship is at radius $r = 150\,\mu$m. For smaller

radii, the spectrum behaves as $r^{-2.8}$. However, the rate of increase of spume droplets production with wind speed is very different. The total area of spume droplets was found to be proportional to the energy flux from the wind, which yields the dependence of this area on the function u_*^3 (Andreas et al., 1995). At higher wind speeds droplets with radii in the range 10–300 μm could contribute most of the heat fluxes.

8.5 Remarks on influence of marine aerosols on climate

8.5.1 Atmosphere-ocean gas exchange due to bubbles generated by wave breaking

The understanding of contemporary gas and aerosol fluxes is of great societal importance as we try to estimate and mitigate the influence of gases and aerosols on the global radiation budget and climate. The importance of air–sea gas transfer follows from the ocean's role in taking up a large fraction (30–40%) of fossil fuel-produced carbon dioxide, while the oceanic source of NO to the atmosphere is approximately equal to the current rate of increase of atmospheric NO. Current estimate shows that the oceans and terrestial systems play an approximately equal role in slowing the rise of atmospheric carbon dioxide (IPCC, 2004).

Knowledge of gas, moisture and heat transfer at the ocean-atmosphere interface is important for parameterization of coupling fluxes between ocean and atmosphere, and subsequently for general circulation models used in long-term climate models. Gas, moisture and heat exchange is particularly intensive for a rough sea, over the breaking waves. However, the gas transfer velocity is usually presented as a function of global wind speed distribution. This approach neglects the high variability of wind fields and the effects of local sea state characteristics, such as breaking wave intensity, bubble production etc. Donelan and Wanninkhof (2002) summarized the studies on the physical and chemical backgrounds of the interfacial gas transfer from the point of view of input of gas transfer on the global flux of carbon dioxide. They showed that presently much work is devoted to estimating the global CO_2 flux. However, despite great efforts, there are significant differences in the results due to uncertainty in the local estimates and lack of field measurements at high wind speeds. Different parameterization yields global CO_2 uptakes that differ by a factor of 3. Thus they suggest applying an approach of determining regional fluxes over a short time scale to determine the global uptake of CO_2. Wanninkhof and McGills (1999) using laboratory and field data discovered a cubic relationship between gas exchange and wind speed. A long-term relationship leads to an increase in the global oceanic CO_2 uptake.

As was shown in the previous chapters, breaking waves eject spray into the atmosphere. Spray evaporates and influences the balance of heat and moisture

above the waves. It is quite reasonable to expect a substantial increase of the air–sea gas exchange in a high sea when breaking waves are present (Woolf, 1993, 1997). Makin (1998) developed a model to account for the impact of evaporating droplets on fluxes of sensible heat and humidity in a stratified atmosphere over a stormy sea. He found that the impact of sea spray on heat and moisture fluxes becomes significant for a wind speed of about 25 m/s and above. This increase in heat and humidity transfer for strong winds is related to a drastic increase in air–sea gas exchange due to bubble transfer for high winds. Bortkovskii (2002) estimates that due to bubble transfer, the air–sea gas exchange during a storm can increase by a factor of 10. The dependence of the trace gas exchange on the thermal stability at the air–sea interface was included in the model proposed by Monahan and Spillane (1984) on the relationship between the surface resistance for the transfer of trace gases across the air–sea interface and the oceanic whitecap coverage.

It should be noted that microscale breaking of very short wind waves without air entrainment is widespread over the oceans, and this type of wave breaking and the near-surface turbulence enhances gas transfer. Zappa et al. (2002) showed that up to 75% of the transfer across the air-water interface under moderate wind speeds is a direct result of microbreaking.

In general, spray and bubbles do not have a significant effect on the density and local dynamics of the surrounding medium. In stormy weather, bubbles can change the average density by up to 0.5 ppt. That is equivalent to the density change produced by a 2°C increase in temperature. However, the effect of spray and bubbles on vertical stability is overwhelmed by the mechanical stirring due to wind stresses. It should be noted that the large-scale chemical effects of bubbles and spray are much more significant than the dynamic effects. Whitecap covered waters are usually supersaturated with oxygen and nitrogen, and other gases (Keeling, 1993). Stramska et al. (1990) examined the influence of the degree of saturation of seawater on the number and the size distribution of the droplets produced during the decay of an individual oceanic whitecap. They found that when the level of dissolved oxygen increased from 100% saturation to 130%, the production of aerosol droplets by the whitecaps generated by a standard laboratory breaking wave increased by a factor of 2.4. They argued that the results obtained from their experiments are applicable to the global ocean, as waves breaking on the sea surface can be regarded as an example of the supersaturation mechanism. Therefore, the degree of saturation has to be included in the various sea surface aerosol generation models.

Moreover, entrained air bubbles can influence chemical reactions occurring in the sea. More corrosive marine atmosphere due to salt-water spray is a major source of airborne condensation nuclei affecting the physics of precipitation and the global climate (Kraus and Businger, 1994). Also, it should be noted that bubbles rising to the surface collect any surface active material, dissolved or particulate, of organic inorganic origin (Murphy et al., 1998; Heintzenberg et al., 2000; Koch et al., 2000). In particular, it was suggested that the spray-borne

transport of bacteria from the sea surface may cause an occasional health problems for people in coastal areas.

Blanchard (1963) argued that spray contributes to the electrification of the atmosphere due to emission of a significant amount of positive charge upward from the sea. On the other hand, sea spray is a dominant factor for the global salt circulation and one of the major contributors to the mass of particulate matter injected into the atmosphere globally. Various estimates provide the annual contribution of the sea salt varying from 0.3×10^{12} kg to 30×10^{12} kg. Assuming a mean oceanic salinity of 33 ppt, an annual flux of salt from the global sea surface area of $4.01 \times 10^{14}\,\mathrm{m}^2$ must be associated with an upward water flux of $7.5 \times 10^{-4}\,\mathrm{kg/(m^2\,year^1)}$ to $7.5 \times 10^{-2}\,\mathrm{kg/(m^2\,year^1)}$.

Existence of the bubble cloud entrained by wave breaking also has a strong influence on ocean reflectance and on water light field characteristics. Stramski and Tęgowski (2001) showed that remote sensing reflectance increases significantly due to bubble entrainment and the bubble cloud effect on ocean reflectance in such a way that the water patch containing bubbles will appear greener or more yellowish than the surrounding waters with no bubbles. Thus, the effects of bubbles on reflectance can be viewed as a source of unwanted noise in the development of common ocean colour algorithms for retrieving in-water constituents such as chlorophyll concentration.

The desire to have better parameterization and prediction of aerosols for assessment of climate change, long-range forecasts, and better representation of heat and moisture exchange in meteorological models has intensified the efforts to include aerosols in climate and chemical models. The logic for such parameterization is as follows (Andreas et al., 1995): droplet temperature determines the rate at which spray droplets evaporate. Higher air temperatures enhance larger spray moisture and latent heat fluxes. The spray sensible heat transfer and the turbulent transfer are driven by the air–sea temperature difference. Therefore, the spray flux will be largest where the air–sea temperature difference is largest, namely in high latitude. In the presence of spray, the near-surface atmosphere is characterized by a droplet evaporation layer. This layer is cooler and moister than the atmospheric surface layer would be without the spray. Moreover, the vertical heat fluxes are no longer constant with height. The Eulerian and Lagrangian models yield the conclusions that in high winds, above about 15 m/s, sea spray begins to contribute significantly to the air–sea fluxes of heat and moisture.

8.5.2 Climate connections

The interaction between the ocean and atmosphere is critical to our understanding of the earth's climate. The ocean has a much greater heat storage capacity than the atmosphere. In particular, the top two and half meters of the ocean will store as much heat as the entire atmosphere, and therefore the ocean serves as a giant thermal reservoir that can moderate and limit climatic excursions

on the short-term and promote long-term climate changes (Rogers, 1995). The ocean is also the major source of water and aerosols in the atmosphere, which largely determines the radiative properties of the atmosphere, and hence the climate-control of the earth system. All of the oceans are at least partly cloud covered what modifies the temperature of the atmosphere and the ocean by absorbing outgoing longwave radiation from the surface and reflecting incoming shortwave radiation. Changes in the temperature may change the amount and type of cloud cover that, in turn, feeds back to the temperature of the ocean and atmosphere.

In the last twenty years, recognition of the potential influence of natural and anthropogenic aerosols in the marine environment on climate has substantially increased. Charlson et al. (1987) described a regulatory feedback mechanism for control of climate by marine phytoplankton. According to this hypothesis, biogenic aerosol particles affecting cloud microphysical properties are the result of emissions of dimethylsulphide (DMS) by marine phytoplankton. An increase in the population of phytoplankton induces an increase in DMS emissions and enhances concentrations of marine aerosol particles, which results in enhanced cloud reflectivity and decreased insolation at the sea surface. This is due to the fact that these gaseous trace species are oxidized in the atmosphere and form sulphate as well as methylsulphonic acid, and condense on existing aerosol particles serving as cloud condensation nuclei. This process increases multiple scattering of sunlight within clouds and therefore increases cloud albedo. On the other hand, decreased insolation of the sea surface induces a decreasing phytoplankton population. Thus, the overall process would constitute a regulatory feedback system for biogenic control of climate.

The biogenic mechanism proposed by Charlson et al. (1987) in subsequent years was advanced by other authors. In particular, Twomey (1991) showed that increases in cloud drop concentrations by anthropogenic aerosol particles leads to enhancement of cloud reflectivity, exerting a cooling influence on climate. In terms of the research described in this book, the fundamental problem is related to distinguishing the influences of anthropogenic aerosols from natural aerosols in the marine atmosphere. In this context it is clear that accurate knowledge of marine aerosols is essential to define the reference case in the absence of influence of anthropogenic aerosols necessary to evaluate the forcing over the industrial period as a difference relative to the present situation (Lewis and Schwartz, 2004). In particular, accurate knowledge of marine aerosol physical properties, such as number concentration and size-dependent and total fluxes, is of special importance.

Chapter 9

Marine aerosol fluxes

9.1 General considerations

Particles of marine aerosol emitted from the sea surface are transported to higher atmospheric layers by turbulent diffusion. At the same time, some portion of aerosol particles is removed from the air by gravitational fallout. To describe the balance of both fluxes, we express the aerosol particle concentration with a given radius r in the form

$$\frac{dN}{dr} = n(r) = \overline{n(r)} + n'(r), \tag{9.1}$$

where $\overline{n(r)}$ is the mean value of particle concentration with a radius r and $n'(r)$ is the fluctuation component of the concentration. After analogous decomposition of the velocity vector $u = \overline{u} + u'$ into the mean value and fluctuation component, the turbulent flux of particles, F_{t}, with a radius r may be expressed as follows (Petelski, 2003)

$$\frac{dF_{\mathrm{t}}}{dr} = \overline{n'(r)\,u'}. \tag{9.2}$$

The bar in (9.2) denotes stochastic averaging over a set of realizations. In practice, time averaging is usually applied (over 1/2 h), which is justified by the assumption of ergodicity of physical fields in the near-water atmospheric layer. In a similar way, the size-dependent deposition flux, F_{d}, of particles with a radius r may be formulated as follows

$$\frac{dF_{\mathrm{d}}}{dr} = v_{\mathrm{d}}(r)\,n(r), \tag{9.3}$$

where $v_{\mathrm{d}}(r)$ is deposition velocity and $n(r)$ is the particle concentration of radius r.

In the case of open sea, we usually assume that aerosol fields are uniform in space and stationary in time. Therefore, the transport equation for aerosol particles of size r becomes

$$\overline{w}\frac{\partial\overline{n(r,z)}}{\partial z} = \frac{\partial}{\partial z}\overline{n'(r,z)w'} + \frac{\partial}{\partial z}\left(v_{\mathrm{d}}\overline{n(r,z)}\right), \tag{9.4}$$

where w is the vertical component of the wind velocity. The vertical velocity component is negligible in the near-surface atmospheric layer, and (9.4) simplifies as follows

$$\overline{n'(r)w'} + v_{\mathrm{d}}(r,z)\overline{n(r,z)} = \text{const.} \tag{9.5}$$

Equation (9.5) expresses the balance of the vertical, turbulent upward fluxes and deposition fluxes in the near-water atmospheric layer under horizontally uniform conditions. However, it should be noted that the assumption of horizontal uniformity is not fulfilled even over an apparently uniform horizontal sea surface, particularly for small aerosol particles, which can travel over long distances. Therefore, when seeking a relationship between sea surface state and aerosol fluxes in the near-water atmospheric layer we must select such sizes of droplets for which the condition of horizontal uniformity of both aerosol concentration and sea surface are satisfied in the same scales.

To provide some estimate of the horizontal advection scale L_{a} for particles of a radius r which guarantees horizontal uniformity, let us adopt L_{a} in the form $L_{\mathrm{a}} = V_{\mathrm{g}}(h_{\mathrm{m}}/v_{\mathrm{d}}(r))$, where V_{g} is geostrophic wind speed and h_{m} mixing layer height. Deposition velocity for particles of radius r from 0.1 to 1.0 µm is a very sharply increasing function, depending strongly on wind speed (Slinn and Slinn, 1981). The value of this function increases from 0.01 to 3 cm/s, when the wind speed is of the order of 10 m/s, and mixing layer height is of the order of 10^2 to 10^3 m. For particles of radius $r = 1\,\mu$m, L_{a} takes values from 100 to 1000 km; however, for particles of $r = 0.1\,\mu$m, L_{a} can be as large as 10^4 to 10^5 km.

9.2 Methods of determining size-dependent sea spray generation functions

To evaluate whether sea spray droplets contribute to the air–sea fluxes, an estimation of the rate at which droplets of any given size is produced is required. This estimation is represented in the form of the so-called sea spray generation function ,f_{sgf}, which quantifies the spray droplet production mechanism. As we noted in Chapter 8, this function is also denoted as the sea aerosol production flux (Lewis and Schwartz, 2004). Blanchard (1963) was one of the first to determine the size-dependent oceanic interfacial production flux. He deduced the spray generation function for wind speeds between 5 and 15 m/s using the sea-salt distribution obtained by Woodcock (1953) in his measurements near Hawaii.

Lewis and Schwartz (2004) reviewed in detail nine methods which at least potentially can be used to determine the sea spray generation functions f_{sgf}. They include: the whitecap method, the dry deposition method, the eddy correlation method, the bubble method, micrometeorological methods, the along-wind flux method, the direct observation method, the vertical impaction method and the wet deposition method.

In this section we will describe only some of them, and additionally we present a new method, named the vertical concentration method, proposed recently by Petelski (2003, 2005) and Petelski and Piskozub (2006). For more details of other methods, the reader should refer to the Lewis and Schwartz (2004) monograph.

9.2.1 Whitecap method

The key assumption of the whitecap method is that the size-dependent sea spray generation function $f_{\mathrm{sgf}}^{(\mathrm{wc})}(r)$ over the whitecap area is independent of the nature and extent of the white area and of its mechanism of production. Thus, it is the same for laboratory and for oceanic whitecaps. This means that in some sense all white areas are equally productive. Therefore, the laboratory or surf zone measurements of size-dependent production flux $f_{\mathrm{prod}}^{(\mathrm{wc})}(r)$ can be approximately extrapolated to the ocean by multiplying by whitecap coverage F_{cov}, discussed in Chapter 7, to give

$$f_{\mathrm{sgf}}^{(\mathrm{wc})}(r) = f_{\mathrm{prod}}^{(\mathrm{wc})}(r)\, F_{\mathrm{cov}}. \tag{9.6}$$

Several parameterizations for size-dependent aerosol production flux $f_{\mathrm{prod}}^{(\mathrm{wc})}(r)$ have been proposed. In the continuous laboratory whitecap method, this function is usually defined as follows

$$f_{\mathrm{prod}}^{(\mathrm{wc})}(r) = \frac{p(r)}{A_{\mathrm{wc}}}, \tag{9.7}$$

where $p(r)$ is the number of particles in a unit linear interval of r produced per unit time from a laboratory whitecap of area A.

Size-dependent production flux over the whitecap area $f_{\mathrm{prod}}^{(\mathrm{wc})}(r)$ was determined from measurements of so-called continuous whitecaps, formed by a continuous waterfall or by bubbling air through a glass filter (Cipriano and Blanchard, 1981), or by collision of two parcels of water which were caused to move toward each other (Monahan et al., 1983, 1986; Stramska, 1987; Stramska et al., 1990). The function developed by Monahan et al. predicts the production rates of both bubble-derived film and jet droplets as well as mechanically produced spume droplets. Stramska (1987) indicated that this function predicting spray production due to bursting bubbles provides very realistic results. However, the spume-production term predicts far too many spume droplets as was mentioned by Andreas et al. (1995).

The final Monahan et al. (1983, 1986) expression for $f_{\mathrm{prod}}^{(\mathrm{wc})}(r)$ is as follows

$$f_{\mathrm{prod}}^{(\mathrm{wc})}(r) = 8.2 \times 10^5\, r^{-2}[1 + 0.057\, r^{1.05}] \times 10^{\gamma}, \tag{9.8}$$

where

$$\gamma = 1.19 \exp\{-2.4[0.38 - \log_{10}(r)]^2\}. \tag{9.9}$$

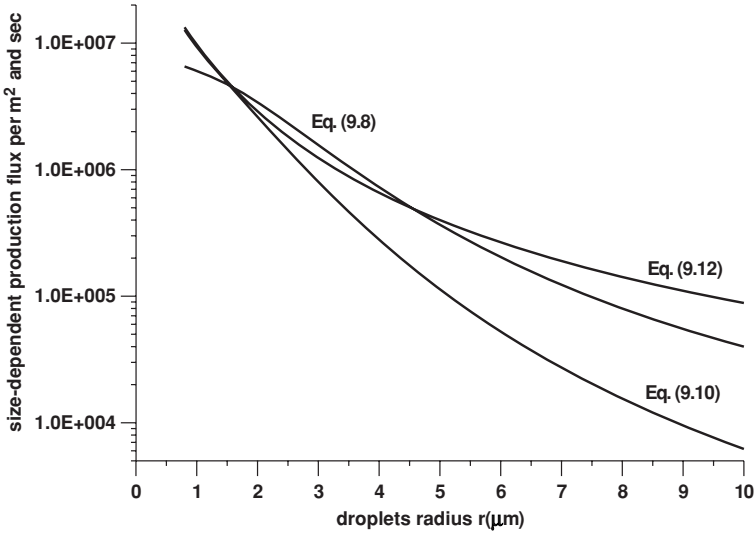

Figure 9.1: Size-dependent aerosol production flux resulting from the whitecap method.

In his following paper, Monahan (1988) proposed a slightly different version of function $f_{\rm prod}^{\rm (wc)}(r)$

$$f_{\rm prod}^{\rm (wc)}(r) = 1.257 \times 10^6\, r^{-3}[1 + 0.057\, r^{1.05}] \times 10^{\gamma}, \tag{9.10}$$

where

$$\gamma = 1.19 \exp\left\{-\left[\frac{0.38 - \log_{10}(r)}{0.65}\right]^2\right\}. \tag{9.11}$$

Equations (9.8) and (9.10) represent production of aerosol in the range $0.8\,\mu{\rm m} < r < 10\,\mu{\rm m}$ per unit surface and unit time.

Woolf et al. (1988) updated the Monahan model with whitecap simulation tank data collected after Monahan et al. (1986) published their work, and proposed the following formula for $f_{\rm prod}^{\rm (wc)}(r)$

$$f_{\rm prod}^{\rm (wc)}(r) = \exp\left[16.1 - 3.43\log(r) - 2.49\log(r)^2 + 1.21\log(r)^3\right] \tag{9.12}$$

Functions (9.8), (9.10) and (9.12) are presented in Fig. 9.1. All these functions show almost monotonous decrease of the size-dependent aerosol production flux $f_{\rm prod}^{\rm (wc)}(r)$ per unit surface covered by whitecaps per μm increment and per unit time for radii r range $0.8\,\mu{\rm m} < {\rm r} < 10.0\,\mu{\rm m}$.

Substituting (9.8) for $f_{\rm prod}^{\rm (wc)}(r)$ and (7.4) for $F_{\rm cov}$ into (9.6), we obtain the size-dependent sea spray generation function $f_{\rm sgf}^{\rm (wc)}(r)$ over the whitecap area suggested by Monahan et al. (1986)

$$f_{\rm sgf}^{\rm (wc)}(r) = 3.15\, V_{10}^{3.41}\, r^{-2}\,[1 + 0.057\, r^{1.05}] \times 10^{\gamma}, \tag{9.13}$$

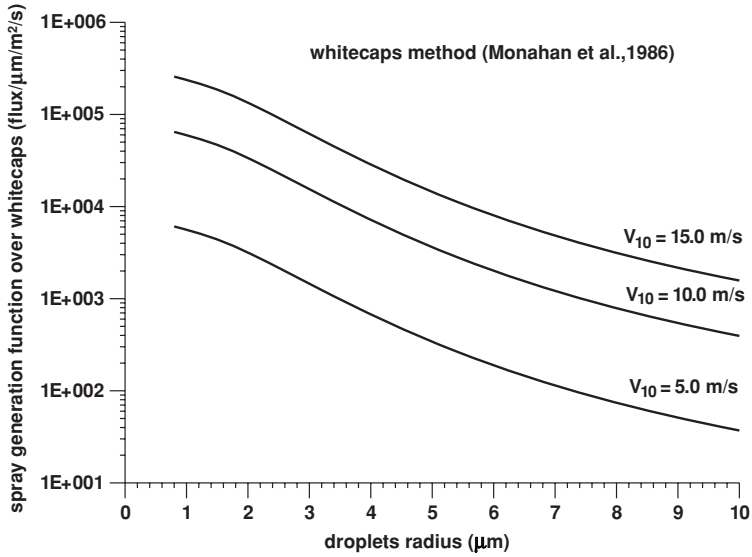

Figure 9.2: Size-dependent sea spray generation function over the whitecap area in terms of a unit linear interval of radius r for three different wind speeds, according to Monahan et al. (1986).

in which droplets radians r are given in µm and wind speed in m/s, while size-dependent sea spray generation function $f_{\mathrm{sgf}}^{(\mathrm{wc})}(r)$ is expressed as the number of particles in a unit linear interval of r produced per unit time and unit area (see Fig. 9.2). Similar results can be obtained by using the size-dependent aerosol production flux given in (9.10) or (9.12).

The total flux of the dry salt mass over the whitecap area resulting from the relationship (8.24) is shown in Fig. 9.3 in terms of wind speeds from 5 m/s to 15 m/s. It should be noted that only the contribution of particles of radii r in the range $0.8\,\mu\mathrm{m} < r < 20.0\,\mu\mathrm{m}$ were taken into account. For all approaches the same expression for F_{cov}, namely (7.4), was used. The order of magnitude of obtained sea salt mass flux corresponds well with values reported by Lewis and Schwartz (2004), taking into account the limited range of the droplet radii used in the calculations.

It should be noted that in the above expressions, the total flux of the dry sea salt mass, shown in Fig. 9.3, is a function of wind speed only. To get a more general relationship for the dry salt mass flux we use the expression (7.34) in which the whitecap coverage, F_{cov}, resulting from the downward acceleration criterion depends on the non-dimensional fetch $\frac{gX}{V_{10}^2}$. When the size-dependent production fluxes $f_{\mathrm{prod}}^{(\mathrm{wc})}(r)$ are still represented by the three different proposals given above, we obtain the results as shown in Fig. 9.4, where the contribution of droplets from 0.8 to 20.0 µm was taken into account. The dependence of total flux on non-dimensional fetch provides an opportunity to examine separately

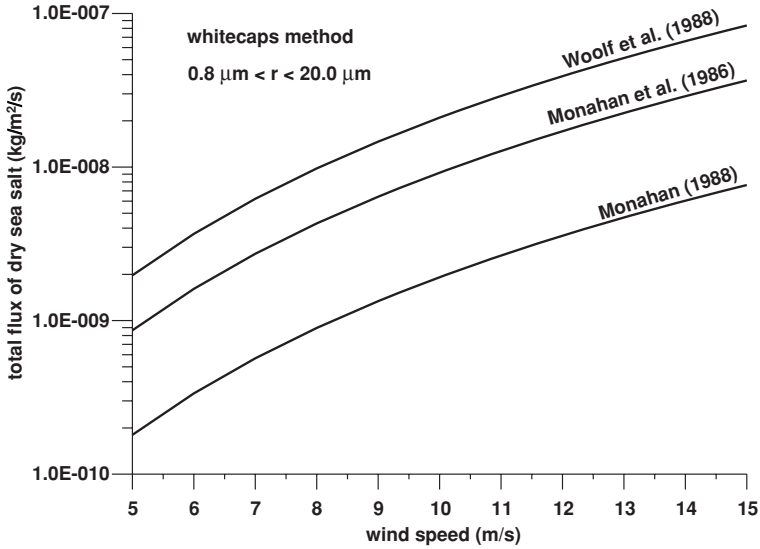

Figure 9.3: Total fluxes of dry sea salt mass over the whitecap area in terms of wind speeds from 5 to 15 m/s.

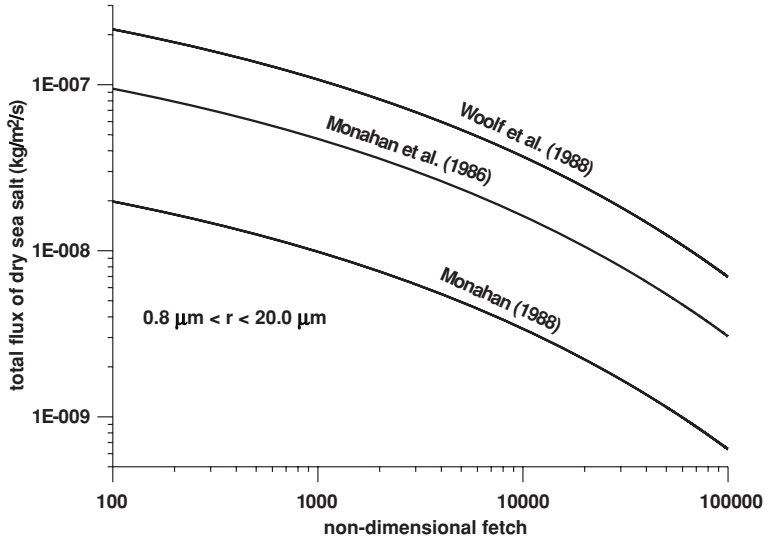

Figure 9.4: Total flux of dry sea salt mass over whitecaps in terms of the non-dimensional wind fetch for different size-dependent production fluxes $f_{\mathrm{prod}}^{(\mathrm{wc})}(r)$.

the influence of wind speed and wind fetch on the produced aerosol fluxes. We will use this opportunity in Chapter 10 to link the total salt fluxes with sea state parameters, such as the significant wave height, H_s, and peak frequency ω_p.

The whitecap method allows a relatively straightforward determination of the interfacial marine aerosol production flux. The assumption that the size-dependent production flux per whitecap area $f_{prod}^{(wc)}(r)$ is independent of the size of the whitecaps is crucial to the whitecap method. This assumption implies that all white areas of the ocean surface are equally efficient producers of marine aerosols. However, there are some concerns over the practical implementation of this method. In particular, there are large differences in the size of laboratory and open ocean whitecaps, and it is not clear to what extent the process of wave breaking in the laboratory accurately simulates that of oceanic waves. Moreover, oceanic whitecaps are several orders of magnitude larger and are manifested by bubble plumes that extend much deeper than those studied in the laboratory. Moreover, droplet production may be modified by many factors, such as thickness of the foam on the sea surface, clustering of bubbles, screening by the overlying bubbles, and others. There is also some concern with the fundamental hypothesis that aerosol production is directly proportional to whitecap coverage. For more details on the properties of the whitecap method, the reader should refer to the Lewis and Schwartz (2004) monograph.

9.2.2 Vertical concentration gradient method

The basic problem of experimental estimation of the aerosol fluxes emitted from the sea surface is the requirement of sufficient particle concentration. To overcome the difficulty, Petelski (2003) developed a method based on the measured vertical gradients of particle concentration. This method requires much lower average concentration at a given level. Therefore, it is particularly suitable for coarse aerosol flux estimation when usually the concentrations are not so high. To collect the required amount of data, Petelski measured particle concentrations on board R/V *Oceania* using a laser particle counter CSASP-100-HV moving vertically from 8 up to 20 m above sea level, while the ship was drifting and when whitecaps were present. The technology of measurements was described by Petelski (2005) and Petelski and Piskozub (2006) in detail. Experimental data from cruises in the Norwegian and Greenland Seas for wind speed range $5\,\mathrm{m/s} < V_{10} < 12\,\mathrm{m/s}$ and aerosol particle radius $0.25\,\mu\mathrm{m} < r < 7\,\mu\mathrm{m}$ showed that the size-dependent number concentration of particles N per metre cube of air can be parameterized by the formula

$$N(r,z) = N_*(r)\ln(z) + C, \tag{9.14}$$

in which $N_*(r)$ is the scale of particle concentration. From formula (9.14) it follows that the vertical concentration profiles may be approximated by straight lines on plane $(\ln(z), n(z))$, from which the scale N_* can be obtained. It should be noted that the scale $N_*(r)$ has a negative value, indicating that there are

negative gradients of aerosol particle concentration in the near water atmospheric layer caused by emission from the sea surface.

Based on many years of observations in the polar waters of the North Atlantic, Petelski (2005) showed also that local emission is not always the most important factor influencing the composition of marine aerosol in the near water atmospheric layer, even for coarse mode aerosols. In particular, higher variations of $N_*(r)$ value were observed for the smallest particle radii from 0.5 to 1.0 µm when the horizontal homogeneity conditions were not satisfied and the advection flow influenced the measurements.

Following Petelski (2003) we show now that the formula (9.14) is confirmed by the Monin–Obukhov self-similarity theory (Monin and Yaglom, 1965). According to Monin and Obukhov, horizontally uniform flow over a water surface is fully defined by momentum flux τ, sensible heat flux Q and buoyancy parameter $\beta = g/T$, expressed by the following scaling parameters

$$\text{friction velocity}: \ \mathrm{u}_* = (\tau/\rho)^{1/2}, \tag{9.15}$$

$$\text{temperature}: \ \mathrm{T} = \frac{-\mathrm{Q}}{\kappa \mathrm{u}_*}, \tag{9.16}$$

and

$$\text{length}: \ \mathrm{L} = \frac{-\mathrm{u}^3}{\kappa\beta\mathrm{Q}} \ - \ \text{Monin} \ - \ \text{Obukhov scale}, \tag{9.17}$$

where κ is the von Kármán constant equal to 0.4.

Using these scales, all non-dimensional gradients of physical parameters, within the layer of constant fluxes, are presented as functions of one non-dimensional parameter, z/L. For example, we can write

$$\frac{\kappa z}{u_*}\frac{\partial u}{\partial z} = \varphi_1(z/L) \text{ and } \frac{z}{T}\frac{\partial \theta}{\partial z} = \varphi_2(z/L), \tag{9.18}$$

in which θ is the potential temperature.

In the same way, for the non-dimensional number concentration gradient of the particles $\frac{\partial N}{\partial z}$ we obtain

$$\frac{z}{N_*}\frac{\partial N}{\partial z} = \varphi_3(z/L), \tag{9.19}$$

where the scale $N_*(r)$ of the particle concentration is defined as

$$N_*(r) = \frac{f_{\text{prod}}(r)}{u_*}, \tag{9.20}$$

in which $f_{\text{prod}}(r)$ defines the size-dependent production flux. After integration in (9.19) we have

$$N(z_2) - N(z_1) = N_*(r)[f(z_2/L) - f(z_1/L)], \tag{9.21}$$

where f is a primary function such as $\frac{\partial f}{\partial z} = \frac{\varphi_3(z/L)}{z}$. The relationship (9.20) provides the size-dependent production flux in the form

$$f_{\text{prod}}(r) = N_*(r)u_* = N_*(r)\sqrt{C_{10}}V_{10}, \tag{9.22}$$

when formula (5.61) for the drag coefficient C_{10} is used, and scale concentration $N_*(r)$ is determined from the experimental data. The flux $f_{\text{prod}}(r)$ denotes the number of particles per unit area and unit time.

The exact form of function f is not known, although in the literature there are several different proposals for this formula. In particular, the Monin–Obukhov theory provides the asymptotic form for function f, when $z/L \to 0$ (neutral stability), as follows: $f \to \ln|z/L|$. For most cases of atmospheric flow over the sea surface, the formula given by (9.14) can be used. Petelski and Piskozub (2006) reported that during all four measurement campaigns, the non-dimensional stability parameter z/L ranged from -0.1 to $+0.01$, which is close to neutral stability conditions, as those defined by Zilitinkevitch et al. (1978). As the exact values of all parameters needed for determination of the scale L were very difficult to obtain in field measurements, the authors assumed that only data with a higher value of the correlation coefficient between measured functions $N(z)$ and $\ln(z)$ were taken into account. Particularly, using a two-side Pearson 80% confidence interval in the logarithmic data fitting it was shown that for five measurement levels, the correlation coefficient was greater than 0.67.

In contrast to the whitecap and dry deposition methods, the sea spray generation function $f_{\text{sgf}}^{(\text{vg})}$ resulting from the vertical concentration gradient method cannot be presented as a product of the wind speed term and particle radius term, and Petelski and Piskozub (2006) found that this function takes the form

$$f_{\text{sgf}}^{(\text{vg})} = \exp[-(0.05V_{10} + 0.64)r + 7.17 + 0.52V_{10}] \tag{9.23}$$

or

$$f_{\text{sgf}}^{(\text{vg})} = \exp(7.17 + 0.52V_{10})\,\exp[-(0.05V_{10} + 0.64)r], \tag{9.24}$$

when the wind speed is given in m/s and radius r is in μm. Then the sea spray generation function is expressed in number of particles per unit area and unit time, per increment of r in μm. It should be noted that for a given wind speed, the relationship (9.23) is a linear function in the plane $(\ln r,\ \ln(f_{\text{sgf}}^{(\text{vg})}))$. Petelski and Piskozub (2006) compared the suggested parameterization (9.23) with their experimental data and with other parameterizations available in the literature. The comparison showed that the spray generation functions resulting from the whitecap and dry deposition methods provide smaller values of the aerosol particle flux than the observed flux in the range of radii from 1 to 8 μm, some of them by a factor of 6.

9.2.3 Dry deposition method

Vertical aerosol fluxes over deep seas are most frequently determined by measuring aerosol concentrations at one level. Such a method, called the dry deposition

Table 9.1: Dependence of dry deposition velocity v_d on particle radius r for wind speed $V_{10} = 10$ m/s (adapted from Lewis and Schwartz, 2004)

	radius $r(\mu m)$	1	2	5	10	15	20	25
$V_{10} = 10\,m/s$	deposition rel. $v_d(cm/s)$	0.05	0.25	1.5	3	5	7	10

method, is based on a local balance between production and removal by dry deposition with the assumption of horizontal uniformity and time stationarity conditions

$$f_{sgf} = v_d \frac{dN}{dr} = v_d\, n(r), \tag{9.25}$$

in which $f_{sgf} = dF/dr$ is the sea spray generation function expressed in terms of the number of particles of radii from r to $r + dr$, emitted in a unit of time from a unit of sea surface area, $n(r)$ is the size-dependent aerosol number concentration, measured in the field, usually at one level, and v_d is the deposition velocity. Equation (9.25) gives a rough approximation only and does not directly result from the transport equation. The aerosol vertical fluxes can be balanced with an accuracy determined within the addition of an arbitrary constant as the transport equation yields the balance of flux gradients, not the fluxes themselves.

The dry deposition velocity is usually determined from one-dimensional models (see, for example Slinn and Slinn, 1980, 1981) assuming that the aerosol particles are sufficiently well mixed to a level above the levels of measurements. Therefore, downward flux does not depend strongly on the level under consideration. In Tables 9.1 and 9.2, the dry deposition velocities calculated from the model of Slinn and Slinn (1980, 1981) are presented for particles of radii in the range from 1 to 25 µm and for selected wind speeds. As can be seen from Table 9.1, the dry deposition velocity v_d increases with increasing radius r due to increasing contribution from gravitational sedimentation. Moreover, Table 9.2 shows that for a given particle radius, the deposition velocity v_d increases with wind speed V_{10} due to more intensive vertical mixing and diffusion.

A widely used estimate for the effective marine aerosol production flux $f_{sgf}^{(dd)}(r)$ was proposed by Smith et al. (1993). In this proposal, aerosol number concentrations $n(r)$ of particles with r in the range 0.09–23.5 µm were obtained from over 700 hours of measurements from a 10 m tower located 14 m above mean sea level at an island off the coast of Scotland, when the wind speed range covered 1–34 m/s. Due to the wide range of meteorological conditions taken into account in the experiments, the spume production was probably reflected in their results. Smith et al. (1993) give their sea spray generation function

Table 9.2: Dependence of dry deposition velocity v_d on wind speed V_{10} for particle radius $r = 1\,\mu m$ and $r = 3\,\mu m$ (adapted from Lewis and Schwartz, 2004)

	wind speed V_{10} (m/s)	0	5	10	15	20	25
$r = 1\,\mu m$	deposition rel. V_d (cm/s)	0.016	0.05	0.05	0.06	0.4	0.7
$r = 3\,\mu m$	deposition rel. V_d (cm/s)	0.15	0.35	0.65	0.70	1.10	1.20

$f_{sgf}^{(dd)}(r)$ in terms of droplets of relative humidity of 80% in the form

$$f_{sgf}^{(dd)}(r) = \sum_{i=1}^{2} A_i \exp\left\{-b_i \left[\ln\left(\frac{r}{c_i}\right)\right]^2\right\}, \tag{9.26}$$

in which

$$\left.\begin{aligned} \log_{10} A_1 &= 0.0676\, V_{14} + 2.43 \\ \log_{10} A_2 &= 0.959\sqrt{V_{14}} - 1.476 \end{aligned}\right\} \tag{9.27}$$

and

$$\left.\begin{aligned} b_1 &= 3.1, \quad c_1 = 2.1\,\mu m \\ b_2 &= 3.3, \quad c_2 = 9.2\,\mu m \end{aligned}\right\} \tag{9.28}$$

for radii in the range $1\,\mu m \le r \le 25\,\mu m$ and for wind speed $0\,m/s < V_{14} < 34\,m/s$. The speed V_{14} can be transferred to the wind speed at the standard 10 m as follows

$$V_{14} = V_{10}\left[1 + \frac{\sqrt{C_{10}}}{\kappa}\ln\left(\frac{14}{10}\right)\right], \tag{9.29}$$

where $\kappa = 0.4$ is the von Kármán constant and C_{10} is the drag coefficient (see Section 5.3.4). Smith et al. (1993) applies for the C_{10} an expression proposed by Large and Pond (1981) in the form

$$10^3 C_{10} = \begin{cases} 1.20 & \text{for} \quad 4 \le V_{10} \le 11\,m/s \\ 0.49 + 0.065\, V_{10} & \text{for} \quad V_{10} \ge 11\,m/s. \end{cases} \tag{9.30}$$

The sea spray generation function (9.26) is illustrated in Fig. 9.5 for radius range 1–20 μm and for three different wind speeds. Smith et al. (1993) suggest that a smaller mode centred around 2 μm radius is associated with particles generated by the bubble bursting mechanism, while the larger mode at 9 μm reflects the contributions of spume droplets at higher wind speeds.

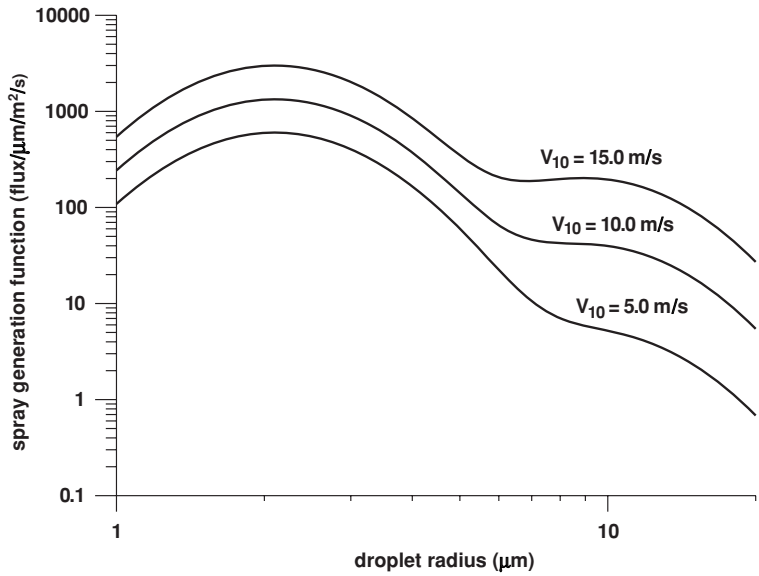

Figure 9.5: Sea spray generation function according to Smith et al. (1993).

Andreas (1998) using the theoretical arguments given in another of his papers (Andreas et al., 1995) found that the above spray generation function underpredicts film and jet-droplet production in comparison with the Monahan et al. (1986) function, while both functions provide roughly the same shape (not values) for droplet radii in the range from 4 to 15 µm. Monahan's function is considered the best one available for predicting spray production by whitecap bubbles for wind speeds up to 20 m/s. Thus, Andreas (1998) suggested that if we multiply the original Smith et al. (1993) functions $f_{\rm sgf}^{(dd)}(r)$ by 3.5, we obtain the spray generation function that in the film and jet-droplet range is comparable to the Monahan et al. (1986) function $f_{\rm sgf}^{(\rm wc)}(r)$. Therefore, should be

$$f_{\rm sgf}^{(\rm wc)}(r) = 3.5 f_{\rm sgf}^{(dd)}(r). \tag{9.31}$$

As was pointed out by Andreas (1998), this function does not cover the range of spume droplet production, which plays a very important role in transferring heat and moisture across the air-sea interface. To formulate a reliable sea spray generation function that would cover the relevant wide droplet radii range from 2 up to 250 µm, Andreas (1998) proposed some modification and an extrapolation of the Smith et al. (1993) function. In particular, he suggested the following sea spray generation function for range of particle radii 1 µm $\le r \le$ 250 µm and wind speed 0 m/s $\le V_{10} \le$ 32.5 m/s

$$f_{\rm sgf}^{(dd)}(r) = \begin{cases} 3.5 \sum\limits_{i=1}^{2} A_i \exp\left\{-b_i \left[\ln\left(\frac{r}{c_i}\right)\right]^2\right\} & \text{for} \quad 1 \le r \le 10\,\mu\text{m} \\ \tilde{f}_{\rm sgf}(r) & \text{for} \quad r \ge 10\,\mu\text{m} \end{cases} \tag{9.32}$$

in which

$$\tilde{f}_{\mathrm{sgf}}(r) = \begin{cases} C_1(V_{10})r^{-1} & \text{for} \quad 10 \leq r \leq 37.5\,\mu\mathrm{m} \\ C_2(V_{10})r^{-2.8} & \text{for} \quad 37.5 \leq r \leq 100\,\mu\mathrm{m} \\ C_3(V_{10})r^{-8} & \text{for} \quad 100 \leq r \leq 250\,\mu\mathrm{m} \end{cases} \tag{9.33}$$

The coefficients C_1, C_2 and C_3 depend on wind speed, and are calculated as follows. First, the $f_{\mathrm{sgf}}(r)$ value for $r = 10\,\mu\mathrm{m}$ is calculated from (9.26) and corresponding coefficient C_1 is obtained from (9.33). Using C_1 we calculate the $\tilde{f}_{\mathrm{sgf}}$ at $37.5\,\mu\mathrm{m}$ and subsequently the coefficient C_2 from the second relation in (9.33), and so on. It should be noted that in the original Andreas (1998) paper, the spray generation function was presented in terms of radius r_0 when

$$f_{\mathrm{sgf}}^{(dd)}(r_0) = f_{\mathrm{sgf}}^{(dd)}(r)\frac{dr}{dr_0}, \tag{9.34}$$

in which

$$\frac{dr}{dr_0} = 0.506\, r_0^{-0.024}. \tag{9.35}$$

In our notation, r_0 denotes the radius at formation while r is the radius at relative humidity of 80%. The modified Smith et al. (1993) sea spray generation function (9.32) is shown in Fig. 9.6 for $1\,\mu\mathrm{m} \leq r \leq 250\,\mu\mathrm{m}$ and three wind speeds, i.e. $V_{10} = 5$, 10 and 15 m/s.

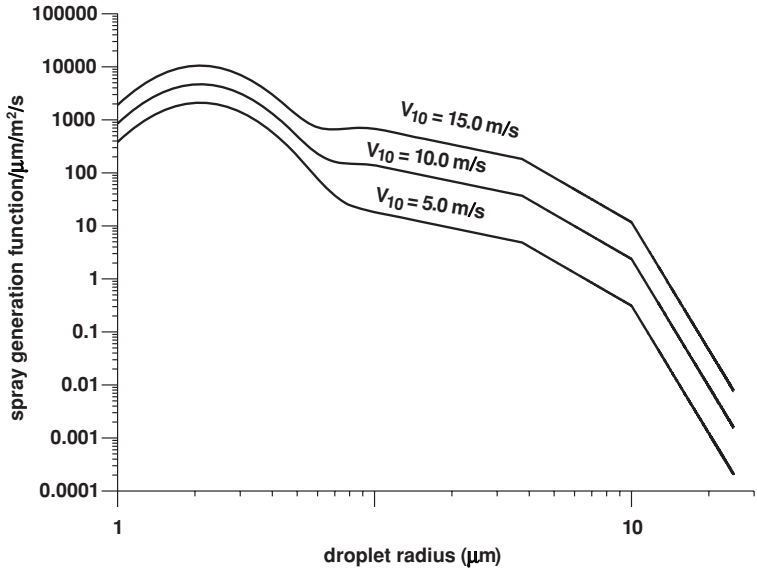

Figure 9.6: Modified sea spray generation function suggested by Andreas (1998).

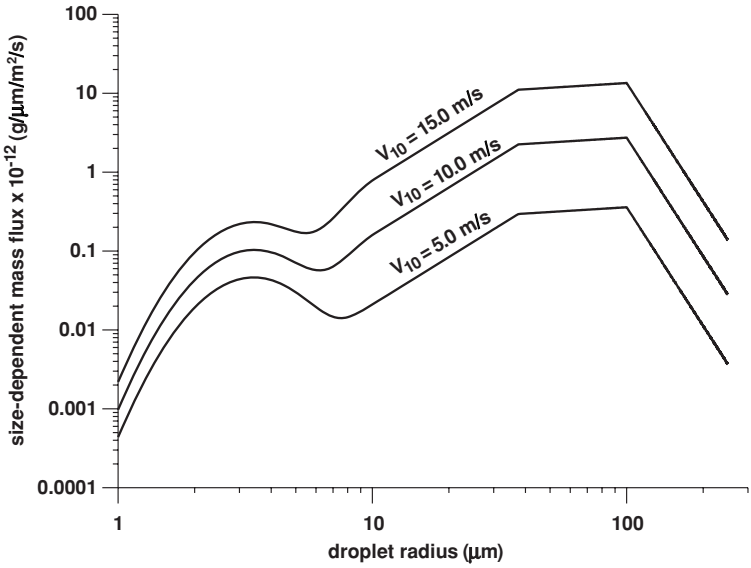

Figure 9.7: The size-dependent dry mass flux corresponding to the sea spray generation function suggested by Andreas (1998).

The corresponding size-dependent dry mass flux $f_{\mathrm{dmass}}(r)$ (see (8.25)) for three different wind speeds is illustrated in Fig. 9.7. The figure shows that the highest contribution to the aerosol mass emitted to the atmosphere is due to droplets of greater radius, around 100 µm.

When the dry deposition velocity v_{d} proposed by Slinn and Slinn (1980, 1981) is used, the sea spray generation function $f_{\mathrm{sgf}}^{(dd)}(r)$ can be presented in a canonical form of the sum of two lognormal functions as follows (Lewis and Schwartz, 2004)

$$f_{\mathrm{sgf}}^{(dd)}(r) = A_1 \exp\left\{-\frac{1}{2}\left[\frac{\ln\left(\frac{r}{2.5}\right)}{\ln 1.49}\right]^2\right\} + A_2 \exp\left\{-\frac{1}{2}\left[\frac{\ln\left(\frac{r}{10.7}\right)}{\ln 1.48}\right]^2\right\} \tag{9.36}$$

or

$$f_{\mathrm{sgf}}^{(dd)}(r) = A_1 \exp\left\{-\frac{1}{2}\left[\frac{\ln r - \ln 2.5}{\ln 1.49}\right]^2\right\} + A_2 \exp\left\{-\frac{1}{2}\left[\frac{\ln r - \ln 10.7}{\ln 1.48}\right]^2\right\}, \tag{9.37}$$

where

$$A_1 = \exp[0.156\, V_{10} + 7.25], \tag{9.38}$$

$$A_2 = \exp[2.21\, \sqrt{V_{10}} - 0.28]. \tag{9.39}$$

In equation (9.36), the mode at $r = 2.5\,\mu m$ consists of the droplets resulting from bubbles bursting and the mode at $r = 10.7\,\mu m$ is related to the spume droplets. Moreover, the droplet radius range of applicability of the above formulae is $1\,\mu m < r < 25\,\mu m$, with wind speeds up to 34 m/s. It should be noted that the wind speed dependence of the sea spray generation function is manifested only in the values of coefficients A_1 and A_2. The function $f_{sgf}^{(dd)}(r)$ does not go to zero at zero wind speed due to the fact that the size-dependent particle concentration does not vanish at low wind speeds. Therefore, steady state conditions in terms of local and temporal balance between removal through dry deposition and production are not exactly achieved.

Another expression for the sea spray generation function $f_{sgf}^{(dd)}(r)$, based on the dry deposition method for level of 10 m above sea surface, was developed by Smith and Harrison (1998), using measurements in the eastern North Atlantic. Their result is relevant for particles from 1 to 150 μm and wind speeds up to about 20 m/s, and the function $f_{sgf}^{(dd)}(r)$ is also expressed as the sum of two lognormal distributions as follows

$$f_{sgf}^{(dd)}(r) = A_1 \exp\left\{-\frac{1}{2}\left[\frac{\ln r - \ln 4.2}{\ln 1.78}\right]^2\right\} + A_2 \exp\left\{-\frac{1}{2}\left[\frac{\ln r - \ln 50}{\ln 2.03}\right]^2\right\}, \tag{9.40}$$

in which

$$A_1 = 1.7\,V_{10}^{3.5} \quad \text{and} \quad \mathrm{A_2} = 0.6\,\mathrm{V_{10}^3}. \tag{9.41}$$

Petelski and Piskozub (2006) parameterized the aerosol fluxes over the Arctic seas in the form of a relationship resulting from the dry deposition method, when the following size-dependent number concentration $n(r)$ for coarse aerosol was used (Petelski, 2005)

$$n(r) = \exp(0.21\,V_{10} + 12.3 \pm 2)\exp(-0.58\,r) \tag{9.42}$$

and the deposition velocity was taken in the form suggested by Caruthers and Choularton (after Smith et al., 1993)

$$v_d = \frac{v_t(r)}{1 - \exp\left[-\left(\frac{v_t(r)}{C_d V_{10}}\right)\right]}, \tag{9.43}$$

in which v_t is the gravitational sedimentation velocity for a given particle radius and C_d is the drag coefficient. After substituting (9.42) and (9.43) into (9.25) they obtained

$$f_{sgf}^{(dd)}(r) = \frac{v_t(r)}{1 - \exp\left[-\left(\frac{v_t(r)}{C_d V_{10}}\right)\right]}\ \exp(0.21\,V_{10} + 12.3 \pm 2)\exp(-0.58\,r). \tag{9.44}$$

As was shown by Petelski and Piskozub (2006), function (9.44) provides slightly smaller aerosol fluxes than another formula of the authors (see (9.23), and smaller than the fluxes measured by them in Arctic waters.

9.2.4 Wet deposition mechanism

Wet deposition of marine particles refers to the transfer of particles from the atmosphere to the surface by precipitation or by in-cloud and below-cloud scavenging. Some measurements (Twomey, 1955) showed that precipitation is a very efficient mechanism in removing sea aerosol particles from the atmosphere above sea surface. According to Lodge (1955), a decrease by nearly an order of magnitude in the number concentration of sea aerosol particles with $r > 3\,\mu\text{m}$, after only a 10 mm shower was observed. The efficiency of the wet deposition mechanism for marine aerosol particles suggests that precipitation affects the relationship between aerosol production and aerosol concentration. However, despite numerous attempts to parameterize the rates of particle removal, these rates remain very uncertain. The same conclusion is valid for in-cloud and below-cloud scavenging, which refer to particles forming cloud drops that are subsequently removed in precipitation through gravitational deposition. Due to the lack of well defined and experimentally confirmed parameterization methods, wet deposition mechanisms will not be taken into account in this book.

9.2.5 Eddy correlation method

The eddy correlation or eddy covariance method is the most direct method to determine turbulent fluxes (Panin, 1985; Nilsson et al., 2003). This method is based on simultaneous measurements of instantaneous wind velocity components and instantaneous values of the quantity which is to be determined. If we assume that the vertical component of velocity w and size-dependent aerosol particle concentration $n(r)$ can be decomposed as follows

$$w = \overline{w} + w'; \quad n(r) = \overline{n(r)} + n'(r), \tag{9.45}$$

we can present the mean vertical flux associated with the aerosol particle concentration n in the form

$$\overline{n(r)w} = \overline{n(r)w} + \overline{n'(r)w'}. \tag{9.46}$$

To remove any mean flow in the vertical direction, a coordinate rotation is applied allowing a determination of the vertical flux $\overline{n'(r)w'}$ due to turbulent diffusion only. The time over which measurements are averaged should be long enough to avoid the influence of individual gusts or breaking waves on the results. Typically, this time is equal to about 30 min. Lewis and Schwartz (2004) listed a set of other factors which should be taken into account during measurements, namely the signal-to-noise ratio of the apparatus and its response time, location of the wind speed sensor against the particle concentration sensor, proper sampling method and others.

9.2.6 Comparison of flux estimates

In the preceding sections, selected proposals to determine the marine aerosol fluxes were discussed. For later convenience, the final formulae of the sea spray

generation functions resulting from these particular methods are summarized as follows:

9.2.6.1 Whitecap method

Three different approaches, based on the concept of aerosol generation over whitecap areas have been discussed above, namely:
- Monahan et al. (1986) approach resulting in formula (9.13)
- Monahan (1988) approach resulting in formulae (9.6) and (9.10)
- Woolf et al. (1988) approach resulting in formulae (9.6) and (9.12)

Functions $f_{\mathrm{sgf}}^{(\mathrm{wc})}(r, V_{10})$ denote the sea spray generation functions in terms of a unit linear interval of radius r. They are applicable for droplet radii in the range $0.8\,\mu\mathrm{m} < 8.0\,\mu\mathrm{m}$ and for wind speed $4.0\,\mathrm{m/s} < V_{10} < 20\,\mathrm{m/s}$.

9.2.6.2 Vertical concentration gradient method

This method was proposed by Petelski and Piskozub (2006). The resulting formula (9.23) is based on the Monin-Obukhov self-similarity theory.

9.2.6.3 Dry deposition method

There are few formulae resulting from the balance equation illustrating the equality of the generation flux and deposition flux. In some of these formulae, the deposition velocity is not always expressed explicitly:
- Smith et. al (1993) approach resulting in formula (9.26)
- Andreas (1998) approach resulting in formula (9.32)
- Slinn and Slinn (1981) approach (9.36)
- Smith and Harrison (1998) approach resulting in formula (9.40)
- Petelski and Piskozub (2006) approach resulting in formula 9.44)

9.2.6.4 Summary remarks

Andreas (1998) in his review compared the available prediction formulae for sea spray generation functions. He found that the prediction functions differ between them by as much as several orders of magnitude. A similar conclusion follows also from the review presented in the Lewis and Schwartz (2004) monograph. In particular, the uncertainty over the spray generation function for high wind speeds is a major obstacle for formulation of the best suited prediction methodology. High wind speed range is of special importance as the spume droplets, generated at high wind speeds, are probably more important than bubble-derived droplets in transferring heat and moisture across the air-sea interface. This is because of the large number and volume of droplets produced by the spume production mechanism, and the speed with which the spume droplets exchange heat and moisture with the air.

Moreover, the observed discrepancies result from the fact that available spray generation models are based on laboratory experiments, and obviously they

do not reflect the aerosol generation conditions in real sea environments, although some features are common for all prediction models. First of all, it was confirmed that small aerosol particles, $r \approx 0.1$–$1\,\mu m$, provide the dominant contribution to size-dependent production fluxes. These particles are mostly due to the bursting of bubbles and these small droplets have long atmospheric residence times and consequently they exhibit little correlation with local conditions (Petelski, 2005). Medium sea aerosol particles, $r \approx 1$–$1.25\,\mu m$, are dominant contributors to many atmospheric processes of interest. These particles are mainly jet droplets resulting from bursting bubbles. There is a large variability in atmospheric residence times for them, ranging from hours to days. The residence time of these particles is controlled by dry deposition as well as by wet deposition when precipitation occurs. The best estimate for the sea spray generation function for these particles' range is that presented by the whitecap and dry deposition methods, presented above in this chapter. Large aerosol particles, $r \geq 20\,\mu m$, provide the dominant contribution of mass and momentum. They belong to the jet droplet class as well as the spume droplet class. However, due to the limited amount of data, little can be stated with confidence concerning the production fluxes (Hoppel et al., 2002).

At present the only sea spray generation function which covers a wide radius range from 2 to $500\,\mu m$ and wind speed range from 0 to $32.5\,m/s$ is the Andreas (1998) parameterization. This proposal is based on the combination of two prediction methods. For small aerosol droplet radii $r \leq 10\,\mu m$, the prediction is compatible with the Monahan et al. (1986) function, while for larger droplet radii Andreas developed an extrapolation function for the spume domain using the experimental data of Smith et al. (1993) collected in the field. Also, we have to mention the data collected by Petelski (Petelski, 2005) and Petelski and Piskozub (2006) in Arctic waters, as well as by Petelski et al. (2005) in the open Baltic Sea. At present both data sets represent very valuable experimental insight into sea aerosol production.

Chapter 10

Aerosol flux as a function of sea state parameters

10.1 Introduction

As was discussed in the previous chapters as well as in Chapter 11, marine aerosols play an important role for climatic, meteorological and chemical models. Such models require accurate representation of aerosol fluxes from the sea surface to the atmosphere and from the atmosphere to the ocean. In modelling aerosol generation and aerosol impact on the climate, two types of approach, namely the diagnostic approach and the seasonal or synoptic scale approach, can be distinguished. In the diagnostic approach we look for marine aerosol fluxes at a given location and at a given time, while in the seasonal or synoptic scale approach we seek to predict aerosol flux variation in the scale of months or seasons for a given sea basin. In general, aerosol fluxes are complex functions of wind speed, wind history, atmospheric stability and sea surface state. The sea state is represented by surface wave statistics, surface wave spectra, intensity of wave breaking and possibly other parameters such as ocean temperature and surface active substances. However, many present representations of sea spray generation functions use only wind speed as the governing parameter. It should be stressed that a description of the sea surface state as a function of wind speed only is highly insufficient. At a given wind speed, sea surface statistical characteristics and wave spectra can be quite different as wave generation mechanisms involve many other parameters, not only wind speed. For more information on wave generation processes, the reader should refer to books by Phillips (1977) and Massel (1996a).

A full set of parameters determining the sea state and the frequency spectra of the surface waves contains (Massel, 1996a): density of air ρ_{a}, density of water ρ_{w}, kinematic viscosity of air ν_{a}, kinematic viscosity of water ν_{w}, wind speed V_{10}, wind fetch X, duration of wind action t, water depth h and the Coriolis parameter f. Under the assumption of irrotational wave motion and under the dominant gravity force as well as under a restriction of the atmospheric

boundary layer adhering only to the sea surface, the number of non-dimensional combinations of parameters listed above can be reduced to the following

$$\frac{gX}{V_{10}^2}, \frac{gt}{V_{10}}, \frac{gh}{V_{10}^2}, \frac{\omega V_{10}}{g}. \tag{10.1}$$

In the following we use the above non-dimensional combinations to express the basic quantities controlling aerosol flux generation, such as whitecap coverage and energy dissipation rate in terms of the sea state parameters. This opens the opportunity to predict aerosol fluxes in terms of hydrodynamic and meteorological factors.

10.2 Governing relationships

In the previous sections, various characteristic quantities, such as whitecap coverage, energy dissipation rate, aerosol fluxes and others, were presented in terms of non-dimensional wind fetch $\left(\frac{gX}{V_{10}^2}\right)$. However, wind fetch is a quality very difficult to determine in natural conditions in sea basins of complicated shape and bathymetry. Therefore, instead of the combinations given in (10.1), we use parameters which are easier to measure and which are in some relations with them.

In particular, for the diagnostic analysis, we assume that wind speed V_{10}, significant wave height H_s and period (frequency) of the spectral peak $\omega_\mathrm{p}\,(T_\mathrm{p})$ are known. On the other hand, in the case of seasonal scale analysis usually the historical or experimental values of wind speed V_{10} and significant wave height H_s only are available. More complete data on significant wave height H_s and peak frequency ω_p for a given atmospheric field can be obtained only from numerical models, for example from such as WAM4 (Komen et al., 1994). Mean values, over months, seasons or years for the significant wave height H_s and peak period T_p, are known for oceans and some regional seas (Massel, 1996a; Young and Holland, 1996; Paplińska and Reda, 2003). In particular, Young and Holland in their atlas present results obtained from three years of global data obtained from the GEOSAT satellite with an attempt to provide some interpretation of the observed results. The monthly average data of the significant wave height H_s and the spectral peak T_p for the Baltic Sea for the period 1998–2001 were simulated by the WAM4 model with the initial atmospheric forcing adopted from the UK Meteorological Centre (Paplińska and Reda, 2003).

It should be noted that the significant wave height H_s is a characteristic measure of wave energy, while T_p is a measure of characteristic wave period. Both these parameters are functions of non-dimensional combinations given above, i.e.

$$\frac{gH_\mathrm{s}}{V_{10}^2} = f_1\left(\frac{gX}{V_{10}^2}, \frac{gt}{V_{10}}\right) \tag{10.2}$$

and

$$\frac{\omega_{\mathrm{p}} V_{10}}{g} = f_2\left(\frac{gX}{V_{10}^2}, \frac{gt}{V_{10}}\right), \tag{10.3}$$

when we assume deep-water conditions.

If $\left(\frac{gt}{V_{10}}\right)$ is sufficiently large so the time does not influence H_{s} and ω_{p}, but rather it is $\left(\frac{gX}{V_{10}^2}\right)$ that controls them, then we are dealing with fetch-limited waves, when the combination $\left(\frac{gt}{V_{10}}\right)$ in (10.2) and (10.3) can be omitted. Conversely for the duration-limited case, the combination $\left(\frac{gX}{V_{10}^2}\right)$ in functions f_1 and f_2 should be omitted. When both the fetch and duration are sufficiently large for H_{s} and ω_{p} to reach limiting values, they will become dependent only upon the wind speed V_{10} and the condition of a fully developed sea will exist.

In this section, the functional dependence of the whitecap coverage, energy dissipation rate and aerosol fluxes on the sea state parameters will be discussed and developed. To achieve this, let us express first the relationship between non-dimensional wind fetch $\left(\frac{gX}{V_{10}^2}\right)$ and significant wave height H_{s} and peak frequency ω_{p}. After substituting (D.5) into (D.10) we obtain

$$\frac{H_{\mathrm{s}}\omega_{\mathrm{p}}^2}{g} = \sqrt{1.216 a_0}\left(\frac{gX}{V_{10}^2}\right)^{-0.11} \tag{10.4}$$

and

$$\frac{gX}{V_{10}^2} = (1.216 a_0)^{4.545}\left(\frac{H_{\mathrm{s}}\omega_{\mathrm{p}}^2}{g}\right)^{-9.09}. \tag{10.5}$$

10.3 Dependence of energy dissipation rate on sea state parameters

Most knowledge on wave dissipation is a result of laboratory and field experiments. The available relationships for the rate of energy lost during wave breaking are listed in Table 6.2. Moreover, in the past a number of theoretical proposals were developed to estimate the energy loss. These proposals are summarized in Table 6.3. Let us express now these theoretical formulae in terms of sea state parameters. In particular, we parameterize the energy dissipation rate and whitecap coverage in terms of significant wave height H_{s} and peak frequency ω_{p}. For a fully developed wind-sea spectrum, the rate of total energy dissipation rate takes the form (see (6.43))

$$E_{\mathrm{dissrate}} = 1.59\,\rho g\left(\frac{m_1^4}{g^2\, m_0^3}\right)^2\left(\frac{m_0\, m_2}{m_1}\right). \tag{10.6}$$

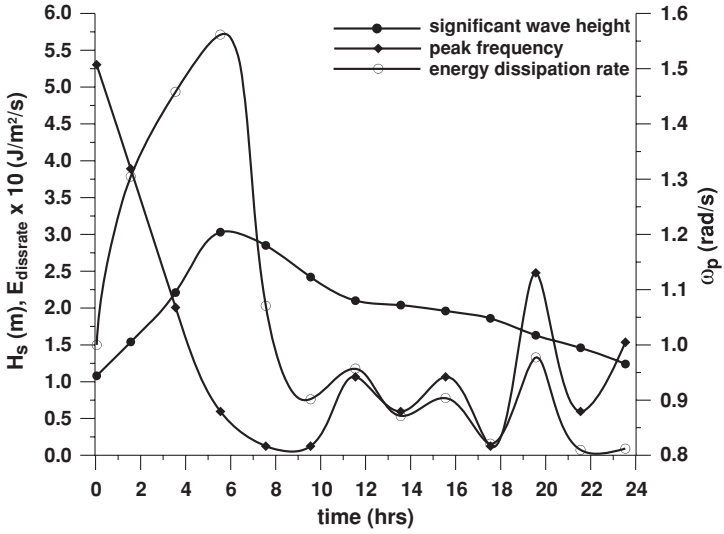

Figure 10.1: Energy dissipation rate according to Komen et al. (1984) model for storm waves in the Baltic Sea on 9 August 1998.

Let the wave field be represented by the JONSWAP spectrum with standard value of $\gamma = 3.3$. After substituting relationships (D.10) into the above expression we obtain

$$E_{\text{dissrate}} = \frac{1.59\,\rho g}{2^{12}} \left(\frac{a_1}{a_0}\right)^7 \left(\frac{a_2}{a_0}\right) \left(\frac{H_\text{s}\,\omega_\text{p}^2}{g}\right)^4 H_\text{s}^2\,\omega_\text{p}. \tag{10.7}$$

To illustrate this dependence we selected real storm conditions at a single point in the Baltic Sea ($54^\circ\,51.234'$ N, $17^\circ\,48.352'$) when a deep-water wave field was generated by a fast moving atmospheric front. On 9 August 1998, wave data were recorded using the Datawell Waverider Buoy (Paplińska, 1999). The measured significant wave heights H_s and peak frequencies ω_p during this day are shown in Figs. 10.1–10.3 by closed circles and diamonds, respectively. The full lines are the interpolated values. The calculated values of E_{dissrate} corresponding to the recorded significant wave heights H_s and peak frequencies ω_p are added to Fig. 10.1.

The dissipation energy rate resulting from Phillips' concept of saturation range is given by (6.24). This relationship is based on the assumption that the spectral slope is proportional to function ω^{-4} as suggested by Toba (1973). For our calculation, we apply the Donelan et al. (1985) formula (3.24) which can be considered as a modification of the JONSWAP spectral model to account for the ω^{-4} rather than the ω^{-5} rear spectrum face slope. Substituting (3.24)

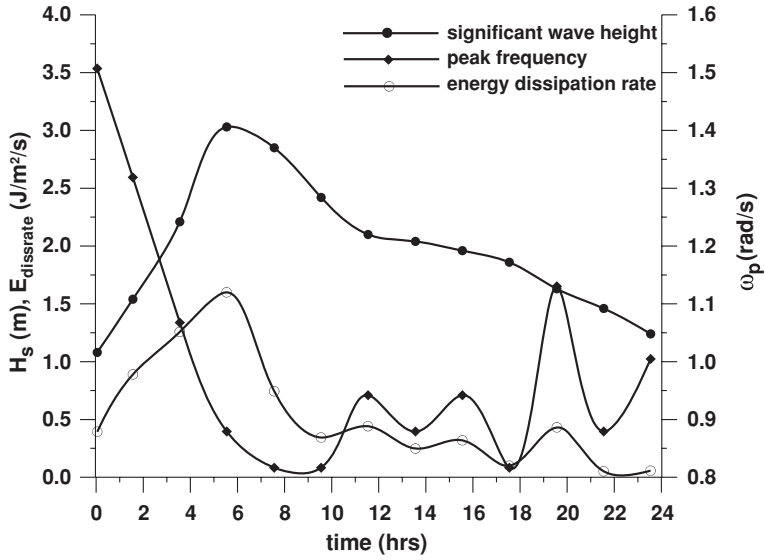

Figure 10.2: Energy dissipation rate according to Phillips' (1985) concept for storm waves in the Baltic Sea on 9 August 1998.

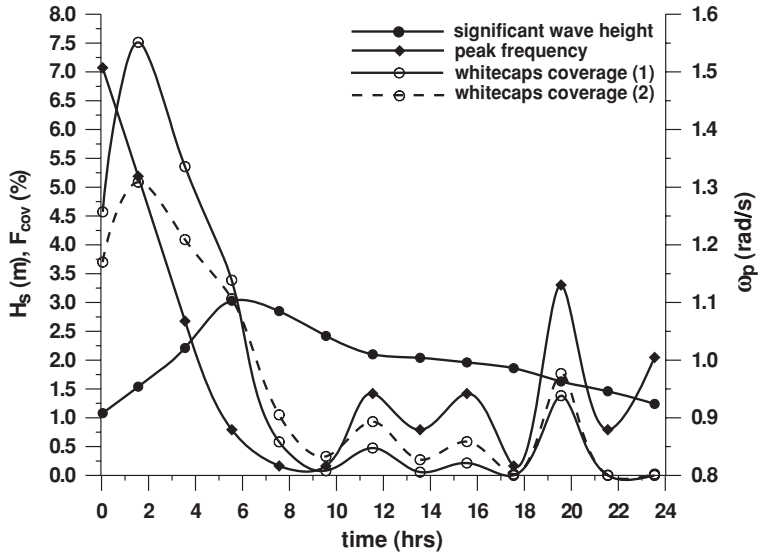

Figure 10.3: Whitecap coverage for storm waves in the Baltic Sea on 9 August 1998. Whitecap coverage (1) denotes the values resulting from the limiting steepness criterion, and whitecap coverage (2) denotes the values resulting from the vertical acceleration criterion.

into (6.24) we obtain

$$E_{\text{dissrate}} = \frac{\gamma_1 I(3s)\alpha_d^3}{16[I(s)]^3}\frac{\rho_{\text{w}} g^3}{\omega_{\text{p}}^3}\int_1^{\frac{\omega_{\text{u}}}{\omega_{\text{p}}}} \hat{\omega}^{-1}\left[\exp\left(-\hat{\omega}^{-4}\right)\gamma_{\text{d}}^{r_1}\right]^3 d\hat{\omega}, \tag{10.8}$$

where $\hat{\omega} = \frac{\omega}{\bar{\omega}}$. The parameter α_{d} can be expressed as a function of significant wave height H_{s} and peak period T_{p} in the form (Massel, 1996a)

$$\alpha_{\text{d}} = 200\, g^{-1.572}\, m_0^{0.786}\, T_{\text{p}}^{-3.142}, \tag{10.9}$$

in which $m_0 = \frac{H_{\text{s}}^2}{16}$.

To illustrate the application of formula (10.8) we assume that $\frac{\omega_{\text{u}}}{\omega_{\text{p}}} = 3$, $\gamma_{\text{d}} = 1.7$ and $\sigma_{\text{d}} = 0.08$ in the power r_1. After integration and rearranging in (10.8) we obtain the energy dissipation rate in the form of the sea state parameters H_{s} and ω_{p} as follows

$$E_{\text{dissrate}} = 1.55\times 10^{-5}\,\frac{\gamma_1 I(3s)}{[I(s)]^3}\,\rho_{\text{w}}\left(\frac{g}{\omega_{\text{p}}}\right)^3\left(\frac{H_{\text{s}}\,\omega_{\text{p}}^2}{g}\right)^{4.716}. \tag{10.10}$$

Estimation (10.8) was also applied for storm waves in the Baltic Sea recorded on 8 August 1998 – see Fig. 10.2. Changing of the energy dissipation rate during a storm in Figs. 10.1 and 10.2 is similar, but in the case of Phillips' concept, the energy dissipation value is about two times higher than for the fully developed wind-sea spectrum according to Komen et al. (1984).

Both figures indicate that for longer waves (smaller ω_{p}), the energy dissipation rate depends strongly on the significant wave height, while for smaller waves, the influence of wave steepness becomes more clearly seen.

Using a similar technique, we can also represent the energy loss resulting from the very narrow frequency spectrum developed by Longuet–Higgins (1969). The final result becomes

$$E_{\text{diss}} = \frac{\rho g}{16}\,H_{\text{s}}^2 \exp\left\{8\alpha^2\left(\frac{a_0}{a_2}\right)^2\left(\frac{H_{\text{s}}^2\,\omega_{\text{p}}^4}{g^2}\right)^{-1}\right\}. \tag{10.11}$$

10.4 Dependence of whitecap coverage on sea state parameters

Let us now parameterize the whitecap coverage F_{cov} in terms of wave height H_{s} and frequency ω_{p}. The first estimate of F_{cov} was based on the limiting wave steepness criterion. When wave field is represented by the JONSWAP spectrum we have (see Section 7.3.2)

$$F_{\text{cov}} = \exp\left[-0.5215\left(\frac{gX}{V_{10}^2}\right)^{0.22}\right]. \tag{10.12}$$

Equation (D.9) relates the non-dimensional fetch and significant wave height H_s and peak frequency ω_p as follows

$$\beta = 0.076 \left(\frac{gX}{V_{10}^2} \right)^{-0.22} = \frac{H_s^2 \, \omega_p^4}{16 a_0 \, g^2} \tag{10.13}$$

in which $a_0 = 0.3048$ for the enhancement peak parameter $\gamma = 3.3$. After substituting (10.13) into (10.12) we obtain

$$F_{cov} = \exp \left\{ -0.1933 \left(\frac{H_s \, \omega_p^2}{g} \right)^{-2} \right\}. \tag{10.14}$$

The whitecap coverage F_{cov} is illustrated for the Baltic Sea storm waves on 9 August 1998 in Fig. 10.3 – see line denoted as 'whitecaps coverege (1)'. The figure indicates that the most extensive whitecap coverage during the considered storm is associated with relatively short waves whose heights increased fast. It should be noted that the significant wave steepness $\varepsilon_s = \frac{H_s}{g T_p^2}$ during one day of storm was in the range 0.0032–0.0065, which corresponds well with values given by Holthuijsen and Herbers (1986).

Let us now develop an expression for the whitecap coverage F_{cov} using the vertical acceleration criterion. From (7.34) for $\alpha = 0.32$ we obtain

$$F_{cov} = 1 - \Phi \left[0.908 \left(\frac{gX}{V_{10}^2} \right)^{0.11} \right]. \tag{10.15}$$

Substitution of (D.9) into (10.15) with $a_0 = 0.2$ for the Pierson–Moskowitz spectrum gives

$$F_{cov} = 1 - \Phi \left[0.447 \left(\frac{H_s \, \omega_p^2}{g} \right)^{-1} \right]. \tag{10.16}$$

Function (10.16) was added for comparison in Fig. 10.3 as line denoted 'whitecaps coverege (2)'. Both breaking criteria yield very similar values of the whitecap coverage for all stormy days in the Baltic Sea.

10.5 Dependence of aerosol flux on sea state parameters

As mentioned in Chapter 9, the sea spray generation functions were most often parameterized in terms of the local wind speed and droplet radii, under the assumption that local wind speed is the dominant factor controlling the production of aerosol particles at the sea surface and their subsequent entrainment upward. It is accepted that wind speed is a factor that plays a major role in forming breaking waves and spume droplets. On the other hand, it is clear that the observed large scatter in value of whitecap coverage at a given wind speed

raises concerns that wind speed alone is insufficient to fully characterize aerosol production. Local sea state parameters, such as wave height and spectral peak frequency, being to some extent dependent on past conditions, are typically not reported with measurements. An exception is the whitecap method by Monahan et al. (1986) when the function $f_{\mathrm{sgf}}^{(\mathrm{wc})}(r)$ is presented in the form of the product of size-dependent production flux $f_{\mathrm{prod}}^{(\mathrm{wc})}(r)$ and whitecap coverage F_{cov}. Function $f_{\mathrm{prod}}^{(\mathrm{wc})}(r)$ is only a function of radius r, while the representation of F_{cov} in terms of the significant wave height H_{s} and peak frequency ω_{p} is given by (10.14) and (10.16), when the limiting wave steepness and limiting vertical acceleration criteria are applied, respectively. Using this fact, the sea spray generation function resulting from the whitecap method can be parameterized both in droplet radii and sea state parameters as follows:

- limiting steepness criterion

$$f_{\mathrm{sgf}}^{(\mathrm{wc})}(r, H_{\mathrm{s}}, \omega_{\mathrm{p}}) = f_{\mathrm{prod}}^{(\mathrm{wc})}(r) \times \exp\left[-0.1933 a_0 \left(\frac{H_{\mathrm{s}}\,\omega_{\mathrm{p}}^2}{g}\right)^{-2}\right] \tag{10.17}$$

- threshold vertical acceleration

$$f_{\mathrm{sgf}}^{(\mathrm{wc})}(r, H_{\mathrm{s}}, \omega_{\mathrm{p}}) = f_{\mathrm{prod}}^{(\mathrm{wc})}(r) \times \left(1 - \Phi\left[0.447 \left(\frac{H_{\mathrm{s}}\,\omega_{\mathrm{p}}^2}{g}\right)^{-1}\right]\right) \tag{10.18}$$

The above relationships provide an opportunity to estimate the aerosol fluxes generated from a given ocean basin during stormy weather. In particular, after integration of the above sea spray generation functions against radius r according to (8.24) and using representation (9.12) for $f_{\mathrm{prod}}^{(\mathrm{wc})}(r)$, we obtain the total flux of dry sea salt emitted from the sea. Results of such calculations are given in Fig. 10.4 for a storm which was recorded on 9 August 1998 in the Baltic Sea for both representations of the whitecap coverage F_{cov}. Variation of the function $f_{\mathrm{dmass}}^{(\mathrm{tot})}$ in time corresponds closely to the variation of the whitecap coverage because the integral of $f_{\mathrm{prod}}^{(\mathrm{wc})}(r)$ against r does not depend on time. There are two peaks of the total flux value. The highest one at time $t = 2$ h corresponds to the largest value of the whitecap coverage due to the higher significant waves. The second peak at time $t = 20$ h is due to shortening of the spectral peak periods, which yields increasing wave steepness.

Under steady state conditions in the open ocean it would be expected that the sea state parameters would be determined solely by local wind speed. In particular, Pierson and Moskowitz (1964) proposed for a fully developed sea the formula given in (3.15) as follows

$$S(\omega) = 0.0081\, g^2 \omega^{-5} \exp\left[-0.74 \left(\frac{g}{\omega V_{19.5}}\right)^4\right], \tag{10.19}$$

in which $V_{19.5}$ is the wind speed at an elevation of 19.5 m above the sea surface. For a steady fully developed sea, Pierson and Moskowitz found experimentally the following relationship for the peak frequency:

$$\omega_{\mathrm{p}} = 0.879\, \frac{g}{V_{19.5}}. \tag{10.20}$$

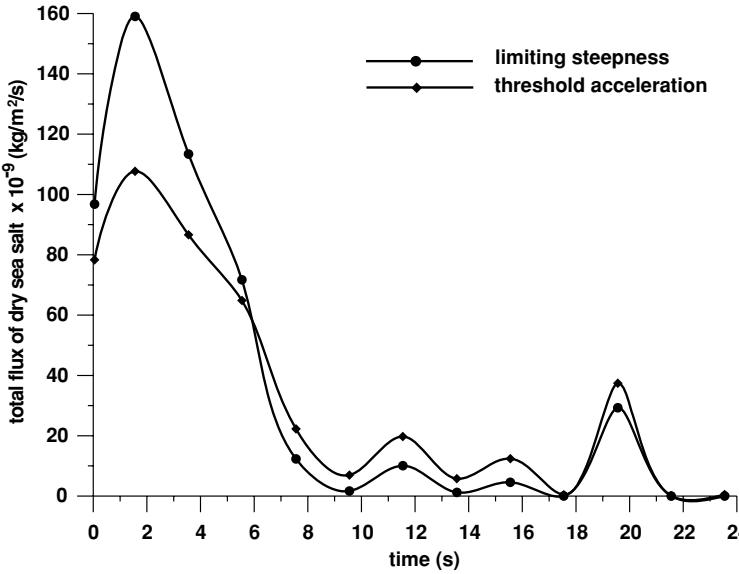

Figure 10.4: Total flux of dry sea salt mass $f_{\mathrm{dmass}}^{(\mathrm{tot})}$ for sea storm recorded on 9 August 1998 in the Baltic Sea for two different breaking criteria.

Another sea state parameter – significant wave height H_{s} – can be found from the moment m_0 of the spectrum (10.19) as follows

$$\frac{H_{\mathrm{s}}^2}{16} = m_0 = 2.736 \cdot 10^{-3} \left(\frac{V_{19.5}^2}{g} \right)^2 . \tag{10.21}$$

Therefore, the significant wave height becomes

$$H_{\mathrm{s}} = 4\sqrt{m_0} = 0.209 \left(\frac{V_{19.5}^2}{g} \right), \tag{10.22}$$

in which wind speed $V_{19.5}$ can be represented in terms of the wind speed at the standard 10 m level by a relationship similar to (9.29).

Equations (10.20) and (10.22) yield the significant wave steepness for a fully developed sea as

$$\varepsilon_s = \frac{H_{\mathrm{s}}}{g T_{\mathrm{p}}^2} = \frac{1}{4\pi^2} \frac{H_{\mathrm{s}} \omega_{\mathrm{p}}^2}{g} = 4.09 \times 10^{-3}. \tag{10.23}$$

In Fig. 10.5 the total flux of dry sea salt $f_{\mathrm{dmass}}^{(\mathrm{tot})}$ defined in (8.24) is shown as a function of wind speeds in range $4 < V_{10} < 20$ m/s under the assumption of fully developed sea conditions. The modified sea spray generation function suggested by Andreas (1998) was used to quantify the size-dependent flux. As should be expected, the aerosol flux increases with wind speed. The significant wave height H_{s} and peak frequency ω_{p} corresponding to a given wind speed are

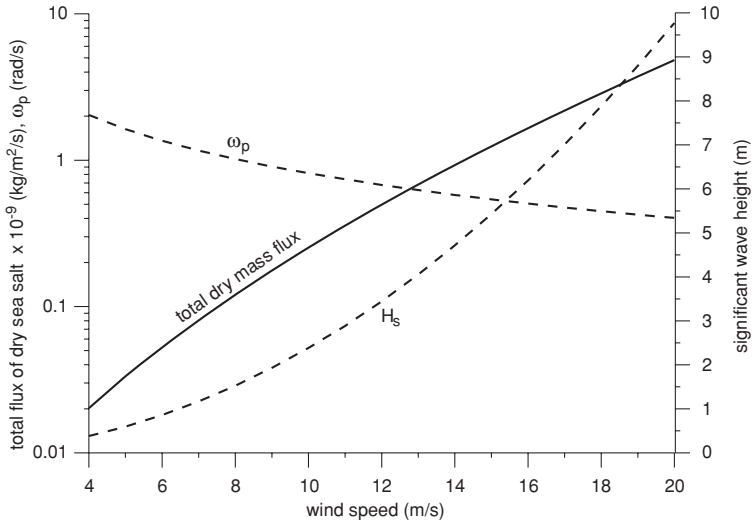

Figure 10.5: Total flux of dry sea salt $f_{\mathrm{dmass}}^{(\mathrm{tot})}$ as a function of wind speed under the assumption of fully developed sea conditions.

added to the figure. To reach a constant value of the significant wave steepness $\varepsilon_s = 4.09 \times 10^{-3}$, an increase of wave height H_s should be compensated with a decrease of the peak frequency ω_p.

Petelski and Chomka (1996) and Chomka and Petelski (1997) reported the results of measurements and modelling of the mean aerosol emission fluxes in the coastal zone during the BAEX Experiment at the Lubiatowo Station on the southern coast of the Baltic Sea. They found that the aerosol fluxes varied from 3.2 to 384 µg/(m^2 s). Assuming that the length of the Polish coastline of the Baltic Sea is about 500 km and the mean width of the coastal zone is 50 m, they found that the mean annual emission from the coastal zone becomes about 150 tonnes per year. Moreover, it was found that the aerosol emission fluxes are proportional to the average wave energy dissipation to the power 3/4 (Chomka and Petelski, 1997). This relationship was based on the estimation of wave energy dissipation in the coastal zone reported by Thornton and Guza (1983). A comprehensive summary of the lidar measurements of the aerosol properties over the coastal area has been recently published by Zieliński (2006).

In contrast to the coastal zone, where the wave energy dissipation area is well defined, the determination of wave energy dissipation in deep water and subsequent estimation of the aerosol fluxes is much more complicated. Marks (1987) showed that the sea aerosol flux in µg/m^3 for particles larger than 0.1 µm and for wind speed V_{10} in the range 1 m/s $< V_{10} <$ 12 m/s, is given by

$$f_{\mathrm{vol}} = 6.08 \times \exp(0.13 V_{10}). \tag{10.24}$$

Moreover, using the sea salt aerosol concentration measured by the impactors,

Marks obtained a relation between the aerosol flux and whitecap coverage in the form

$$f_{\mathrm{vol}} = 10.23 + 15.72 \times F_{\mathrm{cov}}, \tag{10.25}$$

where f_{vol} is the aerosol volume flux in $\mu g/m^3$ and the whitecap coverage is in percent. If we eliminate the wind speed V_{10} from equations (7.6) and (10.24), we obtain another relationship between whitecap coverage and sea aerosol flux

$$f_{\mathrm{vol}} = 6.08 \exp\left[4.75\, F_{\mathrm{cov}}^{0.28}\right]. \tag{10.26}$$

10.6 Dimensional analysis of aerosol flux from the sea surface

The present knowledge of the relationship between dynamics of breaking waves and aerosol fluxes is mostly based on experiments. The experimental data are scattered due to variability of conditions during natural and laboratory experiments. However, in the situation when very well established theoretical foundations of the problems are known, various combinations of experimental data provide us with the possibility to establish the relationship between measured variables. The number of such combinations can be very large. When several variables can be combined in the form of a single dimensionless variable, the number of combinations can be significantly reduced. This approach is the basis of dimensional analysis. Dimensional analysis is a rational method for combining physical variables into dimensionless products. It gives qualitative rather than quantitative relationships. After performing the dimensional analysis, theoretical or experimental judgement is needed to establish the required relationships between dimensional variables.

The total flux of dry sea salt $f_{\mathrm{dmass}}^{(\mathrm{tot})}$ from the sea surface depends on the following set of physical parameters: air density ρ_{a}, water density ρ_{w}, surface tension of water σ, gravity acceleration g, and mean wave energy dissipation per surface unit E_{dissrate}. These six variables ($n = 6$) can be arranged in a dimension matrix as follows (Massel, 1999; Petelski et al., 2005)

	$f_{\mathrm{dmass}}^{(\mathrm{tot})}$	E_{dissrate}	ρ_{a}	ρ_{w}	σ	g
kg	1	1	1	1	1	0
m	−2	0	−3	−3	0	1
s	−1	−3	0	0	−2	−2

(10.27)

The matrix is of order $m = 3$. According to the Buckingham theorem (Massel, 1999) there are $n - m = 3$ non-dimensional quantities, Π_1, Π_2, Π_3, created from the dimensional quantities mentioned above for which the following relationship exists

$$\Pi_1 = \psi\,(\,\Pi_2, \Pi_3) \tag{10.28}$$

The resulting non-dimensional quantities Π_n are as follows (Petelski et al., 2005)

$$\Pi_1 = \frac{\rho_{\rm w}\left(\frac{\rho_{\rm w}}{\sigma g}\right)^{3/4}\left(E_{\rm dissrate}\right)^2}{\left(f_{\rm dmass}^{\rm (tot)}\right)^3};\ \Pi_2 = \frac{\rho_{\rm w}}{\rho_{\rm a}};\ \Pi_3 = \frac{\rho_{\rm w}\rho_{\rm a}}{\left(f_{\rm dmass}^{\rm (tot)}\right)^3}\ \left(E_{\rm dissrate}\right). \tag{10.29}$$

Combining (10.28) and (10.29) we obtain

$$f_{\rm dmass}^{\rm (tot)} = f(\Pi_2,\Pi_3)\rho_{\rm w}^{1/3}\left(\frac{\rho_{\rm w}}{\sigma g}\right)^{1/4}\left(E_{\rm dissrate}\right)^{2/3}. \tag{10.30}$$

If we assume that $f(\Pi_2,\Pi_3)$ is a constant equal to A, the relation (10.30) exhibits the dependence of the total flux of dry sea salt on the energy dissipation rate with power 2/3 (Petelski et al., 2005).

When the energy dissipation rate $E_{\rm dissrate}$ is determined by (10.7) based on the Komen et al. (1984) approach, from (10.30) we obtain

$$\begin{aligned} f_{\rm dmass}^{\rm (tot)} &= 5.32\times10^{-3}\,A\left(\frac{\rho_{\rm w}^{15}\,g^5}{\sigma^3}\right)^{1/12}\left[\left(\frac{a_1}{a_0}\right)^7\left(\frac{a_2}{a_0}\right)\right]^{2/3} \\ &\quad\times\left(\frac{H_{\rm s}\,\omega_{\rm p}^2}{g}\right)^{8/3}\left(H_{\rm s}^2\,\omega_{\rm p}\right)^{2/3}, \end{aligned} \tag{10.31}$$

in which the surface tension $\sigma \approx 0.075\,{\rm N/m}$ (Lewis and Schwartz, 2004).

To determine unknown function A, we use the fact that at present the total flux of the dry salt mass based on the sea spray function suggested by Andreas (1998) – see (9.32) – is probably the most comprehensive representation of the aerosol flux in terms of wind speed. Comparing (10.31) with (9.32) we obtain coefficient A in the form

$$A = 10^8\left(0.7717 - 0.1421\,V_{10} + 0.0127\,V_{10}^2\right), \tag{10.32}$$

Substituting (10.32) into (10.31) yields the final expression for the total flux of the dry sea mass resulting from the dimensional analysis for a fully developed sea as follows

$$\begin{aligned} f_{\rm dmass}^{\rm (tot)} &= 5.321\times10^5\left(0.7717 - 0.1421\,V_{10} + 0.0127\,V_{10}^2\right) \\ &\quad\times\left(\frac{\rho_{\rm w}^{5/4}\,g^{5/12}}{\sigma^{1/4}}\right)\left[\left(\frac{a_1}{a_0}\right)^7\left(\frac{a_2}{a_0}\right)\right]^{2/3}\left(\frac{H_{\rm s}\,\omega_{\rm p}^2}{g}\right)^{8/3}\left(H_{\rm s}^2\,\omega_{\rm p}\right)^{2/3}. \end{aligned} \tag{10.33}$$

Petelski et al. (2005) provide some arguments in favour of a similar dependence of the aerosol flux on the energy dissipation rate for the Baltic Sea case.

10.7 Alternative representation of aerosol flux

We showed above that the dimensional arguments provide the dependence of aerosol flux on energy dissipation in power of 2/3. Let us now find this power

from the point of view of the physics of aerosol generation. First of all it is clear that emission flux $f^{(\mathrm{tot})}_{(\mathrm{dmass})}$ is proportional to the number of bursting bubbles per sea surface unit

$$f^{(\mathrm{tot})}_{(\mathrm{dmass})} \approx A_1 \frac{\pi}{6} \rho_{\mathrm{ss}}\, r_{\mathrm{m}}^3\, N_{\mathrm{b}} \quad [\text{number of droplets/m}^2\text{s}], \tag{10.34}$$

where N_{b} is the number of bubbles per unit surface and unit time, r_{m} is the representative particle radius and A_1 is the proportionality coefficient. The number of bubbles with a representative radius r_{m} should be related to the sea surface covered by whitecaps formed by breaking waves. Thus we have

$$N_{\mathrm{b}} = A_2 \frac{\Delta V}{\frac{4}{3}\pi\, r_{\mathrm{m}}^3}, \tag{10.35}$$

in which ΔV is the volume of water discharged by a single breaking wave (m^3) and the representative radius r_{m} is given in metres. In order to define the volume ΔV we assume that it is equal to the volume of the roller formed on the surface of the breaking wave (Massel, 1996a). Using the rationale presented in Section 6.3.3, we assume that due to breaking, current wave amplitude decreases to the value A_{br} representing the critical saturation level. Hence the portion of the amplitude loss in a unit cycle becomes

$$\Delta A = 2A_{\mathrm{rms}}\, I_1\left(\frac{A_{\mathrm{br}}}{A_{\mathrm{rms}}}\right), \tag{10.36}$$

where function $I_1(x)$ is given in (7.37). The length of the whitecapping area l_{br} is proportional to the representative wavelength L_{rms} (see (7.41). Thus the surface of a roller in the vertical plane, parallel to wave motion, becomes

$$\Delta S = \Delta A\, l_{br} = 2A_{\mathrm{rms}}\, L_{\mathrm{rms}}\, I_1^2\left(\frac{A_{\mathrm{br}}}{A_{\mathrm{rms}}}\right), \tag{10.37}$$

and for the volume of a roller formed by spilling breakers we obtain

$$\Delta V = \Delta S l, \tag{10.38}$$

where $l = 1\,\mathrm{m}$ is a unit distance in the direction perpendicular to the direction of wave motion. After substituting (10.37) into (10.35), the number of bubbles N_{b} is

$$N_{\mathrm{b}} = \frac{3A_2\, A_{\mathrm{rms}}\, L_{\mathrm{rms}}\, I_1^2\left(\frac{A_{\mathrm{br}}}{A_{\mathrm{rms}}}\right) l}{2\pi r_{\mathrm{m}}^3}. \tag{10.39}$$

Thus, the total aerosol flux $f^{(\mathrm{tot})}_{\mathrm{dmass}}$ can be presented as follows

$$f^{(\mathrm{tot})}_{\mathrm{dmass}} = A_3 \frac{\rho_{ss}}{4} A_{\mathrm{rms}}\, L_{\mathrm{rms}}\, I_1^2\left(\frac{A_{\mathrm{br}}}{A_{\mathrm{rms}}}\right) l. \tag{10.40}$$

In Chapter 6, a set of various estimates of the energy dissipated during wave breaking was discussed. For the purpose of this analysis we apply the formula suggested by Longuet–Higgins (1969) as follows

$$E_{\text{diss}} = \frac{1}{2}\rho g A_{\text{rms}}^2 \exp\left(-\frac{A_{\text{br}}^2}{A_{\text{rms}}^2}\right). \tag{10.41}$$

Using (10.41), equation (10.40) takes the form

$$f_{\text{dmass}}^{(\text{tot})} \approx \frac{\sqrt{2}}{4} A_3 \frac{\rho_{ss}}{(\rho_{\text{w}}\, g)^{1/2}} \frac{L_{\text{rms}}\, I_1^2\left(\frac{A_{\text{br}}}{A_{\text{rms}}}\right)}{\left\{\exp\left(-\frac{A_{\text{br}}^2}{A_{\text{rms}}^2}\right)\right\}^{1/2}} (E_{\text{diss}})^{1/2}. \tag{10.42}$$

Longuet–Higgins's formulation of energy dissipation due to wave breaking results in dependence of the aerosol flux on the root square of the energy dissipation rate. This dependence is close to the dependence on power of 2/3 which results from the dimensional analysis given above.

Chapter 11

Seasonal dependence of aerosol fluxes in the Baltic Sea

11.1 Introduction

The Baltic Sea is a semi-enclosed European inland sea forming one of the world's largest brackish water areas. This ecosystem is characterized by fluctuations in the natural environment connected with infrequent and sporadic flushing of the deeper basins with more oxygenated water from outside. Dynamics and variability of the processes affecting water mass exchange and renewal are strongly related to meteorological forcing factors, especially the intensity, pattern and frequency of the air pressure fronts migrating from the North Atlantic (Miętus, 1998; Piechura et al., 2006).

In the second section, the resulting wind climate is shortly characterized on the basis of historical data for some regions of the Baltic Sea. The available data on wind-induced waves are described in Section 3. These data comprise observational as well as numerical simulated wave parameters. Wind and wave data are the incident information for prediction of the sea aerosol budget for the Baltic Sea. The calculation methodology is illustrated using the data for year 1999. In particular, in Section 4, two methods of estimation of sea salt production are used and compared for the very windy December of 1999. Surprisingly, the whitecap method and dry deposition result in very similar monthly averaged sea salt production for this month.

11.2 Wind field in the Baltic Sea

The Baltic Sea is located within the west wind zone where the proximity of the Atlantic Ocean is totally decisive for the climate of this sea basin. The average pressure distributions and winds over Europe in January and July show that the average air flow is strong in winter and weak in summer. Winds of storm force, more than 25 m/s, are almost exclusively formed by deep cyclones occurring mainly from September to March. Winds from the north and east are rare.

Table 11.1: Average wind speed in (m/s) in four different basins of the Baltic Sea (adapted from Defant, 1972)

Basin	Months												Year
	I	II	III	IV	V	VI	VII	VIII	IX	X	XI	XII	average
Kiel Bay (54°, 10°E)	6.4	5.8	5.1	4.6	4.3**	4.4	4.4	4.8	5.3	5.7	6.1	6.6*	5.3
Transect Rugia-Southern Sweden (55°N, 14°E)	7.9	6.4	6.2	5.3	4.6	4.5**	4.6	5.0	5.6	6.8	8.2	8.4*	6.1
Gotland–Gdańsk Bay (56°N, 19°E)	7.9	8.5*	8.2	6.0	5.0	5.4	4.8**	6.3	6.5	7.6	8.2	8.4	6.9
Entrance to Bay of Finland (59.5°N, 23°E)	7.9	7.0	6.7	5.1	4.7**	5.0	5.2	6.1	6.6	8.2	9.1	9.2*	6.7

Note: (*) denotes maximum value and (**) denotes minimum value.

The average wind speed over the Baltic Sea is about 6–9 m/s from October to March with the maximum wind speeds in November and December. The weakest winds, of about 4–5 m/s, are observed from May to July. In Table 11.1, the average wind speeds in (m/s) in four basins of the Baltic Sea are collected, and the frequencies (in %) of the various wind speeds are given in Table 11.2.

Weak winds (0–3°B) are more frequent from May to July (65–70%) and they are rare (29–36%) in November and December. On the other hand the frequency

Table 11.2: Frequency (in %) of wind speeds in two basins of the Baltic Sea versus Beaufort Scale

Basin	Beaufort Scale	Months												Year
		I	II	III	IV	V	VI	VII	VIII	IX	X	XI	XII	average
Transect	0–3	41	36**	44	61	68	64	69*	54	54	44	36**	36**	50.6
Gotland-	4–5	31	36	38*	26	24**	26	24**	33	30	34	33	34	30.8
Bay of Gdańsk	6–7	23*	20	14	10	5**	8	6	10	12	16	21	22	13.9
	8	5	8	4	3	3	2	1**	3	4	6	10*	8	4.8
Entrance	0–3	42	46	52	64	70*	67	65	58	52	34	30	29**	50.8
to Bay	4–5	32	35	35	31	24**	27	28	29	33	42*	40	41	33.1
of Finland	6–7	17	14	10	4**	5	4**	6	9	12	17	22*	21	11.7
	8	9*	5	4	1**	1**	2	1**	4	3	6	8	9*	4.4

Note: (*) denotes maximum value and (**) denotes minimum value.

Table 11.3: Frequency of the wind directions over the Baltic Sea (adapted from Defant, 1972)

Location or region	N	NE	E	SE	S	SW	W	NW	No winds
Lightship 'Kiel' (54.5°N, 10.3°E)									
January	5**	7	9	16	14	23*	18	7	1
April	6**	7	20	9	9	13	21*	11	4
July	5	4**	12	9	7	19	25*	15	4
October	5**	6	13	12	11	19	20*	11	3
Transect Gotland-Bay of Gdańsk (55°–57°N, 18°–20°E)									
January	9	8**	8**	13	15	20*	16	10	1
April	13	14	9**	9**	9**	16*	16*	10	4
July	13	11	6	5**	7	18*	22*	13	5
October	9	8**	9	13	14	18*	15	12	2

Note: (*) denotes maximum value and (**) denotes minimum value.

of storm winds (>8°B) is only 4–5%, and they appear predominantly from October to March. Information on the wind directions over the Baltic Sea is given in Table 11.3. The lightship 'Kiel' represents the region of the Western Baltic Sea while the transect Gotland–Bay of Gdańsk is characteristic for the Southern Baltic. In these regions, all through the year, the winds come from W and SW directions, while in summer W winds predominate and SW winds are more frequent in winter. Sometimes in both areas, NW and S winds appear.

11.3 Wave climate in the Baltic Sea

Strong wind blowing over the Baltic Sea, characterized above, induces waves on all the sea area. The pattern of the wind field and the geometry of the Baltic Proper suggest that the highest and longest waves appear near the entrance to the Gulf of Finland and off the eastern Baltic coast. As mentioned by Broman et al. (2006), wave observations in the Baltic Sea extend back more than 200 years. However, these data represent only visually estimated wave parameters in the near-coastal regions. Contemporary wave measurements in the Baltic are concentrated mostly in the northern part of the sea and in the southern part. In particular, in the northern Baltic Proper (close to Almagrundet lighthouse), and at Ölands södra grund, a bottom-fixed device was installed, while a waverider buoy was installed south of Gotland (Broman et al., 2006). High-quality wave data were obtained in the areas around Finland (Kahma et al., 1983). Valuable data on waves in the Baltic Sea were also reported by Davidan et al. (1978, 1985), and in the southern part of the Baltic Sea, important data sets were obtained by Mårtensson and Bergdahl (1987), Gayer

et al. (1995), Paplińska and Reda (2003). Paplińska (1999) published two series of wave records obtained from the waveriders located in two points in the Southern Baltic at water depths of about 20 m, namely in October–November 1997 (Pomeranian Bay, 54.13°N; 15°E) and in February–May 1998 (Lubiatowo region, 54.8°N; 17.8°E).

Apart from the experimental data, several numerical wave simulations were performed. For the purpose of this book, the numerical results obtained by Paplińska and Reda (2003) will be used. In their calculations, the third generation of the WAM4 wave model was applied (WAMDI, 1988) with the following set-up parameters:

- grid step of 0.15°(∼16.7 km) in both the latitudinal and the longitudinal directions, which results in 1312 grip points over the Baltic Sea
- output time step: 3 h
- frequency-direction grid: 24 frequencies and 24 directions
- propagation time step: 300 s
- source function time step: 150 s

The input data for the model are wind data. The atmospheric model is a mesoscale version of the unified model of the United Kingdom. The wind data were verified and assimilated for calculations every 3 h. The calculations were performed in the Interdisciplinary Centre of Mathematical and Computational Modelling at Warsaw University. In the report of Paplińska and Reda (2003), the spatial distribution of the monthly average of the significant wave height $H_s = 4\sqrt{m_0}$ and peak period T_p were given for years 1998–2001. These values of H_s and T_p will be used in the next section to estimate the monthly averages of the marine aerosol production.

11.4 Seasonal dependence of the aerosol budget over the Baltic Sea

Seasonal wind and wave data for the Baltic Sea provide an opportunity to estimate the aerosol production in particular months over the Baltic surface. First we use the average wind speeds in four basins of the Baltic as given in Table 11.1 to calculate the total flux of dry sea salt, applying the Andreas (1998) formula. Hence, we have

$$f_{\mathrm{dmass}}^{(\mathrm{tot})} \approx \frac{\pi}{6}\,\rho_{\mathrm{ss}} \int r^3 f_{\mathrm{sgf}}(r) dr \quad [\mathrm{kg/m^2/s}], \tag{11.1}$$

where function $f_{\mathrm{sgf}}(r)$ is given by (9.32). The resulting sea salt production depends solely on the droplet radii r and wind speed V_{10}. Fig. 11.1 shows the monthly average of the total flux of dry sea salt for four different regions of the

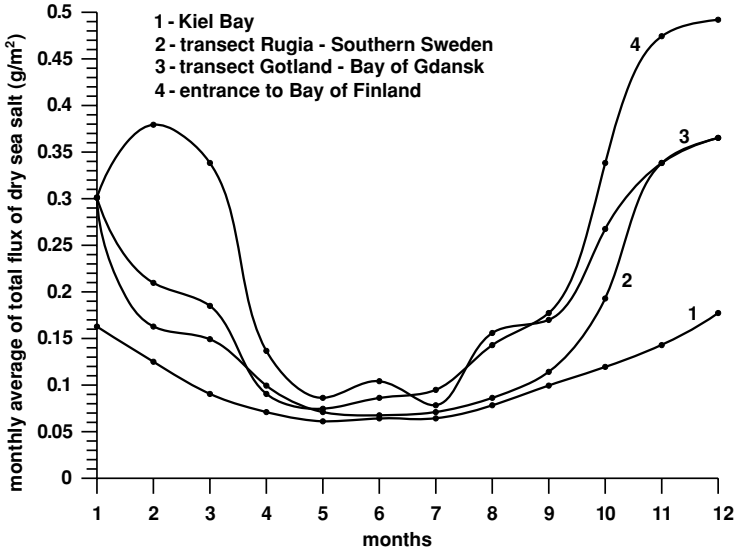

Figure 11.1: Seasonal variation of the total flux of dry sea salt over four different region of the Baltic Sea.

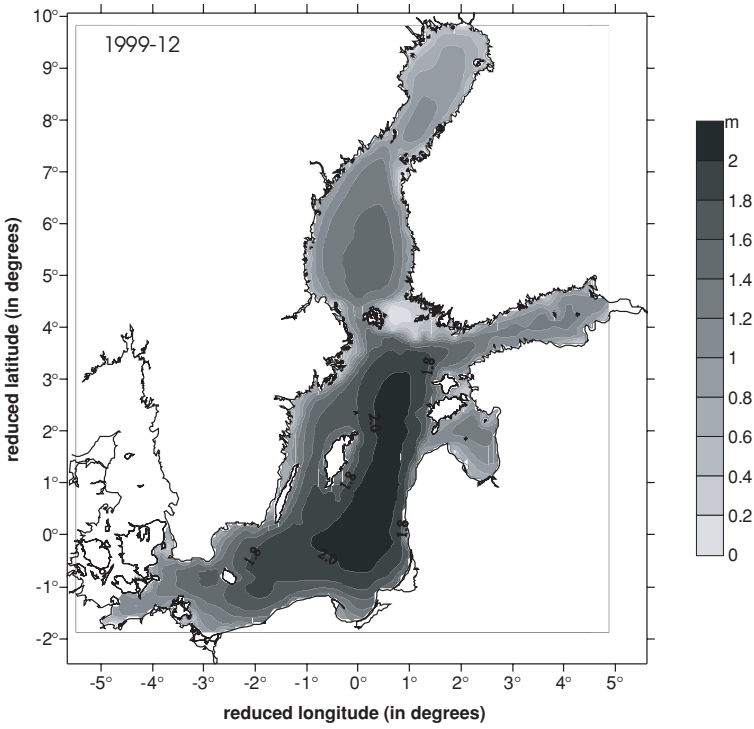

Figure 11.2: Distribution of the significant wave height over the Baltic Sea in December 1999.

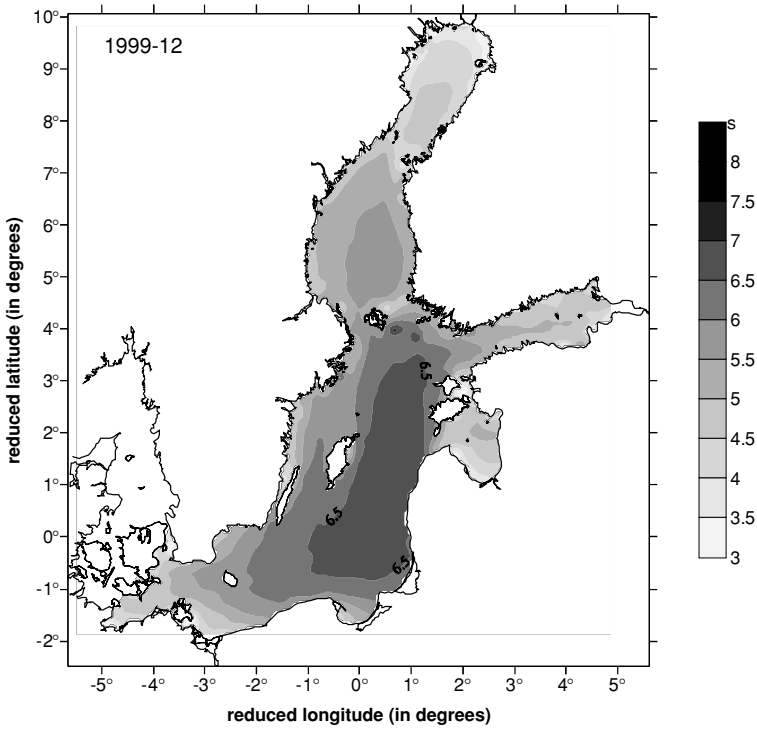

Figure 11.3: Distribution of the peak period over the Baltic Sea in December 1999.

Baltic sea. The pattern of all curves is very similar. The highest aerosol fluxes are in winter and the smallest ones are in summer.

Summarizing the fluxes over all year we obtain the annual average fluxes of dry sea salt in these regions as follows

Kiel Bay – 1.256 g/m^2/year
transect Rugia-Southern Sweden – 2.019 g/m^2/year
transect Gotland-Bay of Gdańsk – 2.720 g/m^2/year
entrance to Bay of Finland – 2.667 g/m^2/year

To get more detailed information on aerosol production over the Baltic Sea, we adopt the distribution of the significant wave height H_s and peak period T_p reported by Paplińska and Reda (2003). For illustration, in Figs. 11.2 and 11.3, the distribution of average height H_s and period T_p for December 1999 is shown. The reduced latitude and longitude are given versus the central point of the following coordinates: 56°N and 19.3°E.

The total dry sea salt production was estimated using the sea spray generation function (10.17) where the size-dependent production flux $f_\mathrm{prod}^{(\mathrm{wc})}(r)$ is given by the Woolf et al. method (9.12) and whitecap coverage results from the limiting wave steepness criterion for the JONSWAP spectrum.

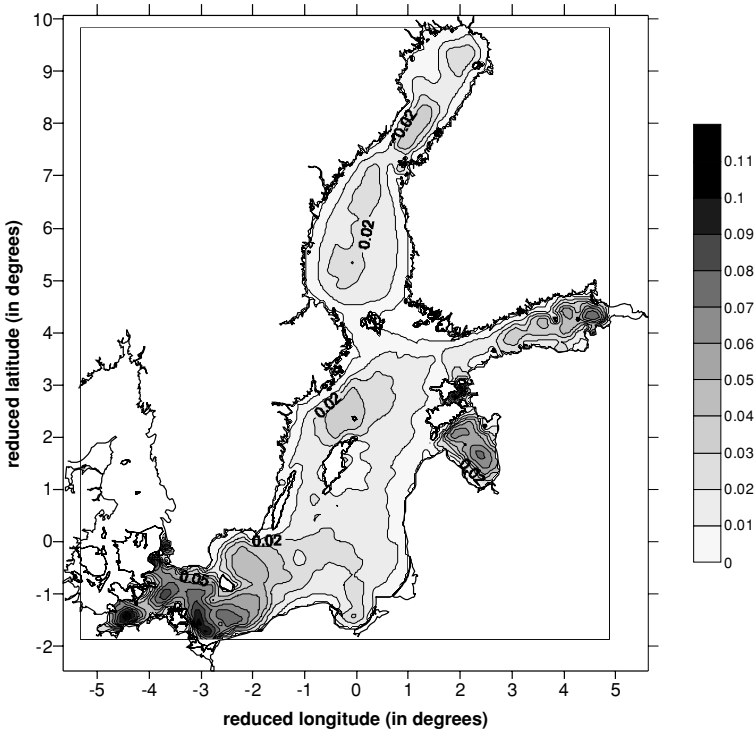

Figure 11.4: Monthly averaged sea salt production over the Baltic Sea in December 1999 (whitecap method).

Table 11.4: Monthly sea salt production in the Baltic Sea in 1999 (in 10^{-6} kg/month)

Month	Criterion for determination of whitecap coverage limiting steepness	limiting vertical acceleration
January	1.39	4.87
February	3.11	8.28
March	0.68	3.07
April	0.62	2.96
May	0.15	1.13
June	0.09	0.69
July	0.17	1.23
August	0.06	0.61
September	0.26	1.60
October	1.70	5.83
November	3.37	8.66
December	7.97	14.96

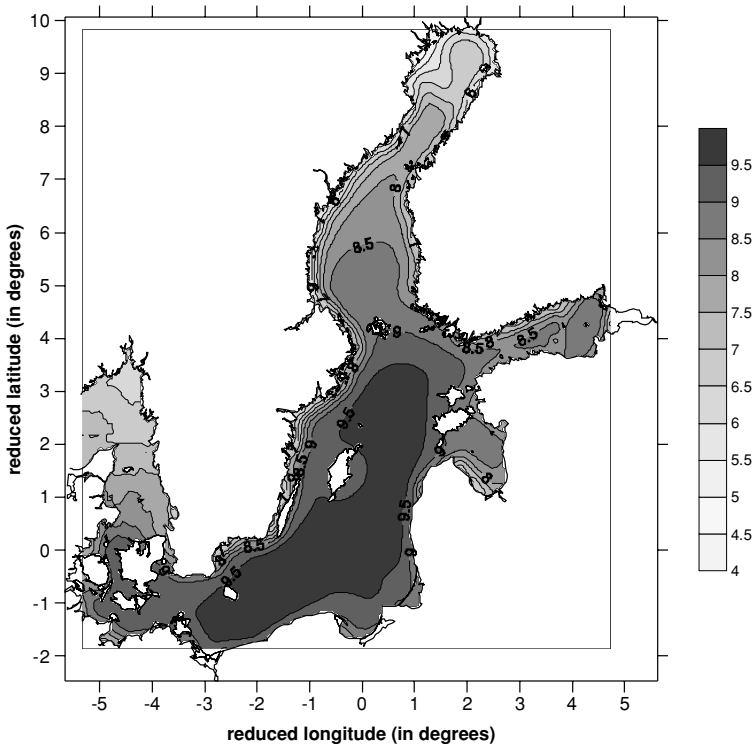

Figure 11.5: Monthly averaged wind speed over the Baltic Sea in December 1999.

The distribution of the monthly average of the sea salt production for December 1999 in g/m^2 is given in Fig. 11.4. Surprisingly, the highest values of production are observed for shallow areas, up to 0.13 g/m^2. This results directly from the whitecap method when the whitecap coverage follows from the wave limiting steepness, when

$$F_{\mathrm{cov}} \sim \left(\frac{H_{\mathrm{s}}\omega_p^2}{g}\right) \sim \frac{H_{\mathrm{s}}}{gT_{\mathrm{p}}^2}. \tag{11.2}$$

During December 1999, waves with relatively high steepness were observed in the shallow areas. Therefore, according to the adopted definition of whitecaps, the sea salt production should also be higher in these regions. Integrating the distribution of the sea salt production over the sea surface area, we obtain average total sea salt production over all the Baltic Sea in December 1999 equal to about 7.97×10^6 kg/month. It should be noted that when the vertical acceleration criterion is used to parameterize the whitecap coverage, the average total sea salt production in December 1999 equals 14.96×10^6 kg/month. In Table 11.4, the monthly sea salt production for all of year 1999 in the Baltic

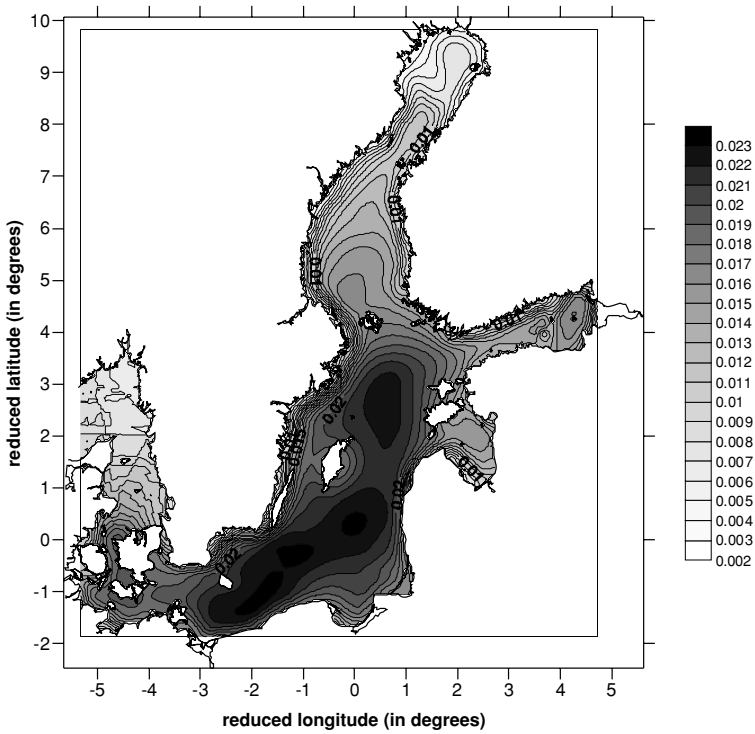

Figure 11.6: Monthly averaged sea salt production over the Baltic Sea in December 1999 (dry deposition method).

Sea is summarized. The highest sea salt production is observed during winter and the smallest one observed during summer. Taking into account that the surface of the Baltic Sea is about 384,700 km^2, the monthly average of sea salt production over the unit km^2 is equal to 20.72–38.90 kg during stormy weather. The above estimates of sea salt production are based on the whitecap method when the whitecap coverage can be parameterized in terms of the sea state parameters through the two wave breaking criteria, i.e. the limiting steepness and the limiting vertical acceleration.

The table indicates that the sea salt production based on the limiting vertical acceleration criterion is higher than that calculated using the limiting steepness criterion. In particular, during winter months the ratio of both production rates is about 2 and for smaller waves in summer, the difference between methods of calculation is much higher.

More accurate estimation of the sea aerosol production requires the wind field over the Baltic Sea. In Fig. 11.5, the distribution of the monthly average of the wind speed in December 1999 is given. The wind speed was relatively high and distributed over all the Baltic Proper. Using this wind field, the sea salt production in December 1999 is calculated by the Andreas (1998) sea

spray production function and it is shown in Fig. 11.6 in g/m^2. It is interesting to note that total sea salt production in December 1999 over all the Baltic Sea becomes 5.95×10^6 kg/month. This result is not much different from the production based on the whitecap method of 7.97×10^6 kg/month, given above.

Appendix A

Amplitudes $M^{(+)}$, $M^{(-)}$, $P^{(+)}$ and $P^{(-)}$

Coefficients $M^{(+)}$, $M^{(-)}$, $P^{(+)}$, $P^{(-)}$, $\Pi^{(+)}$, $\Pi^{(-)}$, $\Pi_1^{(+)}$ and $\Pi_1^{(-)}$ for amplitudes of surface nonlinear wave given by (3.84) are as follows

$$M^{(+)} = -(\omega_{\rm n}+\omega_{\rm m})\,\Pi^{(+)} - \frac{1}{2}\left[\frac{\omega_{\rm n}^2+\omega_{\rm m}^2}{\omega_{\rm n}\omega_{\rm m}}\right] \times \tanh(k_{\rm n}h)\tanh(k_{\rm m}h) - \frac{1}{2}\cos(\theta_{\rm n}-\theta_{\rm m}) \tag{A.1}$$

and

$$M^{(-)} = (\omega_{\rm m}-\omega_{\rm n})\,\Pi^{(-)} - \frac{1}{2}\left[\frac{\omega_{\rm n}^2+\omega_{\rm m}^2}{\omega_{\rm n}\omega_{\rm m}}\right] \times \tanh(k_{\rm n}h)\tanh(k_{\rm m}h) - \frac{1}{2}\cos(\theta_{\rm n}-\theta_{\rm m}) \tag{A.2}$$

in which

$$\Pi^{(+)} = \frac{\Pi_1^{(+)}}{(\omega_{\rm n}+\omega_{\rm m})^2 - g \mid \vec{k}_{\rm n}+\vec{k}_{\rm m} \mid \tanh(\mid \vec{k}_{\rm n}+\vec{k}_{\rm m} \mid h)} \tag{A.3}$$

$$\Pi^{(-)} = \frac{\Pi_1^{(-)}}{(\omega_{\rm m}-\omega_{\rm n})^2 - g \mid \vec{k}_{\rm m}-\vec{k}_{\rm n} \mid \tanh(\mid \vec{k}_{\rm m}-\vec{k}_{\rm n} \mid h)} \tag{A.4}$$

$$\Pi_1^{(+)} = (\omega_{\rm m}+\omega_{\rm n})\cos(\theta_{\rm m}-\theta_{\rm n}) - \frac{1}{2}\left(\frac{\omega_{\rm m}k_{\rm n}}{k_{\rm m}}\right) \times \left[1-\tanh^2(k_{\rm n}h)\right] - \frac{1}{2}\left(\frac{\omega_{\rm n}k_{\rm m}}{k_{\rm n}}\right)\left[1-\tanh^2(k_{\rm m}h)\right] \tag{A.5}$$

and

$$\Pi_1^{(-)} = (-\omega_{\rm m}+\omega_{\rm n})\cos(\theta_{\rm m}-\theta_{\rm n}) - \frac{1}{2}\left(\frac{\omega_{\rm m}k_{\rm n}}{k_{\rm m}}\right) \times \left[1-\tanh^2(k_{\rm n}h)\right] + \frac{1}{2}\left(\frac{\omega_{\rm n}k_{\rm m}}{k_{\rm n}}\right)\left[1-\tanh^2(k_{\rm m}h)\right] \tag{A.6}$$

Appendix B

Wavelet transform

B.1 Introduction

When the time localization of the spectral components is required, the transform of time series which provides the time–frequency representation of the signal should be developed. A transform of such type is the wavelet transform which gives full time–frequency representation of the time series. In contrast to the Fourier transform, the wavelet transform allows exceptional localization in the time domain via translations of the so-called *mother wavelet*, and in the scale (frequency) domain via dilations (Combes et al., 1989; Farge, 1992; Kaiser, 1994; Torrence and Compo, 1998). The wavelet analysis is similar to the Fourier analysis as it breaks a signal down into its constituents. Whereas the Fourier transform breaks the signal into a series of sine waves of different frequencies, the wavelet transform breaks the signal into its *wavelets* which are scaled and shifted versions of the mother wavelet.

Wavelet transform is a relatively new technique and in recent years there has been enormous interest in the application of wavelets. Wavelets have been successfully implemented in signal and image processing, ordinary and partial differential equation theory, numerical analysis and communication theory. The intermittent nature of sea turbulence is a particularly suitable problem for application of the wavelet transform to detect the intermittency of energy input from wind to ocean surface (see, for example, papers by Farge, 1992, Shen and Mei, 1994). In particular Shen and Mei (1994) developed the continuous wavelet transform to analyse the energy balance in the equilibrium spectral subrange of wind-generated gravity waves. Mori and Yasuda (1994), and Liu (1994) applied the wavelet transform to detect wave growth and breaking in a time series. A sudden surface jump associated with a breaking wave is regarded as a shock wave and the wavelet spectrum is defined to detect the occurrence of surface jumps.

Atmospheric cold fronts observed in the boundary layer represent relatively sharp transition zones between air masses of different physical characteristics. Application of the wavelet transform for identification of the energy cascade in

atmospheric turbulence was discussed by Yamada and Ohkitani (1991), while Meyers et al. (1993) demonstrated the usefulness of the wavelet transform in studying dispersion of Yanai waves in a reduced gravity equatorial model, and Torrence and Compo (1998) in their practical step-by-step guide used the wavelet transform to give a quantitative measure of changes in El Niño-Southern Oscillation (ENSO).

B.2 Definition of wavelets

The wavelet transform was proposed in papers of Morlet, Meyer, Grossman, Mallat and others (Massel, 2001b). Wavelets are complex or real functions concentrated in time and frequency and having the same shape. In wavelet analysis, the signal is multiplied with the wavelet, and the transform is separately computed for different segments of the time domain signal. In general, the wavelet transform of the signal, $x(t)$, is defined as the following inner product

$$WT(\tau, b) =< g_{\tau b} \mid x >= \int_{-\infty}^{\infty} x(t) g^*_{\tau b}(t; \tau, b) dt. \tag{B.1}$$

The family of continuously translated and dilated wavelets is generated from mother wavelet $g(t)$

$$g_{\tau b}(t; \tau, b) = \frac{1}{\sqrt{b}} g\left(\frac{t-\tau}{b}\right), \tag{B.2}$$

where τ is the translation parameter, corresponding to the position of the wavelet as it is shifted through the signal, and b is the scale dilation parameter determining the width of the wavelet. The scale $b > 1$ dilates (or stretches out) the signal, whereas scale $b < 1$ compresses the signal. The wavelet coefficients, $WT(\tau, b)$, represent the correlation (in terms of the time-scale functions) between the wavelet and a localized section of the signal. If the signal has a major component of the frequency corresponding to the given scale, then the wavelet at this scale is close to the signal at the particular location and the corresponding wavelet transform coefficient, determined at this point, has a relatively large value. Therefore, the wavelet transform is a sort of microscope with magnification $1/b$ and location given by parameter τ, while the optics of the microscope are characterized by the function $g_{\tau b}(t; \tau, b)$.

One of the most extensively used mother wavelets is Morlet's wavelet

$$g(t) = \exp\left(-\frac{1}{2}t^2\right) \exp(ict). \tag{B.3}$$

Equation (B.3) represents a plane wave of frequency c, modulated by a Gaussian envelope of unit width. For calculations in this chapter only wavelet (B.3) is used. In oceanographic applications, other mother wavelets, such as orthogonal wavelets (Yamada and Ohkitani, 1991; Mori and Yasuda, 1994), Paul's wavelet or DOG wavelet (derivative of a Gaussian) (Torrence and Compo, 1998) are also sometimes applied.

Using the representation (B.2), the Morlet wavelet takes the form

$$g_{\tau b}(t) = \frac{1}{\sqrt{b}} \exp\left[-\frac{1}{2}\left(\frac{t-\tau}{b}\right)^2\right] \exp\left[ic\frac{t-\tau}{b}\right]. \tag{B.4}$$

The frequency nature of the parameter c is clearly seen if we take $c = 2\pi$. Then Eq. (B.4) becomes

$$g_{\tau b}(t) = \frac{1}{\sqrt{b}} \exp\left[-\frac{1}{2}\left(\frac{t-\tau}{b}\right)^2\right] \exp\left[i\frac{2\pi}{b}(t-\tau)\right]. \tag{B.5}$$

Now the term $\exp\left[i\frac{2\pi}{b}(t-\tau)\right]$ represents the plane sinusoidal wave of frequency $2\pi/b$; thus the scale dilation b can be treated as a period.

B.3 Time and frequency resolution in wavelets

In wavelet analysis the signal is multiplied with a window (the wavelet). However, the window width has been changed as the transform is computed for every single spectral component. This is the most significant characteristic of the wavelet transform (Massel, 2001b). Changing the window width influences the resolution of the transform, which is illustrated in Fig. B.1. Every box corresponds to the value of the wavelet transform in the translation-scale plane. Although the widths and heights of the boxes change, their areas are constant

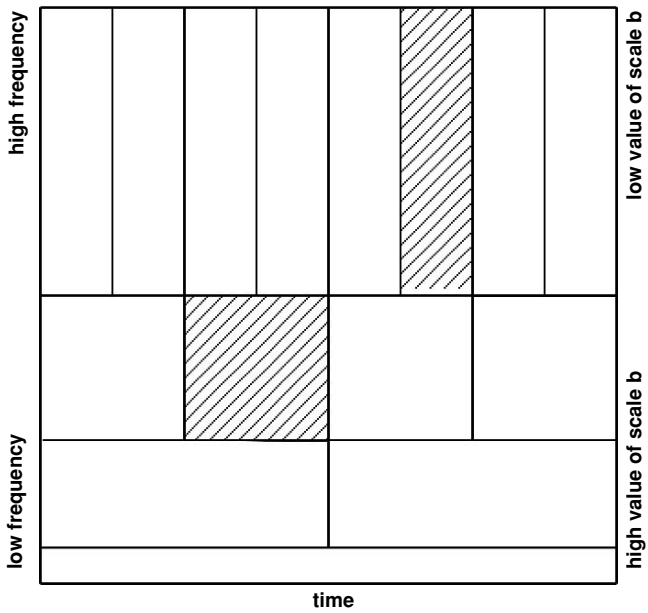

Figure B.1: Resolution scheme in the time–frequency plane (adapted from Massel, 2001b)

(see two hatched boxes in Fig. B.1). Each box represents the same portion of the time–frequency plane, but gives a different ratio of time and frequency. At low frequency (high value of scale b), the height of the box is small, but its width is large, i.e. the frequency resolution is better but time resolution is poor (more ambiguity regarding the value of the exact time). On the other hand, at higher frequencies (low scale b), the height of the boxes increases and the width of the boxes decreases. This corresponds to a very narrow window when the frequency resolution is getting poorer and the time resolution better.

The selection of the proper window width is related to what is known as the Heisenberg uncertainty principle (Van Name, 1960). This principle, originally applied to the momentum and location of moving particles in quantum mechanics, can also be applied to time–frequency information of a signal. We do not know what spectral components exist at what instances of time. Narrow windows give a good time resolution, but poor frequency resolution. Wide windows give good frequency resolution, but poor time resolution.

For a more detail discussion on wavelet transform application to oceanography, the reader should consult the paper by Massel (2001b). In the following section, we will examine some energy properties of wavelet transform only.

B.4 Energy properties of wavelets

First we should note that the wavelet transform conserves the total energy, i.e.

$$\int_{-\infty}^{\infty} |x(t)|^2 \, dt = C^{-1} \int_0^{\infty} \int_0^{\infty} \mid WT(\tau, b) \mid^2 b^{-2} d\tau db, \tag{B.6}$$

in which the coefficient C is given by

$$C^{-1} = \int_{-\infty}^{\infty} (\omega^{-1} \mid G(\omega) \mid^2) d\omega \tag{B.7}$$

and $G(\omega)$ is the Fourier transform of function $g(t)$. Therefore, so-called *time-scale energy density* becomes

$$E_1(\tau, b) = \frac{\mid WT(\tau, b) \mid^2}{b}. \tag{B.8}$$

By integrating Eq. (B.8) versus scale b, we obtain the *local energy density* (Farge, 1992):

$$E_2(\tau) = C^{-1} \int_0^{\infty} E_1(\tau, b) \frac{db}{b}. \tag{B.9}$$

On the other hand, the integration of Eq. (B.8) versus time τ, gives the *global wavelet energy spectrum* $E_3(b)$ as

$$E_3(b) = \int_0^{\infty} E_1(\tau, b) d\tau. \tag{B.10}$$

Torrence and Compo (1998) noted that the smoothed Fourier spectrum approaches the global wavelet spectrum when the amount of necessary smoothing decreases with increasing scale. Moreover, Percival (1995) showed that the global wavelet spectrum provides an unbiased and consistent estimation of the true power spectrum.

Finally, the *total energy* of the time series $x(t)$ becomes

$$E = C^{-1} \int_0^\infty E_3(b) \frac{db}{b}. \tag{B.11}$$

After substituting Eqs. (B.8) and (B.10) into Eq. (B.11) we get

$$E = C^{-1} \int_0^\infty \int_{-\infty}^\infty E_1(\tau, b) \frac{d\tau db}{b} = C^{-1} \int_0^\infty \int_{-\infty}^\infty \mid WT(\tau, b) \mid^2 \frac{d\tau db}{b^2}, \tag{B.12}$$

which confirms again the conservation of energy (B.6).

Appendix C

Hilbert transform and instantaneous frequency

C.1 Definition of Hilbert transform

The Hilbert transform of a real-valued time domain signal $\zeta(t)$ is another real-valued time domain signal $\xi(t)$ such that

$$\eta(t) = \zeta(t) + i\xi(t) \tag{C.1}$$

is an analytical signal, also in time domain. This is a substantial difference when comparing with the Fourier transform which transforms signal $\zeta(t)$ into a complex-valued frequency domain signal $Z(f)$. To determine the function $\xi(t)$, let us assume that a real-valued function $\zeta(t)$ extends over the range $-\infty < t < \infty$. Then its Hilbert transform becomes (Bendat and Piersol, 1986)

$$\xi(t) = H[\zeta(t)] = P \int_{-\infty}^{\infty} \frac{\zeta(t)}{\pi(t - t_1)}\, dt_1, \tag{C.2}$$

in which P denotes the Cauchy principle value. Equation (C.2) indicates that $\xi(t)$ is the convolution integral of $\zeta(t)$ and $\frac{1}{\pi t}$.

A very useful property of the Hilbert transform is its linearity, as we have

$$H[a_1\zeta_1(t) + a_2\zeta_2(t)] = a_1 H[\zeta 1(t)] + a_2 H\zeta_2(t)]. \tag{C.3}$$

Moreover, it can be shown that the Hilbert transform changes any cosine term to a sine term and any sine term to a minus cosine term. Taking into account that $\cos(\omega t - \frac{\pi}{2}) = \sin(\omega t)$ and $\sin(\omega t - \frac{\pi}{2}) = -\cos(\omega t)$, the Hilbert transform in the time domain corresponds to a phase lag of $(-\frac{\pi}{2})$ of all harmonic terms of the Fourier spectrum.

If the signal $\zeta(t)$ is represented in the form of a series, we can write

$$\zeta(t) = \sum_{n=0}^{\infty} [a_n \cos(n\omega t) + b_n \sin(n\omega t)] \tag{C.4}$$

and

$$\xi(t) = \sum_{n=0}^{\infty} [a_n \sin(n\omega t) - b_n \cos(n\omega t)]. \tag{C.5}$$

C.2 Digital computation of Hilbert transform

Let us assume that we have a record of N values ($n = 0, 1, 2, \ldots, N-1$) of function $\zeta(t)$ sampled at Δt. Thus the Fourier transform $Z(k\Delta f)$ of $\zeta(t)$ becomes

$$Z(k\Delta f) = \Delta t \sum_{n=0}^{N-1} \zeta(n\Delta t) \exp\left(-i\frac{2\pi kn}{N}\right), \tag{C.6}$$

where $\Delta f = \frac{1}{N\Delta t}$. The values of $Z(k\Delta f)$ are needed only from $k = 0$ up to $k = (N/2)$, where the Nyguist frequency occurs. Now using the values of $Z(k\Delta f)$ we can obtain the $\xi(n\Delta t)$ values as follows

$$\xi(n\Delta t) = 2\Delta f\, \Im\left[\sum_{k=0}^{N/2} Z(k\Delta f) \exp\left(i\frac{2\pi kn}{N}\right)\right], \tag{C.7}$$

in which $\Im$ denotes the imaginary part of the given value.

C.3 Stream function as a Hilbert transform of velocity potential

Let the complex velocity potential $w(z,t) = \phi(z,t) + i\psi(z,t)$ at any time instant be an analytic function in the lower half plane of z ($z = x + iy$), that is within the fluid region. Therefore, the contour integral in the lower half plane along any closed path should be equal to zero, i.e.

$$\oint_{-\infty}^{\infty} \frac{w(z_1)}{z - z_1}\, dz_1 = 0 \tag{C.8}$$

for every fixed point z lying outside the path of integration. Exploring the integral (C.8) we find that

$$\int_{-\infty}^{\infty} \frac{w(\eta)}{x - \eta} d\eta = -i\pi w(x) \quad \text{for} \quad y = 0. \tag{C.9}$$

The above integral has to converge for diminishing inner radius of the contour even if the integrand is singular at $x = \eta$. Separating the real and imaginary parts in Eq. (C.9) and using the Cauchy principal value notion we obtain

$$\psi(x) = \frac{1}{\pi} P \int_{-\infty}^{\infty} \frac{\phi(\xi)}{x - \xi} d\xi \quad \text{for} \quad y = 0 \tag{C.10}$$

and

$$\phi(x) = -\frac{1}{\pi} P \int_{-\infty}^{\infty} \frac{\psi(\xi)}{x-\xi} d\xi \quad \text{for} \quad y = 0. \tag{C.11}$$

Thus, the stream function $\psi(x)$ appears to be the Hilbert transform of the velocity potential at the sea surface.

C.4 Instantaneous frequency

Now we rewrite (C.1) in the form

$$\eta(t) = A(t) \exp(i\theta(t)), \tag{C.12}$$

in which $A(t)$ is called the envelope signal of $\zeta(t)$ and $\theta(t)$ is called the instantaneous phase signal of $\zeta(t)$. Thus, we have

$$A(t) = \sqrt{\zeta^2(t) + \xi^2(t)} \tag{C.13}$$

and

$$\theta(t) = \arctan\left(\frac{\xi(t)}{\zeta(t)}\right) = \omega_0 t. \tag{C.14}$$

Representation (C.12) provides the best local fit of an amplitude and phase for varying trigonometric function of $\zeta(t)$. The "instantaneous frequency" ω is now given by

$$\omega = \frac{d\theta(t)}{dt}. \tag{C.15}$$

In contrast to the instantaneous envelope of the signal, the notion of the instantaneous frequency is somewhat controversial. When applying Fourier analysis, we need at least one full oscillation to define the local frequency value. Therefore a process shorter than a full wave cannot be considered in signal analysis. To overcome this difficulty, Huang et al. (1998) provided a comprehensive discussion on the nature of the instantaneous frequency ω. They found that at any given time, there is only one frequency value which can only represent one component. To satisfy this requirement, some limitations on the data are necessary. Probably the most obvious restriction is the assumption that the process under consideration is of narrow band, when the bandwidth parameter ν (see Eq. 3.7) is much smaller than one, and the expected numbers of extrema and zero crossings have to be equal. However, the bandwidth definition given by Eq. (3.7) has a global sense and it lacks precision. This means that filtering the data within the bandwidth requirement does not necessarily guarantee a meaningful instantaneous frequency. Sometimes non-physical negative frequencies can appear (see for example Melville (1983)). In order to avoid such difficulties Huang et al. (1998) suggested applying the Gabor (1946)

statement that for any function to have a meaningful instantaneous frequency, the real part of its Fourier transform has to have only positive frequency. Subsequently Huang et al. modified this requirement by imposing the restriction that the function should be symmetric with respect to the local zero mean, and have the same numbers of zero crossings and extrema. To define the local zero mean, the local mean of the envelopes determined by the local symmetry is used. The first restriction is equivalent to the traditional narrow band requirements for a stationary Gaussian process. However, the second requirement in fact modifies the classical global requirement to a local one in such a way that the instantaneous frequency will not have the unwanted fluctuations induced by asymmetric wave forms.

Huang et al. (1998) proposed the so-called intrinsic mode function (IMF) satisfying both above conditions. In fact when we assume that $\eta(t)$ is an intrinsic mode function (IMF) and perform a Fourier transform on $\eta(t)$, we obtain

$$F[\eta(t)] = \int_{-\infty}^{\infty} A(t)e^{i\theta(t)}e^{-i\omega t}dt = \int_{-\infty}^{\infty} A(t)e^{i(\theta(t)-\omega t)}dt. \tag{C.16}$$

By the method of stationary phase it can be found that the maximum contribution to $F[\eta(t)]$ is given by the frequency satisfying the condition

$$\frac{d}{dt}[\theta(t) - \omega t] = 0, \tag{C.17}$$

and frequency ω becomes

$$\omega = \frac{d\theta(t)}{dt}, \tag{C.18}$$

which is in agreement with Eq. (C.15)

It should be pointed out that we do not need a whole oscillatory period to define the instantaneous frequency value. In fact it follows from Eq. (C.18) that frequency ω can be defined for every point with the value changing from point to point. To use the above definition of instantaneous frequency, we have to transfer an arbitrary data set into IMF components from which an instantaneous frequency value can be obtained for each IMF component. The method of reduction of the data into the IMFs is called empirical mode decomposition, and it is described by Huang et al. (1998, 1999) in detail. Some application of the empirical mode decomposition method to the surface waves transformation in the surf zone was recently published by Veltcheva (2002).

Appendix D

Relationships between spectral moments and sea state parameters

D.1 Spectral moments as a function of non-dimensional wind fetch

Many basic processes of wave breaking and aerosol flux generation are expressed in terms of spectral moments. However, for practical use it is more convenient to deal with observed or directly measured sea state parameters. Thus in this appendix we develop the fundamental relationships linking moments with such parameters as significant wave height H_{s}, peak frequency ω_{p}, wind speed V_{10}, and wind fetch X.

In general, the moment m_{n} of the frequency spectrum becomes

$$m_{\mathrm{n}} = \int_{\omega_{\mathrm{l}}}^{\omega_{\mathrm{h}}} \omega^n \, S\left(\omega\right) d\omega = \omega_{\mathrm{p}}^n \int_{\hat{\omega}_{\mathrm{l}}}^{\hat{\omega}_{\mathrm{h}}} \hat{\omega}^n S\left(\hat{\omega}\right) d\hat{\omega}, \qquad \hat{\omega} = \frac{\omega}{\omega_{\mathrm{p}}}. \tag{D.1}$$

To express the formulae (D.1) in terms of spectral densities, we assume that surface waves are characterized by the Pierson–Moskowitz (3.17) or JONSWAP (3.19) spectra. Theoretically, the lower and upper limits of integration in (D.1) should be equal to 0 and ∞, respectively. However, the form of the Pierson–Moskowitz and JONSWAP spectra, based on experimental data, indicates that negligible energy is contained in the frequency band $0 < \hat{\omega} < 0.5$; thus we set $\hat{\omega}_{\mathrm{l}} = 0.5$. The upper limit $\hat{\omega}_{\mathrm{h}}$, which is not necessarily equal to ∞, requires more attention as its influence on spectral moments, especially for higher moments, is substantial. After substitution of (3.19) into (D.1) we obtain the m_{n} moment as

$$m_{\mathrm{n}} = \beta g^2 \omega_{\mathrm{p}}^{n-4} \int_{\hat{\omega}_{\mathrm{l}}}^{\hat{\omega}_{\mathrm{h}}} \hat{\omega}^{n-5} \exp\left(-\frac{5}{4}\hat{\omega}^{-4}\right) \gamma^r d\hat{\omega}, \tag{D.2}$$

Let us assume for a moment that $\hat{\omega}_\mathrm{l} = 0$, $\hat{\omega}_\mathrm{h} = \infty$, and $\gamma = 1$ (the Pierson–Moskowitz spectrum). Hence, the moment m_n becomes (Massel, 1998)

$$\begin{aligned} m_\mathrm{n} &= \beta g^2 \omega_\mathrm{p}^{n-4} \times \int_0^\infty \hat{\omega}^{n-5} \exp\left(-\frac{5}{4}\hat{\omega}^{-4}\right) d\hat{\omega} \\ &= \frac{\beta g^2 \omega_\mathrm{p}^{n-4}}{4} \times \left(\frac{5}{4}\right)^{\frac{n-4}{4}} \times \Gamma\left(\frac{4-n}{4}\right), \end{aligned} \tag{D.3}$$

in which $\Gamma(x)$ is a gamma function (Abramowitz and Stegun, 1975). Equation (D.3) indicates that the fourth moment m_4 becomes infinite as $\Gamma(0) = \infty$. The only way to calculate this moment for practical applications is to impose some threshold frequency $\hat{\omega}_\mathrm{h} \neq \infty$. Taking into account the peak frequency values observed in practice, it has been assumed that $\hat{\omega}_\mathrm{h} = 6$. Waves with frequency $\omega = 6\,\omega_\mathrm{p}$ can still be considered gravity waves, as the viscous effects are still negligible.

Using (D.2), the moments m_n from the spectral density functions (3.17) and (3.19) take the form

$$m_\mathrm{n} = a_\mathrm{n}(\gamma,\, \hat{\omega}_\mathrm{l},\, \hat{\omega}_\mathrm{h}) \beta g^2 \omega_\mathrm{p}^{n-4}, \tag{D.4}$$

in which the coefficients a_n are collected in Table D.1 for three different values of the peak enhancement factor $\gamma = 1$, 3.3 and 7, $\hat{\omega}_\mathrm{l} = 0.5$ and $\hat{\omega}_\mathrm{h} = 6$. It should be noted that the constants a_n for $n = 0$, 1, 2, 3 and for $\gamma = 1.0$ were calculated by the exact formula (D.3), while other constants were obtained through numerical integration in (D.2).

The function β is a measure of the energy content in the spectrum. From the JONSWAP experiment, this function, known as the Phillips constant, depends on the non-dimensional wind fetch $\left(\frac{gX}{V_{10}^2}\right)$ given in (3.22). After substituting this relationship into (D.4) we have

$$m_\mathrm{n} = 0.076 a_\mathrm{n}(\gamma,\, \hat{\omega}_\mathrm{l},\, \hat{\omega}_\mathrm{h}) g^2\, \omega_\mathrm{p}^{n-4} \left(\frac{gX}{V_{10}^2}\right)^{-0.22}. \tag{D.5}$$

Table D.1: Constants a_n for spectral moments m_n

a_n	Peak enhancement factor γ		
	1.0	3.3	7.0
a_0	0.2000	0.3048	0.4448
a_1	0.2592	0.3640	0.5056
a_2	0.3963	0.4908	0.6345
a_3	0.8572	0.8014	0.9476
a_4	1.5919	1.7057	1.8551

Moreover, if we assume the peak frequency ω_p following from the same JONSWAP experiment (see (3.23)), relationship (D.5) takes the form

$$m_\mathrm{n} = 0.076 a_\mathrm{n} \left(7\pi \frac{g}{V_{10}}\right)^{n-4} g^2 \left(\frac{gX}{V_{10}^2}\right)^{1.1-0.33\mathrm{n}}. \tag{D.6}$$

It should be noted that for the moment m_4, the above expression simplifies considerably

$$m_4 = 0.076 a_4 \, g^2 \left(\frac{gX}{V_{10}^2}\right)^{-0.22} \tag{D.7}$$

showing that moment m_4 does not depend on the wind speed V_{10}, but only on non-dimensional fetch $\left(\frac{gX}{V_{10}^2}\right)$.

D.2 Spectral moments as a function of significant wave height and peak frequency

In laboratory experiments, the non-dimensional fetch is not relevant. More suitable dependence is that on the significant wave height H_s and peak frequency ω_p. From (3.157) we have

$$H_\mathrm{s}^2 = 16 \, m_0. \tag{D.8}$$

After substituting (D.8) into (D.4) we obtain

$$\beta = \frac{H_\mathrm{s}^2 \, \omega_\mathrm{p}^4}{16 a_0 \, g^2}. \tag{D.9}$$

Therefore, a general expression for the moments m_n takes the form

$$m_\mathrm{n} = \frac{a_\mathrm{n}}{16 a_0} H_\mathrm{s}^2 \, \omega_\mathrm{p}^\mathrm{n}. \tag{D.10}$$

References

Abramowitz, M. and Stegun, I. A. (1975). *Handbook of Mathematical Functions*. Dover Publ., New York, 1045 pp.

Afeti, G. M. and Resch, F. J. (1990). Distribution of the liquid aerosol produced from bursting bubbles in sea and distilled water. *Tellus*, **42**B: 378–384.

Andreas, E. L. (1992). Sea spray and turbulent air-sea heat fluxes. *J. Geophys. Res.*, **97**(C7): 11429–11441.

Andreas, E. L. (1998). A new sea spray generation function for wind speeds up to 32 m s^{-1}. *J. Phys. Oceanogr.*, **28**(11): 2175–2184.

Andreas, E. L., Edson, J. B., Monahan, E. C., Ronault, M. P. and Smith, S. D. (1995). The spray contribution to net evaporation from the sea: a review of recent progress. *Boundary-Layer Meteorol.*, **72**: 3–52.

Anguelova, M. D., Barber, R. P., Jr. and Wu, J. (1999). Spume drops produced by the wind tearing of wave crests. *J. Physical Oceanogr.*, **29**(6): 1156–1165.

Anguelova, M. D., Bettenhausen, M.H., Germain, K. St., Gaiser, P. W. and Bevilacqua, R. M. (2005). Improved satellite retrievals of whitecaps coverage and sea-salt aerosols. Abstracts of the European Aerosol Conference, Ghent, Belgium, 193 p.

Banner, M. L. and Grimshaw, R. H. J. (Eds) (1992). *Breaking Waves*. In: Proceedings of IUTAM Symposium. Sydney, Springer–Verlag, 387 pp.

Banner, M. L. and Peregrine, D. H. (1993). Wave breaking in deep water. *Annu. Rev. Fluid Mech.*, **25**: 373–397.

Banner, M. L. and Tian, X. (1998). On the determination of the onset of breaking for modulating surface gravity water waves. *J. Fluid Mech.*, **367**: 107–137.

Banner, M. L., Babanin, A. V. and Young, I. R. (2000). Breaking probability for dominant waves on the sea surface. *J. Phys. Oceanogr.*, **30**: 3145–3160.

Banner, M. L, Gemmrich, J. R. and Farmer, D. M. (2002). Multiscale measurements of ocean wave breaking probability. *J. Phys. Oceanogr.*, **32**: 3364–3375.

Banner, M. L. and Song, J. B. (2002). On determining the onset and strength of breaking for deep water waves. Part II: Influence of wind forcing and surface shear. *J. Phys. Oceanogr.*, **32**: 2559–2570.

Batchelor, G. K. (1967). *An Introduction to Fluid Dynamics*. Cambridge University Press, Cambridge, 615 pp.

Benjamin, T. B. (1967). Instability of periodic wavetrains in nonlinear dispersive systems. *Proc. R. Soc.* Lond., **A299**: 59–67.

Benjamin, T. B. and Feir, J. E. (1967). The disintegration of wave trains in deep water. Part 1. Theory. *J. Fluid Mech.*, **27**: 417–430.

Bendat, J. S. and Piersol, A. G. (1986). *Random Data. Analysis and Measurement Procedures*. John Wiley and Sons, New York, 566 pp.

Biesel, F. (1982). Second order theory of manometer wave measurement. *Proc. Coastal Eng. Conf.*, Cape Town, **1**: 129–135.

Blanchard, D. C. (1954). Bursting of bubbles at an air-water interface. *Nature*, **173**, 104.

Blanchard, D. C. (1963). The electrification of the atmosphere by particles from bubbles in the sea. In: Sears, M. (Ed). *Progress in Oceanography*. Pergamon Press, pp. 73–202.

Blanchard, D. C. (1983). The production, distribution and backterial enrichment of the sea salt aerosol. In: Liss, P. S. and Slinn, W. G. N. (Eds). *The Air-Sea Exchange of Gases and Particles*. Reidel Publ. Comp., Dordrecht, pp. 407–454.

Blanchard, D. C. (1989). The size and height which jet drops are ejected from bursting bubbles in seawater. *J. Geophys. Res.*, **94**(C8): 10999–11002.

Blanchard, D. C. and Syzdek, L. D. (1988). Film drop production as a function of bubble size. *J. Geophys. Res.*, **93**: 3649–3654.

Boccotti, P. (1981). On the highest waves in a stationary Gaussian process. *Atti. Acc. Lig.*, **38**: 45–73.

Boccotti, P. (1989). On mechanics of irregular gravity waves. *Atti. Acc. Naz. Lincei Mem.*, **19**: 109–170.

Bonmarin, P. (1989). Geometric properties of deep water breaking waves. *J. Fluid Mech.*, **209**: 405–433.

Bonmarin, P. and Kjeldsen, S. P. (2001). Some geometric and kinematic properties of breaking waves. In: Olagnon, M. and Athanassoulis, G. A. (Eds). *Rogue Waves 2000*. Proceedings Workshop, Brest, Editions Ifremer, pp. 169–180.

Bortkovskii, R. S. (1987). *Air-Sea Exchange of Heat and Moisture During Storms*. D. Reidel Publ. Comp., Dordrecht, 194 pp.

Bortkovskii, R. S. (2002). Atmosphere-ocean gas exchange due to bubbles generated by wind wave breaking. In: Donelan, M. A., Drennan, W. M., Salzman, E. S. and Wanninkhof, R. (Eds). *Gas Transfer at Water Surfaces*, Geophysical Monographs **127**. American Geophysical Union, Washington, DC, pp. 261–264.

Bretherton, F. P. and Garrett, C. J. R. (1969). Wavetrains in homogeneous moving media. *Proc. R. Soc.*, **A302**: 529–554.

Broman, B., Hammarklint, T., Rannat, K., Soomere, T. and Valdmann, A. (2006). Trends and extremes of wave fields in the north-eastern part of the Baltic Proper. *Oceanologia*, **48**(8): 165–184.

Cardone, V. J. (1970). Specification of the wind distribution in the marine boundary layer for wave forecasting. New York University, New York, 131 pp.

Carey, W. M., Fitzgerald, J. W., Monahan, E. C. and Wang, Q. (1993). Measurements of sound produced by a tapping through with fresh and salt water. *J. Acoust. Soc. Am.*, **93**: 3178–3192.

Cartmill, J. W. and Su, M. Y. (1993). Bubble size distribution under salttwater and freshwater breaking waves. Dynamics of Atmospheres and Ocean, **20**: 25–31.

Cartwright, D. E. and Longuet–Higgins, M. S. (1956). The statistical distribution of the maxima of a random function. *Proc. R. Soc.*, **A237**: 212–232.

Caulliez, G. (2002). Statistics of geometric properties of breaking wind waves observed in laboratory. In: Donelan, M. A., Drennan, W. M., Salzman, E. S. and Wanninkhof, R. (Eds). *Gas Transfer at Water Surfaces*, Geophysical Monographs **127**. American Geophysical Union, Washington, DC, pp. 31–37.

Chappelear, J. E. (1961). Direct numerical calculation of waves properties. *J. Geophys. Res.*, **66**: 501–508.

Charlson, R. J., Lovelock, J. E., Andreae, M. O. and Warren, S. G. (1987). Oceanic phytoplankton, atmospheric sulphur, cloud albedo and climate. *Nature*, **320**: 655–661.

Chen, G. and Belcher, S. E. (2000). Effects of long waves on wind-generated waves. *J. Phys. Oceanogr.*, **30**: 2246–2256.

Chomka, M. and Petelski, T. (1997). Modelling the sea aerosol emission in the coastal zone. *Oceanologia*, **39**: 211–225.

Cipriano, R. J., Blanchard, D. C. (1981). Bubble and aerosol spectra produced by a laboratory "breaking wave". *J. Geophys. Res.*, **86**(C9): 8085–8092.

Cipriano, R. J., Blanchard, D. C., Hogan, A. W. and Lala, G. G. (1983). On the production of Aitken nuclei from breaking waves and their role in the atmosphere. *J. Atmosph. Sci.*, **40**: 469–479.

Cointe, R. and Boudet, L. (1991). Nonlinear and breaking waves in biochromatic wave-trains: experiments and numerical simulations. Proceedings of 1st International Offshore and Polar Engineering Conference, pp. 517–522.

Cokelet, E. D. (1977). Steep gravity waves in water of arbitrary uniform depth. *Phil. Trans. R. Soc. Lond.*, **A286**: 183–230.

Combes, J. M., Grossman, A., Ychamitchian, P. (Eds.). (1989). *Wavelets. The Time-Frequency Methods and Phase Space.* Springer-Verlag, Berlin, Heidelberg.

Csanady, G. T. (1990). The role of breaking wavelets in air-sea transfer. *J. Geophys. Res.*, **95**: 749–759.

Davidan, I. N., Lopatouchin, L. I. and Rozhkov, V. A. (1978). *Wind Waves as a Probabilistic Hydrodynamic Process.* Gidrometeoizdat, Leningrad, 287 pp. (in Russian).

Davidan, I. N., Lopatouchin, L. I. and Rozhkov, V. A. (1985). *Wind Waves in the World Ocean.* Gidrometeoizdat, Leningrad, 256 pp (in Russian).

Dawson, T. H., Kriebel, D. L. and Wallendorf, L. A. (1993). Breaking waves in laboratory-generated JONSWAP seas. *Appl. Ocean Res.*, **15**: 85–93.

Deane, G. B. and Stokes, M. D. (2002). Scale dependence of bubble creation mechanisms in breaking waves. *Nature*, **418**: 839–844.

Defant, F. (1972). Klima und Wetter der Ostsee. Kieler Meeresforschungen, Bd 28, H. 1, Kiel.

Dekker, H. and de Leeuw, G. (1993). Bubble excitation of surface waves and aerosol droplet production: a simple dynamical model. *J. Geophys. Res.*, **98**(C6): 10223–10232.

Dera, J. (1992). *Marine Physics.* Elsevier–Polish Scientific Publ., Amsterdam, Warszawa, 516 pp.

Ding, L. and Farmer, D. M. (1994). Observations of breaking surface wave statistics. *J. Phys. Oceanogr.*, **24**: 1368–1387.

Dold, J. W. and Peregrine, D. H. (1986). Water-wave modulation. *Proc. 20th Int. Conf. Coastal Eng., Taipei*, **1**: 163–175.

Dommermuth, D. G., Yue, D. K. P., Lin, W. M., Rapp, R. J., Chan, E. S. and Melville, W. K. (1988). Deep water plunging breakers: a comparison between potential theory and experiments. *J. Fluid Mech.*, **189**: 423–442.

Donelan, M. A. (1987). The effect of swell on the growth of wind waves. *Johns Hopkins APL Tech. Dig.*, **8**: 18–23.

Donelan, M. A., Hamilton, J. and Hui, W. H. (1985). Directional spectra of wind-generated waves. *Phil. Trans. R. Soc. Lond.*, **A315**: 509–562.

Donelan, M. A., Drennan, W. M., Salzman, E. S. and Wanninkhof, R. (Eds). (2002). *Gas Transfer at Water Surface*, Geophysical Monograph **127**. American Geophysical Union, Washington DC.

Donelan, M. A. and Wannikhof, R. (2002). Gas transfer at water surface – concepts and issues. In: Donelan, M. A., Drennan, W. M., Salzman, E. S. and Wanninkhof, R. (Eds). *Gas Transfer at Water Surfaces*, Geophysical Monographs **127**. American Geophysical Union, Washington, DC, pp. 6–10.

Druet, Cz. (2000). *Sea Dynamics*. Gdańsk University Publ., 288 pp.

Duncan, J. H. (1981). An investigation of breaking waves produced by a towed hydrofoil. *Proc. R. Soc. Lond.*, **A377**: 331–348.

Duncan, J. H. (1983). The breaking and non-breaking wave resistance of a two-dimensional hydrofoil. *J. Fluid Mech.*, **126**: 507–520.

Duncan, J. H., Philomin, V., Behres, M. and Kimmel, J. (1994a). The formation of spilling breaking water waves. *Phys. Fluids*, **6**: 2558–2560.

Duncan, J. H., Philomin, V., Qiao, H. and Kimmel, J. (1994b). The formation of a spilling breakers. *Phys. Fluids*, **6**: S2.

Dysthe, K. B. (1979). Note on a modification to the nonlinear Schrödinger equation for application to deep water waves. *Proc. R. Soc. Lond.*, **A364**: 105–114.

Fairall, C. W. and Larsen, S. E. (1984). Dry deposition, surface production and dynamics of aerosols in the marine boundary layer. *Atmos. Environ.*, **18**: 69–77.

Farge, M. (1992). Wavelet transform and their applications to turbulence. *Annual Rev. Fluid Mech.*, **24**: 395–457.

Farmer, D. M. and Vagle, S. (1988). On the determination of breaking surface wave distribution. *J. Geophys. Res.*, **93**(C4): 3591–3600.

Farmer, D. M. and Ding L. (1992). Accoustical measurement of breaking surface waves. In: Banner, M. L. and Grimshaw, R. H. L. (Eds). *Breaking Waves*. Proceedings of IUTAM Symposium, Sydney, 109–118.

Felizardo, F. C. and Melville, W. K. (1995). Correlations between ambient noise and the ocean surface wave field. *J. Phys. Oceanogr.*, **25**: 513–532.

Fenton, J. D. (1985). A fifth-order Stokes theory for steady waves. *J. Waterway, Port, Coastal Ocean Eng.*, **111**: 216–234.

Fitzgerald, J. W. (1975). Approximation formulas for the equilibrium size of an aerosol particle as a function of its dry size and composition and the ambient relative humidity. J. Appl. Meteorol., **14**: 1044–1049.

Gabor, D. (1946). Theory of communication. *Proc. IEE*, **93**: 429–457.

Gayer, G., Günther, H. and Winkel, N. (1995). Wave climatology and extreme value analysis for the Baltic Sea area off the Warnemünde harbour entrance. *Dt. Hydrogr. Z.*, **47**: 109–130.

Geernaert, G. L. (1990). Bulk parameterizations for the wind stress and heat fluxes. In: Geernaert, G. L. and Plant, W. J. (Eds). *Surface Waves and Fluxes - Current Theory*. Kluwer Academic Publ., Dordrecht, pp. 91–172.

Gemmrich, J. R. and Farmer, D. M. (1999). Observations of the scale and occurence of breaking surface waves. *J. Phys. Oceanogr.*, **29**: 2595–2606.

Glazman, R. E. (1986). Statistical characteristics of sea surface geometry for a wave field discontinuous in the mean square. *J. Geophys. Res.*, **91**(C5): 6629–6641.

Goda, Y. (1985). *Random Sea and Design of Maritime Structures*. University Tokyo Press, Tokyo, 323 pp.

Gradshteyn, I. S. and Ryzhik, I. M. (1980). *Table of Integrals, Series and Products*. Academic Press, New York, 1160 pp.

Graham, A., Woolf, D. K. and Hall, A. J. (2004a). Aeration due to breaking waves. Part I: Bubble populations. *J. Phys. Oceanogr.*, **34**: 989–1007.

Graham, A., Woolf, D. K. and Hall, A. J. (2004b). Aeration due to breaking waves. Part II: Fluxes. *J. Phys. Oceanogr.*, **34**: 1008–1018.

Greenhow, M. (1983). Free-surface flows related to breaking waves. *J. Fluid Mech.*, **134**: 259–275.

Griffin, O. M., Peltzer, R. D., Wang, H. T. and Schultz, W. W. (1996). Kinematic and dynamic evolution of deep water breaking waves. *J. Geophys. Res.*, **101**(C): 16515–16531.

Hanson, J. L. and Phillips, O. M. (1999). Wind sea growth and dissipation in the open ocean. *J. Phys. Oceanogr.*, **29**: 1633–1647.

Hasselmann, K. (1974). On the spectral dissipation of ocean waves due to whitecapping. *Boundary Layer Meteor.*, **6**: 107–127.

Hasselmann, K., Barnett, T. P., Bouws, E., Carlson, H., Cartwright, D.E., Enke, K., Ewing, J. A., Gienapp, H., Hasselmann, D. E., Kruseman, P., Meerburg, A., Müller, P., Olbers, D. J., Richter, K., Sell, W. and Walden, H. (1973). Measurements of wind-wave growth and swell decay during the Joint North Sea Wave Project (JONSWAP), *Deutsches Hydr. Zeit.*, **A12**: 1–95.

Hasselmann, D. E., Dunckel, M. and Ewing, J. A. (1980). Directional wave spectra observed during JONSWAP 1973. *J. Phys. Oceanogr.*, **10**: 1264–1280.

Heintzenberg, J., Cover, D. C. and van Dingenen, R. (2000). Size distribution and chemical composition of marine aerosols: a compilation and review. *Tellus*, **52**B: 1104–1122.

Holthuijsen, L. H. and Herbers, T. H. C. (1986). Statistics of waves observed as whitecaps in open sea. *J. Phys. Oceanogr.* **16**: 290–297.

Hoppel, W. A., Frick, G. M. and Fitzgerald, J. W. (2002). Surface souces function for sea-salt aerosol and aerosol dry deposition to the ocean surface. *J. Geophys. Res.*, **107**(D19),4382.

Huang, N. E. (1981). An estimate of the influence of breaking waves on the dynamics of the upper ocean. In: Phillips, O. M. and Hasselmann, K. (Eds). *Wave Dynamics and Radio Probing of the Ocean Surface*. Plenum, New York, pp. 295–313.

Huang, N. E., Long, S. R., Tung, C. C., Yuan, Y. and Bliven, L. F. (1983). A non-Gaussian statistical model for surface elevation of nonlinear random wave fields. *J. Geophys. Res.*, **88**: 7597–7606.

Huang, N. E., Long, S. R., Tung, C. C., Donelan, M. A., Yuan, Y. and Lai, R., (1992). The local properties of ocean waves by the phase-time method. *Res. Lett.*, **19**(7): 685–688.

Huang, N. E., Shen, Z., Long, S. R., Wu, M. C., Shih, H. H., Zeng, Q., Yen, N. C., Tung, C. C. and Liu, H. H. (1998). The empirical mode decomposition and the Hilbert spectrum for nonlinear and non-stationary time series analysis. *Proc. R. Soc. Lond.*, **A454**: 903–995.

Huang, N. E., Shen, Z. and Long, S. R. (1999). A new view of nonlinear water waves: The Hilbert Spectrum. *Annu. Rev. Fluid Mech.*, **31**: 417–457.

Hudspeth, R. T. and Chen, M. C. (1979). Digital simulation of nonlinear random waves. *J. Waterway, Port, Coastal and Ocen Div.*, **105**: 67–85.

Hwang, P. A., Xu, D. and Wu, J. (1989). Breaking of wind-generated waves: measurements and characteristics. *Fluid Mech.*, **202**: 177–200.

Hwang, P. A. and Wang, D. W. (2002). Directional distributions and mean square slopes of surface waves. In: Donelan, M. A., Drennan, W. M., Salzman, E. S. and Wanninkhof, R. (Eds). *Gas Transfer at Water Surfaces*, Geophysical Monographs **127**. American Geophysical Union, Washington, DC, pp. 65–70.

IPCC. (2004). *Climate Change 2001: The Scientific Basis*. Executive summary. Third assessment report.

Jessup, A. T., Zappa, C. J., Loewen, M. R., Hesany, V. (1997). Infrared remote sensing of breaking waves. *Nature*, **385**: 52–55.

Junge, C. (1953). Die Rolle der Aerosole und der gasformigen Beimengungen der Luft im Spurenstoffhaushalt der Troposphare. *Tellus*, **5**: 1–26.

Kahma, K., Rautanen, E. and Saarinen, J. (1983). Wave data from the Southern Bothnian Sea, 1973–1975, 1981. Finn. Inst. Mar. Res., Inter. Rep. No. 1/1983 (in Finnish with English summary).

Kaiser, G. (1994). A Friendly Guide to Wavelets. Birkhauser, Boston.

Katsaros, K. B. and Atakturk, S. S. (1992). Dependence of wave breaking statistics on wind stress and wave development. In: Banner, M. L. and Grimshaw, R. H. J. (Eds). *Breaking Waves*, Proc. IUTAM Symposium, Sydney, 119–132.

Kawai, S., Okuda, K. and Toba, Y. (1977). Field data support of three-seconds power law and $gu_*\sigma^{-4}$ spectral form for growing wind waves. *J. Oceanogr. Soc. Jp.*, **33**: 137–150.

Keeling, R. F. (1993). On the role of large bubbles in air-sea gas exchange and supersaturation in the ocean. *J. Mar. Res.*, **51**: 237–271.

Kerman, B. R. (1986). Distribution of bubbles near the ocean surface. *Atmosphere-Ocean*, **24**: 169–188.

Kerman, B. R. and Szeto, K. (1994). Fractal properties of whitecaps. *Atmosphere-Ocean*, **32**: 531–551.

Kharif, C. and Pelinovsky, E. (2003). Physical mechanisms of the rogue wave phenomenon. *Eur. J. Mech.* B/Fluid, **22**: 603–634.

Kientzler, C. F., Arons, A. B., Blanchard, D. C and Woodcock, A. H. (1954). Photographic investigation of the projection of droplets by bubbles bursting at a water surface. *Tellus*, **6**: 1–7.

Kitaigorodskii, S. A. (1962). Application of similarity methods to the analysis of wind waves. *Izv. Akad. Nauk, Ser. Geophys.*, **1**: 105–117 (in Russian).

Kitaigorodskii, A. S. (1983). On the theory of the equilibrium range in the spectrum of wind-generated gravity waves. *J. Phys. Oceanogr.*, **13**: 816–827.

Kitaigorodskii, A. S. (1992). The dissipation subrange of wind-wave spectra. In: Banner, M. L. and Grimshaw, R. (Eds). *Breaking Waves*, Proc. IUTAM Symposium, Sydney, pp. 200–206.

Kjeldsen, S. P. (1990). Breaking waves. In: Torum, A. and Gudmestad, O. T. (Eds). *Water Wave Kinematics*. Kluwer Academic Publ., Dordrecht, pp. 453–473.

Knudsen, V. O., Alford, R. S. and Emling, J. W. (1948). Underwater ambient noise. *J. Mar. Res.*, **7**: 410–429.

Koch, M. K., Vossnacke, A., Starflinger, J., Schutz W. and Unger, H. (2000). Radionuclide re-entrainment at bubbling water pool surfaces. *J. Aerosol Sci.* **31**(9): 1015-1028.

Koepke, P. (1984). Effective reflectance of oceanic whitecaps. *Appl. Optics*, **23**(11): 1816–1824.

Koepke, P. (1986). Remote sensingsignatures of whitecaps. In: Monahan, E. C. and MacNiocaill, G., (Eds). *Oceanic Whitecaps and Their Role in Air-Sea Exchange Processes*. D. Reidel Publ. Comp., Dordrecht, pp. 251–260.

Koga, M. (1982). Direct production of droplets from breaking wind-waves and its observation by a multi-coloured overlapping exposure photographic technique. *Tellus*, **33**: 552–563.

Kolaini, A. R. and Crum, L. A. (1994). Observations of underwater sound from laboratory breaking waves and implications concerning ambient noise in the ocean. *J. Acoust. Soc. Am.*, **96**: 1755–1765.

Komen, G. J., Hasselmann, S. and Hasselmann, K. (1984). On the existence of a fully developed wind-sea spectrum. *J. Phys. Oceanogr.*, **14**: 1271–1285.

Komen, G. J., Cavaleri, L., Donelan, M., Hasselmann, K., Hasselmann, S. and Janssen, P.A.E.M. (1994). *Dynamics and Modelling of Ocean Waves*. Cambridge University Press, Cambridge, 532 pp.

Krasitskii, V. P. (1974). On the wind waves spectrum transformation due to refraction. *Izv. Akad. Nauk SSSR, Ser. Fiz. Atm. i Okeana*, **10**: 72–82 (in Russian).

Krasitskii, V. P. (1994). On reduced equations in the Hamilton theory of weakly nonlinear surface waves. *J. Fluid Mech.*, **272**: 1–20.

Kraus, E. B. and Businger, J. A. (1994). *Atmosphere-Ocean Interaction*. Oxford University Press, Oxford, 362 pp.

Kriebel, D. L. and Dawson, T. H. (1993). Distribution of crest amplitudes in severe seas with breaking. *J. Offshore Mech. Arct. Eng.*, **115**: 9–15.

Krylov, Y. M., Strekalov, S. S. and Tsyplukhin, V. F. (1966). Study on directional spectrum of wind waves. *Izv. Akad. Nauk SSSR, Ser. Fiz. Atm. i Okeana*, **7**: 729–739 (in Russian).

Krylov, Y. M., Strekalov, S. S. and Tsyplukhin, W. F. (1976). *Wind Waves and their Interaction with Structures*. Gidrometeoizdat, Leningrad, 255 pp. (in Russian).

Kway, J. H. L., Loh, Y. and Chan, E. S. (1998). Laboratory study of deep-water breaking waves. *Ocean Eng.*, **25**(8): 657–676.

Lader, P. F., Grytoyr, G., Myrhaug D. and Pettersen, B. (1998). Breaking wave geometry with emphasis on steepness and curvature. In: Proceedings of Conference on Ocean Wave Kinematics, Dynamics, and Loads on Structures, Houston, pp. 281–288.

Lake, B. M., Yuen, H.C., Rungaldier, H. and Ferguson, W. E. (1977). Nonlinear deep-water waves: theory and experiment. Part 2. Evolution of a continuous wave train. *J. Fluid Mech.*, **83**: 49–74.

Lamarre, E. and Melville, W. K. (1991). Air entrainment and dissipation in breaking waves. *Nature*, **350**: 469–472.

Large, W. G. and Pond, S. (1981). Open ocean momentum flux measurements in moderate to strong winds. *J. Phys. Oceanogr.*, **11**: 324–336.

de Leeuw, G. (1986). Vertical profiles of giant particles close above the sea surface. *Tellus*, **38B**: 51–61.

de Leeuw, G. and Cohen, L.H. (2002). Bubble size distributions on the North Atlantic and North Sea. In: Donelan, M. A., Drennan, W. M., Saltzman, E. S. and Wanninkhof, R. (Eds). *Gas Transfer at Water Surfaces*, Geophysical Monographs **127**. pp. 271–277.

Leifer, I. and de Leeuw, G. (2002). Bubble measurements in breaking-wave generated bubble plumes during the LUMINY wind-wave experiment. In: Donelan, M. A., Drennan, W. M., Saltzman, E. S. and Wanninkhof, R. (Eds). *Gas Transfer at Water Surfaces*, Geophysical Monographs **127**. pp. 303–309.

Lewis, E. R. and Schwartz, S. E. (2004). *Sea Salt Aerosol Production. Mechanisms, Methods, Measurements, and Models*. Geophysical Monograph 152. American Geophysical Union, Washington, DC, 412 pp.

Lighthill, M. J. (1975). *Fourier analysis and generalised functions*. Camb. Univ. Press, Cambridge, 79 pp.

Liu, P. C. (1994). Wavelet spectrum analysis and ocean wind waves. In: Faufoula–Georgian, E. and Kumar, P. (Eds). *Wavelets in Geophysics*. Academia Press, New York, 151–166.

Liu, P. C. (2000a). Is the wind wave frequency spectrum outdated. *Ocean Eng.*, **27**: 577–588.

Liu, P. C. (2000b). Wave grouping characteristics in nearshore Great Lakes. *Ocean Eng.*, **27**: 1221–1230.

Liu, P. C. and Mori, N. (2001). Characterising freak waves with wavelet transform analysis. In: Olagnon, M. and Athanassoulis, G. A. (Eds). *Rouge Waves 2000*. Proceedings of Workshop, Brest, Editions Ifremer, 151–166.

Lodge, J. P. (1955). A study of se-salt particles over Puerto Rico. *J. Meteor.*, **12**: 493–499.

Loewen, M. R. and Melville, W. K. (1991). Microwave backscatter and acoustic radiation from breaking waves. *J. Fluid Mech.*, **224**: 601–623.

Loewen, M. R., O'Dor, M. A. and Skafel, M.G. (1996). Bubbles entrained by mechanically generated breaking waves. *J. Geophys. Res.*, **101**(C9): 20759–20769.

Longuet–Higgins, M. S. (1957). The statistical analysis of a random, moving surface. *Phil. Trans. R. Lond.*, **249**: 321–387.

Longuet–Higgins, M. S. (1962). Resonant interactions between two trains of gravity waves. *J. Fluid Mech.*, **27**: 395–397.

Longuet–Higgins, M. S. (1963). The effect of nonlinearities on statistical distributions in the theory of sea waves. *J. Fluid Mech.*, **17**: 459–480.

Longuet–Higgins, M. S. (1964). Modified Gaussian distribution for slightly nonlinear variables. *Radio Sci. J. Res.*, **68**: 1049–1062.

Longuet–Higgins, M. S. (1969). On wave breaking and the equilibrum spectrum of wind-generated waves. *Proc. R. Soc. Lond.*, **A310**: 151–159.

Longuet–Higgins, M. S. (1976). The deformation of steep surface waves on water. I. A numerical method of computation. *Proc. R. Soc. Lond.*, **A350**: 1–26.

Longuet–Higgins, M. S. (1977). On the nonlinear transformation of wave train in shallow water. *Arch. Hydrot.*, **XXIV**: 425–435 (in Polish).

Longuet–Higgins, M. S. (1978a). The instabilities of gravity waves of finite amplitude in deep water. I. Superharmonics. *Proc. R. Soc. Lond.*, **A360**: 471–488.

Longuet–Higgins, M. S. (1978b). The instabilities of gravity waves of finite amplitude in deep water. II. Subharmonics. *Proc. R. Soc. Lond.*, **A360**: 489–505.

Longuet–Higgins, M. S. (1980). Modulation of the amplitude of steep wind waves. *J. Fluid Mech.*, **99**: 705–713.

Longuet–Higgins, M. S. (1982). Parametric solutions for breaking waves. *J. Fluid Mech.*, **121**: 403–424.

Longuet–Higgins, M. S. (1983a). Rotating hyperbolic flow: particle trajectories and parametric representation. *Q. J. Mech. Appl. Maths.*, **36**: 247–270.

Longuet–Higgins, M. S. (1983b). On the joint distribution of wave periods and amplitudes in a random wave field. *Proc. R. Soc.*, **A389**: 241–258.

Longuet–Higgins, M. S. (1985a). A new way to calculate steep gravity waves. In: Toba, Y. and Mitsuyasu, H. (Eds). *The Ocean Surface*. Reidel Publ. Comp., Dordrecht, pp. 1–15.

Longuet–Higgins, M. S. (1985b). Acceleration in steep gravity waves. *J. Phys. Oceanorg.*, **15**: 1570–1579.

Longuet–Higgins, M. S. (1986). Eulerian and Lagrangian aspects of surface waves. *J. Fluid Mech.*, **173**: 683–707.

Longuet–Higgins, M. S. (1990). Flow separation near the crests of short gravity waves. *J. Phys. Oceanogr.*, **20**: 595–593.

Longuet–Higgins, M. S. (1994). The initiation of spilling breakers. In: Isaacson, M. and Quick, M. (Eds). In: Proceedings of International Symposium. *Waves–Physical and Numerical Modelling*. Vancouver, Vol **1**, pp. 24–48.

Longuet-Higgins, M. S., Cartwright, D. E. and Smith, N. D. (1961). Observations of the directional spectrum of sea waves using the motions of a floating buoy. In: *Ocean Wave Spectrum*. Prentice-Hall Inc., Englewood Cliffs, NJ, pp. 111–136.

Longuet-Higgins, M. S. and Stewart, R. W. (1964). Radiation stresses in water waves: a physical discussion with applications. *Deep Sea Res.*, **11**: 529–562.

Longuet–Higgins, M. S. and Turner, J. S. (1974). An "entrainment plume" model of a spilling breaker. *J. Fluid Mech.*, **63**: 1–20.

Longuet–Higgins, M. S. and Cokelet, E. D. (1976). The deformation of steep gravity waves on water. I. A numerical method of computation. *Proc. R. Soc. Lond.*, **A350**: 1–26.

Longuet–Higgins, M. S. and Fox, M. J. H. (1977). Theory of the almost-highest wave: the inner solution. *J. Fluid Mech.*, **80**: 721–741.

Longuet–Higgins, M. S. and Cokelet, E. D. (1978). The deformation of steep surface waves on water. II. Growth of normal-mode instabilities. *Proc. R. Soc. Lond.*, **A364**: 1–28.

Longuet–Higgins, M. S. and Fox, M. J. H. (1978). Theory of the almost-highest waves. Part 2. Matching and analytical extension. *J. Fluid Mech.*, **85**: 769–786.

Longuet–Higgins, M. S. and Smith, N. D. (1983). Measurement of breaking waves by a surface jump meter. *J. Geophys. Res.*, **88**(C14): 9823–9831.

Longuet–Higgins, M. S., Kerman, B. R. and Lunde, K. (1991). The release of air bubbles from an underwater nozzle. *J. Fluid Mech.*, **230**: 365–390.

MacIntyre, F. (1968). Bubbles: a boundary-layer "microtome" for micronthick samples of a liquid surface. *J. Phys. Chem.*, **72**(2): 589–592.

Makin, V. K. (1998). Air-sea exchange of heat in the presence of wind waves and spray. *J. Geophys. Res.*, **103**(C1): 1137–1152.

Marks, R. (1987). Marine aerosols and whitecaps in the North Atlantic and Greenland Sea regions. *Dt. Hydrogr.*, **40**: 71–79.

Marks, R. (1990). Preliminary investigations on the influence of rain on the production, concentration, and vertical distribution of sea salt aerosol. *J. Geophys. Res.*, **95**(C12): 22299-22304.

Mårtensson, E. M. and Bergdahl, L. (1987). On the wave climate of the Southern Baltic. Dept. Hydraulics, Chalmers Univ. Techn., Göteborg, Rep. Ser. A:15.

Mårtensson, E. M., Nilsson, E. D., de Leeuw, G., Cohen, L. H. and Hansson, H. C. (2003). Laboratory simulation and parameterization of the primary marine aerosol production. *J. Geophys. Res.*, **108**(D9),4297.

Marthinsen, T. and Winterstein, S. R. (1992). On the skewness of random surface waves. Proc. 2nd ISOPE Conf., **3**: 472–478.

Mason, B. J. (2001). The role of sea salt particle as cloud condensation muclei over the remote oceans. *Quart. J. R. Meteorol. Soc.*, **127**: 2023–2032.

Massel, S. R. (1973). Wind waves on finite water depth; their structure and interaction with maritime structures. *Eng. Trans.*, **32** (Suppl): 3–105 (in Polish).

Massel, S. R. (1981). On the nonlinear theory on mechanically generated waves in laboratory channels. Mitteilungen des Leichtweiss Institut für Wasserbau der Technischen Universität Braunschweig, Heft 70, 332–376.

Massel, S. R. (1989). *Hydrodynamics of Coastal Zones.* Elsevier Science Publ., Amsterdam, 336 pp.

Massel, S. R. (1996a). *Ocean Surface Waves: their Physics and Prediction.* World Scientific Publ., Singapore, 491 pp.

Massel, S. R. (1996b). On the largest wave height in water of constant depth. *Ocean Eng.*, **23**: 553–573.

Massel, S. R. (1998). The limiting wave height in wind-induced wave trains. *Ocean Eng.*, **25**(9): 735–752.

Massel, S. R. (1999). *Fluid Mechanics for Marine Ecologists.* Springer, Heidelberg, 566 pp.

Massel, S. R. (2001a). On the relationship between wave breaking and marine aerosol concentration in deep sea areas. *Arch. Hydro-Eng. Environ. Mech.*, **48**(2): 31–45.

Massel, S. R. (2001b). Wavelet analysis for processing of ocean surface wave records. *Ocean Eng.*, **28**: 957–987.

Massel, S. R. and Brinkman, R. M. (1998). On the determination of directional wave spectra for practical applications. *Appl. Ocean Res.*, **20**: 357–374.

Massel, S. R. and Sobey, R. J. (2000). Distribution of the highest wave in record. *Coastal Eng. J.*, **42**: 153–177.

Massel, S. R., Tęgowski, J., Chomka, M., Wichorowski, M., Dąbrowski, J., Stansberg, C. T. and Moe, V. (2001). Experimental study of the formation of steep waves and breakers. *Oceanologia*, **43**(3): 353–363.

Melville, W. K. (1982). The instability and breaking of deep-water waves. *J. Fluid Mech.*, **115**: 165–185.

Melville, W. K. (1983). Wave modulation and breakdown. *J. Fluid Mech.*, **128**: 489–506.

Melville, W. K. (1994). Energy dissipation by breaking waves. *J. Phys. Oceanogr.*, **24**: 2041–2049.

Melville, W. K. (1996). The role of surface-wave breaking in air-sea interaction. *Annu. Rev. Fluid Mech.*, **28**: 279–321.

Melville, W. K. and Rapp, R. J. (1988). The surface velocity field in steep and breaking waves. *J. Fluid Mech.*, **189**: 1–22.

Melville, W. K., Loewen, M. R. and Lamarre, E. (1992). Sound production and air entrainment by breaking waves: a review of recent laboratory experiments. In: Banner, M. L. and Grimshaw, R. H. J. (Eds). *Breaking Waves.* Proc. IUTAM Symposium, Sydney, 139–146.

Melville, W. K. and Matusov, P. (2002). Distribution of breaking waves at the ocean surface. *Nature*, **417**: 58–63.

Meyers, S. D., Kelly, B. G. and O'Brien, J. J. (1993). An introduction to wavelet analysis in oceanography and meteorology with application to the dispersion of Yanai waves. *Monthly Weather Rev.*, **121**: 2856–2866.

Meza, E., Zhang, J. and Seymour, R. J. (2000). Free-wave energy dissipation in experimental breaking waves. *J. Phys. Oceanogr.*, **30**: 2404–2418.

Miche, R., (1944). Wave motion on the finite water depth. *Ann. Ponts Chaussees*, **121**: 285–318 (in French).

Middleton, D. (1960). *Introduction to Statistical Communication Theory.* McGraw–Hill, New York, 650 pp.

Miętus, M. (co-ordinator). (1998). The climate of the Baltic Sea Basin, Marine meteorology and related oceanographic activities. World Meteor. Org., Geneva, Rep. No. 41.

Millinazzo, F. A. and Saffman, P. G. (1990). Effect of surface shear layer on gravity and gravity-capillary waves of permanent form. *J. Fluid Mech.*, **216**: 93–101.

Mitsuyasu, H. (1966). Interactions between water waves and wind. *Rep. Inst. Appl. Mech. Kynshu Univ.*, **14**: 67–88.

Mitsuyasu, H., Suhaya, T., Mizuno, S., Ohkuso, M., Honda T. and Rikiishi, K. (1975). Observations of the directional spectrum of ocean waves using a cloverleaf buoy. *J. Phys. Oceanogr.*, **5**: 750–760.

Monahan, E. C. (1971). Oceanic whitecaps. *J. Phys. Ocean*, **1**: 139–144.

Monahan, E. C. (1988). Modelling the generation of marine aerosols at the sea surface. *Oceanologia*, **26**: 19–22.

Monahan, E. C. and Zieltow, C. R. (1969). Laboratory comparisons of fresh-water and salt-water whitecaps. *J. Geophys. Res.*, **74**: 6961–6966.

Monahan, E.C. and O'Muircheartaigh, I. (1981). Optimal power-law description of oceanic whitecap coverage dependence on wind speed. *J. Phys. Oceanogr.*, **10**: 2094–2099.

Monahan, E. C., Fairall, C. W., Davidson, K. L. and Jones-Boyle, P. (1983). Observed inter-relations between 10m winds, ocean whitecaps and marine aerosols. Q. J. R. Meteorol. Soc., **109**: 379–392.

Monahan, E. C. and Spillane, M. C. (1984). The role of oceanic whitecaps in air-sea gas exchange. In Brutsaert, W. and Jirka, G. H. (Eds). *Gas Transfer at Water Surfaces*, 495–503.

Monahan, E. C., Spiel, D. E. and Davidson, K. L. (1986). A model of marine aerosol generation via whitecaps and wave distribution. In: Monahan, E. C. and MacNiocaill G. (Eds). *Oceanic Whitecaps and Their Role in Air-Sea Exchange Processes.* D. Reidel, Dordrecht, pp. 167–174.

Monahan, E. C. and Woolf, D. K. (1988). Comprehensive model relating the marine aerosol population of the atmospheric boundary layer to the bubble population of the oceanic mixed layer. In: Wang, T. G. (Eds). *Third International Colloquium on Drops and Bubbles*. American Institute of Physics, Monterey, pp. 451–457.

Monahan, E. C., Wilson, M. B. and Woolf, D. K. (1988). HEXMAX whitecap climatology. In: Monahan, E. C., Cipriano, R. J., Fitzgerald, W. F., Marks, R., Mason, R., Nolan, P. R., Torersen, R., Wilson, M. B. and Woolf, D. K. (Eds). *Oceanic Whitecaps and the Fluxes of Droplets from Bubbles to and Gases through the Sea Surface*. Whitecap Report 4, Marine Sciences Institute, University of Connecticut, Groton, pp. 20–39.

Monahan, E. C. and Woolf, D. K. (1989). Comments on "Variations in whitecap coverage with wind stress and water temperature". *J. Phys. Oceanogr.*, **19**: 706–709.

Monahan, E. C. and Van Patten, M. A. (1989). The climate and health implications of bubble-mediated sea-air exchange. The Connecticut Sea Grant College Program, 170 pp.

Monahan, E. C. and Lu, M. (1990). Acoustically relevant bubble assemblages and their dependence on meteorological parameters. IEEE, J. *Ocean Eng.*, **15**: 340–349.

Monin, A. S. and Yaglom, A. M. (1965). *Statistical Fluid Mechanics*. Izdatelstwo Nauka, Moscow, 720 pp (in Russian).

Mori, N. and Yasuda, T. (1994). Orthonormal wavelet analysis for deep water breaking waves. *Proc. 24th Conf. on Coastal Eng., ASCE, Kobe*, **1**: 412–426.

Myrhaug, D. and Kjeldsen, S. P. (1986). Steepness and asymmetry of extreme waves and the highest waves in deep water. *Ocean Eng.*, **13**(6): 549–568.

Murphy, D. M., Anderson, J. R., Qunin, P. K., McInnes, L. M., Brechtel, F. J., Kreidenwies, S. M., Middlebrook, A. M., Pósfai, D. S., Thomson, D. S. and Buseck, P. R. (1998). Influence of sea-salt on aerosol radiative properties in the southern ocean marine boundary layer. *Nature*, **392**: 62–65.

New, A. L. (1983). A class of elliptical free-surface flows. *J. Fluid Mech.*, **130**: 219–239.

Niedzwecki, J. M. and Whatley, C. P. (1991). A comparative study of some directional sea models. *Ocean Eng.*, **18**: 111–128.

Nilsson, E. D., Mårtensson, E. M., van Ekeren, S. J., de Leeuw, G., Moerman, M. and O'Dowd, C. (2003). The primary marine aerosol source measured by eddy correlation for particles of different size. *J. Aerosol Sci.* **34**: 539–540.

Nukiyama, S. and Tanasawa, Y. (1938). Experiments on atomization of liquid by means of air stream. *Trans. Soc. Mech. Eng. Jp.*, **4**(14): 86–93.

Oakey, N. S. and Elliot, J. A. (1982). Dissipation within the surface mixed layer. *J. Phys. Oceanogr.*, **12**: 171–185.

Ochi, M. K. (1990). *Applied Probability and Stochastic Processes in Engineering and Physical Sciences*. John Wiley and Sons, New York, 499 pp.

Ochi, M. K. and Tsai, C. H. (1983). Prediction of occurence of breaking waves in deep water. *J. Phys. Oceanogr.*, **13**: 2008–2019.

Olagnon, M. and Athanassoulis, G. A. (Eds) (2001). *Rogue waves 2000*. Proc. Workshop organised by Ifremer, Brest, Editions Ifremer, 395 pp.

Olagnon, M. and van Isegham, S. (2001). Some cases of observe rogue waves and an attempt to characterise their occurrence conditions. In Olagnon, M. and Athanassoulis, G. A. (Eds). *Rogue Waves 2000*. Proc. Workshop, Brest, Editions Ifremer, 105–116.

Pairaud, I. and Auclair, F. (2005). Combined wavelet and principal component analysis (WEof) of a scale-oriented model of coastal ocean gravity waves. *Dynamics Atmos. Oceans*, **40**(4): 254–282.

Panin, G. N. (1985). *Heat and Mass Exchange between Water and Atmosphere in the Real Conditions*. Publ. Nauka, Moscow, 205 pp (in Russian).

Papadimitrakis, Y. A. (2005). On the probability of wave breaking in deep waters. *Deep-Sea Res. II*, **52**: 1246–1269.

Paplińska, B. (1999). Wave analysis at Lubiatowo and in the Pomeranian Bay based on measurements from 1997–1998–comparison with modelled data (WAM4 model). *Oceanologia*, **41**: 241–254.

Paplińska, B. and Reda, A. (2003). Atlas of the Wave Climate in the Baltic Sea in Years 1998–2001. Institute of Oceanology, Sopot (Poland). Internal Report, 102 pp (in Polish).

Peltzer, R. D. and Griffin, O. M. (1992). Spatial and temporal properties of deep water breaking waves. In: *Proceedings of 45th APS Fluid Dynamics. Meeting, Florida State* University, Tallahassea.

Percival, D. P. (1995). On estimation of the wavelet variance. *Biometrika*, **82**: 619–631.

Peregrine, D. H., Cokelet, E. D., McIver, P. (1980). The fluid mechanics of waves approaching breaking. *Proc. 17th Coastal Eng. Conf., Sydney*, **1**: 512–528.

Petelski, T. (2003). Marine aerosol fluxes over open sea calculated from vertical concentration gradients. *Aerosol Sci.*, **34**: 359–371.

Petelski, T. (2005). Coarse aerosol concentration over the North Polar Waters and the Atlantic. *J. Aerosol Sci. Tech.*, **39**(8): 695–700.

Petelski, T. and Chomka, M. (1996). Marine aerosol fluxes in the coastal zone - BAEX Experiment. *Oceanologia*, **38**: 469–484.

Petelski, T., Piskozub, J. and Paplińska-Swerpel, B. (2005). Sea spray emission from the surface of the open Baltic Sea. *J. Geophys. Res.*, **110**(C10)023.

Petelski, T. and Piskozub, J. (2006). Vertical coarse aerosol fluxes in the atmospheric surface layer over the North Polar Waters and Atlantic. *J. Geophys. Res.*, **111**(C06).

Pierson, W. J. and Moskowitz, L. (1964). A proposed spectral form for fully developed wind seas based on the similarity theory of S.A. Kitaigorodskii. *J. Geophys. Res.*, **69**: 5181–5190.

Phillips, O. M. (1958). The equilibrium range in the spectrum of wind-generated waves. *J. Fluid Mech.*, **4**: 426–434.

Phillips, O. M. (1977). *The Dynamics of the Upper Ocean*. Second Edition. Cambridge University Press, Cambridge, 336 pp.

Phillips, O. M. (1985). Spectral and statistical properties of the equilibrium range in wind-generated gravity waves. *J. Fluid Mech.*, **156**: 505–531.

Philips, O. M. and Banner, M. L. (1974). Wave breaking in the presence of wind drift and swell. *J. Fluid Mech.*, **66**: 625–640.

Phillips, O. M., Gu, D. and Donelan, M. A. (1993a). Expected structure of extreme waves in a Gaussian sea. Part I: Theory and SWADE buoy measurements. *J. Phys. Oceanogr.*, **23**: 992–1000.

Phillips, O. M., Gu, D. and Wash, E. J. (1993b). On expected structure of extreme waves in a Gaussian sea. Part: SWADE scanning radar altimeter measurements. *J. Phys. Oceanogr.*, **23**: 2297–2309.

Phillips, O. M., Posner, F. L. and Hansen, J. P. (2001). High range resolution radar measurements of the speed distribution of breaking events in wind-generated ocean waves: surface impulse and wave energy dissipation rates. *J. Phys. Oceanogr.*, **31**: 450–460.

Piechura, J., Pempkowiak, J., Radziejewska, T. and Uścinowicz, Sz. (2006). What we know about the Baltic Sea: a summary of BSSC 2005. *Oceanologia*, **48(S)**: 3–19.

Pierson, W. J., Neumann, G. and James, R. W. (1955). Practical methods for observing and forecasting ocean waves by means of wave spectra and statistics. Publ. No. 603, U.S. Naval Hydrographic Office.

Pierson, W. J. and Moskowitz, L. (1964). A proposed spectral form for fully developed wind seas based on the similarity theory of S.A. Kitaigorodskii. *J. Geophys. Res.*, **69**: 5181–5190.

Preobrazhenskij, L. Y. (1973). Estimation of the content of spray-drops in the near water layer of the atmosphere. *Fluid Mech.-Sov. Res.*, **2**(2): 95–100.

Ramberg, S. E. and Griffin, O. M. (1987). Laboratory studies of steep and breaking deep water waves. *J. Waterways, Port, Coastal Ocean Div.*, **113**: 493–506.

Rapp, R. J. and Melville, W. K. (1990). Laboratory measurements of deep-water breaking waves. *Philos. Trans. R. Soc. Lond.*, **A331**: 735–800.

Reinke, N., Vossnacke, A., Schutz, W., Koch, M. K. and Unger, H. (2001). Aerosol generation by bubble collapse at ocean surfaces. In: Fowler, D., Pitcairn C. and Erisman J. W. (Eds). *Air Surface Exchange of Gases and Particles.* Kluwer Academic Publishers, Dordrecht, 333–340.

Resch, F. J. and Afeti, G. M. (1991). Film drop distributions from bubbles bursting in seawater. *J. Geophys. Res.*, **96**: 10681–10688.

Resch, F. J. and Afeti, G. M. (1992). Submicron film drop production by bubbles in seawater. *J. Geophys. Res.*, **97**: 3679–3683.

Rice, O. (1944). Mathematical analysis of random noise. *Bell System Tech. J.*, **23**: 282–332.

Rogers, D. P. (1995). Air-sea interaction: connecting the ocean and atmosphere. *Rev. Geophys.*, **33**, Suppl.

Rosenberg, A. and Ritter, M. (2005). Laboratory study of the fine structure of short surface waves due to breaking: two-directional wave propagation. *J. Geophys. Res.*, **110**: 1–14.

Ross, D. B. and Cardone, V. J. (1974). Laboratory study of the fine structure of short surface waves due to breaking: two-dimensional wave propagation. *J. Geophys. Res.*, **110**: 1–14.

Schultz, W. W., Griffin, O. M. and Ramberg, S. E. (1987). Steep and breaking deep water waves. In: *Proceedings of 16th ONR Symposium on Naval Hydrodynamics. National Academy* Press, Washington, DC, pp. 106–115.

Schultz, W. W., Huh, J. and Griffin, O. M. (1994). Potential energy in steep and breaking waves. *J. Fluid Mech.*, **278**: 201–228.

Schwartz, L. W. (1974). Computer extention and analytic continuation of Stokes' expansion for gravity waves. *J. Fluid Mech.*, **104**: 119–137.

Sharma, J. N. and Dean, R. G. (1981). Second order directional seas and associated wave forces. *J. Soc. Petroleum Eng.*, **7**: 129–140.

Shen, Z., Mei, L. (1994). Fine structure of wind wave analyzed with wavelet transform. *J. Phys. Oceanogr.* **24**: 1085–1094.

Slinn, S. A. and Slinn, W. G. N. (1980). Predictions for particle deposition on natural waters. *Atmos. Environm.*, **14**: 1013–1016.

Slinn, S. A. and Slinn, W. G. N. (1981). Modelling of atmospheric particulate deposition to natural waters. In: Eisenreich, S. J. (Ed). *Atmospheric Pollutants in Natural Waters*. Ann Arbor Science, Arbor, pp. 23–25.

Smith, M. H., Park, P. M. and Consterdine, I. E. (1993). Marine aerosol concentrations and estimated fluxes over the sea. *Quart. J. R. Meteor. Soc.*, **19**: 809–824.

Smith, M. H. and Harrison, N. M. (1998). The sea spray generation function. *J. Aerosol Sci.*, **29**: S189–S190.

Snyder, R. L. and Kennedy, R. M. (1983). On the formation of whitecaps by a threshold mechanism. Part I: Basic formalism. *J. Phys. Oceanogr.*, **13**: 1482–1492.

Snyder, R. L., Smith, L. and Kennedy, R. M. (1983). On the formation of whitecaps by a threshold mechanism. Part III: Field experiment and comparison with theory. *J. Phys. Oceanogr.*, **13**: 1505–1518.

Sobey, R. J. (1992). A local Fourier appeoximation method for irregular wave kinematics. *Appl. Ocean Res.*, **14**: 93–105.

Sobey, R. J., Chandler, B. D. and Harper, B. A. (1990). Extreme waves and wave counts in a hurricane. *Proc. 22nd Conf. Coastal Eng.*, **1**: 358–370.

Song, J. B. and Banner, M. L. (2002). On determining the onset and strength of breaking for deep water waves. Part I: Unforced irrotational wave groups. *J. Phys. Oceanogr.*, **32**: 2541–2558.

Spedding, G. R., Browand, F. K., Huang, N. E. and Long, S. R. (1993). A 2-D complex wavelet analysis of an unsteady wind-generated surface wave field. *Dynamics Atmos. Oceans*, **20**: 55–77.

Spiel, D. E. (1992). Acoustical measurements of air bubbles bursting at a water surface: bursting bubbles as Helmholtz resonators. *J. Geophys. Res.*, **97**(C7): 11443–114522.

Spiel, D. E. (1994). The number and size of jet drops produced by air bubbles bursting at a water surface. *J. Geophys. Res.*, **99**(C5): 10289–10296.

Spiel, D. E. (1995). On the birth jet drops from bubbles bursting on seawater surface. *J. Geophys. Res.*, **100**(C3): 4995–5006.

Spiel, D. E. (1997). More on the birth jet drops from bubbles bursting on seawater surface. *J. Geophys. Res.*, **102**(C3): 5815–5821.

Spiel, D. E. (1998). On the births of film drops from bubbles bursting on seawater surface. *J. Geophys. Res.*, **103**(C11): 24907–24918.

Srokosz, M. A. (1986). On the probability of wave breaking in deep water. *J. Phys. Oceanogr.*, **15**: 382–385.

Srokosz, M. A. and Longuet–Higgins, M. S. (1986). On the skewness of sea-surface elevation. *J. Fluid Mech.*, **164**: 487–497.

Stansberg, C. T. (1998). Non-Gaussian extremes in numerically generated second-order random waves in deep water. In: *Proceedings of 8th ISOPE Conference, Montreal*, Vol. **3**, pp. 103–110.

Stansberg, C. T. (2000). Laboratory reproduction of extreme waves in a random sea. In: *International Workshop on Natural Disaster by Storm Waves and Their Reproduction in Experimental Basin*, Kyoto, 13 pp.

Stansell, P. and MacFarlane, C. (2002). Experimental inwestigation of wave breaking criteria based on wave phase speeds. *J. Phys. Oceanogr.*, **32**: 1269–1283.

Stokes, G. G. (1847). On the theory of oscillatory waves. *Trans. Camb. Phil. Soc.*, **8**: 441–455.

Stokes, G. G. (1880). Considerations relative to the greatest height of oscillatory waves which can be propagated without change of form. *Math. Phys. Papers*, **1**: 225–228.

Stokes, M. D., Deane, G. B., Vagle, S. and Farmer, D. M. (2002). Measurements of large bubbles in open-ocean whitecaps. In: Donelan, M. A., Drennan, W. M., Saltzman, E. S. and Wanninkhof, R. (Eds). *Gas Transfer at Water Surfaces*, Geophysical Monographs **127**. American Geophysical Union, Washington, DC, pp. 279–284.

Strahler, A. H. and Strahler, A. N. (1992). *Modern Physical Geography*. John Wiley & Sons New York, 638 pp.

Stramska, M. (1987). Vertical profiles of sea salt aerosol in the atmospheric surface layer: A numerical model. *Acta Geophys. Polonica*, **35**: 87–100.

Stramska, M., Marks, R. and Monahan, E.C. (1990). Bubble-mediated aerosol production as a consequence of wave breaking in super-saturated (hyperoxic) seawater. *J. Geophys. Res.*, **95**(C10): 18281–18288.

Stramska, M. and Petelski, T. (2003). Observations of oceanic whitecaps in the north polar waters of the Atlantic. *J. Geophys. Res.*, **108**(C3),3086.

Stramski, D. and Tęgowski, J. (2001). Effects of intermittent entrainment of air bubbles by breaking wind waves on ocean reflectance and underwater light field. *J. Geophys. Res.*, **106**(C12): 31345–31360.

Stuhlman, D. J. (1932). The mechanics of effervescence. *J. Appl. Phys.*, **2**: 457–466.

Su, M. Y. and Green, A. W. (1985). Wave breaking and nonlinear instability coupling. In: Toba, Y. and Mitsuyasu, H. (Eds). *The Ocean Surface*. Reidel Publ. Comp., Dordrecht, pp. 31–38.

Su, M. Y. and Cartmill, J. (1992). Breaking wave statistics obtained during "Swade". In: Banner, M. L. and Grimshaw, R. H. J. (Eds). *Breaking Waves*. Proc. IUTAM Symposium, Sydney, pp. 161–163.

Svendsen, T. A. (1984). Mass flux and undertown in a surf zone. *Coastal Eng.*, **8**: 347–365.

Tayfun, M. A. (1980). Narrow-band nonlinear sea waves. *J. Geophys. Res.*, **85**: 1548–1552.

Tayfun, M. A. (1981). Breaking-limited wave heights. *J. Waterway, Port, Coastal and Ocean Eng.*, **107**: 59–69.

Tayfun, M. A. and Al-Humond (2002). Least upper bound distribution for nonlinear wave crests. *J. Waterway, Port, Coastal and Ocean Eng.*, **128**: 144–151.

Teles da Silva, A. F. and Peregrine, D. H. (1988). Steep, steady surface waves on water of finite depth with constant vorticity. *J. Fluid Mech.*, **195**: 281–302.

Terray, E. A., Donelan, M. A., Agrawal, Y. C., Drennan, W. M., Kahma, K. K., Williams III, A. J., Hwang, P. A. and Kitaigorodskii, S. A. (1996). Estimates of kinetic energy dissipation under breaking waves. *J. Phys. Oceanogr.*, **26**: 792–806.

Tęgowski, J. (2004). A laboratory study of breaking waves. *Oceanologia*, **46**: 365–382.

Thornton, E. B. and Guza, R. T. (1983). Transformation of wave height distribution. *J. Geophys. Res.*, **88**: 5925–5938.

Thorpe, S. A. (1992). Bubble clouds and the dynamics of the upper ocean. *Quart. J. R. Meteor. Soc.*, **118**: 1–22.

Thorpe, S. A. (1993). Energy loss by breaking waves. *J. Phys. Oceanogr.*, **23**: 2498–2502.

Thorpe, S. A. and Humphries, P. N. (1980). Bubbles and breaking waves. *Nature*, **283**: 463–465.

Tikhonow, W. I. (1966). *Statistical Radiotechnics*. Sov. Radio Publ., Moscow, 678 pp (in Russian).

Toba, Y. (1959). Drop production by bursting air bubbles on the sea aurface. *J. Oceanogr. Soc. Jpn.*, **15**: 1–10.

Toba, Y. (1973). Local balance in the air-sea boundary processes. Part III. On the spectrum of wind waves. *J. Oceanogr. Soc. Jpn.*, **29**: 209–220.

Toba, Y. and Chaen, M. (1973). Quantitative expression of the breaking of wind waves on the sea surface. *Rec. Oceanogr. Works Jpn.*, **12**: 1–11.

Torrence, C., Compo, G. P. (1998). A practical guide to wavelet analysis. Bulletin to the American Meteorological Society, **79**: 61–78.

Trulsen, K. and Dysthe, K. B. (1996). A modified nonlinear Schrödinger equation for broader bandwidth gravity waves on deep water. *Wave Motion*, **24**: 281–289.

Tucker, M. J., Car, A. P. and Pitt, E. G. (1983). The effect of an off-shore bank in attenuating waves. *Coastal Eng.*, **7**: 133–144.

Tulin, M. P. and Li, J. J. (1992). A mechanism for wave deformation and breaking intermediated by resouant side-bands. In: Banner, M. L. and Grimshaw, R. H. J. (Eds). *Breaking Waves*, Proc. IUTAM Symposium, Sydney, pp. 251–256.

Tulin, M. P. and Waseda, T. (1999). Laboratory observations of wave group evolution, including breaking effects. *J. Fluid Mech.*, **378**: 197–232.

Tung, C. C., Huang, N. E., Yuan, Y. and Long, S. R. (1989). Probability function of breaking-limited surface elevation. *J. Geophys. Res.*, **94**(C1): 967–972.

Twomey, S. (1955). The distribution of sea-salt nuclei in air over land. *J. Meteor.*, **12**: 81–86.

Twomey, S. (1991). Aerosols, clouds and radiation. *Atmos. Environ.*, **25A**: 2435–2442.

UNESCO (1987). International oceanographic tables. *UNESCO Technical Papers in Marine Science*, Vol. 40. UNESCO, Paris.

Van Name, F. W. (1960). *Modern Physics*. Prentice–Hall, Inc., Englewood Clifs, NJ.

Veltcheva, A. D. (2002). Wave and group transformation by a Hilbert spectrum. *Coastal Eng. J.*, **44**: 283–300.

Vinje, T. and Brevig, P. (1980). *Breaking Waves on Finite Water Depths: a Numerical Study*. Ship Res. Inst. of Norway, R118.81, 126 pp.

Vinje, T. and Haver, S. (1994). On the non-Gaussian structure of ocean waves. Proceedings of 2nd BOSS Conference, Cambridge.

WAMDI group: S. Hasselmann, K. Hasselmann, E.Bauer, P. A. E. M. Janssen, G. J. Komen, L. Bertotti, P. Lionello, A. Guillaume, V. C. Cardone, J. A. Greenwood, M. Reistad, L. Zambesky and J. A. Ewing (1988). The WAM model – a third generation ocean wave prediction model. *J. Phys. Oceanogr.*, **18**: 1775–1810.

Wanninkhoff, R. and McGills, W. R. (1999). A cubic relationship between air-sea CO_2 exchange and wind speed. *J. Geophys. Res.*, **26**: 1889–1892.

Waseda, T. and Tulin, M. P. (1999). Experimental study of the stability of deep-water wave trains including wind effects. *J. Fluid Mech.*, **401**: 55–84.

Weibull, W.A. (1951). A statistical distribution of wide applicability. *J. Appl. Mech.*, **18**: 293–297.

Weissman, M. A., Atakturk, S. S. and Katsaros, K. B. (1984). Detection of breaking events in a wind-generated wave field. *J. Phys. Oceanogr.*, **14**: 1608–1619.

Weller, R. A., Donelan, M. A., Briscoe, M. G. and Huang, N. E. (1991). Riding the crest – a take of two wave experiments. *Bull. Am. Met. Soc.*, **72**(2): 163–183.

Whitham, G. B. (1974). *Linear and Nonlinear Waves.* Wiley Interscience Publ., New York, 636 pp.

Williams, J. M. (1981). Limiting gravity waves in water of finite depth. *Phil. Trans. R. Soc. Lond.*, **A302**: 139–188.

Winterstein, S. R. (1988). Nonlinear vibration models for extremes and fatigue. *J. Eng. Mech.*, **114**: 1772–1790.

Woodcock, A. H. (1953). Salt nuclei in marine air as a function of attitude and wind force. *J. Meteorol.*, **10**: 362–371.

Woolf, D. K. (1993). Bubbles and the air-sea transfer velocity of gases. *Atmosphere-Ocean*, **31**(4): 517–540.

Woolf, D. K. (1997). Bubbles and their role in air-sea gas exchange. In: Liss, P. S. and Duce, R. A. (Eds). *The Sea Surface and Global Change.* Cambridge University Press, Cambridge, pp. 173–205.

Woolf, D. K., Bowyer, P. A. and Monahan, E. C. (1987). Discriminating between the film drops and jet drops produced by a simulated whitecap. *J. Geophys. Res.*, **92**(C5): 5142–5150.

Woolf, D. K., Monahan, E. C. and Spiel, D. E. (1988). Quantification of the marine aerosol produced by whitecaps. In: *Seventh Conference on Ocean-Atmosphere Interaction.* Anaheim, pp. 182–185.

Wright, J. W. (1976). The wind drift and wave breaking. *J. Phys. Oceanogr.*, **6**: 402–405.

Wu, J. (1973). Spray in the atmospheric surface layer: laboratory study. *J. Geophys. Res.*, **57**: 511–519.

Wu, J. (1979). Oceanic whitecaps and sea state. *J. Phys. Oceanogr.*, **16**: 2172–2178.

Wu, J. (1980). Wind-stress coefficients over sea surface near neutral conditions – a revisit. *J. Phys. Oceanogr.*, **10**: 727–740.

Wu, J. (1982). Wind-stress coefficients over sea surface from breeze to hurricane. *J. Geophys. Res.*, **87**: 9704–9706.

Wu, J. (1988a). Bubbles in the near-surface ocean: a general description. *J. Geophys. Res.* **93**: 587–590.

Wu, J. (1988b). Variations of whitecap coverage with wind stress and water temperature. *J. Phys. Oceanogr.*, **18**: 1448–1453.

Wu, J. (1989). Contributions of film and jet drops to marine aerosols produced at the sea surface. *Tellus*, **41**B: 469–473.

Wu, J. (1992). Bubble flux and marine aerosol spectra under various wind velocities. *J. Geophys. Res.*, **97**: 2327–2333.

Wu, J. (1993). Production of spume drops by the wind tearing of wave crests: the search for quantification. *J. Geophys. Res.*, **98**: 18221–18227.

Wu, J. (2000). Concentrations of sea-spray droplets at various wind velocities: separating productions through bubble bursting and wind tearing. *J. Phys. Oceanogr.* **30**: 195–200.

Wu, J. (2001). Production functions of film drops by bursting bubbles. *J. Phys. Oceanogr.*, **31**(11): 3249–3257.

Xu, D., Huang, P. A. and Wu, J. (1986). Breaking of wind-generated waves. *J. Phys. Oceanogr.*, **16**: 2172–2178.

Xu, D., Liu, X. and Yu, D. (2000). Probability of wave breaking and whitecap coverage in a fetch-limited sea. *J. Geophys. Res.*, **105**(C6): 14253-14259.

Yamada, M. and Ohkitani, K. (1991). An identification of energy cascade in turbulence by orthonormal wavelet analysis. *Prog. Theor. Phys.*, **86**: 799–815.

Young, I. R., Verhagen, L. A. and Banner, M. L. (1995). A note on the bimodal directional spreading of fetch limited wind waves. *J. Geophys. Res.*, **100**: 773–778.

Young, I. R. and Holland, G. J. (1996). *Atlas of the Oceans: Wind and Wave Climate*. Elsevier Science, Amsterdam, 241 pp.

Yuan, Y., Tung, C. C. and Huang, N. E. (1986). Statistical characteristics of breaking waves. In Phillips, O. M. and Hasselmann, K. (Eds). *Wave Dynamics and Radio Probing of the Ocean Surface*. Plenum, New York, pp. 265–272.

Zakharov, V. E. (1968). Stability of periodic waves of finite amplitude on the surface of deep fluid. *Zh. Eksp. Teor. Fiziki*, **2**: 190–194 (in Russian).

Zakharov, V. E. and Zaslavskii, M. M. (1982). The kinetic equation and Kolmogorov spectra in the weak turbulence theory of wind waves. *Izv. Atmos. Oceanic Phys.*, **18**: 747–753.

Zakharov, V. E. and Zaslavskii, M. M. (1983). Shape of the spectrum of energy-carrying components of a water surface in the weak-turbulence theory of wind waves. *Izv. Atmos. Oceanic Phys.*, **19**: 207–212.

Zakharov, V. E. and Shrira, V. I. (1990). On the formation of directional spectrum of wind waves. *Zh. Eksp. Teor. Fiziki*, **98**: 1941–1958 (in Russian).

Zappa, C. J., Asher, W. E., Jessup, A. T., Klinke, J. and Long, S. R. (2002). Effect of microscale wave breaking on air-water gas transfer. In: Donelan, M. A., Drennan, W. M., Saltzman, E. S. and Wanninkhof, R. (Eds). *Gas Transfer at Water Surfaces*, Geophysical Monographs **127**. American Geophysical Union, Washington, pp. 23–29.

Zhang, J., Chen, L., Ye, M. and Raudall, R. E. (1996). Hybrid wave model for unidirectional irregular waves. Part 1: Theory and numerical scheme. *Appl. Ocean Res.*, **18**: 77–92.

Zhang, K. M., Kaipping, E. M., Wexler, A. S., Bhave, P. V. and Tonnesen, G. S. (2005). Size distribution of sea-salt emissions as a function of relative humidity. *Atmos. Environ.*, **39**: 3373–3379.

Zieliński, T. (2006). *Physiacal properties of the near-water aerosol layer in coastal areas*. Monographs Series, No. 18. Institute of Oceanology, Sopot (Poland), 164 pp (in Polish).

Zilitinkievitch, S. S., Monin, S. S. and Chalikov, D. W. (1978). The interaction between the sea and the atmosphere. *Stud. Mater. Oceanol.*, **22**, 282 pp (in Polish).

Zimmermann, C. A. and Seymour, R. (2002). Detection of breaking in a deep water wave record. *J. Waterway, Port, Coastal and Ocean Eng.*, **128**: 72–78.

Symbols and Notations

a	wave amplitude
$a^{(E)}$	Eulerian (apparent) vertical acceleration
$a^{(L)}$	Lagrangian (real) vertical acceleration
$a^{(2)F}$	second free harmonic
$a^{(2)S}$	second bound harmonic
A	wave amplitude
A_{br}	maximum wave amplitude
A_{rms}	root–mean–square wave amplitude
b	dilation scale
C	phase velocity
C_{br}	phase speed of breaking waves
C_{dr}	surface drift velocity
C_g	group velocity
C_0	phase speed of the dominant wave
C_{10}	drag coefficient
D	directional spreading function
e	ocean surface emissivity
$erf(x)$	error function
$erfc(x)$	supplemented error function
E	energy
E_{diss}	spectral dissipation term
$E_{dissrate}$	rate of energy loss per unit surface area
$E(x)$	average value of the random variable x
f	probability density function, frequency
f_{dep}	size–dependent deposition flux
f_{dmass}	size–dependent dry mass flux
f_p	peak wave frequency [Hz]
f_{prod}	size–dependent production flux
f_{sgf}	sea spray generation function
f_{vol}	volume flux
$f_{sgf}^{(dd)}$	sea spray generation function based on dry deposition method

$f_{sgf}^{(vg)}$ sea spray generation function based on vertical concentration gradient method
$f_{prod}^{(wc)}$ size–dependent production flux over whitecap area
$f_{sgf}^{(wc)}$ sea spray generation function based on whitecap area
F probability (cumulative) distribution
F_{br} probability of breaking waves
F_{cov} whitecap coverage
F_n net irradiance

g gravitational acceleration

h ejection height
H wave height
$\overline{H}$ mean wave height
H_d dominant wave height
H_{m0} significant wave height based on frequency spectrum
H_{rms} root mean square wave height
H_s significant wave height

i imaginary unit
I_0 modified Bessel function of zero order

J Jakobian of transformation

k wave number
$\overline{k}$ mean wave number

l wave number
L Monin–Obokhov scale, wavelength

m_{dr} dry particle mass
m_n spectral moments of$n$-order

N number concentration of particles, wave action density
N_{br} number of breaking waves
N_{film} number of film droplets
N_{jet} number of jet droplets

p pressure

Q_a heat flux in the atmosphere
Q_w heat flux in the ocean

r radius, radius of droplet at ambient relative humidity 80%
r_{bub} radius of bubble
r_{film} radius of film droplets
r_{jet} radius of jet droplets

r_0	radius of particle at its formation
R	normalized wave amplitude
s	empirical function
S	frequency spectral density, salinity
S_{diss}	spectralenergy loss by breaking
S_{nl}	spectral flux of energy due to resonant wave–wave interactions
S_w	spectral input from the wind
t	time
T	temperature, wave period
$\overline{T}$	mean wave period
T_p	peak period
ΔT	temperature difference
u	horizontal component of velocity
u_*	friction velocity
U	current velocity
V	wind speed
V_{10}	wind speed at level of 10m above sea surface
$V_{19.5}$	wind speed at level of 19.5m above sea surface
w	vertical component of velocity
w_b	terminal rising velocity of droplets
w_d	terminal fall velocity of droplets
We	Weber number
WT	wavelet transform
x	horizontal axis of the rectangular coordinate system
X	wind fetch
z	vertical axis (directed upward when positive) of the rectangular coordinate system
α	empirical constant
β	Phillips's constant
β_{BF}	initial growth rate according to Benjamin and Feir
β_K	initial growth rate according to Krasitskii
γ	peak enhancement factor, surface tension
γ_1	distribution skewness
γ_2	distribution kurtosis
Γ	gamma function
δ	delta function, growth rate, small quantity
δ_{th}	threshold growth rate

ε wave steepness
ε_d dominant wave steepness
ε_f crest front steepness
ε_g global limiting wave steepness
ε_k characteristic breaking parameter
ε_l local surface slope
ε_s significant wave steepness
ε^2 spectral width parameter

ζ surface displacement
ζ_{max} max. surface displacement
ζ_s fifth-order Stokes' profile

η analytic signal

θ angle
$\theta(t)$ local phase function
$\Delta\theta$ discrete angle interval
Θ potential temperature

κ von Kármán constant

λ_h horizontal asymmetry parameter
λ_v vertical asymmetry parameter

μ coefficient of dynamic viscosity
μ_3 statistical third moment
μ_4 statistical fourth moment

ν coefficient of kinematic viscosity
ν_a coefficient of kinematic viscosity of air
ν_w coefficient of kinematic viscosity of water
ν^2 spectral width parameter

ξ normalized surface displacement
ξ Hilbert transform of ζ

Π Buckingham theorem

ρ density
ρ_a air density
ρ_v vapour density
ρ_w water density
ρ_{ss} density of dry sea salt

σ_ζ standard deviation of surface displacement
σ_ζ^2 variance of surface displacement

τ normalized wave period, shear stress, translation

ϕ velocity potential
Φ probability integral, velocity potential
φ phase angle

Ψ wave number spectrum

ω angular frequency
ω_c mean carrier frequency
ω_l local radial frequency
ω_p peak radial frequency
$\Delta\omega$ discrete frequency interval
ϖ mean radial frequency

Ω frequency

Author Index

Subject Index

ATMOSPHERIC AND OCEANOGRAPHIC SCIENCES LIBRARY

1. F.T.M. Nieuwstadt and H. van Dop (eds.): *Atmospheric Turbulence and Air Pollution Modelling*. 1982; rev. ed. 1984
   ISBN 90-277-1365-6; Pb (1984) 90-277-1807-5
2. L.T. Matveev: *Cloud Dynamics*. Translated from Russian. 1984 ISBN 90-277-1737-0
3. H. Flohn and R. Fantechi (eds.): *The Climate of Europe: Past, Present and Future*. Natural and Man-Induced Climate Changes: A European Perspective. 1984
   ISBN 90-277-1745-1
4. V.E. Zuev, A.A. Zemlyanov, Yu.D. Kopytin, and A.V. Kuzikovskii: *High-Power Laser Radiation in Atmospheric Aerosols*. Nonlinear Optics of Aerodispersed Media. Translated from Russian. 1985 ISBN 90-277-1736-2
5. G. Brasseur and S. Solomon: *Aeronomy of the Middle Atmosphere*. Chemistry and Physics of the Stratosphere and Mesosphere. 1984; rev. ed. 1986
   ISBN (1986) 90-277-2343-5; Pb 90-277-2344-3
6. E.M. Feigelson (ed.): *Radiation in a Cloudy Atmosphere*. Translated from Russian. 1984
   ISBN 90-277-1803-2
7. A.S. Monin: *An Introduction to the Theory of Climate*. Translated from Russian. 1986
   ISBN 90-277-1935-7
8. S. Hastenrath: *Climate Dynamics of the Tropics*. Updated Edition from *Climate and Circulation of the Tropics*. 1985; rev. ed. 1991 ISBN 0-7923-1213-9; Pb 0-7923-1346-1
9. M.I. Budyko: *The Evolution of the Biosphere*. Translated from Russian. 1986
   ISBN 90-277-2140-8
10. R.S. Bortkovskii: *Air-Sea Exchange of Heat and Moisture During Storms*. Translated from Russian, rev. ed. 1987 ISBN 90-277-2346-X
11. V.E. Zuev and V.S. Komarov: *Statistical Models of the Temperature and Gaseous Components of the Atmosphere*. Translated from Russian. 1987 ISBN 90-277-2466-0
12. H. Volland: *Atmospheric Tidal and Planetary Waves*. 1988 ISBN 90-277-2630-2
13. R.B. Stull: *An Introduction to Boundary Layer Meteorology*. 1988
    ISBN 90-277-2768-6; Pb 90-277-2769-4
14. M.E. Berlyand: *Prediction and Regulation of Air Pollution*. Translated from Russian, rev. ed. 1991 ISBN 0-7923-1000-4
15. F. Baer, N.L. Canfield and J.M. Mitchell (eds.): *Climate in Human Perspective*. A tribute to Helmut E. Landsberg (1906–1985). 1991 ISBN 0-7923-1072-1
16. Ding Yihui: *Monsoons over China*. 1994 ISBN 0-7923-1757-2
17. A. Henderson-Sellers and A.-M. Hansen: *Climate Change Atlas*. Greenhouse Simulations from the Model Evaluation Consortium for Climate Assessment. 1995
    ISBN 0-7923-3465-5
18. H.R. Pruppacher and J.D. Klett: *Microphysics of Clouds and Precipitation*, 2nd rev. ed. 1997 ISBN 0-7923-4211-9; Pb 0-7923-4409-X
19. R.L. Kagan: *Averaging of Meteorological Fields*. 1997 ISBN 0-7923-4801-X
20. G.L. Geernaert (ed.): *Air-Sea Exchange: Physics, Chemistry and Dynamics*. 1999
    ISBN 0-7923-5937-2
21. G.L. Hammer, N. Nicholls and C. Mitchell (eds.): *Applications of Seasonal Climate Forecasting in Agricultural and Natural Ecosystems*. 2000 ISBN 0-7923-6270-5
22. H.A. Dijkstra: *Nonlinear Physical Oceanography*. A Dynamical Systems Approach to the Large Scale Ocean Circulation and El Niño. 2000 ISBN 0-7923-6522-4
23. Y. Shao: *Physics and Modelling of Wind Erosion*. 2000 ISBN 0-7923-6657-3
24. Yu.Z. Miropol'sky: *Dynamics of Internal Gravity Waves in the Ocean*. Edited by O.D. Shishkina. 2001 ISBN 0-7923-6935-1
25. R. Przybylak: *Variability of Air Temperature and Atmospheric Precipitation during a Period of Instrumental Observations in the Arctic*. 2002 ISBN 1-4020-0952-6
26. R. Przybylak: *The Climate of the Arctic*. 2003 ISBN 1-4020-1134-2
27. S. Raghavan: *Radar Meteorology*. 2003 ISBN 1-4020-1604-2
28. H.A. Dijkstra: *Nonlinear Physical Oceanography*. A Dynamical Systems Approach to the Large Scale Ocean Circulation and El Niño. 2nd Revised and Enlarged Edition. 2005 ISBN 1-4020-2272-7 Pb; 1-4020-2262-X
29. X. Lee, W. Massman and B. Law (eds.): *Handbook of Micrometeorology*. A Guide for Surface Flux Measurement and Analysis. 2004 ISBN 1-4020-2264-6
30. A. Gelencsér: *Carbonaceous Aerosol*. 2005 ISBN 1-4020-2886-5
31. A. Soloviev and L. Roger: *The Near-Surface Layer of the Ocean. Structure, Dynamics and Applications*. 2006 ISBN 1-4020-4052-0

32. G.P. Brasseur and S. Solomon: *Aeronomy of the Middle Atmosphere: Chemistry and Physics of the Stratosphere and Mesosphere*. 2005
ISBN 1-4020-3284-6; Pb 1-4020-3285-4
33. B. Wozniak and J. Dera: *Light Absorption and Absorbants in Sea Water*. 2006
ISBN 0-387-30753-2
34. A. Kokhanovsky: *Cloud Optics*. 2005 ISBN 1-4020-3955-7
35. T.N. Krishnamurti, H.S. Bedi, V.M. Hardiker, and L. Ramaswamy: *An Introduction to Global Spectral Modeling, 2nd Revised and Enlarged Edition*. 2006
ISBN 0-387-30254-9
36. L. Pratt and J. Whitehead: *Rotating Hydraulics.* 2007 ISBN 0-387-36639-5
37. Y. Shao: *Physics and Modelling of Wind Erosion*. 2007
38. S.R. Massel: *Ocean Waves Breaking and Marine Aerosol Fluxes*. 2007
ISBN 0-387-36638-8
39. H.M. van Aken: *The Oceanic Thermohaline Circulation*. 2006 ISBN 0-387-36637-1